Design for a logo for the MAGIC Telescope project based on a scene from the Bayeux Tapestry (about 1075 A.D.). The original scene depicts the observation of comet Halley shortly before the battle of Hastings.

Logo Design by S.M.Bradbury and D. Petry.

Design of front cover: K.F. Oetzbach, Presse- und Informationsstelle, Bergische Universität, Wuppertal

March 1998, Version 5

The MAGIC Telescope*

Design study for the construction of a 17 m Čerenkov telescope for Gamma-Astronomy above 10 GeV ‡

J. A. Barrio[1,2], G. Blanchot[12], H.G. Börst[6], O. Blanch[12], M. Bosman[12], S.M. Bradbury[1,a], M. Cavalli-Sforza[12], A. Chilingarian[13], J.L. Contreras[2], J. Cortina[2], M. Dosil[12], E. Feigl[1], D. Ferenc[7], E. Fernandez[12], J. Fernandez[1], V. Fonseca[2], H.J. Gebauer[1], J.C. González[1,2], E. Haag[1], I. Holl[1], D. Hrupec[7], A. Ibarra[2], A. Karle[10,b], H. Kornmayer[1], H. Krawcynski[3,c], X. Llompart[12], E. Lorenz[1], N. Magnussen[5], M. Mariotti[8], M. Martinez[12], M. Merck[4,d], H. Meyer[5], R. Mirzoyan[1], A. Moralejo[2], H. Möller[5], N. Müller[6], T. Odeh[5,e], A. Ostankov[12], L. Padilla[2], D. Petry[1,5], R. Plaga[1], C. Prosch[1], C. Raubenheimer[11], G. Rauterberg[6], P. Sawallisch[1], T. Schmidt[5,f], N. Turini[9], A. Wacker[1]

*This study is supported in part by the German BMBF, contract no. 05 2MP664(1), the Spanish research organisation CYCIT and the European Union TMR grant ERBFMBICT960991.

‡Contact persons: Eckart Lorenz (ecl@HEGRA1.mppmu.mpg.de) and Norbert Magnussen (magnus@wpos7.physik.uni-wuppertal.de)

1. Max-Planck-Institut für Physik, Föhringer Ring 6, D-80805 München, Germany
2. Universidad Complutense, Facultad de Ciencias Fisicas, E-28040 Madrid, Spain
3. University of Hamburg, II Inst. für Experimentalphysik, D-22761 Hamburg, Germany
4. Max-Planck-Institut für extraterrestrische Physik, D-85748 Garching, Germany
5. Universität Wuppertal, Fachbereich Physik, Gaußstr.20, D-42119 Wuppertal, Germany
6. University of Kiel, Institut für Kernphysik, Olshausenstr. 40, D-24118 Kiel, Germany
7. Ruder Boscovic Institute, 10000 Zagreb, Croatia
8. Dipartimento di Fisica & INFN Padova, I-35132 Padova, Italy
9. INFN, Sez. di Pisa, I-56010 S. Piero a Grado, Italy
10. DESY Zeuthen, Platanenallee 6, D-15738 Zeuthen, Germany
11. Space Research Unit, Potchefstroom University, ZA-2520 Potchefstroom, South Africa
12. Instituto de Fisica d'Altas Energias, Universidad Autonoma de Barcelona, E-08193 Bellaterra (Barcelona), Spain
13. Cosmic Ray Division, Yerevan Physics Institute, 2 Alikhanyan Brothers Str., Yerevan 36, Armenia

(a) present address: Dept. of Physics and Astronomy, University of Leeds, LS2 9JT, UK

(b) present address: Physics Dept., University of Wisconsin, Madison, Wisconsin, USA

(c) present address: Max-Planck-Institut für Kernphysik, Heidelberg, Germany

(d) present address: Fa. Giesecke & Devrient, Munich, Germany

(e) present address: GSI Darmstadt, Germany

(f) present address: DESY-Zeuthen, Germany

Pictures on pages 1, 13, 119, 143, 183, 189, 209, and 213 taken from 'Astronomy' by Fred Hoyle, Crescent Books, Inc., 1967.
Picture on page 35 taken from 'Cloud Chamber Photographs Of The Cosmic Radiation' by G.D. Rochester and J.G. Wilson, Pergamon Press Ltd, London, 1952.
Picture on page 53 by M.C. Escher.
Picture on page 223 taken from 'Early Astronomy' by Hugh Thurston, Springer-Verlag, 1993.

Abstract

A project to construct a 17 m ø imaging air Čerenkov telescope, dubbed MAGIC Telescope (**M**ajor **A**tmospheric **G**amma **I**maging **C**erenkov Telescope), for the observation of high energy cosmic gamma rays is described. The main aim is to explore gamma-ray sources in the up to now unexplored energy range between 20-200 GeV. The telescope will incorporate several novel features such as a high quantum efficiency (QE), red-sensitive camera, an active mirror control and a light weight construction for facilitating rapid repositioning during a gamma-ray burst search. The energy threshold will be between 10 and 30 GeV depending on the type of camera used. Red extended high QE light sensors will permit observations of sources at large zenith angles and in the presence of moonlight. It should be possible to observe high redshift, extragalactic sources which are very likely unobservable at higher energies because of the interaction of γ-rays with the IR and the 2.7 K microwave background radiation. A 5σ detection limit for point sources with a flux of $6 \cdot 10^{-11}$ cm^{-2} s^{-1} at 20-50 GeV is expected for 100 hours of 'on-source' observation time. Another advantage of this telescope will be its high sensitivity towards gamma-ray bursters (GRBs) of prolonged ($\geq$ 100 s) HE/VHE gamma emission, provided fast and precise information on the burster's position is available. We estimate that an investment of $\approx$ 6 million DM and a construction time between 2.5 and 3.5 years will be needed.

Some information for the readers

1. In order to facilitate fast reading for those not interested in details we have listed at the beginning of each chapter a series of key words and, whenever relevant, some performance parameters.
2. This document has been produced over an extended time. In order to include the latest progress and test results, additional reports are added in the appendix.
3. In some cases alternative solutions for a specific problem have been worked out. Instead of choosing only one, we opted to present alternatives as well. Some of the options are either not yet within the limits of the financial resources or need further developments. In order to distinguish the various options from the design considered at present as being the most realistic one, we have named the latter MTD96 (Model Telescope Design 96).

Contents

Appendixes on separates files

List of Figures

List of Tables

Chapter 1

Introduction

In observational astrophysics currently there exists a completely unexplored energy window in the electromagnetic spectrum from about 20 GeV to 200 GeV. The history of astronomy has shown that the opening up of a new wave band of the electromagnetic spectrum, the development of new technologies, and the application of new concepts in physics have led to revolutions in astrophysics and cosmology, and to a deeper understanding of the physical processes responsible for the origin and evolution of the Universe. In this report we present the MAGIC Telescope project for γ-ray astronomy which for the first time will allow one to explore the above-mentioned gap in the spectrum and to measure with very high sensitivity in the extended very high energy (VHE) range from 10 GeV to 100 TeV.

The cosmic-ray (CR) spectrum extends in energy up to at least 10^{20} eV. For our understanding of the Universe it is necessary to investigate the processes that generate and accelerate these energetic particles. Gamma-rays (γs) are the extremely rare messengers of these distant processes and are an important aid to our understanding of them. Below 10 GeV observations are carried out by satellite detectors which have at most only a square meter of detection area. Due to the steeply falling fluxes of γ-rays from cosmic sources with increasing energy and the above-mentioned limited surface area of the detectors their sensitivity to energies $\geq$ 10 GeV is finally limited by very low count statistics. Conversely, current ground-based air Čerenkov telescopes (ACTs) provide an effective collection area of $\geq$ 30,000 m^2 and operate at energies $\geq$ 250 GeV.

The EGRET detector on-board the Compton Gamma-Ray Observatory produced a wealth of observations of extragalactic sources [88]. High redshift sources are believed to be unobservable already above (a few) hundred GeV due to the interaction of γs with the various low-energy background photon fields such as the starlight and the infrared background. The recent observations of rapid flaring of the only extragalactic VHE γ sources that have been observed, Mkn 421, Mkn 501 and 1ES2344+514 (at distances z between 0.031 and 0.044) [2, 57, 38, 16, 106], indicate that one has to be prepared in future studies for rapidly changing signals, i.e.

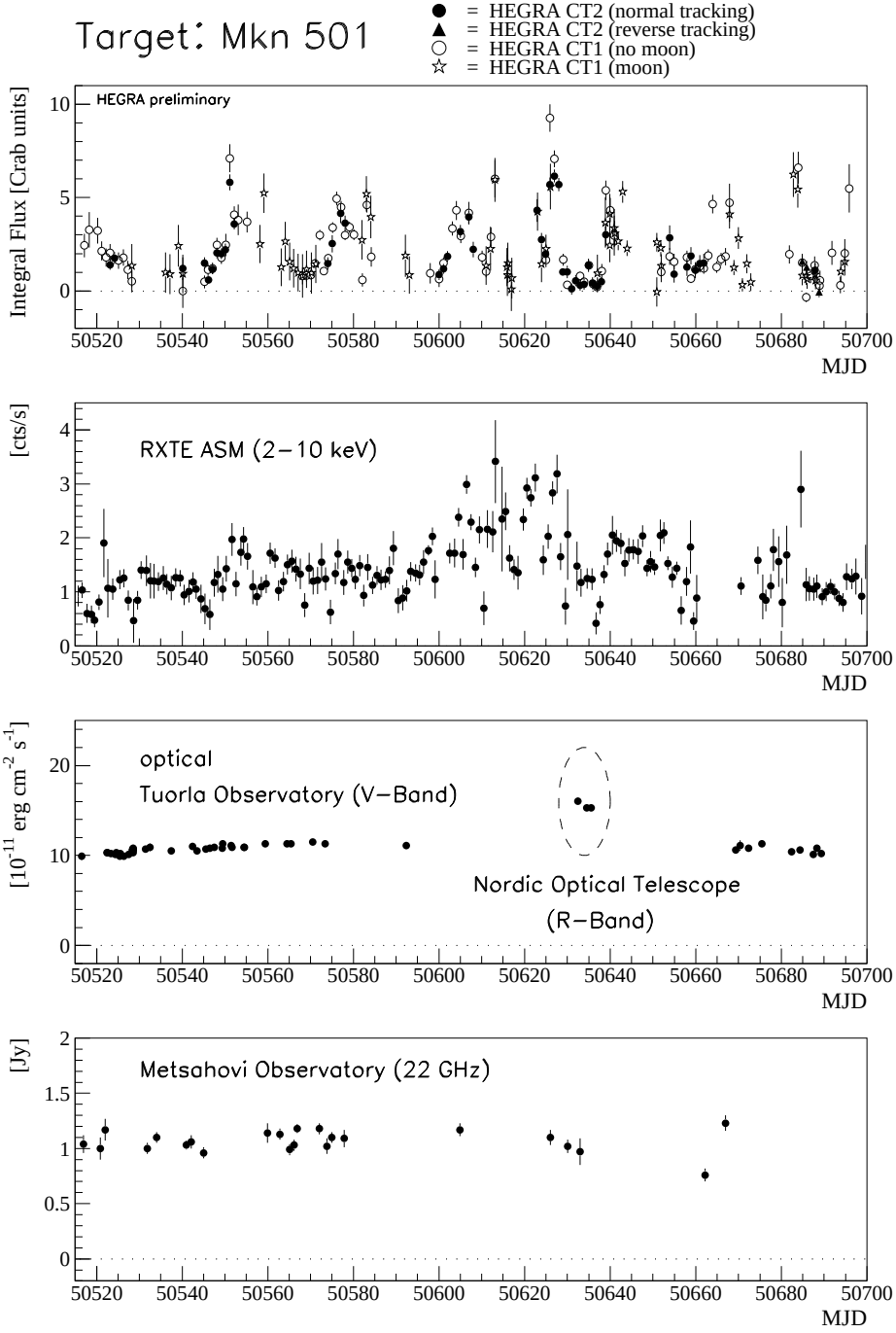

Figure 1.1: The light curves of the active galaxy Mkn 501 from March to September 1997 in the energy bands: > 1 TeV, 2 - 10 keV, optical and 22 GHz. Note that the encircled data points in the optical light curve were taken in a different filter band.

instruments with very high sensitivity are needed. As an example for rapid flaring we show in Fig. 1.1 the light curve of the active galaxy Mkn 501 for γ energies above $\approx$1 TeV as measured by the CT1 and CT2 Čerenkov telescopes of the HEGRA collaboration from March to September 1997 (top figure). In Fig. 1.1 we also show the light curves measured in selected X-ray, optical and radio energy bands by the X-ray satellite RXTE, and the Tuorla and Metsahovi observatories, respectively.

The seeming lack of γ-emission in the TeV range from shell-type supernova

remnants (SNR), which are considered to be the principal origin of cosmic-rays up to at least 10^{14} eV, may be explained by the fact that the assumed shock-wave acceleration has already faded out at a few tens of TeV. In this case γ-emission from SNRs may still be observable in the 10-100 GeV range. Also, pulsed γ emission from pulsars is expected to extend at most up to 100 GeV. Gamma-ray bursts are an enigma in high energy astrophysics. They may be in the halo of our Galaxy or at cosmological distances. A decisive test of this may come from the study of γ -emission in the GeV to TeV energy range. In summary, the exploitation of the above-mentioned energy window is of great importance and requires high sensitivity detectors. Another important consideration is that EGRET will cease operation in the near future when its gas supply is exhausted and the next high energy γ-satellite (GLAST) will only be launched in about a decade from now. We are confronted with the triple challenge of:

(i) closing the energy gap between, say, 10 GeV and 200 GeV,

(ii) having the detector ready within the next few years,

(iii) enhance the point source sensitivity by several orders of magnitude ($\geq 10^3$ times) compared to the EGRET sensitivity in the overlapping energy range.

The third point is of special interest because, for example, during the target of opportunity (ToO) campaign for Mkn 501 in spring 1997 the EGRET detector has observed the source between April 9 and 16, but no statistically significant signal has been detected. This result is remarkable, because at the same time several Čerenkov telescopes have measured the source to be in a very active phase (see e.g. Fig. 1.1 for MJD around 50550), and it illustrates the importance of performing high sensitivity measurements also in the sub-100 GeV energy domain.

There are ongoing studies into the use of solar power plants such as STACEE [86], CELESTE [84] or GRAAL [80] as sub-100 GeV air Čerenkov detectors. Their main advantage is the ready availability of a large reflector system; however, the expected performance seems to be far from optimal due to limited angular range, the non-ideal optics and the larger time spread of the signals as a result of the extended geometry. Also it seems to be very difficult to build efficient trigger systems and to develop gamma/hadron (γ/h) selection procedures for the sub-100 GeV range for solar plants. Alternatively one can push the very successful concept of large reflector telescopes, such as the Whipple telescope, by (a) increasing the light collection area, (b) using high quantum efficiency (QE) light sensors, (c) extending the upper end of the spectral range to, say, 600 nm, (d) using a very high resolution camera, (e) incorporating a high rate recording system with a powerful multistage trigger system, (f) implementing several small improvements based on the experience gathered from the operation of current ACTs.

There are certain limitations that prevent the diameter of a single telescope from being increased well beyond that of current telescopes. Based on general scaling factors in technical design, the cost of increasing the reflector area would be proportional at least to the third power of the diameter. Also there are optical problems: for a telescope with more than 20 m diameter the images are blurred to such an extend that the γ/hadron separation power strongly deteriorates[1]. The problem is linked to the fact that one has to observe an extended shower at 5-15 km above the telescope rather than to observe a point-like source as in astronomy. We propose to construct a 17 m ø reflector, following the concept of a large solar parabolic concentrator which was already built and tested a few years ago. This concentrator, which has a 17 m ø reflector dish, was built in 1987 as part of the German solar power research programme. Fig. 1.2 shows a photograph of the concentrator at its current location in Lampoldshausen near Stuttgart[2]. The octagonal reflector of the MAGIC Telescope of 236 m^2 area will be segmented and consist of 936 square mirrors of 50×50 cm^2 each and 40 triangular ones with a base length of 50 cm. For a quick-response for gamma-ray-burst searches, it is necessary to reduce the weight of the telescope to a minimum. Nevertheless, the structure must be sufficiently rigid so as to prevent deformations of the reflector during tracking. We plan to construct a light-weight space-frame by using the carbon fibre tube technology. An active mirror control will be employed to counteract the remaining small frame deformations due to the varying altitude when tracking sources as well as to facilitate optical adjustments.

The existing ACTs have a poor conversion factor of Čerenkov photons to a measurable signal, i.e. photoelectrons (ph.e.). Typical values of the conversion factors for light between 300 nm and 600 nm are 4-12%. Therefore a large potential for improvements exists. The single most promising action is to try to use photosensors of high quantum efficiency (QE) and red-extended sensitivity, provided they have low intrinsic noise. It seems possible to improve altogether the photoelectron yield by a factor of 3-5 (up to 10 for observations under large zenith angles).

The main aim of this report is to present the design of the advanced 17 m ø MAGIC Telescope. The construction will be based on a series of innovative features:

(a) a light-weight construction allowing one to reposition the telescope towards a given source coordinates within less than 60 s,

(b) diamond-machined all-aluminium light-weight mirrors with integral heating,

(c) active mirror control for optimal optics,

[1] A better solution then would be to use many telescopes and superimpose electronically the various low intensity images after the appropriate corrections have been made. However, the technology for such an approach is still in its infancy and would be very costly.

[2] During one test the reflector was damaged beyond repair and the device will soon be decommissioned. Two similar telescopes are still in operation in Saudi Arabia.

Figure 1.2: Photograph of the 17 m ø solar concentrator at its current location in Lampoldshausen near Stuttgart.

(d) novel high QE, red-extended hybrid photomultipliers allowing observations up to a zenith angle of $\sim 80^\circ$ and also in the presence of moonlight,

(e) a fast optical-fibre connection for analog data transmission from the camera to the ground station,

(f) a $\sim$300 MHz FADC readout system for improved background reduction and γ/hadron separation.

The proposed telescope will have an unprecedented light flux sensitivity of ~ 1 photon m^{-2} (300-600 nm), i.e. a factor 15 over the best existing telescopes.

This project description will deal first with the scientific motivation for the construction of such a telescope (chapter 2); then in chapter 3 general features of air

showers in the 10-200 GeV energy range will be discussed. The main part of the report is a description of the design of the telescope (chapters 4 and 5), followed by a performance Monte Carlo study (chapter 6). A series of important items (such as specific backgrounds, the observation planning, possible sites, etc.) are discussed in chapters 7-11. The cost-and-construction-time estimate will be given in chapters 12-13 followed by short presentations of the future array concept, the possible auxiliary use of the telescope, the educational prospects of the project, and the spin-offs of the technology items in chapters 14-17.

The framework of this report has been written about two years ago while some of the technology items have been newly developed or are continuously improving. Based on this framework we incorporate some of the newest developments, reflecting the rapid evolution of the entire field, in the format of appendices. Due to this constant progress in the technology of ACTs and cosmic-ray observation techniques and as a result of new concepts (proven to be successful in high energy physics experiments), better electronics, and much more powerful computers, one may expect further updates of some of the items in the future. In addition, this progress is accompanied by a better understanding of fundamental air-shower mechanisms and processes in astroparticle physics.

The second important aim of this report is that it should serve as a basis for the proposal to build such a telescope in a relatively short time and to explore unknown territory in an energy range in which many interesting phenomena can be expected.

1.1 The single telescope vs. the telescope array

At the beginning we want to stress that the formulation of the problem of comparing a single telescope with an array of telescopes is ambiguous. First, for a given type of telescope, one can compare a single one with an array of N ($N \gg 1$) identical telescopes. Obviously the price of this type of array is essentially N times the price of the single telescope. Second, within price-performance-constraints (i.e. providing a fixed budget), one can compare a single large telescope with an array of N smaller telescopes. Of course, the mechanical mount of the single large telescope will be more expensive than that of a single small telescope. However, for a given type of light sensor (e.g. classical photomultiplier tubes) and readout electronics (e.g. CAMAC or FADC), the price for the camera for a single large or a single small telescope are comparable. Note that for an imaging ACT the cost of the camera and the readout electronics constitutes a rather substantial fraction of the total price. Therefore the higher price of the large mechanical mount should be compared to the nearly N-fold price for cameras and readout electronics of an array of N smaller telescopes.

Let us now, on the basis of our present knowledge, briefly discuss the performance of a single telescope compared to that of an array of N identical telescopes located at distances ≤ 100 m (i.e. for coincident measurements).

In contrast to the observation of air fluorescence, no true stereo observation is possible with Čerenkov detectors because of the strong beaming characteristics of the Čerenkov light. This can be easily understood by observing a single straight track of, say, a meson or a muon, using 2 telescopes located at different distances from the impact point but still within the Č-light pool. In this case the more distant telescope would "see" the upper part of the track while the closer telescope would "see" only the lower section. In the case of a large shower there is a statistical spread of the direction of the secondary particles such that a pseudo-stereo observation is possible. Nevertheless, the two telescopes always see different parts of the shower unless they are at the same distance from the impact point. At lower energies the fluctuations (both in Č-light and secondary direction) in the showers are becoming large due to the small number of secondary particles and high altitudes of their development where the Čerenkov threshold is higher due to the lower air density. Only if one can measure light from the shower maximum, $x_{\max}$, and determine the accurate position of $x_{\max}$ itself one can hope to correct for the energy fluctuations which dominate over the uncertainty of measuring the impact distance with a single or multiple telescope setup.

Currently the telescope array concept is being developed by several groups. A few array installations have taken data, are in the test phase or start to take data, while some others are still under construction or have proposal status [1, 20, 53, 107, 3, 62, 97]. Although it has not yet been fully investigated, results show that in the TeV energy range an array of telescopes provides a better rejection of hadronic background as well as a somewhat better energy and angular resolution compared to a single telescope of the same type. However, for energies close to the threshold where the bulk of the data is measured, the trigger probability is still small, and an array of telescopes thus provides a significantly smaller effective collection area and correspondingly smaller rate of γ showers (for coincident events ≥ 2 telescopes must trigger) compared to a single telescope at a fixed energy in the overlapping energy range (note that an array of coincident telescopes can provide a slightly lower energy threshold compared to an identical single telescope). This large difference in the collection areas and the γ rates between a single telescope and an array of coincident telescopes becomes even more pronounced when using the large zenith angle observation technique because an air shower "sees" only the projected area of the array of telescopes.

When discussing the single telescope setup one should mention that all of the known TeV γ sources (see Fig. 2.4) have been discovered by single telescope setups and we believe that the single telescope potential is still far from being exhausted. The field of ACTs is developing rapidly and, for example, the development of new analysis techniques allow one to improve the energy as well as the angular resolutions of a single telescope [13, 100, 60]. In addition, the application of a very high resolution camera based on very high quantum efficiency light sensors in combination with an advanced readout system (i.e. recording more charge and resolving fine

structures in images) would further improve the energy and angular resolutions as well as provide a better background rejection.

Concerning the background rejection one should note that in (sub) 100 GeV γ-detection the cosmic electron flux forms an irreducible background that cannot be fully suppressed by any configuration of telescopes. Therefore, above a certain γ/hadron separation power one is dominated by the electron background and the signal/noise ratio can only be enhanced by increasing the collection area or by prolonged observation time (see further discussions in Section 8.3.2 and Chapter 10).

Let us now turn to the comparison of a single large telescope with a telescope array setup within price-performance-constraints. In the imaging air Čerenkov technique the effective detection of γs and the strong suppression of the overwhelming hadronic background is facilitated by analyzing the shape and orientation of the recorded shower images. For a successful image analysis one needs to measure a minimum number of signal ph.e.s in at least a few pixels in the imaging camera of a Čerenkov telescope. The experience has shown that one needs ≈ 100 ph.e.s per image in order to parametrize it reliably. As the Čerenkov photon density at the observation level is approximately scaling with energy, the necessary step towards extending the current ground-based measurements down into the observation gap is thus to increase the reflector area of the telescope. Providing the type of the used light sensor is chosen, the energy threshold, $E_{thres.}$, of an imaging telescope thus relates to the reflector surface area, $A_{reflector}$, as $E_{thres.} \propto 1/A_{reflector}$. If the given reflector surface area of a single large telescope will be shared between N small telescopes, located about 100 m from each other, obviously each of the latter ones and the array itself will have a $\approx N$ times higher energy threshold. Thus, a comparison of both detector performances could only be made in the limited overlapping energy range, i.e., for energies several times higher than the threshold of the large telescope (see Chapter 10 for further discussion).

Our main aim is to lower the energy threshold of the telescope down to $\sim$10 GeV in order to close the existing observation gap in the electromagnetic spectrum. Therefore we chose to first develop a single large advanced telescope. In summary the arguments are:

1. For the same amount of money one can build a single advanced large telescope with a much lower energy threshold than an array of N telescopes and explore new territories.

2. The aim of covering a solid angle of nearly 2π in the sky with stereo power would necessitate either a large array ($\gg$3 telescopes) or a movable arrangement. Either version would add significantly to the costs.

3. In the first exploratory phase it would be better to concentrate on maximizing the discovery potential rather than to optimize telescopes for a precision study of a limited number of objects at higher energies.

4. A strong argument against limiting the collection area for stereo observations is the need to maximize the sensitivity towards short-term episodic signals such as γ-ray bursts or events such as the recent 1-3 hour flare from Mkn 421 seen by the Whipple group on May 7th 1996.

   Clearly, once the first exploratory phase is finished (when the MAGIC Telescope's new technologies will also have matured), one will add more telescopes and shift the emphasis to precision studies.

Obviously, multiple telescopes provide the opportunity either to perform precision measurements or to search for multiple sources. An argument that has not yet been well studied, but which might support stereo observations concerns the handling of bright background stars. Quite often such stars, if close to the camera centre, might lead to large noise signals at the camera centre which can lead to problems in image reconstruction. Coincident observations would considerably suppress these events. In principle one should also be able to reject these events by requiring that the central pixel(s) has (have) no signal (see, for example the MC-simulated events which show (in the case of clean events with impact parameters larger than 30 m) almost no photons hitting the centre). A reflector with a minimal point spread function and small pixel size camera (e.g. where star images are confined to one pixel) will ease some of the problems.

Finally, the maturing of the field of γ-ray astronomy will soon require international observatories covering the whole energy range from 10 GeV to 100 TeV. Large amounts of international time should then be made available for outside observers. Already for the first MAGIC Telescope it is planned to make a sizable fraction of the observation time available to the community. However, the expected multitude of physics targets and tasks will soon require an observatory consisting of several MAGIC Telescopes which may then be used independently or jointly depending on the physics questions (see Appendix H).

Chapter 2

The Physics Case

Keywords: The MAGIC Telescope will explore the energy regime above 10 GeV where important astrophysics, cosmology, and particle physics questions can be addressed. It will do so with unprecedented sensitivity such that precision measurements of already known sources and first detections of a large number of weak sources above 10 GeV can be expected.

2.1 Introduction

The launch of the Compton Gamma Ray Observatory (CGRO) satellite in 1991 started a new chapter in the exploration of the high energy universe. While the window between 100 MeV and 10 GeV had already been slightly opened in the seventies by previous satellites (especially COS-B: see Fig. 2.1 for the high energy (HE) γ-ray sky before the launch of CGRO), it was now fully opened by the EGRET experiment onboard CGRO and immediately a wealth of γ-ray point sources was discovered (until now about 160). Many of these could be identified with sources known from observations at longer wavelengths, but a considerable part has remained unidentified until now (see Fig. 2.2).

The distribution of the luminosities of the EGRET sources is strongly peaked at the lower end near the sensitivity limit. This suggests that in case the sensitivity of the detector could be improved, the number of detected sources would strongly increase. In fact, a more sensitive successor to EGRET, named GLAST, is presently being planned at NASA. Careful estimations predict the launch of this new satellite to happen not before 2005.

At energies above 100 GeV, the Very High Energy (VHE) regime, the whole development has been much more recent: Fig. 2.3 shows the VHE sky before 1989. Up to that time no VHE γ-ray source had been discovered with certainty. One of the reasons was that in this energy regime only ground-based instruments can hope to reach the necessary collection area to detect significant signals from point sources of

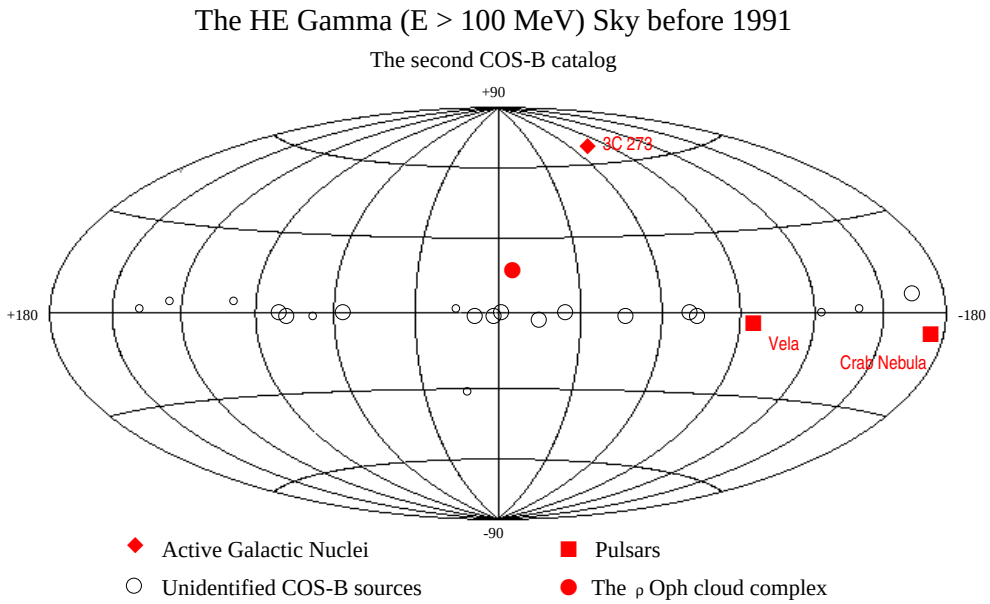

Figure 2.1: The galactic coordinates of point sources of Gamma-radiation of energy > 100 MeV as observed by the COS-B satellite experiment [95].

γ-radiation. So far, the only technology which has been able to produce convincing and significant detections is the Imaging Atmospheric Čerenkov Telescope (IACT). After the first employment of the IACT by the Whipple group in 1989 and the detection of the Crab Nebula as a source of Gamma-radiation above 500 GeV [105], several groups around the world have built such telescopes, one of the leading groups being the HEGRA collaboration with their telescopes on the Canary island La Palma (see table 10.4 for the main parameters of the leading ACTs).

Up to now, 4 sources of VHE gamma-radiation have been detected with certainty while another 7 have been detected by individual groups but need further confirmation (see Fig. 2.4).

The technology is continuously being improved in terms of sensitivity and low energy threshold. Present telescopes can detect gamma-rays above $\approx$ 200 GeV. Their sensitivity for 50 hours of observation time is between 5 and 10% of the flux of the Crab Nebula at 1 TeV which is about $1.5 \times 10^{-11}\,\mathrm{cm}^{-2}\mathrm{s}^{-1}$.

This leaves

- a large unexplored "gap" between 10 and 200 GeV
- a lack of sensitivity at TeV energies where most detectable sources are expected to show fluxes of the order of 1% of the Crab Nebula flux or less.

As for the EGRET energy regime, the number of detectable sources is expected to rise exponentially with the improvement of the sensitivity.

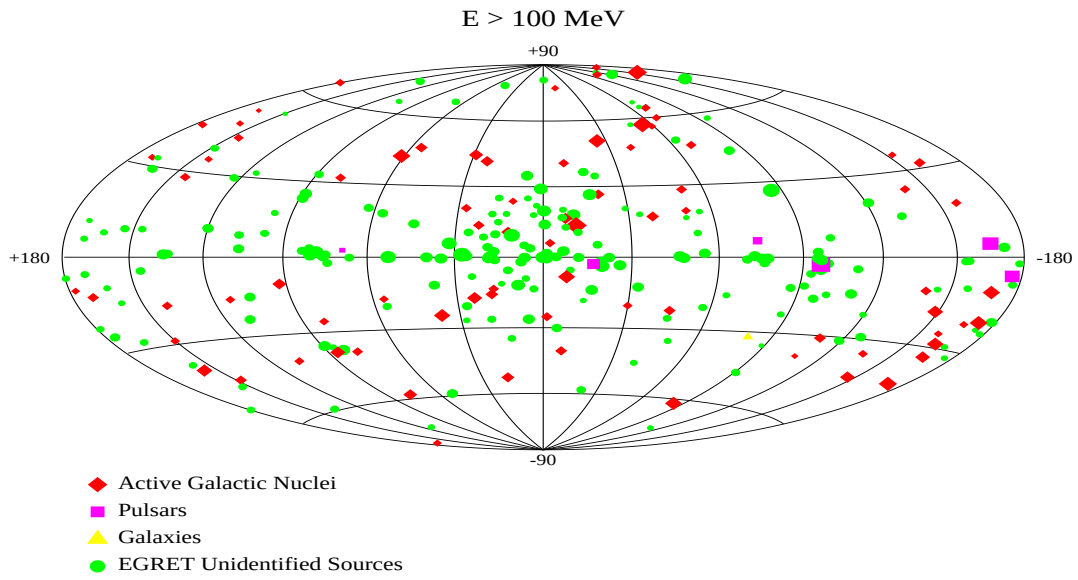

Figure 2.2: The galactic coordinates of point sources of Gamma-radiation of energy 100 MeV $< E <$ 10 GeV as observed by the EGRET experiment onboard the CGRO satellite (Courtesy G. Kanbach). For the second EGRET catalog, with slightly fewer sources, see [98, 99].

It is the aim of the MAGIC Telescope project to exploit all presently available technologies in order to obtain a Čerenkov telescope with maximum possible sensitivity above the threshold energy of 10 GeV and thus create the instrument needed to explore both the "gap" and the very high energy domain.

As it turns out, a Čerenkov telescope which accomplishes a very low threshold energy simultaneously reaches the maximum possible sensitivity at higher energies by means of large zenith angle observations. Effective collection areas of the order of $10^6\,\mathrm{m}^2$ at TeV energies can be achieved.

In the following paragraphs we discuss the main observational targets for the MAGIC Telescope and enumerate the scientific questions which the observations could help answer.

2.2 Gamma astronomy

2.2.1 Active galactic nuclei

About 1% of all galaxies are "active". An active galaxy (also active galactic nucleus, AGN) is defined by the presence of highly luminous and variable, non-thermal emis-

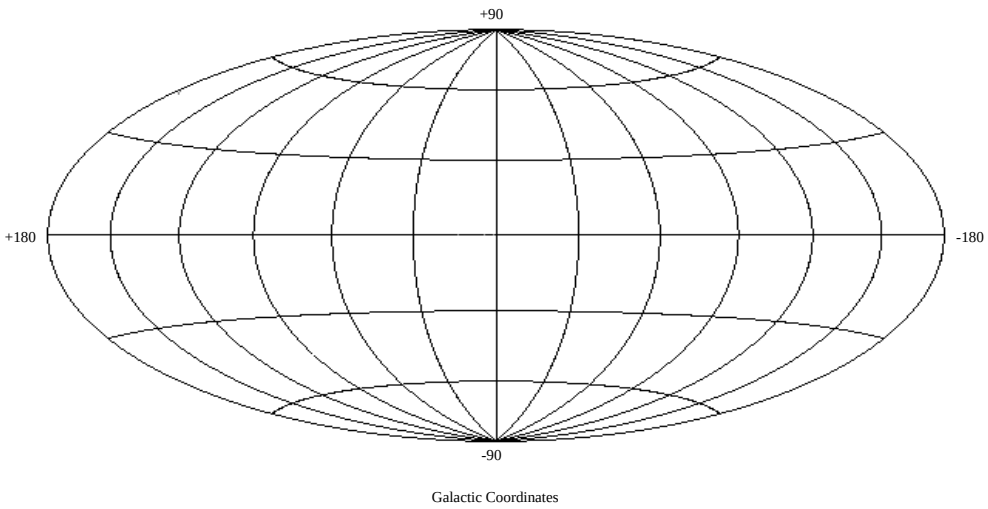

Figure 2.3: The empty VHE Gamma Ray sky ($E > 300\,\mathrm{GeV}$) before 1989 when requiring detections with high significance ($> 6\sigma$).

sion from the galaxy's core. Among the objects constituting the AGN class are Seyfert galaxies, quasi-stellar radio objects (Quasars), BL Lacertae objects (BL Lac objects), and radio galaxies. The closest systems of this type are about hundred million light years away while the most distant ones are tens of billions of light years away.

Since the detection of now more than 60 AGN by EGRET and the observation of Mkn 421 and Mkn 501 by Whipple [83, 85] and HEGRA [77, 15], attention has been focussed on the *blazar* subclass of AGN. This subclass consists of the BL Lac objects and a part of the Quasars, namely the Flat Spectrum Radio Quasars (FSRQs). Blazars are the main candidates for HE- and VHE-γ-emitters.

The key questions concerning AGN which the MAGIC Telescope will help to answer are:

- How do AGN form and develop?
- What do the jets (relativistic plasma outflows) from AGN consist of and how is this plasma accelerated?
- At what energies do the photon spectra from AGN cut off? Are the cutoffs externally or internally caused, i.e. are they due to the γ-γ-absorption in the Infrared-Background-Field or internal absorption mechanisms in the jets themselves?

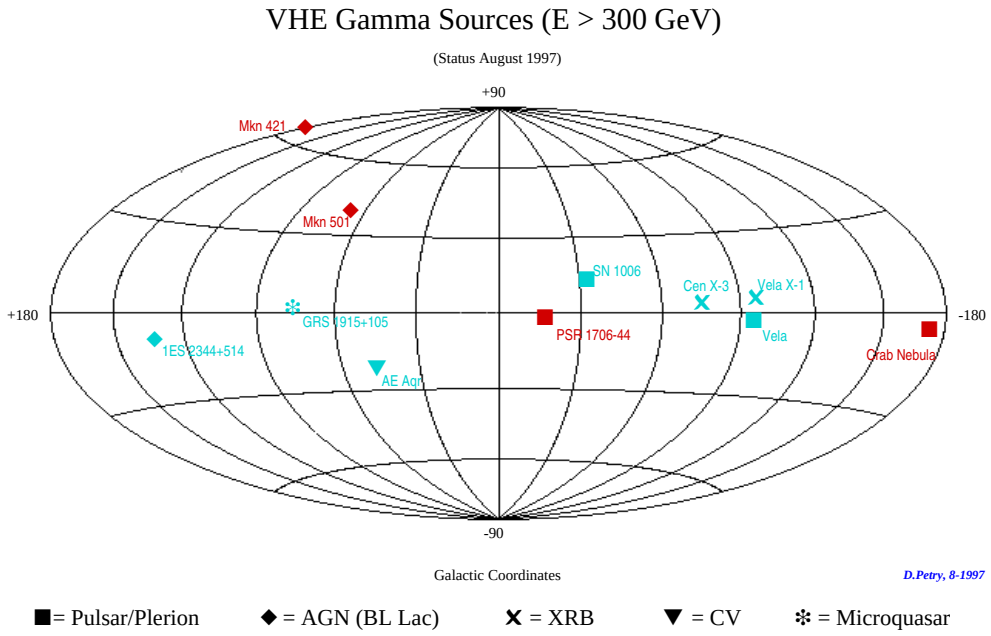

Figure 2.4: The galactic coordinates of point sources of Gamma-radiation of energy $E > 300\,\mathrm{GeV}$ as observed by the various Čerenkov telescope observatories around the world [76]. Red symbols indicate sources detected with certainty, blue symbols those which need further confirmation.

- What are the mechanisms which lead to the strong temporal variability of AGN signals in the VHE regime?
- Is there a class of "typical" VHE-γ-emitting AGN with a standard spectrum which can be used to probe the redshift-dependence of the Infrared-Background-Field and maybe the cosmological distance scales?
- Is there a class of AGN which is only visible at the highest energies and are the extragalactic EGRET unidentified sources among them?

Whether these questions can be answered depends mainly on how large a sample of sources can be detected. The more sources, the better statistical evaluations can take place. As mentioned above, we expect the number of detectable sources to rise exponentially with increasing sensitivity. It is therefore essential that the sensitivity is maximized and this is exactly what the MAGIC Telescope design group is aiming for.

The sensitivity not only decides on the number of detectable sources but also on the accuracy with which spectral and temporal features can be measured.

So far the maximum energy of photons seen from an AGN is at least 10 TeV (Mkn 501 observations in 1996 and 1997). Although the MAGIC Telescope is optimized to

reach a low energy threshold, it will be - as mentioned above - very competitive also at these highest energies of several 10 TeV because its superior light collection power combined with the high-quantum-efficiency camera will result in an extremely large collection area when observing at large zenith angles (up to ≈85°, limited by the background light conditions). Simulations indicate that collection areas up $6 \cdot 10^6$ m^2 can be reached. Here, Mie-scattering leads to a reddening of the Čerenkov spectrum produced by air showers while the larger distance to the shower maximum leads to smaller shower images in the camera. The innovative, more red-sensitive camera of the MAGIC Telescope will maximize the number of collected Čerenkov photons while the fine pixelization of the camera is adequate for the small shower images.

Fig. 2.5 shows the sensitivity levels of present experiments (for the HEGRA CT system an extrapolation of the sensitivity from the currently operational 4 telescope to the full 5 telescope system is shown). Furthermore, it shows the average spectrum of the 68 blazars detected by EGRET. The fact that up to now above 300 GeV only 3 blazars have been detected (the third one only by Whipple and only in a short flare), and that only one of these (Mkn 421) has been detected by EGRET shows two things:

1. In the unexplored gap between 10 GeV and a few hundred GeV, most of the EGRET-detected AGN must cut off. An interesting assumption, however, can be made based on the *diffuse* extragalactic γ background in the 30 MeV to 100 GeV energy range as measured by EGRET [94]. The analysis shows that the diffuse flux in this energy region can be well described by a power law spectrum with an index of -(2.10±0.03) which is very close to the *average* spectral index observed for the EGRET blazars of -(2.15±0.04) [102, 71] (see also Fig. 2.5). The assumption, as formulated in [94], is the following: if the diffuse background is the sum of emission of unresolved blazars it implies that the average *quiescent* energy spectra of blazars extend to at least 50 GeV and maybe up to 100 GeV without a significant change in slope. This, together with the fact that most EGRET AGN are undiscovered above the observation gap, makes the observation of the spectral shape of the expected cutoffs in the 50 to 100 GeV energy range especially interesting for the modeling of blazars.

2. There is probably a whole class of AGN which has its second spectral energy distribution peak in the range above 10 GeV (the first peak for blazars is normally in the UV to X-ray regime). These sources would be difficult to detect by γ-ray-satellite experiments, but the MAGIC Telescope would be an ideal tool for their exploration.

The investigation of many of the key-questions mentioned at the beginning of this section will require the integration of the MAGIC Telescope in *multi-wavelength campaigns* together with Radio, Infrared, Optical and X-ray observatories. The possibility of large zenith angle observations will widen the daily observation window

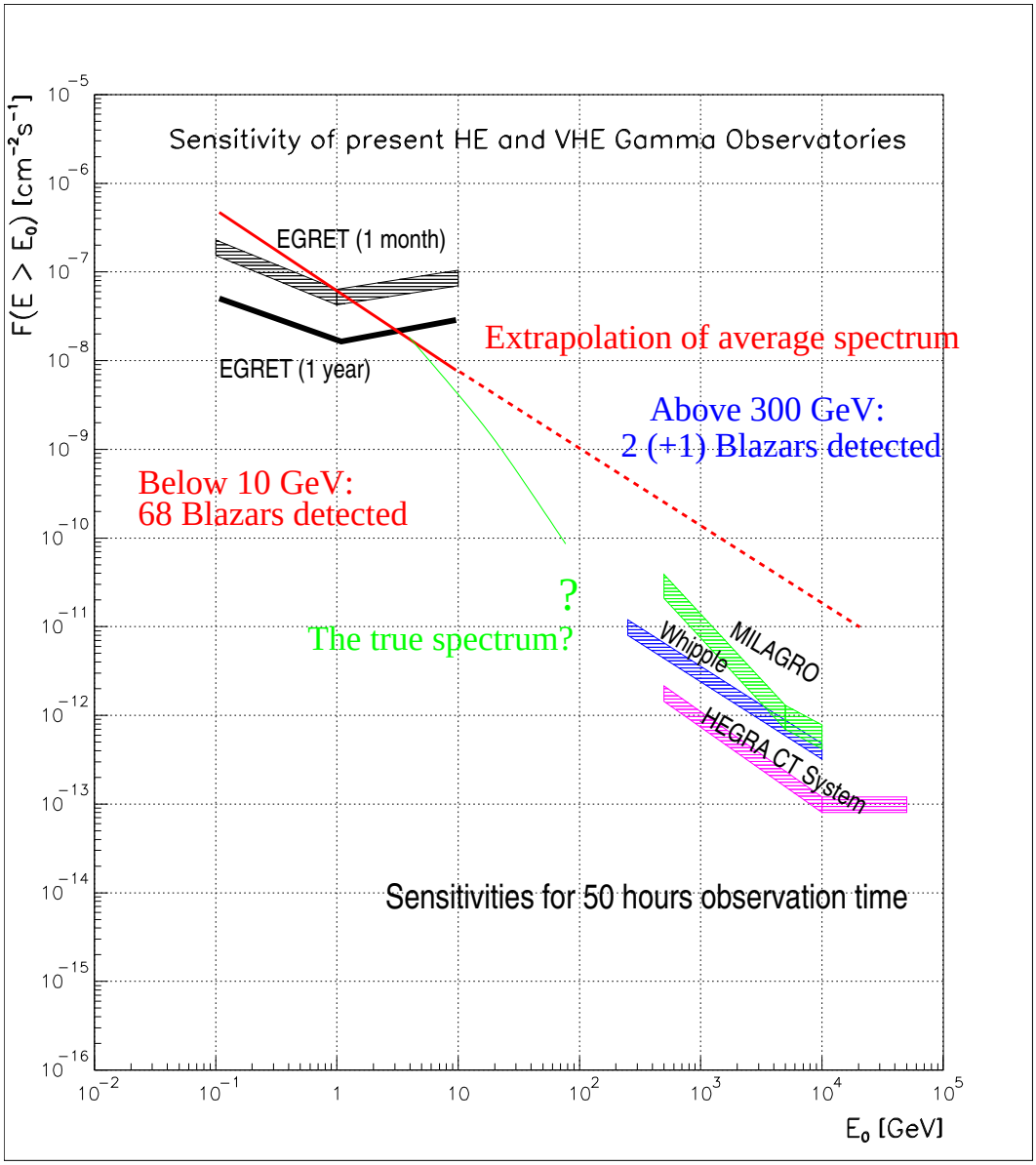

Figure 2.5: The present sensitivity levels for existing detectors in the High and Very High Energy regime. Also shown is the average spectrum of the 68 blazars (AGN) detected by EGRET (differential spectral index = 2.2) and the naive extrapolation which has not been confirmed by Čerenkov telescope experiments.

for individual sources and ease the organization of multi-wavelength campaigns with really concurrent observations.

2.2.2 Supernova remnants

The community of Supernova Remnant (SNR) experts is presently realizing that SNRs are more complex systems than previously thought. To put it with the words of Jones, Jun, Borkowski et al. [50]: "We have just started to understand SNRs and there is a long way to go." With three SNRs (Crab Nebula, Vela and SN1006) already detected at very high energies, it is indisputable that these objects can be observed at energies above 10 GeV. The theoretically favoured production mechanisms for γ-radiation are presently inverse Compton scattering of synchrotron and background field photons by VHE electrons and π^0 decay into γs after the interaction of accelerated hadrons with target matter external to the remnant.

In the mentioned article, which is a summary of the recent Minnesota SNR workshop, a long list of open questions concerning SNRs is given. The main questions to which observations with the MAGIC Telescope will be able to contribute are

- How are the particles accelerated which produce HE and VHE γ-rays in SNRs?
- In which class of SNRs do we find which production mechanism for HE and VHE γ-rays?
- Are SNRs the site of acceleration of the major part of hadronic cosmic rays? And if so, which classes of SNR are responsible for the highest energy galactic cosmic rays above the *knee* ($\approx$ 2000 TeV)?

The classification mentioned in these questions will always include features of the medium surrounding the individual SNR.

Whether measurements at energies above 10 GeV can help to solve these problems depends again on the number of sources one is able to detect. Hence, all arguments for a maximization of the sensitivity at all reachable energies apply in the same way as for the AGN in the previous section.

Presently 215 SNRs are catalogued in our galaxy. Approximately 50% of these are observable with one ground based telescope. The characterization of each of these SNRs in the region above 10 GeV is a clear-cut task which can be met by the MAGIC Telescope within a few years (assuming that also other sources are observed): Already two nights (10 hours) of observations on one SNR result in a minimum detectable flux above 10 GeV of less than 1% of the minimum detectable flux which can be reached with one year of EGRET observations.

Studies with the HEGRA Čerenkov telescope CT1 (illustrated in Figs. 2.6 and 2.7) and Monte-Carlo studies for the MAGIC Telescope (see chapter 6) have shown, that two close point sources can be resolved as separate sources if they are more than 0.2° apart. The position of an individual point source can be reconstructed to an accuracy which is only limited by the mechanical positioning accuracy of the telescope and the event statistics. We expect the absolute accuracy to be 0.01°. For

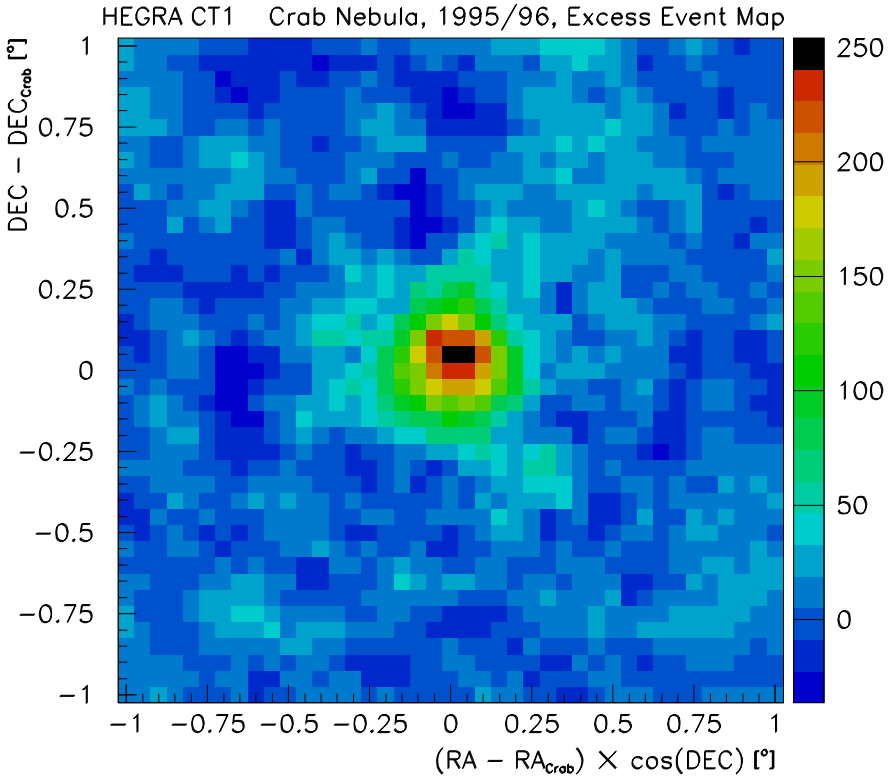

Figure 2.6: Image of the Crab Nebula above 1.5 TeV obtained with the HEGRA Čerenkov telescope CT1 [76]. The absolute pointing accuracy of CT1 is 0.02° which is about 2 times worse than what we expect for the MAGIC Telescope.

SNRs which are often larger than 0.1° in diameter, this means that the MAGIC Telescope can resolve separate emission regions in the remnant.

Again, as for the AGN, the results of the observations will have to be correlated with those at other wavelengths. However, for the mainly constant emission from SNRs there is no need for really concurrent observations.

2.2.3 Stellar accretion-driven systems

Compact stellar objects, i.e. white dwarfs, neutron stars and black holes, can very probably produce HE and maybe even VHE γ-rays if they have the chance to accrete matter. This is typically possible if they are part of a close binary system with a non-degenerate star from which matter can be extracted and fall onto the compact object. The transferred matter typically forms an accretion disk.

Although there is some scepticism about these sources, they have to be considered for the following two reasons: (a) It has been shown many times that in principle VHE gamma-rays can be produced in these systems without the need to apply new

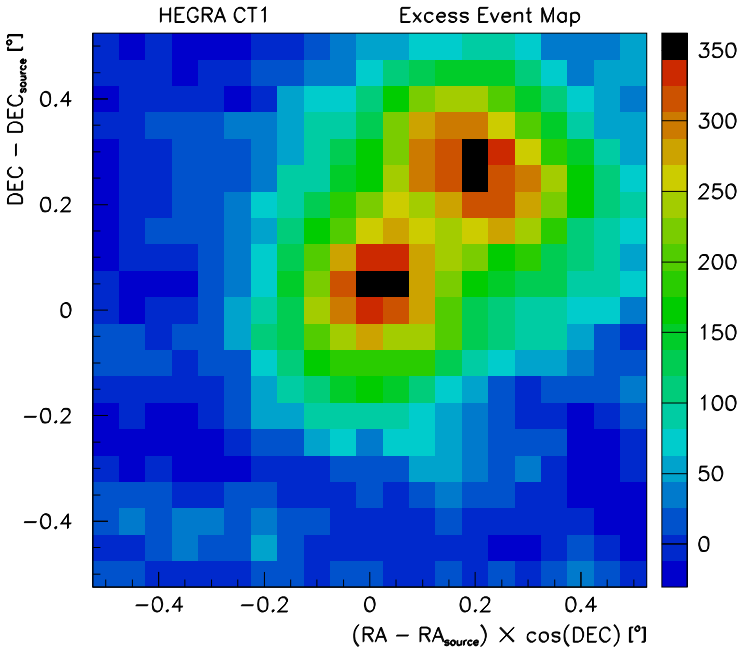

Figure 2.7: Image of a hypothetical double-source obtained from observations of the blazar Mkn 501 with the HEGRA Čerenkov telescope CT1 [76]. The source was first observed on-axis, then with a shift of 0.3° (0.212° degrees along both axes). The data was then mixed as if a weaker double-source had been observed for twice the time. The angular distance of the two sources seen in this image is reconstructed with an accuracy of 0.02° which is the tracking accuracy of the telescope. With the MAGIC Telescope we expect to reach tracking accuracies of 0.01° and minimum resolvable separations of 0.1°.

physics, and (b) both Vela X-1 and Cen X-3 have now been detected by the Durham Group above 300 GeV using the imaging technique [21]. In our context, the following systems are interesting:

2.2.3.1 X-ray binaries

In particular, the so-called high-mass X-ray binaries (HMXRBs) are prime targets since the production of VHE gamma-rays through π^0-decay in the accreting material around the neutron star is highly likely. The tell-tale periodic signature which can be expected could be of extra help in the detection process. A few examples of candidates are Her X-1, Vela X-1, Cen X-3, 4U 0115, LMC X-4 (for a review, see [19]).

Since HMXRBs are complex systems, it will be necessary to observe them in a multiwavelength mode, in which X-ray observations would be a prerequisite.

2.2.3.2 Microquasars

The term "Microquasar" was invented only recently when the first representative of this class, GRS 1915+105, was observed to have a jet of relativistic plasma traveling at a velocity of $0.92c$ [68]. The object shows strong variability and is often the strongest X-ray emitter in our Galaxy. Evidence for a TeV signal from GRS 1915+105 was reported by HEGRA at the 1996 European Cosmic Ray Symposium [4].

In a miniature version of the unified AGN model, the microquasar model introduced by Mirabel and Rodriguez [68] contains a black hole of stellar mass, an accretion disk fed by a stellar companion, and collimated relativistic jets along the rotational axis of the black hole. The microquasars are probably a subclass of the X-ray binaries.

Microquasars have many orders of magnitude smaller mass than AGN. Their lower absolute luminosity is made up for by their much smaller distance (the presently known ones are all galactic). The development of these downscaled AGN proceeds much faster and it is therefore possible to observe properties of AGN which are in the real AGN only observable over hundreds of years [68]. One can hope that the observation and monitoring of objects from this class of galactic sources will greatly help towards an understanding of the physical processes occurring in accretion on both stellar and supermassive black holes.

A reasonably complete understanding of these objects can only be reached by multi-wavelength observations. Because of their strong variability on time scales less than hours, really concurrent observations with high sensitivity are needed. Thus the arguments enumerated for AGN apply.

2.2.3.3 Cataclysmic variables

A Cataclysmic variable is made up of a white dwarf and a cool M-type secondary that fills its Roche lobe. Although these systems do not contain neutron stars, the rotation dynamics place them in the same category as neutron stars with respect to magnetic moments [67]. There have been extensive reports on the source AE Aqr as well as a report from AM Her - both magnetic CVs (of which about ten are known). The expected γ-rays are also produced when hadrons collide with accreting material, creating pions which subsequently decay into γ-rays.

2.2.4 Pulsars

2.2.4.1 Radio pulsars

Radio pulsars are the expected energy sources in Plerion type supernova remnants like the Crab Nebula and are therefore a group which should be investigated. There

are more than 800 radio-pulsars cataloged today. The questions to be addressed by MAGIC Telescope observations are:

- How do rotation-powered pulsars produce pulsed HE and VHE-γ-rays and how is this emission related to that observed at lower energies?

- What is the role of the X-ray nebulae if they exist around the pulsars?

Apart from the Crab Nebula, two more pulsars have so far been detected at very high energies: The Vela Pulsar/Plerion and PSR 1706-44. The latter is probably isolated.

Inspecting the seven radio pulsars so far discovered by EGRET [98, 99, 54], the main impression is that they all differ from each other in various respects. No two show the same multiwavelength behaviour and the pulse profiles in the GeV region are also different. The most recent theoretical model calculations [29] suggest that pulsed emission from isolated pulsars is not to be expected beyond 6 - 20 GeV if the γ-radiation originates in the vicinity of the pulsars polar region (polar cap model), but may extend to 100 GeV if the γ-radiation is produced at the light cylinder (i.e. the radial distance from the pulsar where the orbital velocity of the corotating magnetic field lines is equal to the speed of light) where discontinuities in the magnetic fields may accelerate electrons and protons (outer gap model [23, 24, 25, 90, 89]). Since both of these models have problems in describing the details of the available data, especially the measurement of the detailed structure of the uppermost end of the emission spectrum beyond the reach of the EGRET instrument is necessary to gain further insights into the pulsar acceleration mechanism.

In Fig. 2.8 and Fig. 2.9 we show examples of the energy spectra which result in case of the polar cap model for a special set of parameters applicable for the Vela pulsar in comparison to the EGRET data [29] and the characteristic phase-averaged pulsed energy spectrum for the outer gap model for a young pulsar [89].

The large model uncertainty makes it absolutely necessary to measure with high statistics in the 20 GeV to 50 GeV energy domain in order to gain further insights into the mechanism for high energy γ-ray production in pulsar systems. In addition, due to its very high sensitivity, the MAGIC Telescope will not only be an unique instrument for the study of the known γ-ray pulsars, but it will probably be able to discover several additional radio-pulsars at GeV energies.

The huge mirror area also makes the MAGIC Telescope an optical telescope with a very large aperture. The optical emission of the observed pulsar could therefore - according to our calculations - be monitored by measuring the light intensity variations of the central camera pixel with high precision. This will offer the possibility to correlate a possible γ-flux modulation with the pulsar's optical period and phase. We note that the Whipple collaboration has recently succeeded to measure the optical period of the Crab pulsar with their Čerenkov telescope [104].

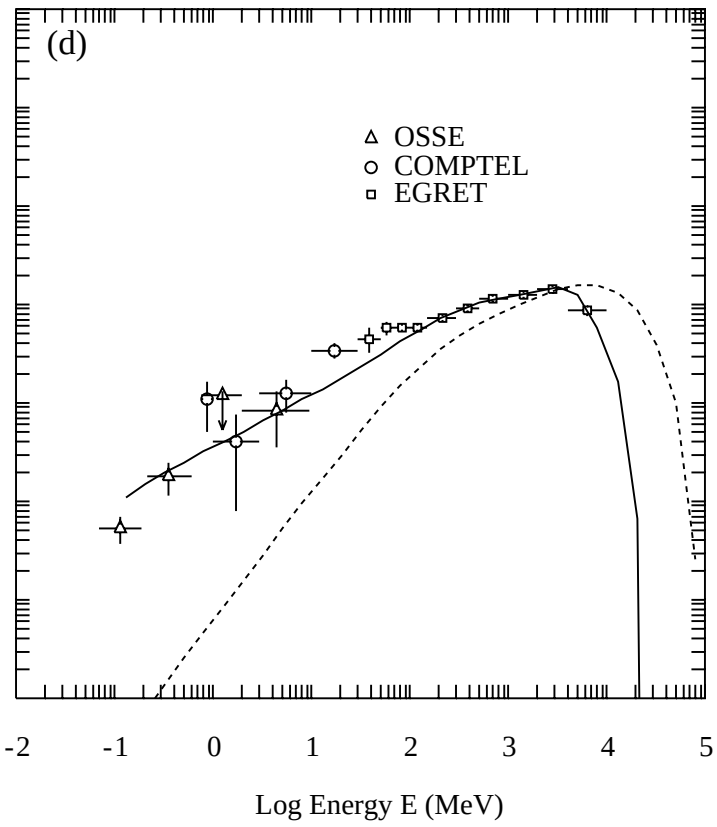

Figure 2.8: Total pulsed energy spectra for Vela model D. Solid lines show emergent cascade gamma emission and dashed lines the pure curvature radiation (CR) emission when ignoring magnetic pair production and cascade formation. Taken from [29].

2.2.4.2 Radio-quiet pulsars

Only one radio-quiet pulsar has so far been detected at high energies: the Geminga pulsar. Assuming, that Geminga is the closest object of its type, one can estimate the number of such objects in our galaxy to be ≈ 1600 [56].

By its high sensitivity, the MAGIC Telescope will be able to look for fainter Geminga-like objects which could not be detected by EGRET.

Candidates for Geminga-like pulsars are also the faint unidentified EGRET-sources which have in the EGRET-data too low signal-to-noise for periodicity analysis.

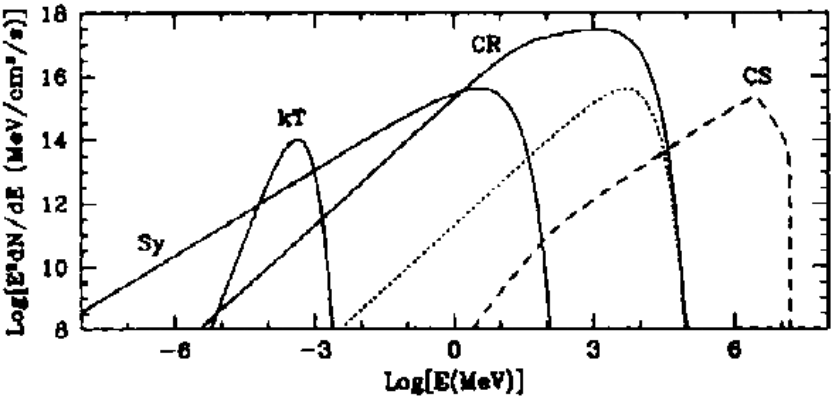

Figure 2.9: Characteristic phase-averaged energy spectrum for a young gamma ray pulsar. Solid lines show the curvature spectrum (CR), the synchrotron emission near the gap closure point (Sy), and the thermal surface flux (kT). The dashed curve shows the TeV pulsed spectrum from Compton up scattering of the synchrotron spectrum on the primary $e^{\pm}$. Taken from [89].

2.2.5 Unidentified EGRET sources

The nature of the large number of unidentified sources discovered by the EGRET experiment, can maybe be partially uncovered by a more accurate determination of their position. About 40% of these sources have hard power law spectra which seem to extend beyond 10 GeV. With the high sensitivity of the MAGIC Telescope, these objects can be located with accuracies of $\approx 0.02^{\circ}$ while the best accuracy reached by EGRET is 0.1°.

Furthermore, the increased statistics for faint objects improve the accuracy of periodicity analysis (search for radio-quiet pulsars, see the previous section). The spectral measurements beyond 10 GeV will - together with the results from EGRET - help to classify the sources and identify possible classes of couterparts from statistical arguments.

2.3 Gamma-ray bursts

Clearly the detection of only one Gamma-Ray Burst by the MAGIC Telescope and the measurement of its energy spectrum would have very important consequences for our understanding of the nature of this enigma, especially if cut-off features are detected which point to IR absorption and thus to an extragalactic origin. At the time when the MAGIC Telescope will be operational, very fast burst information from satellites with delay times of the order of a few seconds and burst position uncertainties of a few arcminutes will be available.

Although the time duration of GRBs in the BATSE energy band (20 keV - 1 MeV) varies between ms and about 1000 s, in most cases the bulk of the flux in this energy range is recorded in less than 100 s. An especially interesting GRB was observed on December 8, 1997 (GRB971208), where the duration of the single-peaked burst was longer than previously observed bursts of this type by about an order of magnitude: it lasted about 800 s. This diverse character of the GRB time structures shows that the MAGIC Telescope has a non-negligible chance to observe GRBs, if a high-energy component is emitted at all. In general two aspects of GRBs can be addressed by the MAGIC Telescope which are briefly discussed in the following.

2.3.1 Direct measurement of GRBs

Since the EGRET bursts lasted approximately 10 - 100 s, there would only be a fair chance of detecting a burst with the MAGIC Telescope if the position of the burst can be reached within 10 - 30 s. The movement should be as fast as possible, but if the telescope can be turned through 360° in one minute this would be sufficient. A burst warning from measurements in the 100 MeV region does not seem to be necessary as all EGRET bursts also showed very strong signals at lower energies. For an energy spectrum of E^{-2} the sensitivity of the MAGIC Telescope will be 75 (190) times better at 10 GeV (100 GeV) than that of EGRET at 100 MeV.

2.3.2 Delayed component

One EGRET burst shows a delayed high energy component about one hour later. No corresponding activity at lower energies has been detected. The observation of this delayed component does not demand special telescope features, except the ability to be sensitive at large zenith angles, thus increasing the time window. With its red-sensitive photo-sensors, the MAGIC Telescope will be ideal for observations at large zenith angles.

2.4 Particle physics questions

2.4.1 Search for Supersymmetric Particle Decays

Keywords: The search for supersymmetric particles is presently one of the major aims of particle physics. Most of the supersymmetric extensions of the Standard Model of particle physics predict the existence of a stable lightest supersymmetric particle (LSP) which may annihilate with a self-conjugate anti-particle into leptons, quarks or photons. The photon signal from the Galactic centre may be searched for with the MAGIC Telescope.

Assuming an inflationary cosmology with $\Omega \simeq 1$, at least 90% of the matter in the Universe must be unseen non-baryonic dark matter. In the standard theory of structure formation, where structure was initiated by an approximately scale-invariant Gaussian random field of density fluctuations, the dark matter should be preferentially cold. From COBE data the scale of the density perturbations, μ, defined as

$$\frac{\delta\rho}{\rho} \simeq \mu^2 \, G_N$$

can be estimated to

$$\mu \; \simeq \; 10^{16} \text{ GeV}$$

which is close to the usual estimate of the scale of supersymmetric grand unification. The observation of less perturbation power than expected in a pure cold dark matter scenario has led to the preferred scenario today being an admixture of hot and cold dark matter with the three contributions to Ω (assuming for the cosmological constant $\Lambda = 0$) being

$$\Omega_{cold} \; \simeq \; 0.7, \; \Omega_{hot} \; \simeq \; 0.2, \; \Omega_{baryons} \; \simeq \; 0.1.$$

From COBE and other astrophysical observations we can thus conclude that also the halo of our galaxy must contain a large fraction of non-baryonic cold dark matter.

A favourite candidate for this cold dark matter is the lightest supersymmetric particle (LSP) which is stable in many supersymmetric models because of conserved R-parity and therefore constitutes a cosmological relic of the Big Bang. In order to avoid condensation of these particles into galaxies, stars and planets, where they could in principle be detected in searches for anomalous heavy isotopes, it was argued in [32] that any supersymmetric relic LSP should be electromagnetically neutral and only possess weak interactions (weakly interacting massive particles (WIMPS)). With a light sneutrino excluded by the LEP data on the Z-width, the main contender for a detectable LSP is the neutralino, χ, which is a mixture of the photino, the two neutral Higgsinos (in the minimal supersymmetric extension of the standard Model), and the Zino. Direct searches in accelerator experiments place lower limits on its mass of

$$m_\chi \gtrsim (10 - 20) \text{ GeV}.$$

The cosmologically interesting neutralino mass range, i.e., for which

$$0.1 \lesssim \Omega_\chi \lesssim 1$$

corresponds to

$$20 \text{ GeV} \lesssim m_\chi \lesssim 300 \text{ GeV}.$$

This coincides well with the preferred mass range for the neutralino in most supersymmetric models where the upper limit on the neutralino mass is generally about 150 GeV.

Theoretical calculations show that a gas of these weakly interacting particles would concentrate around the centre of our Galaxy. Assuming that these particles do in fact constitute the dark matter within the Galaxy it thus becomes possible that two self-conjugate χ-particles may annihilate each other according to

$$\chi\chi \rightarrow l\overline{l},\ q\overline{q},\ \gamma\gamma,\ \ldots$$

which would result in a flux of stable particles ($\overline{p},\ e^+, \gamma, \nu$) in cosmic rays.

The derived actual distribution of the dark matter in different analyses and estimates, however, give a wide range of values for the expected density at the centre of the Galaxy, e.g. [48], [8], [27], [35], [37], [40], [41], [72], [73]. This wide range in density profiles translates into an uncertainty in the expected $\gamma-$fluxes of several orders of magnitude (see e.g. [10], [17]) The LSP-annihilation (precisely calculable in a given SUSY model) is expected to lead to a 2γ annihilation line (with energy $E = m\chi$) and a continuum of γ-rays at lower energies. Because the preferred mass of the LSP lies above $\approx$ 20 GeV and below about 2 TeV (from unitarity arguments), both the continuum and the line radiation are likely to be within the energy range explored by the MAGIC Telescope. The range of predicted intensities as a function of the SUSY parameter space are within reach of the MAGIC Telescope sensitivity even for those halo models that lead to comparatively low fluxes from the Galactic centre (see [17] for an extensive discussion). Fig. 2.4.1 shows the exposure (effective area times observation time) required to achieve a 3σ signal from the Galactic centre as a function of the neutralino mass and for different sets of the supersymmetric parameters applied in the calculation by Jungman and Kamionkowski [51], [52].

In order to achieve the necessary exposure the MAGIC Telescope with its very low energy threshold could e.g. aim for observing the Galactic centre exclusively under large zenith angles, i.e., with effective collection areas that are an order of magnitude larger than for observations under small zenith angles. For the Galactic centre this means observations from the northern hemisphere, i.e., from a site where, due to the different angular velocities, the Galactic centre trajectory will for longer times be visible under large zenith angles as compared to large zenith angle observations from a southern site. In conclusion, the analyses of MAGIC data on possible γ-radiation from the Galactic centre will yield important particle physics results or constraints.

2.4.2 Cosmological Magnetic Fields

Keywords: Delayed γs from transient emission phenomena, e.g. Gamma Ray Bursts, due to cascading initiated by $\gamma\gamma-$ interactions on the diffuse extragalactic background

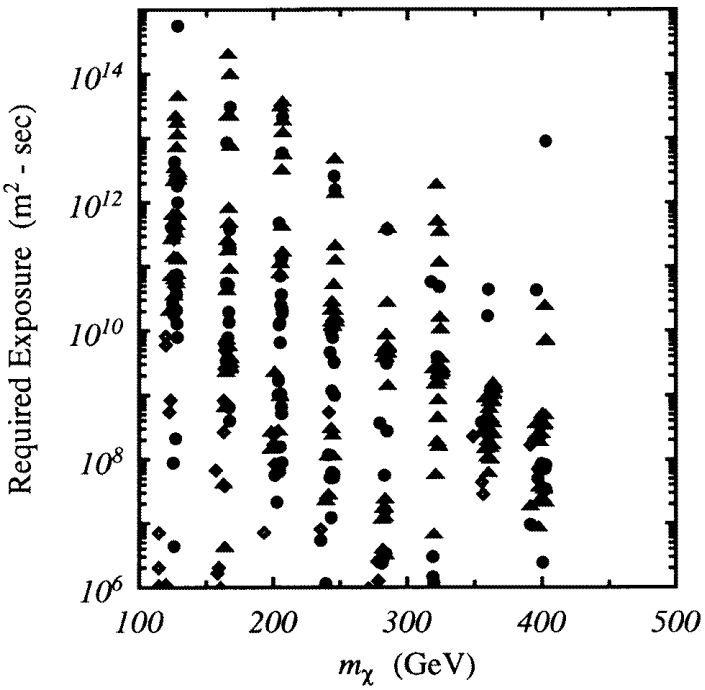

Figure 2.10: Minimum exposure, i.e., effective collection area times observation time, required for a 3σ detection of γ-rays from neutralino annihilation in the Galactic centre, versus the mass of the neutralino. The different groups of points were calculated for different sets of parameters in the supersymmetric parameter space [52]. The symbols hereby indicate different dominating amplitudes in the cross sections. See [52] for details.

fields and subsequent deflection of electrically charged particles in the electromagnetic cascades may serve to detect or constrain the still unknown intergalactic magnetic fields.

One of the prime ingredients of the Standard Model of particle physics is the concept of phase transitions. A possible signature of phase transitions which may have occurred in the early Universe are cosmological magnetic fields. Until now it is still unclear whether large-scale intergalactic magnetic fields exist. This lack of knowledge is intimately connected to the basic enigma of the origin of all the large-scale magnetic fields observed on scales like galaxies or clusters of galaxies. Among the possibilities for the origin of these fields are primordial magnetic seed fields generated during the eras of inflation, the electroweak phase transition, or the QCD phase transition in the early Universe.

Experimental information on these fields is difficult to obtain due to their expected weakness. As Plaga has shown [79] one of the possible experimental signa-

tures for large-scale magnetic fields in the intergalactic medium might come from Čerenkov telescope measurements when analysing time profiles of transient γ-sources (Gamma-Ray Bursts) or short duration flares of very high activity.

Chapter 3

Some features of air showers related to the 10-200 GeV energy range

Keywords: Air showers between 10 and 200 GeV differ significantly from TeV showers. These differences have to be taken into account for the telescope design.

In this chapter we wish to elaborate on some basic shower parameters in the 10 to 100 (200) GeV domain, examine their differences from typical TeV showers, and discuss some specific features relevant to large diameter imaging telescopes.

The reader interested in the fundamentals of particle absorption in the atmosphere (i.e. air shower development) and in air Čerenkov observation techniques is referred to the well-known basic publications in the field, for example [39, 49, 46, 33]. Here we intend to discuss only the problem of detecting γ-showers in the 10–200 GeV range (for simplicity we will refer to these showers as sub-100 GeV showers), mostly on a qualitative basis (quantitative aspects are presented in the MC simulation chapter (Chapter 6)). For the quick reader some of the qualitative features are summarized in Table 3.1.

When taking up the challenge to carry out research in the unexplored energy range between 20 and 200 GeV with "γ" satellites or ACTs, one has to take a closer look at the basic limitations of both instruments (apart from the costs, the time needed to put a new instrument into operation, etc.). Apart from a few exceptions, nearly all energetic particle processes in our universe show a power law like spectrum with coefficients mostly below -1. As a consequence, most detectors can only span one to three decades in energy. Gamma-ray satellite detectors such as EGRET are well suited for γ astronomy in the 10–10000 MeV range. On the one hand, these "γ" satellites have a very high γ/hadron separation power due to a highly efficient scintillation counter veto; on the other hand they are flux-limited because of their small collection area. Since there is a steep drop in flux as function of energy, it

Table 3.1: Qualitative comparison between 10–200 GeV and 1–5 TeV γ showers

Feature	10–200 GeV γ showers	1–5 TeV γ showers
Light flux	1–25 photons/m^2	200–1200 photons/m^2
Shower maximum	Higher, $\approx$ 12 km	Lower, $\approx$ 8 km
Shower (parameter) fluctuations	Larger	Smaller
γ shower images	More condensed, close to camera center	Images well extended principal axis well defined; some leakage out of camera
Difference between γ/h images	Generally larger	Images more similar
Natural hadron suppression	Larger	Smaller
How much more energy a proton must have for the same # ph.e.s	8–5 times	$\approx$ 2 times
Electron background	High, $\leq$ 1 % of hadron background	Lower, 0.01–0.03 % of hadron background
Telescope's sensitivity to muons	Very high	Can be made low
Resolution parameters	Worse	Better
Expected event rate	Higher	Lower

will be very difficult to raise the upper energy limit of future satellites in the next few years by more than one order of magnitude above the EGRET upper limit. On the other hand, Čerenkov light is produced in γ-induced electromagnetic showers of primary energy down to below 500 MeV, albeit with very low intensity and high up in the atmosphere.

3.1 The Čerenkov photon density caused by sub-100 GeV showers at a detector altitude of 2200 m

Keywords: 15 GeV γ showers generate a photon density of $\sim$1 photon/m^2 at 2200 m altitude.

Gamma rays interact with the atmosphere. An air mass of 1 corresponds to 27 radiation lengths (rl) and 11 hadronic absorption lengths. Air showers induced by 10–100 GeV γs have their shower maximum around 4–5 rl (i.e. at around 10–14 km a.s.l.). Table 3.2 lists the Čerenkov threshold for various particles as a function of altitude as well as the Čerenkov emission angle θ_C for $\beta = 1$ particles.

Gammas of a few GeV have sufficient energy to be able to produce air showers that contain many energetic electrons above the high altitude Čerenkov threshold. Per GeV of incident energy about 5×10^3 photons in the spectral range between

Table 3.2: Čerenkov angle ($\beta = 1$) and Čerenkov threshold energy as a function of altitude for various particles.

Altitude	Atm. depth	θ_C	Čerenkov threshold energy [GeV]				
[km]	[g/cm^{-2}]	[°]	e	μ	π	K	p
0	1036	1.33	0.0225	4.56	6.03	21.33	40.54
1	950	1.29	0.0232	4.70	6.21	22.00	41.77
2.2	800	1.21	0.0247	5.00	6.61	23.38	44.43
5	550	1.05	0.0286	5.78	7.64	27.02	51.35
10	250	0.75	0.0400	8.10	10.70	37.84	71.91
15	110	0.51	0.0586	11.86	15.66	55.41	105.30
20	55	0.36	0.0820	16.60	21.92	77.54	147.38
30	10.1	0.16	0.1890	38.25	50.53	178.73	339.69
40	2.5	0.08	0.3780	76.51	101.06	357.46	679.38

300 nm and 600 nm will be generated into a narrow forward cone. A significant fraction of these photons will be lost due to Rayleigh and/or Mie scattering and O_3 absorption because the light from low energy showers has to pass through a layer of air that is usually 8–15 km thick. Because of the natural angular spread of the shower particles (which are driven by multiple scattering in electromagnetic showers and by the transverse momentum kick in hadronic showers) and the Čerenkov emission angle, the light will be spread over a large area on ground. On the one hand, this allows one to detect showers over a large range of impact parameters; on the other hand, it dilutes the light flux to such an extent that very large collecting mirrors are needed. The basic correlation between the light flux at ground, incident energy and the type of the incident particle has recently been calculated for the STACEE experiment [22], and is shown in Fig. 3.1.

When interpreting these curves one must consider various effects:

a) The flux numbers presented have been integrated over 20 ns. Photons from hadronic showers have a significantly wider spread in time compared to photons from electromagnetic showers. This difference can be used for γ/h separation provided very fast FADCs are available and a finely pixelized camera is used. Moreover, depending on the integration time of the discriminators, the response for hadrons and γs might be different even at the trigger level. Also the time spread of photons from off axis particles will be larger due to simple geometrical effects. This can be used to determine the head-tail orientation of the shower images. At higher energies the relative differences in the time spread will be washed out.

b) Averaging over an area of 50 000 m^2 dilutes some of the local variations and ignores the light fraction falling outside this area. The light spread of γ showers is relatively smooth, with some modest enhancement at an impact distance

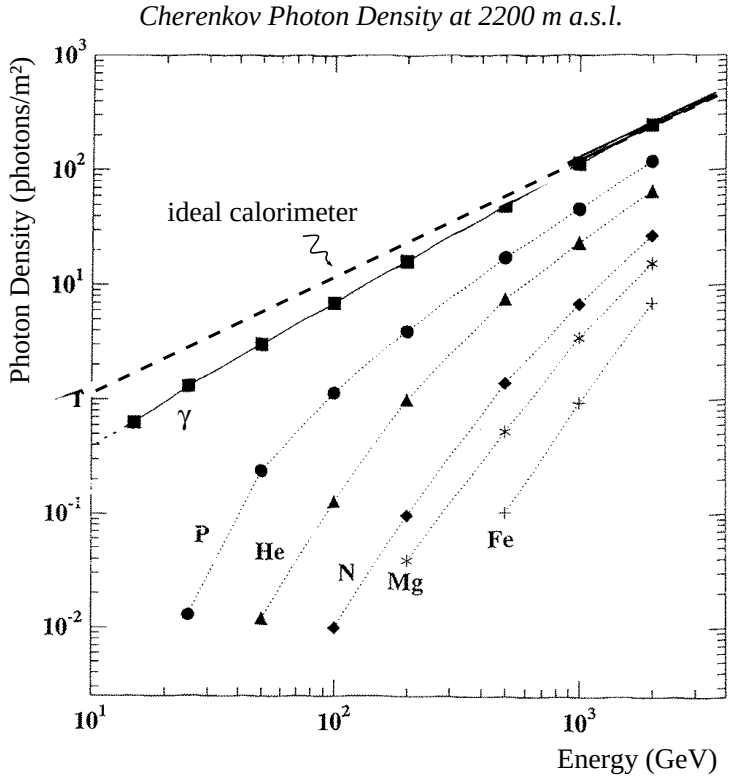

Figure 3.1: Photon density (300–600 nm) at 2000 m a.s.l. as a function of the incident energy and type of particle. The photon density is averaged over an area of 50 000 m^2. Taken from [22].

of about 80–120 m and a steep fall beyond 125 m (see Fig. 3.2). Proton (hadron) showers can produce locally much higher photon densities due to deeply penetrating hadrons (and muons from π, K decays). On the other hand, light from hadron showers can be spread to much larger distances as a result of a large transverse momentum kick exerted on some of the secondary particles.

From Fig. 3.1, one can deduce that around a γ-energy of 20 GeV only protons of $\geq$ 120 GeV will contribute significantly to the background, whereas heavy elements, such as Fe, will negligibly contribute to the background. This compares favourably with the situation above 1 TeV where the γ/proton light ratio is ≈ 2.

If one requires at least 80–100 photoelectrons per image (here we assume that the night sky background can be held significantly below this level), one needs a value for the collection area $\times$ the system quantum efficiency $\times$ photons/m^2 in the order of 100. For a 236 m^2 mirror and a system QE ≈ 0.3, one would basically achieve a γ-threshold of 10-15 GeV, i.e., one will be able to close the gap in the electromagnetic energy spectrum.

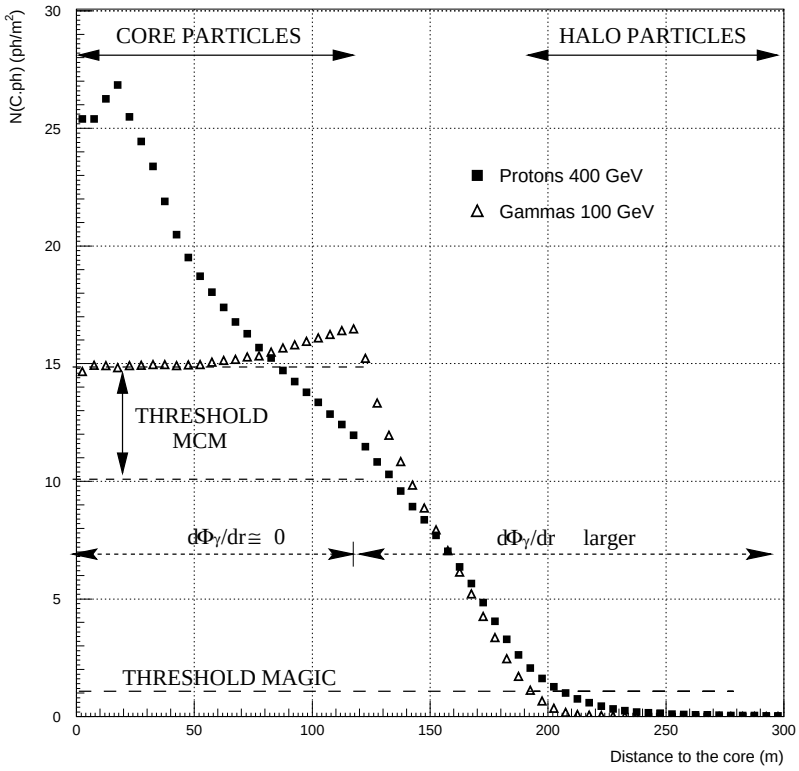

Figure 3.2: Lateral distributions of Čerenkov photon densities (N(C.ph)) for 100 GeV γ and 400 GeV proton showers at an altitude of 2220 m for vertical incidence. Threshold MCM stands for the range of threshold that could be achieved by 'Mini-Classical MAGIC' telescopes, i.e. classical 10 m ø diameter telescopes.

For a detector altitude of 2200 m, Fig. 3.2 shows the averaged lateral light flux for 100 GeV γ-showers using a linear scale. The main feature is the nearly flat distribution up to an impact distance of about 125 m. Up to about 130 m, the light is mainly generated by the "shower core" particles whereas light of $r > 130$ m originates mainly from shower halo particles. At 10 GeV the mean lateral light distribution has a very similar shape but with a slightly more peaked hump around 100-120 m and an intensity that is lower by a factor of 12 (see also MC simulations by Portocarrero and Arqueros [81]). For comparison, we have included in Fig. 3.2 the averaged radial photon density from 400 GeV proton showers of vertical incidence.

The following conclusions can be drawn from these Čerenkov light curves:

a) At 100 GeV an ACT like the MAGIC Telescope with a photon threshold of 1 photon/m^2 has a collection radius of $\approx$ 180 m (i.e., a collection area of $\approx 10^5$ m^2).

b) At large impact parameters one will only detect light from the halo particles. This light should have a larger time spread.

c) In the core area up to 130 m the gradient $\mathrm{d}\Phi/\mathrm{d}r$ and therefore the correlated gradient $\mathrm{d}E/\mathrm{d}r$ is very small and the energy resolution is weakly dependent on the error in the impact parameter determination[1]. The remaining energy error will be mainly influenced by longitudinal shower fluctuations and the depth of the shower maximum.

d) If $r > 130$ m, it will be necessary to measure it with greater precision in order to calculate the energy from the photons measured and to achieve a good energy resolution. This is not possible with a single telescope[2]. On the other hand it is obvious that one of the strengths of the stereo concept is that it makes possible a more precise determination of the impact parameter and therefore a better energy measurement for showers with an impact distance of > 130 m. Moreover, if a stereo arrangement allows one to measure the position of the shower maximum with a precision of well below 1 rl, then further improvements in energy resolution will be possible.

   From Fig. 3.2 it follows that a stereo configuration of the 10-m class telescopes with classical photomultipliers and a threshold at 10 photons/m^2 would have a γ-threshold of around 100 GeV. In first order the collection area is then the overlap of circles with a radius of 130 m around the coincident telescopes.

e) The γ/h ratio becomes less favourable at very small values of r (but with low statistics) and at very large values of r. Therefore the best range for γ/h separation will be between ≈ 40 m and 150 m.

3.2 Correlation between the diameter of the dish and the observed particle track length

Keywords: With a 17 m ø dish one records Čerenkov light over a track length of 1.7 rl ($\beta = 1$).

Since there is a correlation between the angular emission of the Čerenkov light and altitude, there exists a nearly linear relation between the "seen" length of a

[1] From the shower image parameters — width, length and concentration (and to a lesser extent from the time distribution) — one can estimate, even with a single telescope, the shower impact distance, assuming a "standard" shower development. This is a consequence of the strong "peaking" of the Čerenkov light and the small transverse spread of an electromagnetic shower.

[2] The impact of showers of large r on measurements of energy spectra is not too severe. Because the photon density drops steeply when $r > 130$, one would normally assign too low an energy to showers. In the case of steeply falling power law spectra, the data at the upper energy end would not be very much influenced.

$\beta = 1$ track and the mirror diameter of an ACT. If the track length is expressed in units of the radiation length or the hadronic absorption length one can see a straight track over the length of l [rl] = $0.1 \times \emptyset$ ($\emptyset$ in m), i.e. the 17-m dish of the MAGIC Telescope sees a track length of 1.7 rl or a hadronic absorption length of 0.7. From this follows in zeroth approximation that each on-axis, non-interacting track will produce 150–300 photoelectrons (under the assumptions of an overall system QE of 33% and 50% light loss due to Rayleigh and Mie scattering). In sub 200 GeV showers most radiating electrons have a β value slightly larger than β_C (= β at the Čerenkov threshold). Therefore, most of the electron tracks will undergo bremsstrahlung and change direction already within the field of view of the telescope; and their β values are also likely to drop below β_C. In contrast, hadrons (or muons) will mostly pass the field of view without interaction or decay. Therefore the image of a hadron shower will be more structured than that of an electromagnetic shower. For mirrors with small diameters, this structural difference would be less pronounced.

A second by-product of mirrors with large diameters is the reduced light fluctuation in a shower image. Ultimately, in a shower whose impact distance and angle are known, the energy resolution is given by the fluctuations of the small sub-showers — i.e. the energy resolution is not limited by the square root of the number of detected photoelectrons[3] ($\times$ an impact and angle-dependent conversion factor) — but by the fluctuations in the number of sub-showers. With a 17-m dish one integrates over more sub-showers and over a longer sub-shower length (see previous argument), so that fluctuations should be in first order by a factor of $\sqrt{3}$ smaller than in a case of a 10-m dish.

3.3 Use of fast-time information from individual pixels

Keywords: In shower images time spreads of a few ns can be observed.

In the new telescope all pixels will be equipped with $\geq$ 300 MHz FADCs. These are needed to reduce night-sky noise, for event buffering allowing for some trigger decision delay, and later for the use of correlated observation with other telescopes (stereo observation). Also, with the help of FADCs it should be possible to improve γ/h separation. This should function particularly well for sub-100 GeV showers where the difference in time spread between γ and hadron showers is larger than at higher energies. Even in sub-100 GeV showers all electrons producing light are ultra-relativistic, relatively confined in a small tube around the shower axis and restricted to high altitudes. In 'low' energy hadron showers many secondary particles

[3]It should be noted that one has to take the excess noise factor of the photosensors into account. For classical photomultipliers the excess noise factor F is about 1.5-2, i.e. the resolution limit for n observed photoelectrons is $\sqrt{(F \cdot n)}$.

of $\beta < \beta_C$ can produce, through π^0 production, electromagnetic sub-showers which are the generators of Čerenkov light. Because of the long flight paths involved, the small differences between the actual β and 1 are sufficient to create measurable time differences at the ns level. The effect is augmented by the transverse momentum kick in hadronic interactions, enhancing the geometrical width difference between low energy γ and hadron showers.

A quantity not yet explored in γ/h separation is the analysis of so-called islands in addition to the shower core image. With timing it is possible to test the correlation of these islands with the main shower. Hadronic showers of low energy should have a relatively large number of islands with a significant time spread in relation to the time cog of the core image. This is a consequence of the above β and p_t kick arguments. Therefore timing information from the islands should help to improve γ/h separation after the discrimination power of the shower core image analysis is exhausted.

The use of a 300 MHz FADC for each pixel will allow one to record a full correlation between time and pulse height around the mean event time with about 1 ns resolution.

3.4 Correlation between γ-energy and Čerenkov light in sub-100 GeV showers

Keywords: The photon intensity is a good measure of the incident energy up to 130 m impact parameter.

Čerenkov light is considered to be a good measure of the incident particle energy. For $\beta \approx 1$ or $\beta \gg \beta_C$ particles, the ionisation loss is proportional to the amount of emitted Čerenkov photons. In VHE electromagnetic showers the proportional relationships between ultra-relativistic electrons and the initial energy is reasonably well fulfilled, and fluctuations are small due to the enormous number of secondary electrons. The only remaining effect is the "running" refractive index with altitude resulting in a larger light signal for showers with their maximum deeper in the atmosphere (see for example Fig. 2 in ref. [65]). In sub-100 GeV showers less and less electrons will be above the Čerenkov threshold and fluctuations become more important. For example a 100 MeV $\gamma \rightarrow e^+e^-$ conversion at 15 km altitude might produce electrons of nearly equal energy and therefore produce no light, whereas in the case of an asymmetric decay one electron might emit photons. Similar arguments hold for the variation of the shower maximum and shower spread which increase with decreasing energy. Therefore the measurement of energy in low-energy showers become less and less precise and the error increases well beyond the $\sqrt{(\text{number of photoelectrons})}$ value. A simple estimate shows that around 10 GeV

an energy resolution of only 50% could be achieved, regardless of whether a single large dish or a stereo arrangement is used.

3.5 Images of sub-100 GeV γ showers

Keywords: Images of sub-100 GeV γ showers are small and condensed.

Electromagnetic showers of 10–200 GeV energy will have their shower maximum around 4–6 rl, i.e. they will be far away even from a telescope installed at 2200 m asl. Because of the previously discussed high Čerenkov threshold in the upper layers of our atmosphere, the light producing section of these low energy showers will be further restricted to the upper part of the shower, i.e. the visible shower will be further away and the telescope will see only a very short image close to the camera center. This has two consequences:

(a) The principal shower axis of the image is less precisely defined than for higher energy showers and the shower image is very concentrated.

(b) The trigger area can be restricted to a small disk around the camera center.

A follow-up consequence of (a) for the design of the camera is that the required pixel size must allow one to still extract meaningful values for the image parameters, i.e. the pixel size must be much smaller than the image size (or the image structure one can use for γ/h separation). A further follow-up argument is that the quality of the mirror optics must be adapted to a small pixel size.

A follow-up argument of (b) is that the camera diameter for recording the full image can be smaller than that for the TeV energy range.

As the MAGIC Telescope should also be used for TeV γ-astronomy, a simple solution is to extend the camera section needed for sub-100 GeV observations by a ring of classical photo multiplier tubes (PMTs) so that the VHE shower images would be fully contained. Because of the large collection area, lower QE photodetectors are more than sufficient (except for γ/h separation where low energy hadron shower images are spread over a larger camera section compared to sub-100 GeV γ-images and a large camera with only high QE pixels would be beneficial). Another motivation for building a large high QE camera would be the search for and study of extended sources.

3.6 Low energy showers at large zenith angles

Keywords: At large zenith angles shower images are close to the camera axis and the UV-Čerenkov light is strongly suppressed.

One of the aims of the MAGIC Telescope collaboration will be to carry out observations at large zenith angles, either of sources that culminate at large zenith angles, such as sources in the southern sky observed from a northern location or sources that one wants to study over long periods in a year. For example, the recently flaring AGN Mkn 501 could be observed from the La Palma site regularly for at least 9 months for at least one hour per night by tracking the source down to a zenith angle of 75°. If one could track the source down to 85°, one could sample Mkn 501 nearly the whole year round.

At large zenith angles the showers of low energy γs would be entirely confined to the upper layer of the atmosphere. Therefore all the previously given arguments about fluctuations, rising threshold, small images etc. would be even more valid. The most noticeable effect would be the rise of the threshold, being a consequence of:

(a) the higher Čerenkov threshold and in turn the lower fraction of electrons producing light and larger fluctuations;

(b) the lower photon density at the position of the telescope because of the larger distance. In first order the $1/r^2$ dilution is partly compensated for by a smaller Čerenkov emission angle;

(c) increased photon loss due to Rayleigh and Mie scattering.

On the other hand nature offers some compensation:

(a) The collection area will be much larger than for small zenith angle observations, see [93];

(b) Čerenkov light from hadron showers will be even more suppressed and images will be relatively more extended, the time spread in the images will also be enlarged;

(c) The number of muons will increase because the decay length of π, K stays constant while the geometrical interaction length increases. In the case of the MAGIC Telescope, one can use muon images for γ/h separation; the suppression of hadrons should thus improve.

3.7 Low energy shower observation with red-extended photosensors

Keywords: Red-extended photosensors increase the sensitivity to low energy showers.

As mentioned above, sub-100 GeV γ showers are confined to the upper layer of the atmosphere. Until the Čerenkov light reaches the ground-based detector, it has to pass at least 5-10 km of air which absorbs or scatters part of the photons. This loss/scattering increases dramatically when observations are made at large zenith angles. The dominant loss is due to Rayleigh scattering, which might completely suppress the UV component of the Čerenkov light, while also reducing the blue component for large angle observations. For example, at a zenith angle of 80° the light has to pass through nearly 4.5 air masses as opposed to 0° zenith angle where it has to pass through an air mass of only 1. The change of the spectrum can be well observed from the solar spectrum seen through different air masses (see Fig. 3.3). As low energy showers are already absorbed in the first 0.3 air masses, the solar curves are quite representative for the spectral attenuation of low-energy γ-showers (see also the O_3 discussion below). Therefore the use of photosensors with high red sensitivity is beneficial. Simulations show that at a zenith angle of 70° a high QE, red extended camera should "see" about 4.5 to 8 times more (for Hybrid PMT or avalanche photo diode, respectively) more photoelectrons than do cameras equipped with classical Bialkali PMTs. In the zenith position the corresponding gains are about 3.9 and 7. We did not yet perform extended simulations at even larger zenith angles. From Fig. 3.3 is it clear, however, that one would achieve a further increase in the relative gain factor, i.e. the ratio of the large zenith angle gain to the gain at 0° when using red-extended sensors.

Since TeV γ showers have nearly all their energy absorbed below an altitude of 12 km (zenith position), their Čerenkov light is only modestly affected by O_3 absorption above 300 nm. On the other hand at large zenith angles small showers are already stopped above 16 km distance from the detector. Depending on the latitude and time of the year, the ozone layer of the earth's atmosphere can reach down to 12 km and the tail of the O_3 absorption can influence the Čerenkov light above 300 nm. Fig. 3.4 shows the spectral absorption curve of Ozone [31] while Fig. 3.5 [31] shows the atmospheric ozone distribution as a function of altitude, latitude and winter/summer time. Tropical, subtropical and temperate-zone sites are much better suited than more northern or southern sites, with the exception of a site at the South Pole at which observations are made during the Antarctic winter and where the ozone layer has beed depleted by man-made air pollution.

It is obvious that the O_3 absorption has to be taken in to account (and even the difference between summer and winter) when making a precise study of the energy spectra in the 10-100 GeV range.

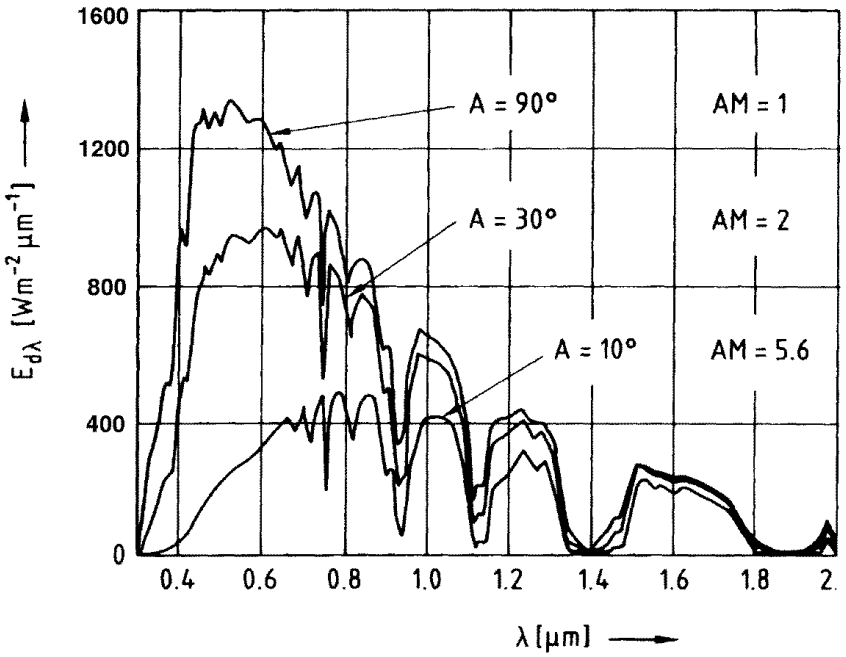

Figure 3.3: Solar spectrum seen through different air masses. "A" stands for the elevation angle. Taken from [111].

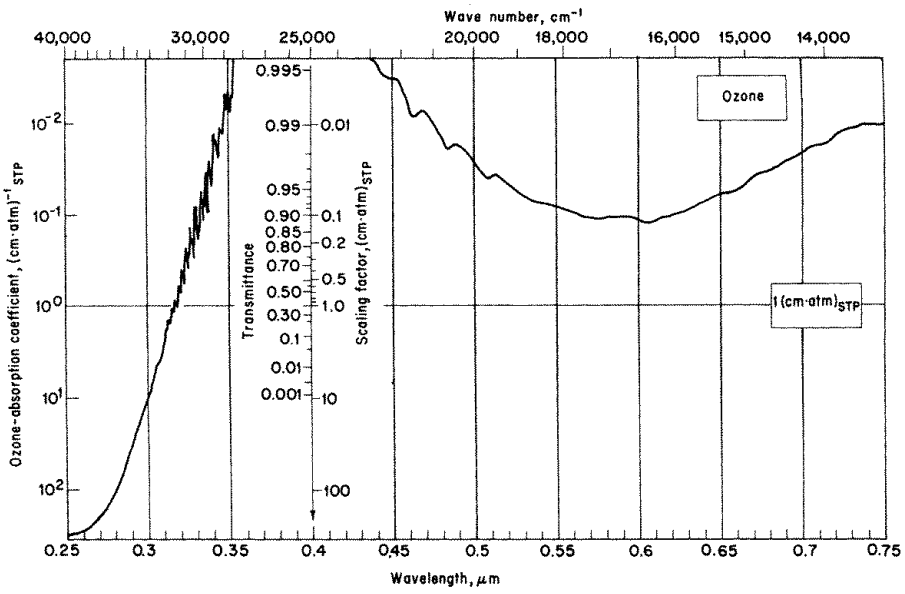

Figure 3.4: Ozone absorption as a function of wavelength. Taken from [31].

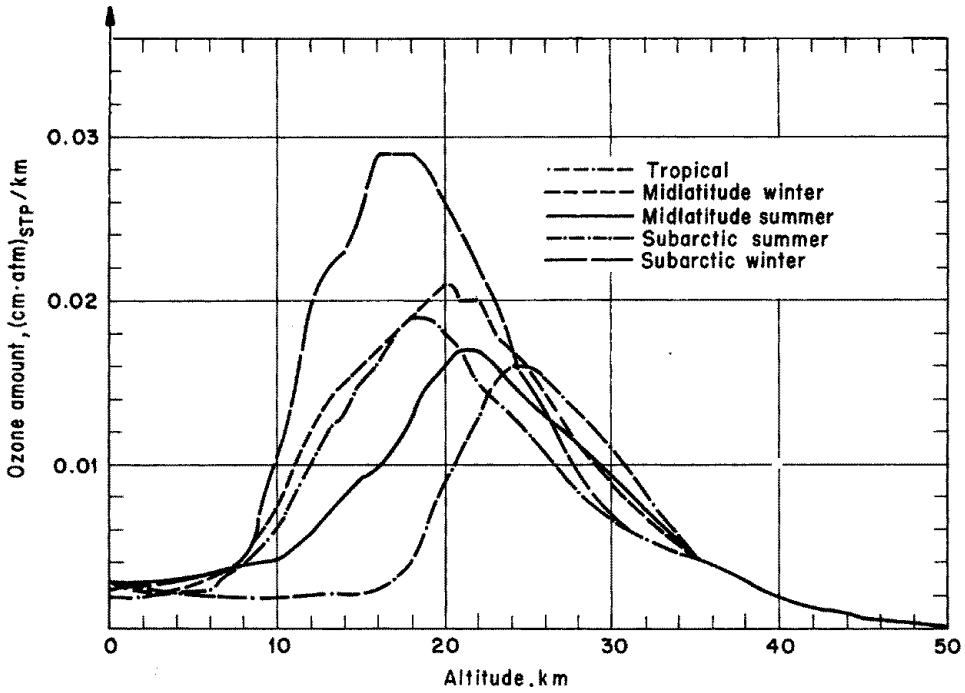

Figure 3.5: Concentration of atmospheric ozone as a function of altitude. The various curves show the influence of the parameters latitude and season. Taken from [31].

3.8 Measurements in the presence of moonlight

Keywords: Measurement in the presence of moonlight can double the observation time.

This section is not specifically concerned with the observation of low energy showers but is a natural extension of the argumentation in favour of using red-extended photosensors.

Recently it was shown by HEGRA that it is possible to carry out observations in the presence of moonlight by reducing slightly the PMT high tension (HT) or the gain [87]. In turn the detection threshold will rise.

Sunlight is scattered from the lunar surface without significant changes in the spectral distribution. Therefore the moonlight scattered by the atmosphere exhibits the same colour distribution as the sunlight scattered by the atmosphere (i.e. the night sky is also 'blue'). Fig. 3.6 shows the spectral distribution of the scattered sunlight as a function of the visibility length, which is also a measure of the aerosol scattering. It is expected that most sites have a visibility that is even better than that described by curve A, which peaks around 400 nm. Therefore, by using red-extended sensors, one will not suppress the blue moonlight but rather enhance the signal over the background. Of course, the photocathode must be able to handle

the increased background light.

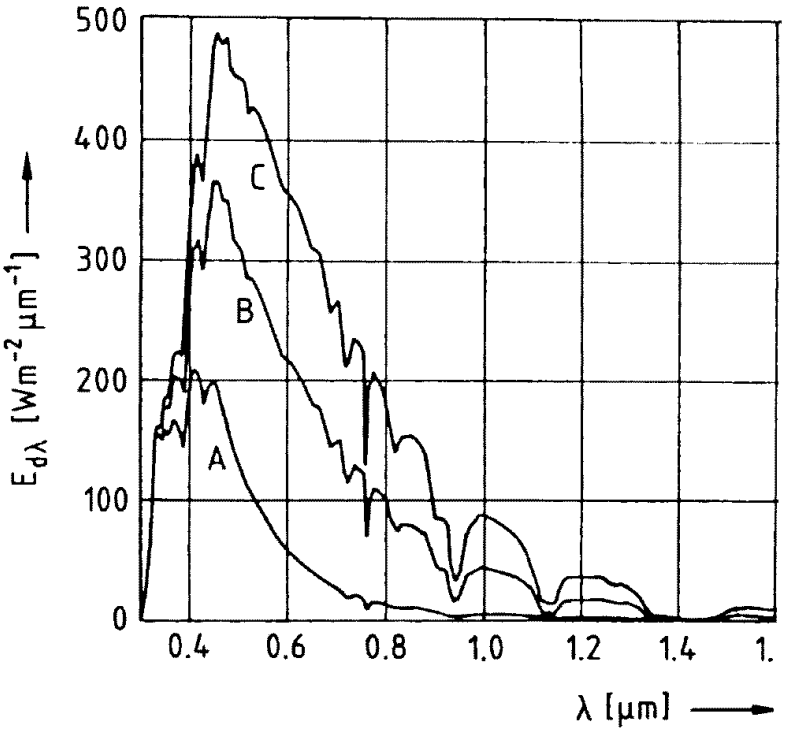

Figure 3.6: Spectral distribution of the clear day-time sky. Parameters A, B, C correspond to improving visibility due to less and less aerosol scattering, respectively. Taken from [111].

3.9 Selection of low energy γ shower images

Keywords: At low energies shower images change rapidly with energy. New energy-dependent selection procedures are needed.

Historically, γ-events were selected by applying a fixed set of cuts to the so-called image parameters, reconstructed from the pixel information of a fine granularity camera. Recently, refined cut procedures were developed by various groups, taking into account the change of image parameters as a function of energy (correlated quantity: number of photoelectrons, also called SIZE), the impact parameter (correlated quantity DISTANCE) and the zenith angle. Fig. 3.7 shows an example of the improvement from a recent observation of Mkn 501 with the HEGRA prototype telescope. Applying 'dynamical' Supercuts [59] to the shape of the shower one could

reduce the hadronic background by a factor of ≈ 60 while losing only 35% of all γ-candidates.

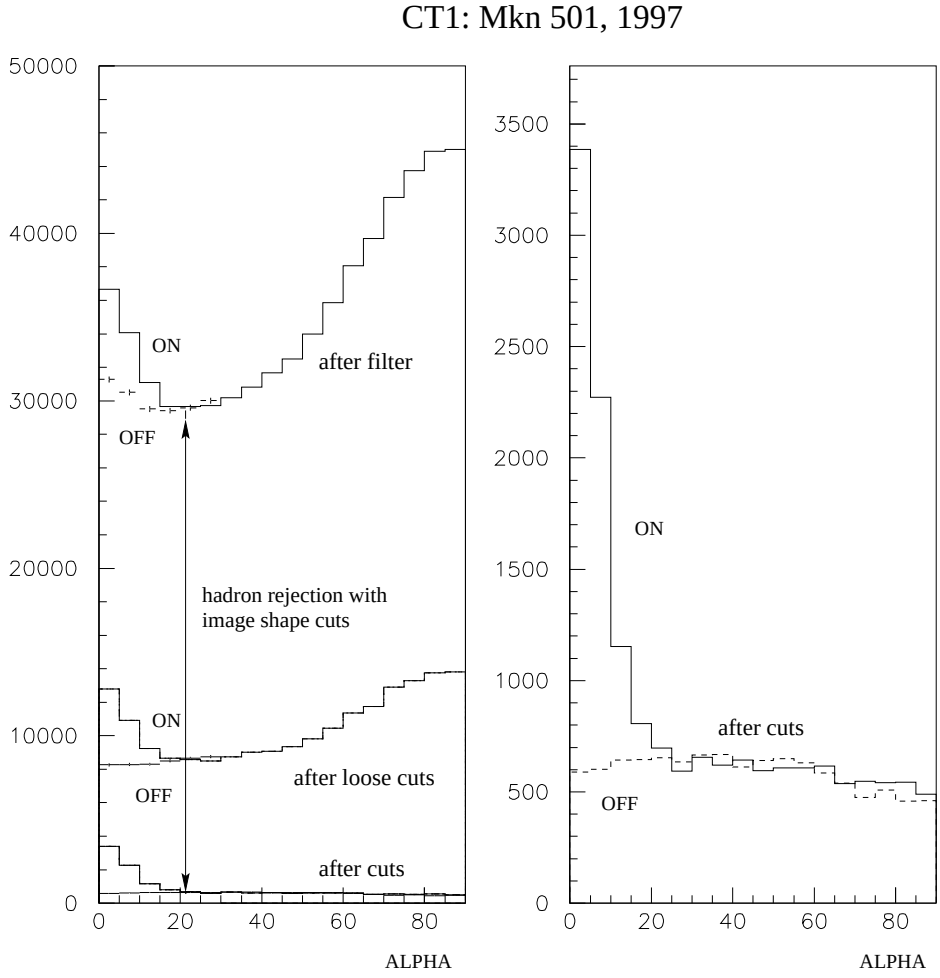

Figure 3.7: Example of the presently possible γ/h separation from a recent observation of Mkn 501 with the HEGRA prototype telescope. The γ-induced events are those with small ALPHA values (typical cut values are at ALPHA $< 10°$). Right figure: the ALPHA distribution after cuts from the left figure depicted on an expanded scale.

Extending the range of operation into a domain where fluctuations (and hence image parameter variations) will be larger compared to the TeV domain, one has to improve the dynamical cuts still further in order to exploit the full power of the MAGIC Telescope.

The presently used procedure of second-moment analysis has proved highly successful for finding the first VHE γ sources. Nevertheless, it is obvious that, with finer pixels, the shower images will contain more information which could be used for further improving γ/h separation.

Chapter 4

The basic design

Keywords: MTD96 reference design and parameters of the telescope

Figure 4.1 shows an overall design of the 17 m ø MTD96 configuration.

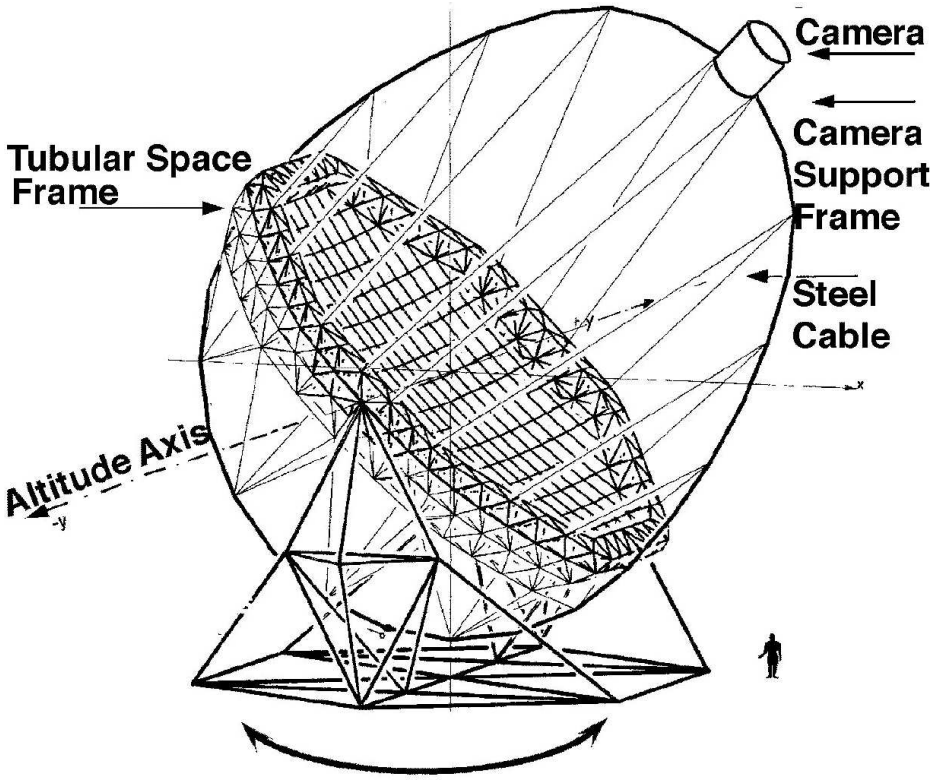

Figure 4.1: The basic design of the MTD96 telescope.

The basic elements are:

i) a concrete foundation with a circular rail of 20 (18) m diameter and a central axis.

ii) the azimuth undercarriage with 4 (6) bogeys and the motors for the azimuth rotation

iii) a tubular space frame with a basked like reinforcement ring supporting the tessellated reflector

iv) the 236 m^2 tessellated reflector

v) the declination drive ring sector and the declination drive motor

vi) the camera support frame (gothic arc shaped) fixed with cables to the declination axis stubs and space frame reinforcement ring

vii) the fine granularity photosensors camera

In addition, the telescope will have a control room with the data acquisition system and various auxiliary elements needed for safety, backup etc. These elements are all omitted in Fig. 4.1 but will be discussed later. The telescope will not have a protective dome. Table 4.1 summarizes the essential telescope parameters

Table 4.1: Telescope parameters

1. Gross reflector geometry: octagonal, $\approx$ 17 m diameter, edges 4 $\times$ 7 m, 4 $\times$ 7.07 m ($= 5 \times \sqrt{2}$); gross area: 239 m^2

2. Individual mirrors: 49.5 $\times$ 49.5 cm = 2450 cm^2

   - Number of full mirrors : 936,
   - number of 1/2 mirrors: 40
     - light weight, diamond turned, sandwich aluminium mirrors with internal heating

   Total reflecting surface: 236 m^2

3. Focal length of reflector: 17 m
   f/d = 1

4. Gross reflector shape: parabolic (isochronous within < 0.3 ns)

5. Adjustment of individual mirrors: for a point source at 10 km a. s. l.

6. Angular range for telescope: $\geq 400°$ in φ, $+110°$, $-80°$ in Θ
7. Stability parameters:
    - Mirror frame deformation within $\Delta\Theta = 180°$: < 3 mm against reference curvature
    - Focal point spread for individual mirror elements: < 5 mm (80% of light)
    - Focal point spread of gross mirror < 8 mm (80% of light)
8. Rotation time of telescope: < 30 s for 70% of the sky; < 1 min for any point on sky
9. Telescope mass, moveable section: ≤ 30 tons
10. Shadowing of structure above reflector plane: ≤ 4 m^2
11. Tracking precision: $\sim 0.01°$
12. Mechanical control of telescope angular position: by 14-bit shaft encoders, gray coded
13. Video control of camera position relative to star position ≥ 9 mag.: $\leq 0.01°$
14. Limit to resist wind speed: operation in any position up to 70 km h^{-1}.
    In minimal wind resistance position: ≥ 165 km h^{-1}, 3 cm ice layer.
15. Camera ø: 3.6° (staged : 4–5° ø)
    - Central high resolution section: 1.25° radius
    - Low resolution section ring: 1.25° – 1.8°
16. Sensors:
    - High QE red extended IPCs in high resolution area
    - Standard 2" Bialkali PMs in outer ring (later also high QE sensors)
17. Pixel geometry and size:
    - Hexagonal, small axis 0.10° in high resolution ring
    - Hexagonal, small axis 0.24° in low resolution ring
18. Active light collection area: $> 97\%$
19. Trigger area diameter: 1.6°

20. Gain of light sensors: 10 000 – 50 000, followed by AC coupled amplifiers

21. Analog signal transport to control room: optical fibers.

22. Readout: 8-bit $\geq$ 250 MHz FADC, $\geq$ 10 K byte deep memory, 1 electron $\equiv$ 2 channels, dynamic range 1–125 e: linear, 125–5000 e: log scale (time over threshold)

23. Trigger: Multi-level trigger (2 hardware, 1 software)

24. Max. sustained event rate to be stored: 1 KHz

In the following sections, the various components are described in detail and often alternatives are discussed. In such cases the preferred solution is noted as the MTD 96 design.

4.1 The alt-azimuth mount

Keywords: The telescope has an alt-azimuth mount following the concept of a 17 m ø solar concentrator

The weight of the moving parts of the telescope, i.e. the reflector and support structure, should be as low as possible in order to permit very fast turns and repositioning. We aim for a weight of 8–9 tons for the mirrors and the dish. To this one has to add $\sim$ 1 ton for the camera ($<$ 150 kg), camera support ring (250 kg) and drive ring section ($\approx$ 600 kg) and $\sim$ 0–1 ton of counter weight.

The MAGIC Telescope has an alt-azimuth mount. The design follows a 17 m solar concentrator of the DFVLR. The MTD96 lateral reflector geometry will be approximated by an octagon of 7 m side length, i.e. by an inscribed circle of about 17 m diameter. The reflector is a tessellated one composed of $\approx 50 \times 50$ cm^2 elements. The gross reflector profile follows a parabola for minimal time spread while the individual mirror elements are spherical with a radius that gives the best image quality extended over 3.6° diameter in the focal plane. The reflector is supported by a 3 layer space frame surrounded by a space frame stiffening ring. The dish is fixed at two sides onto the azimuth drive by means of stub-axes. Also the dish is mounted inside a ring (dubbed θ -ring) which holds the camera at its upper apex while the lower section is equipped with a drive chain for altitude movements. The θ-ring is fixed by 10 pairs of 8 mm steel cables to the two axis stubs, resembling the spokes of a bicycle wheel. See Fig. 4.1 for the basic configuration, omitting details.

For optical reasons (low astigmatism over 3.6° diameter in the focal plane) we had to increase the f/d of the original solar concentrator from 0.7 to 1 for MTD96. The original design had a circular drive ring which also supported the focal instrument at the upper apex. In order to avoid the need for an approximately 30–32 m diameter

circular drive ring we adopted an elliptical shape (Gothic arc) for the top half and kept the circular shape for the lower section for the altitude drive. Figs. 4.2 and 4.3 show side views of the telescope when pointing at the zenith and the horizon, respectively.

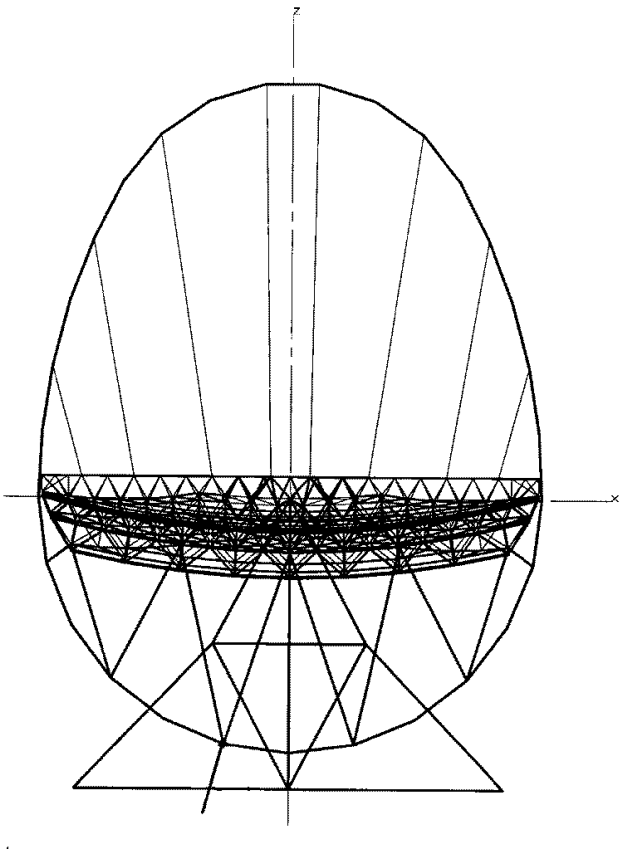

Figure 4.2: Side view of the telescope when pointing at the zenith.

4.1.1 The reflector support frame

Keywords: the tessellated reflector is supported by a lightweight space frame, weighing ca. 3-5 tons

The tessellated reflector is composed of 976 elements with always four of them grouped on panels of $\sim 1 \times 1$ m^2 area. The panels are supported by a 3 layer (i.e., 3 layers separated by 2 spacers) space frame. In addition, the space frame is stiffened at its circumference by a 1 m high "ring" similar to the CAT [30] or the TACTIC construction [11].

Fig. 4.4 shows computer generated views of the space frame under different angles of rotation.

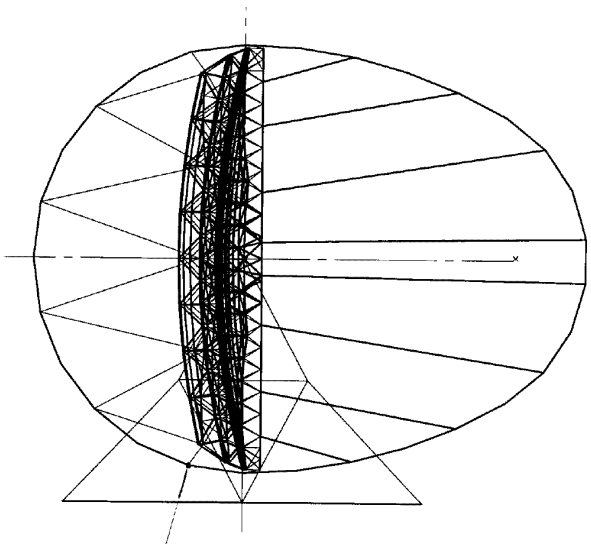

Figure 4.3: Side view of the telescope when pointing at the horizon.

The space frame is assembled from very strong low-weight carbon fiber-epoxy tubes and knots made from aluminium (MERO principle)[1]. Each tube has two screws at each end which can be screwed into the knots at threaded holes premachined at appropriate angles. Fig. 4.6 shows an exploded view of the main features of the fastening.

Fig. 4.7 shows a photograph of a 1:1 section made from commercially available steel elements.

The main reason for using carbon fiber tubes is to reduce the weight while maintaining the rigidity of the 17-m frame. The tubes are optimized in strength by using a blend of high modulus (HM) fibers and high tensile strength (HT) fibers. It is possible to achieve nearly the elasticity parameters of steel at about one quarter of the weight, i.e., the carbon fiber space frame would weigh at least a factor 10 less than an equally deforming one made from steel tubes.

The space frame geometry has been generated and optimized by the company MERO which has recently produced a similar (welded) steel frame construction for the 11 m ø optical Hobby-Eberly telescope [91]. (In the Hobby-Eberly telescope the reflector dish is kept at a fixed declination angle and is only rotated in the azimuth. Therefore the deformations are static and require only initial corrections.)

The space frame geometry follows the shape of the reflector profile. The top layer has a grid spacing size of about 1 m, the intermediate layer (rotated by 45° against the top layer) has a grid of ca. $1.14 \cdot \sqrt{2}$ m while the bottom layer has a grid of ca. 2 m. The three layers are separated by spacing tubes with a top-to-middle

[1]This construction principle is nowadays used quite commonly for large roof constructions and halls.

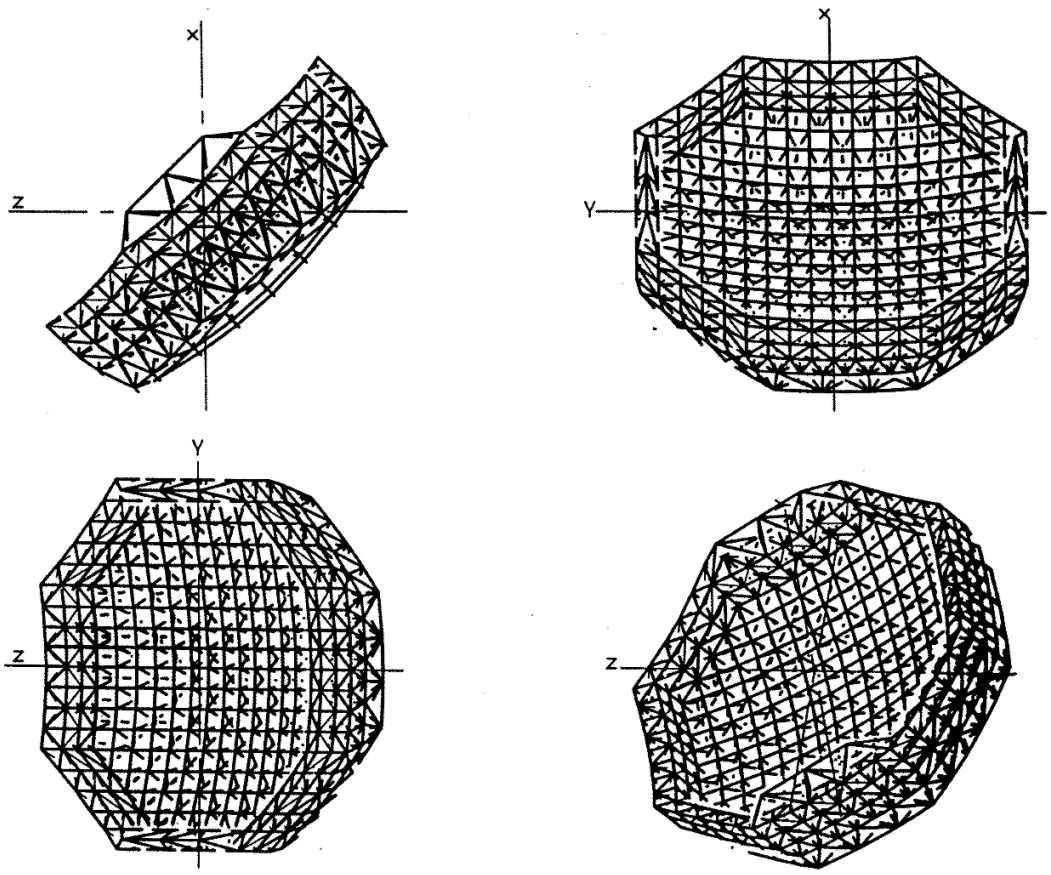

Figure 4.4: Computer generated views of the space frame consisting out of a 3 layer structure stiffened at the circumference by an additional 1 m high structure under different angles of rotation.

layer separation of 0.7 m and middle-to-bottom layer separation of ca. 1 m. The stiffening ring on the circumference is ca. 1 m high and between 0.7 and 1 m wide.

Using their standard finite element analysis program, MERO calculated the deformation under load at various angular positions (including wind and ice loads). The analysis yielded for each tube and knot the tension/compression and displacement with respect to the ideal zero-weight geometry. The initial restriction was that the real space frame should not deviate from its original geometry (zero gravity) by ≥ 3 mm.

Fig. 4.8 lists (perpendicular to the surface) the sagging of each knot against its nominal position for the carbon fiber space frame. In the zenith position the maximum sagging is 3.7 mm[2] (in the most distant corner away from the axis) and 1.2 mm along the connection line between the axis stubs. At none of the positions does the difference in sagging between two neighbouring knots exceed 0.2 mm. This

[2]At the horizontal position the displacement is still 0.5 mm due to the off-center mount of the axis; therefore the sagging between vertical and horizontal position is 3.2 mm.

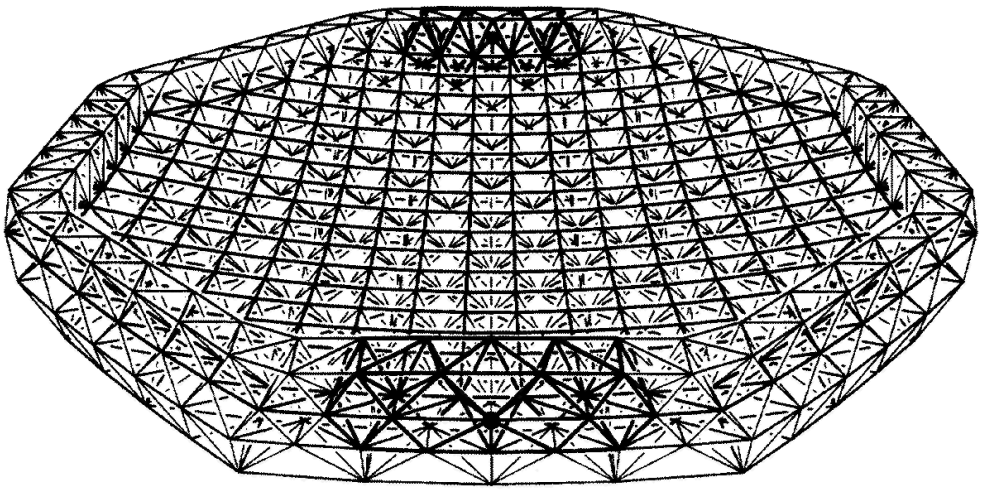

Figure 4.5: Computer generated view of the space frame consisting out of a 3 layer structure stiffened at the circumference by an additional 1 m high structure. The thicker lines correspond to the inset welded steel frame construction in the area of the axis of the dish.

relative sagging can be converted into a local reflector tilt, which, in case of a relative sag of $\Delta s = 0.2$ mm, converts into a light-spot displacement of $34 \times \Delta s$, i.e., of 7 mm in the focal plane. Allowing for a safety margin of factor 2, this is acceptable for a pixel size of 0.1° (= 29 mm pixel diameter) as different mirrors move in different directions while active mirror control is absolutely essential if the pixel size needs to be further reduced for the avalanche photodiode camera. Fig. 4.9 and 4.10 list the comparable sagging for an aluminium and steel space frame, both with a sagging of ≈ 7 mm.

It is interesting to note that a more rigid frame avoiding active control would require a much heavier construction, making the price much higher than for active mirror control. (We see basically the same effect as in large optical telescopes.)

The finite element analysis also allowed the weight of the tube to be tailored to the load requirement. For economical reasons only three classes of wall thickness are used. In the area of the axis one expects that some of the tubes will be subjected to excessive local tension/compression. In this area we will use a welded steel frame construction (see thicker lines in Fig. 4.5). In total the space frame needs ca. 3600 m (ca. 2600 elements) of carbon fiber tubes and 1200 knots. The space frame will weigh 5000 kg without mirrors.

We are presently in contact with leading European carbon fiber manufacturers to discuss possible production procedures and methods to reduce prices. The so-called protrusion fabrication method for composite tubes seems to be well suited for our needs. As a guideline we estimate on the basis of various offers a price of $\sim 250 \pm 50$

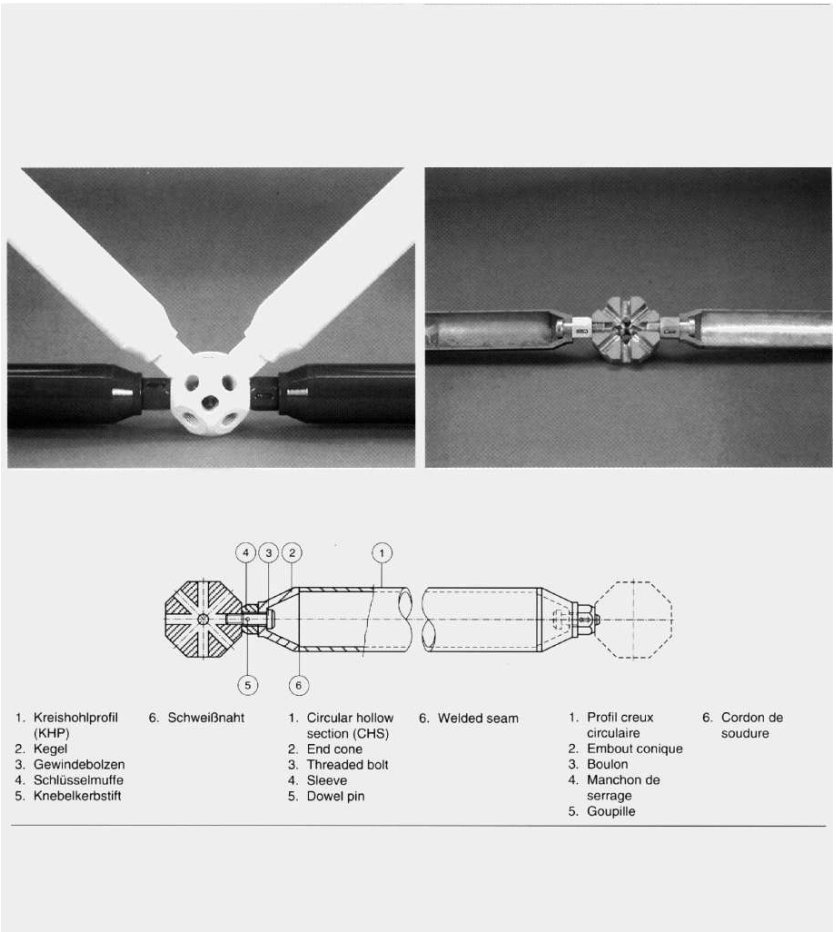

Figure 4.6: Example of a node of the telescope space frame.

DM/m for the raw cut tubes with carbon fibers of high Young's modulus.

The CAD program lists the length of each tube. The fabrication would proceed by cutting the tubes to their precalculated length and glueing the end pieces onto a special rig at the required length with ± 0.2 mm (possible correction by using under-/oversized spacers for the screws, see Fig. 4.6). The glue joints are possible areas of failure under stress. A safety factor of six times the nominal force will be used, i.e. the area of glueing will be quite large (for the reader's information: the shear forces of modern glues are in excess of 200 kg cm^{-2}; the tensile strength of the used M12 screws is $\sim$ 4 tons).

An additional advantage of the chosen construction is the easy assembly/disassembly method and the high modularity. The space frame will be delivered as a kit of preworked tubes and knots. The entire space frame can be stored in a single 6 m container. At the site a small team of skilled workers can assemble the frame within 2 weeks.

Contacts with possible tube producers have been established, including Dornier, Excel (Finland, supplier for the carbon fiber masts for the HEGRA telescopes), Kempel and Verbundwerkstoffvertrieb (the latter two companies supply Airbus in-

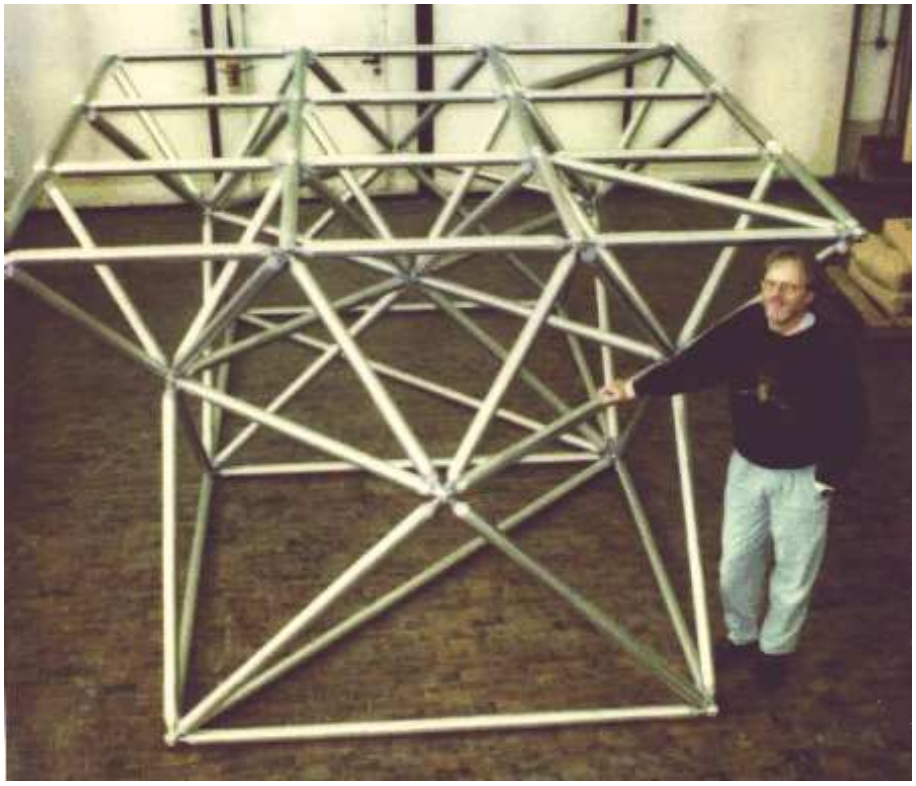

Figure 4.7: Photograph of a 1:1 section of the space frame made from commercially available steel elements.

Material	Density ρ (g/cm)	Young's modulus (10^3 N/mm^2)	Tensile strength (N/mm^2)
Steel	7.85	210	2600
Aluminium	2.7	75	–
HM-carbon fiber 1	1.82	400	2000
HT-carbon fiber	1.77	295	4700
IM-carbon fiber	1.75	240	3500
E-glass fiber	2.6	73	2500

Table 4.1: Intrinsic data for fibers, in practical cases tubes contain 60% fibers and 40% Epoxy. Note also that tensile strength and Young's modulus apply only for forces along the fiber.

dustries with carbon fiber-epoxy components).

In the following table we summarize for the more generally interested readers some parameters of materials under consideration.

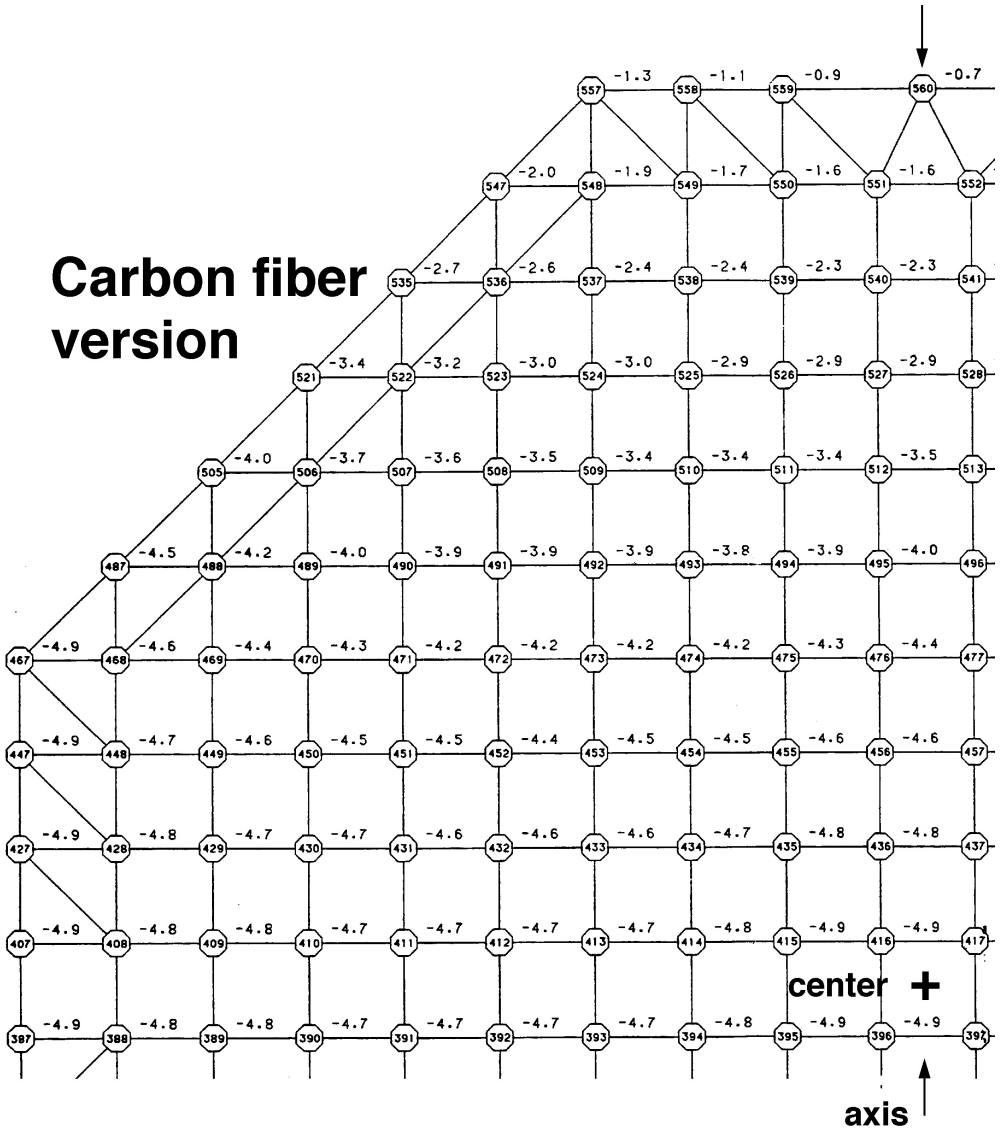

Figure 4.8: Sagging of individual knots of one quadrant of the carbon fiber space frame.

Examples of typical glue parameters:

Glue type	ρ (g/cm)	Tensile strength	Shear modulus	Youngs modulus
Epoxy-Dicyandiamid[1]	~ 1.4	50 N/mm^2	1100 N/mm^2	3000 N mm^2
Epoxy-Polyester[1]	”	70 ”	1500 ”	4200 ”
Epoxy-Polyester[2]	”	40 ”	700 ”	2100 ”

Due to ageing, elevated temperature, humidity and surface contact problems a typical reduction factor of 0.3 has to be for the tensile strength.

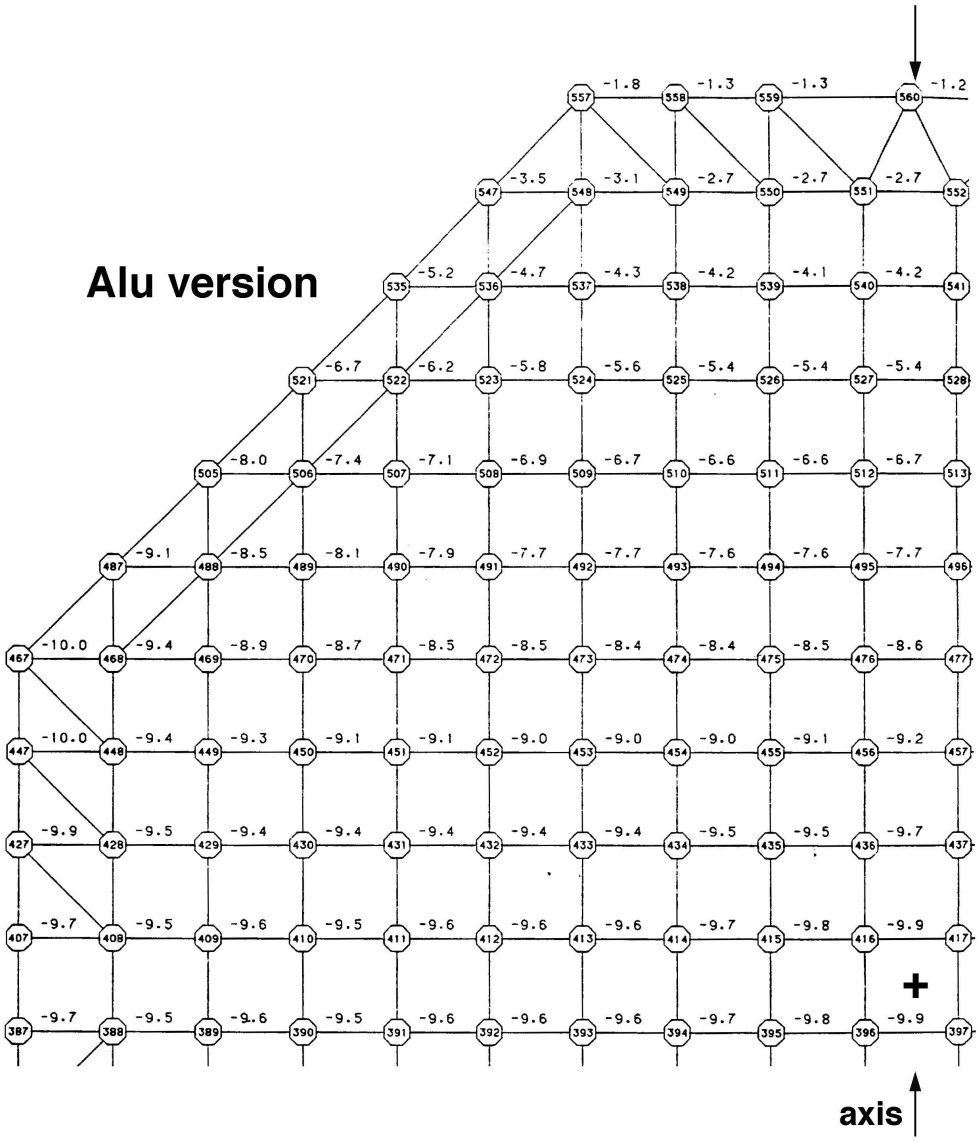

Figure 4.9: Sagging of individual knots of one quadrant of the aluminium space frame.

4.1.2 The azimuth undercarriage

Keywords: The telescope runs on a circular, 20 m ø rail with an angular range of 400°

The azimuth undercarriage is nearly identical to that of the 17 m solar concentrator. Fig. 4.11 shows the configuration. The undercarriage pivots around a central axis and runs on a circular rail of 20 m diameter.

Four (6) bogeys with four wheels each carry a tubular frame made from alu-

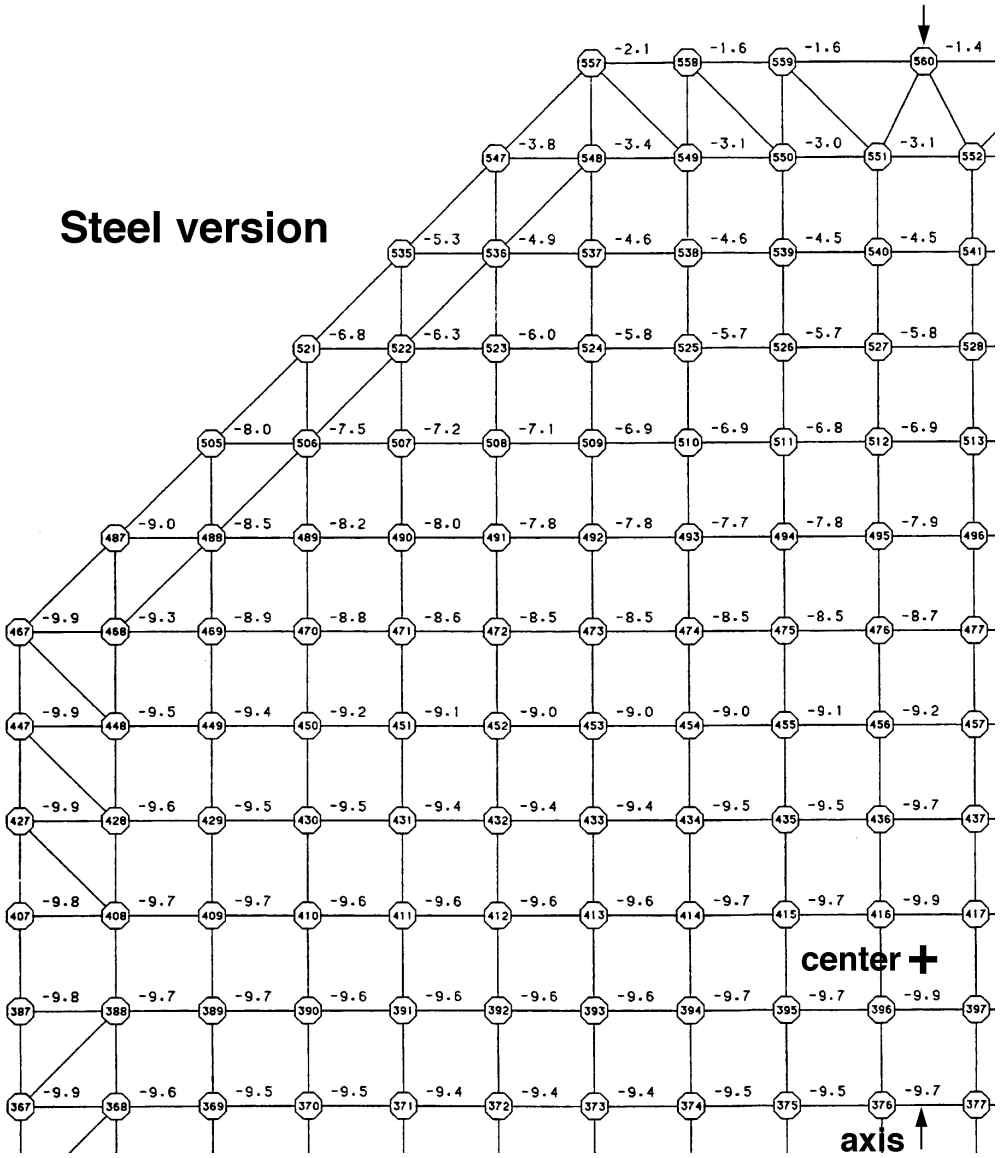

Figure 4.10: Sagging of individual knots of one quadrant of the steel space frame.

minium. The tubes are connected to each other by knots following the MERO principle. The rail is bolted every 50 cm to the concrete foundation. Depending on the site, the foundation will be anchored to the underlying natural rock or weigh at least 60 tons to ensure enough stability for normal operation and to prevent the telescope from being turned over in the case of strong winds. Fig. 4.12 shows an artist's impression of the concrete foundation and a cross section of one of the design suggestions. The weight of the movable section of the azimuth undercarriage is about 12–14 tons. The addition of a permanent co-rotating working platform is

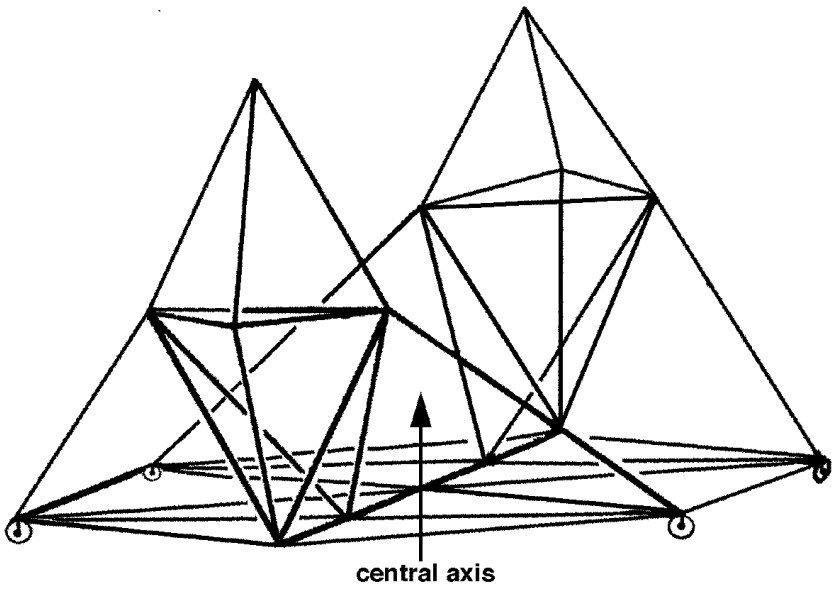

Figure 4.11: Schematic view of the azimuth undercarriage which will run on a circular, 20 m ø rail with an angular range of 400°.

also being considered. It would cover the entire foot of the undercarriage and rotate with the telescope, similar to the one currently being used by HEGRA ACTs 2–6. It might also be necessary to add some type of lifting device in order to have access in a simple and safe manner to the underside of the reflector dish.

4.1.3 The altitude drive ring and the camera support

Keywords: The declination range is $+110°$ *to* $-80°$*. The camera is supported by a Gothic-arc shaped ring held in place by steel cables.*

The camera will be carried by the θ-ring, whose lower section forms the drive connection to the azimuth undercarriage. Fig. 4.1 shows the basic configuration. The "Gothic arc" section above the reflector is held in shape by a number of prestressed steel cables, thereby minimizing obscuration of the reflector. The lower circular section is both connected by a tubular construction and steel cables to the reflector space frame. A box profile of outer cross section 20×10 cm and 1 cm wall thickness is chosen for the θ-ring. Prefabricated sections of a typical length of 6 m will be riveted together at the site. The hollow ring profile has enough room to carry the optical fibers and cables for the camera. At its apex the ring is cut and a guide frame for the camera is inserted. This frame allows one to install cameras with a field of view of up to 120×120 cm. Rails at four corners of the frame allow one to

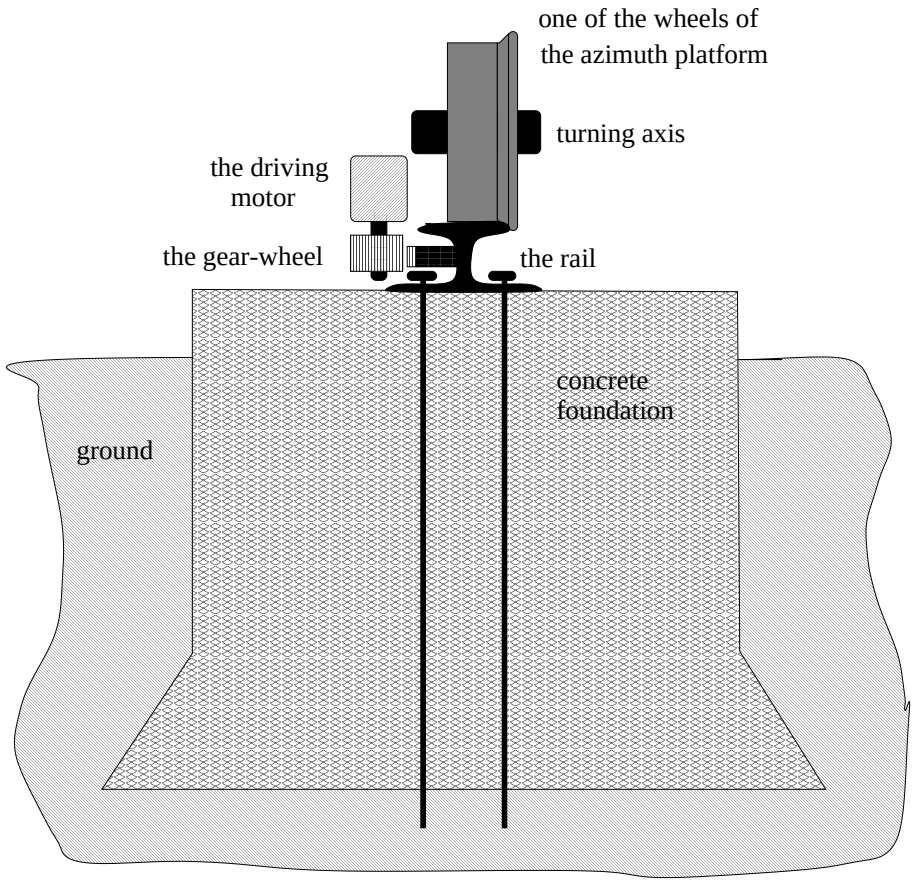

Figure 4.12: Cross section of the foundation and of the circular rail. The concrete foundation is $\approx$ 1m in width.

slide in or to remove the camera for quick access, exchange or repair. It is foreseen to have a small working tower to which the telescope can be aligned and with which the camera can be moved into a repair area. The tower will be located opposite to the direction of the sun at noon, i.e., at the normal parking position of the telescope.

4.1.4 The drive system

Keywords: The telescope is driven by electrical servomotors. Max. positioning time is < 60 s.

The telescope needs on one hand a highly precise drive for normal tracking and on the other hand a fast drive for quick repositioning in order to respond on GRBs. The telescope will have angular range of 400° in φ and +110° to −80° in θ. The drive system consists of the following basic functional elements:

(i) the mechanical links,

(ii) the drive motors,

(iii) power supply,

(iv) motor control/steering electronics,

(v) the backup emergency system.

The mechanical drive links are formed by chains riveted every few centimeters to the circular rail and also to the lower section of the θ-ring one the one hand and by motors fixed to the azimuth carriage on the other hand. The motors are engaged to the chains by toothed wheels. Figs. 4.12 and 4.13 show the (simplified) links. Four motors, one at each bogey, turn the undercarriage. Two synchronized

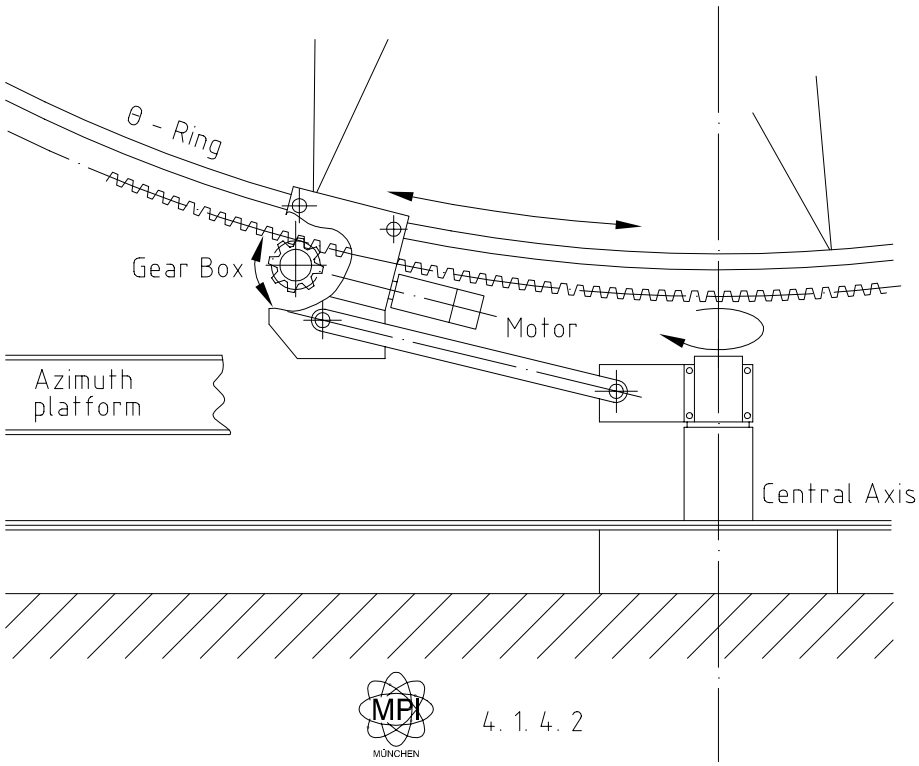

Figure 4.13: Cross section of the mechanical drive of the θ-ring.

10 HP servomotors (on opposite bogeys) are permanently engaged and are sufficient to drive the telescope during normal tracking or positioning. Two additional, higher power, torque-driven motors with simpler regulation are normally not engaged and only used for very fast repositioning in gamma-ray-burst studies. Because of their short-term use and the high peak power demands, we are investigating the use of compressed air motors because of the simplicity of storing "energy" in a battery of bottles. Alternatively, DC motors driven from a set of starter batteries (48 V with 200 A peak current for 3 min) might be used.

For the altitude drive a single 10 HP servo motor is sufficient because of the lower weight ($\sim 40\%$ of the telescope), lower inertial momentum and typically displacements at half the azimuthal angular range. This motor will be mounted on the lever arm which is force-coupled to the θ-ring such that it can follow the changing distance when passing from the circular section to the "Gothic arc" section. The motor is also offset by about two meters from the lower apex of the θ-ring such that the reflector can be moved to a zenith angle of 110°, a position which is needed for easy access to the camera, for reflector protection in the case of hail, for exchanging mirror elements, for cleaning the mirrors and for protection from the sun.

The servomotors and their electronic drives will be commercially acquired and chosen from the vast spectrum of drives that are manufactured for engineering works. The steering input will be generated by a control computer that uses the coordinates of the object being observed together with signals from both the shaft encoders and the guide-star video camera (for further details see Section 4.1.6).

The power demands for normal tracking and positioning are rather modest, typically 1–3 kW, and they can come from the electricity supply system. As already mentioned, the peak power needed for fast positioning of the telescope has to be supplied by a buffer system.

In remote areas of the world, a highly reliable electricity supply system is unlikely and emergency power will be needed. For normal operation, an interrupt free back-up supply of 15 kW/10 min is foreseen. This should be sufficient to bridge short interruptions (and also supply electricity at a well regulated voltage of 220) and to allow one to drive the telescope to its storage position opposite to the midday sun.

But for the θ-ring drive system the full mechanical setup of the MAGIC Telescope can be seen in Fig. 4.14 which shows a photograph of a 1:20 model of the telescope.

4.1.5 Frame deformation monitoring

Keywords: The lightweight reflector support dish will deform when turned. Deformations might need monitoring.

The design and function of a deformation monitoring system depend very much on the absence or presence of an active mirror control. In the second case permanent deformation monitoring while operating the telescope is not needed. In any case we need measurements of frame deformations before using the telescope. For this study, and if needed also for permanent monitoring, we can apply a method which was developed at the MPI in Munich for tracking displacements of detectors in the ATLAS experiment [12]. In a nutshell, this method uses a laser beam and several semitransparent silicon strip sensors, placed at the relevant positions of the detector.

For laser light of 790 nm wavelength transmission of above 90% per sensor was

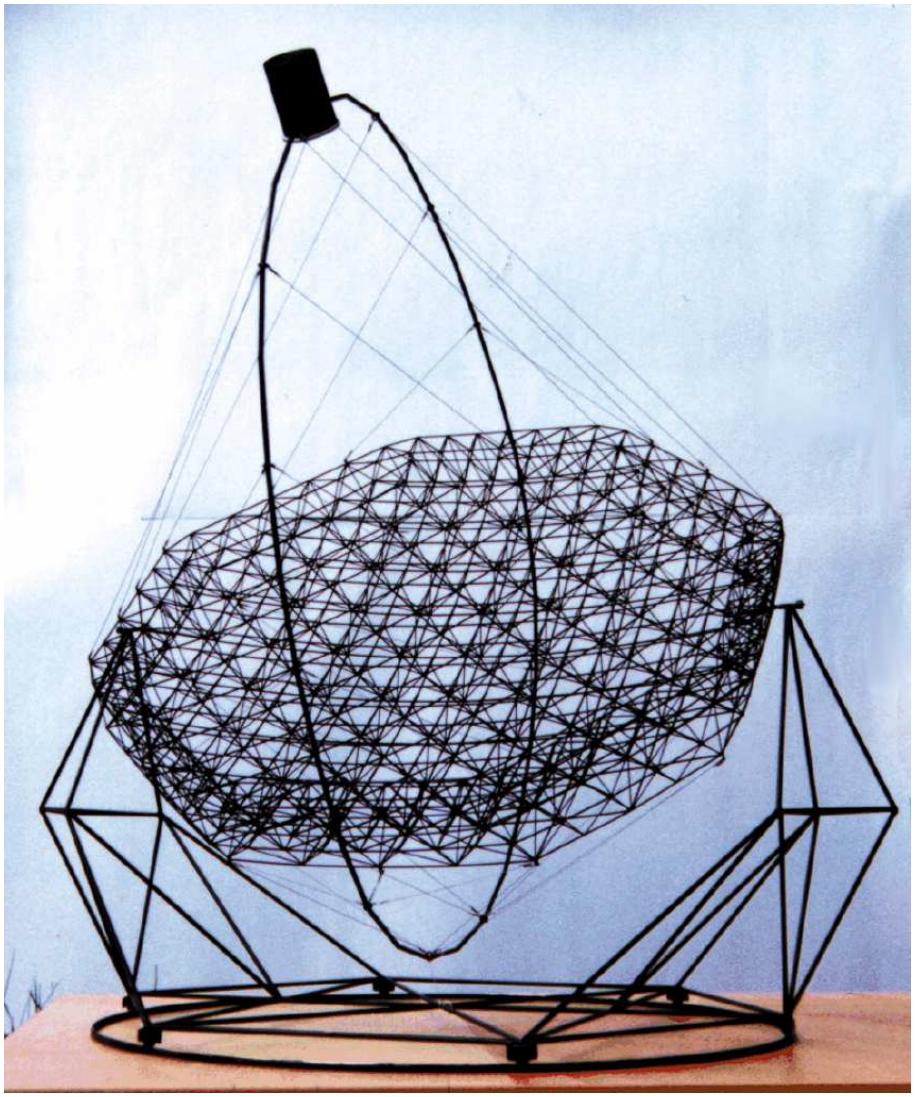

Figure 4.14: Photograph of a 1:30 model of the MAGIC Telescope. Not included in the model is the drive system for the θ-ring.

reached, allowing more than 30 sensors to be placed along one laser beam. The resolution, measured with the test set-up, was a few micrometers or even better.

For the deformation measurement of the MAGIC Telescope it should be sufficient to install one x-y-sensor close at each corner of the octagonal shaped frame. Two lasers, one for each half of the frame, will be fixed above the two horizontal axis mountings, which are expected to be the most stable points and can therefore be used as reference. Mirrors at each corner guide the laser beams along the frame edges.

Any radial or axial movement of the frame corners lead to a linearly correlated displacement of the related x-y-sensor against the laser beam. Each sensor is

equipped with complete readout electronics, including data memory which can be addressed via a VME interface.

4.1.6 Monitoring the position of the telescope during tracking

Keywords: Angular positions have to be monitored with 0.02° precision

We plan to use a redundant system for monitoring the angular position of the telescope. It will also monitor the position of the camera with respect to the normal of the telescope reflector because the lightweight construction will deform slightly and be displaced against its nominal position. Furthermore, camera oscillations at sub-1-Hz frequencies might occur. These small and relatively fast (in terms of mechanical oscillations) amplitude deviations cannot be easily corrected by mechanical actuators. A better approach is to measure the actual camera position during tracking, to record it within a few milliseconds of the event trigger and to correct the displacement by software. The position monitoring is needed as input for the drive control and also for data correction. The following devices are foreseen:

(a) 14-bit Gray-coded shaft encoders will be mounted onto both stubs of the declination axis and onto the azimuth axis. The azimuth shaft encoder is supplemented by a slightly less precise encoder acting on the azimuth drive chain. We plan to use Hengstler RA58 encoders, which are also used for the current HEGRA ACTs. These encoders have a very large signal swing for noise immunity and can be read out over cables up to 100 m in length.

The encoder's least count of 0.02° is sufficiently smaller than the pixel size of 0.06–0.12°. The shaft encoder signals will be used as control input to the telescope drive servomotors. The dual equipment of each axis will give a high redundancy in case of failures.

(b) The second control is carried out by high sensitivity ($\sim$ 0.01 lux) night vision CCD camera with a field of view of $\sim$ 10°. The details of this concept which is also used by the CAT telescope will be described in the next section.

4.1.7 CCD video camera system

Keywords: A CCD video camera system controls the position of the telescope camera and monitors stars in the field of view

A system of highly sensitive CCD video cameras will be used to control on-line the position of the telescope's camera and to observe stars in the telescope's field of view. CCD video cameras with a sensitivity of $\approx$ 0.01 lux should allow one to observe 9th magnitude stars, 4–12 of which will nearly always be in the field of view.

The system consists of two cameras, one for controlling the relative position of the telescope camera, and one with high sensitivity for monitoring stars in the telescope's field of view. The best place for mounting the two cameras is about 2 m away from the center of the reflector dish. At this place the CCD video cameras would have a nearly unobscured field of view, and also the mechanical vibrations would be low. The first CCD video camera is used for controlling the position of the telescope camera with respect to stars of the night sky. The idea is to have some red or infrared LEDs around the telescope camera and to watch them together with the stars by means of the CCD video camera. From the known position of the stars and the actual position in the CCD video camera we could calculate the actual position of the telescope camera with respect to the sky map. The telescope camera which has a diameter of 3.6° should be completely inside the field of view of the CCD video camera, which should be $15° \times 15°$. A standard CCD video camera has a CCD element with 512 x 512 pixels. In this case the angular resolution should be equal or slightly better than 0.03°. Increasing the number of pixels of the CCD element would give a better angular resolution, e.g. 1024×1024 pixels $\approx 0.015°$, which is nearly 1/7 of the pixel size of the telescope (0.1°).

The read-out will be done by a computer with a frame grabber card; so the position of the camera could be calculated directly on-line and could be saved together with the event data. A comparison of the digitized image with the relevant star position of the area to be studied allows for fine corrections of the telescope's drive system. The 24 Hz readout (very much more frequent than the oscillating frequency of the camera mount) of the LED markers will enable us to calculate the actual camera position during source tracking and thus to make the software correction of the shower image with respect to the difference between the actual to the nominal position of the camera. This is important because the construction holding the camera cannot be made more rigid without using thicker frames and additional masts which would obscure a still larger fraction of the mirrors.

The second CCD video image will be used for checking the sky quality in the telescope's field of view. A good knowledge of sky conditions and the positions and magnitudes of stars is necessary for understanding the status of the telescope camera. As the telescope has much higher sensitivity the problem with background light from stars will be much more important than in today's ACTs.

Compared with the PM camera of the telescope, a CCD video camera is not very light sensitive because the light collection area is much smaller. In the best case the sensitivity (light collection area × exposure time × QE) of a CCD video camera is about 20% of that of the telescope. The easiest way to get a better efficiency for the CCD video camera is to use a longer light collection time. For a good monitoring of the dark sky it seems to be necessary to have a CCD video camera which integrates the light much longer than the CCD video camera that is used for controlling the movements of the telescope camera. A good collecting time could be in the range of 1–10 s because for such time intervals there will not be so many problems with

the cooling of the CCD element and the vibration of the telescope dish. The field of view of this camera should be substantially larger than the field of view of the PM camera of the telescope, e.g. 10 - 15° vs. 3.6° of the camera.

For analyzing the pictures of this camera, we propose to use astronomy software packages that can automatically identify stars and measure their brightness on the image. Such software packages are available, e.g. for the Linux operating system from the European Space Organisation (ESO).

4.1.8 Survival of the telescope in strong winds

Keywords: The telescope has to operate at up to 80 km h^{-1} wind speed and survive 165 km h^{-1} storms

Because of the expense, the telescope will have no protective dome. Therefore it might be exposed occasionally to strong winds. Two cases have to be distinguished:

(a) the maximum wind speed at which measurements can still be made;

(b) survival of strong storms.

In clear weather, e.g. observation conditions, the wind speed will rarely exceed 50 - 60 km h^{-1}. At the Carlsberg Observatory on La Palma a clear-sky wind speed exceeding 60 km h^{-1} was measured only for 6 h in 1994 and 1995. Therefore it is reasonable to fix the upper wind speed for measuring at 20 m s^{-1}. At this speed the most noticeable effect would be camera oscillation. Assuming that the CCD camera for monitoring the camera position with respect to the night sky works as expected, we could set the amplitude limit at 3 cm. This defines the strength of the camera support ring and the reinforcement steel cables.

Preliminary engineering studies show that the goal can be met with 10 steel cables (5 on each side) prestressed to a tension of 100 kg for each cable.

The 8 mm ø cables (and support frame) are capable of withstanding winds of up to 300 km h^{-1} (hitting the telescope's camera at the most unfavourable position) without breaking. The survivability of the telescope dish was simulated by MERO using their very detailed simulation program for a space frame construction covered by panels.

The wind resistance was simulated for a wind speed of 165 km h^{-1} for three positions: one at a favourable orientation, the other two at less favourable orientations:

(a) With the telescope dish in its horizontal position so that the surface area "seen" by the wind is minimal.

(b) With the dish vertical so that the reflector side is directly facing the wind.

(c) Same position as (b) but with only the upper half exposed to the wind so that considerable torque is exerted on the declination axis and drive.

The calculations were done in compliance with the norm DIN 1044 section 4.

The c_P value for cases (b) and (c) is	$c_p =$ 0.8 according to DIN 1044
Total area (including the rim space frame)	$A_t =$ 285.95 m^2 [case = b]
Assumed wind speed	$V_w = 45.6$ m s^{-1}
Resulting static overpressure	$q = 1.3$ kN m^{-2}
Wind force w (pressure m^{-2}) at	$w = c_p \cdot q = 1.04$ kN m^{-2}
Force for the total telescope [case (b)] of	$w_t = 283.95 \cdot 1.04$ kN m^{-2} = 295 kN

i.e., the wind force would result in about 30 tons pulling horizontally and acting on the declination axis [15 tons in case (c) above the declination axis].

For case (a) a complicated model calculation, taking the space frame structure into account, gave a total wind force of

$W = 52.85$KN for the rim above the axis and
$W = 162.01$KN for the section below the declination axis,

i.e. a sum of

$$w_{\text{tot}} \text{ [case (a)]} = 214 \text{ KN}\,.$$

The somewhat surprising result is that the horizontal and vertical positions differ only by ca. 30% of the force exerted on the axis.

It should be noted that in position (a) the area exposed to the wind is nearly 100 m^2 with a rather high c_p value due to the numerous distributed carbon fiber tubes.

From an FEM analysis that includes the weight of the reflector dish and the space frame (total ca. 8 tons) the following extreme loads for the most stressed rods (at both sides of the dish, assuming single point axis connection) are obtained:

Case	Max. force [kN]	Min. force (e.g. compression) [kN]
(a)	+156.1	−56.8
(b)	+11.8	−12.2
(c)	+11.4	−12.6

The wind loads on the most exposed knot (coupled to the axle stubs) are:

Case	x [kN]	y [kN]	z [kN]
(a)	0	216	0
(b)	184	0	0
(c)	142	0	23

The calculations show that the expected maximum forces for the carbon fiber rods and at the axes can be counteracted by using somewhat thicker profiles (the weakest elements being the bolts and the glue joint between the carbon fiber rods and the aluminium end pieces), but for the final construction it was decided the section close to the axes be replaced by a welded steel space frame of high strength and oversize tube diameter. The carbon fiber space frame would then be connected to at least 10 points at each side. In turn the load would be distributed much more evenly and the load peak on the most stressed carbon fiber tube would be reduced to a value of less than 20 kN in case (a).

The calculations indicate that the substructure must be relatively strong and must include precautionary measures to prevent the telescope from being lifted off the circular rail of the foundation. As an additional safety installation in the case of storms, we consider having the declination axis points anchored to the ground by means of steel cables.

The 1:30 model of the telescope could be used for wind tunnel tests in order to confirm the calculations and to find perhaps a minimal wind resistance position at around, say, 20° inclination. It should be noted that the similar sized DFVLR solar concentrator survived 3 hurricanes/violent storms in the winter of 1990 without damage.

One option for reducing wind resistance in position (a) would be to cover the space frame with a lightweight skin and thus reduce the c_p value significantly.

In positions (b) and (c) the force on a 1 m^2 panel is 1 kN in case of 165 km h^{-1} wind speed. Using a 3-point fixing and a safety factor of 3 brings the breaking limit of each fixing point again to 1 kN. Similarly each fixation for a mirror element onto the 1 m^2 panel must withstand at least 250 N in the compression mode whereas in the "suction" mode the pulling forces would be reduced due to the shielding of the support panel.

4.1.9 Compliance with TÜV rules

Keywords: The telescope has to comply with generally accepted safety rules

The telescope with a height of ≈ 29 m and 20 m overall diameter is considerably larger than any existing ACT. Catastrophic failures due to inadequate construction or under- dimensioned components can be a considerable safety risk. Therefore the mechanical construction has to comply with the general safety rules for large constructions such as bridges, steel towers etc. In Germany these rules are set up by the TÜV (Technischer Ueberwachungsverein). As we intend to order the telescope frame as a so-called turnkey item it is assumed that the necessary inspections and tests of compliance with the TÜV rules are at the responsibility of the manufacturer. (Other safety aspects during operation are discussed elsewhere).

4.2 A new tessellated mirror

Keywords: the telescope has a 17 m ⊘ tessellated mirror

Mirror design parameters

1. Focal length for central mirrors 17 m
2. Mirror element size: 49.5×49.5 cm^2
3. Mirror element weight: 3.5 kg/unit
4. Weight of 4 mirrors + adjustment support: 22 kg m^{-2}
5. Mirror reflectivity (320 - 600 nm) $\geq 85\%$; in the range 280 - 320 nm at least 70%
6. Focal point spot size of a mirror element: ≤ 5 mm (80% of light)
7. Precision of the focal distance of individual elements: $\sigma \leq 10$ cm (Gaussian distribution)
8. Different sets of focal distances due to gross parabolic mirror shape: ~ 8
9. Total mirror area: 236 m^2
10. Time to readjust a 1-m^2 segment: ≤ 5 s to 2 mm deviation in focal plane
11. Heating power of mirror element: ca. 20 Watt ($\Delta T < 1.5°$ over the mirror)
    Emergency peak power 100 W
12. Reliability condition of active mirror adjustment: < 1 failure per 10 years/panel of 1 m^2
    Telescope drive motors < 1 failure per 2 years
13. Mirrors should withstand 1 cm ø hail
14. Deterioration time of mirror reflectivity: drop of reflectivity $< 3\%$/year

The mirror of the DFVLR 17 m ⊘ solar concentrator is unusable for our purposes. The reasons are insufficient optical quality, unfavourable f/d and a previous suffered, irrepairable damage. Therefore we envisaged a completely new design that retains only the dimension of the mirror (17 m ⊘) and the general mounting concept. The new construction will be based on an octagonal tessellated mirror with 50×50 cm mirror elements supported by the above described space frame. A simple type of active mirror control will be used in order to correct small frame deformations. The design is defined by the following parameters:

(i) the mirror area,

(ii) the focal length,

(iii) the mirror shape and resulting aberrations,

(iv) the reflectivity in the spectral range of the sensors,

(v) the point spread function,

(vi) the weight.

The surface area is slightly larger than that of the old solar concentrator with its area of 220 m^2. Assuming some losses at the edges, a 5 mm gap between mirror elements, and some obscuration by the declination ring, the camera and the prestressed cables, we will have an effective mirror area of 236 m^2. Figure 1 in appendix A shows the layout of the mirror.

The focal length of the original design was 14 m, i.e. the solar concentrator had an aperture of ca. 0.8. The best practical value of today's ACTs is considered to be around f/D $\geq$ 1. Changing the focal length to 17 m was impossible without a major redesign of the mounting; therefore the perfect ring concept of the solar mirror was abandoned. Now in the proposed design the lower drive ring section will still be circular with a radius about 9.5 m but the upper section carrying the camera will have an elliptical shape (Gothic arc).

This configuration will still allow us to maintain (a) the drive concept along the ring up to at least 190°, (b) a low cross section support arc for the camera with an f of 17 m and (c) the stiff bicycle wheel concept with prestressed cables stringing the camera and support arc to the declination axis.

4.2.1 Optimisation of the optics

Keywords: The optical configuration is a compromise of contradicting parameters

The curvature of the mirror has to be a compromise between contradicting parameters. One constraint is that time spread between photons arriving onto the camera from different areas of the mirror should be kept to a minimum. This means that the mirror has to be parabolic. On the other hand we need to minimize aberrations for the field of view that will always have a large diameter of 2.5 to 5°, i.e. a large f/d is preferred. An f/d greatly exceeding 1 poses serious mechanical problems, also any camera with a diameter of a few degrees will obscure a non-negligible fraction of the main mirror in this case. One other consequence of a small aberration is that the main mirror must be fine segmented (or have aspherical mirror elements which can, in principle, be produced by means of diamond-machining of the elements). The solutions of our optimization are summarized in the preceding list of the mirror design parameters while the detailed optimization procedure is discussed in appendix A ("Optics of the MAGIC Telescope").

4.2.2 The mirror elements

Keywords: The main mirror will consist of lightweight, diamond-milled all-aluminium mirrors 49.5 × 49.5 cm^2 size in size. Machining allows for easy variations of the focal distance.

The large number of mirror elements of different focal lengths encourages the production of light weight mirror elements with surfaces machined on a numerically controlled machine. We plan to use all-aluminium sandwich mirrors and diamond milling to produce the reflective surface. This type of mirrors has been already successfully produced for the HEGRA CT1 Čerenkov telescopes. Fig.4.15 shows an exploded view of the mirror components. Each element consists of a sandwich containing a 5 mm $AlMgSi1$ alloy (anodic oxidation quality) front plate glued onto a prefabricated sandwich panel comprising a 0.5 mm front plate and a 1 mm rear plate interspersed by 2 cm of aluminium (Al) HEXCELL[3]

The HEXCELL's outer circumference cells are filled with low density epoxy compound (glue filled with microspheres, $\rho = 0.6$ g ml^{-1}) in order to form a rigid frame and a seal. Fig 4.16 shows a photo of a production HEXCELL spacer with the filled rim cells for a similar design with hexagonal shape (for the HEGRA CT1 telescope).

The elements are glued together by a two-component aerospace glue which can withstand a prolonged temperature of $> 200°$ C. Inside the sandwich construction an isolated heating wire is embedded for mirror heating in order to prevent dew, frost or icing. Small transverse holes in the HEXCELL allow for ventilation in the case of air pressure changes. Three fixation plates, acting as links to the adjustment screws, are glued onto the rear plate.

The reflecting surface is produced in two steps. In the first one, the 5 mm front plate is milled down on an ordinary numerically controlled machine to about the correct spherical shape (within 0.1 mm of the final curvature) and 1.6 mm thickness at the center. In a second step, the final reflecting surface is milled on a high precision, computer controlled lathe with a diamond head fly cutter. This operation has to be carried out at specialized industry facilities. Appendix C ("Production sequence of aluminium sandwich mirror blanks ...") summarizes the production steps based on experience collected from the sucessful mirror upgrade of the HEGRA CT1 telescope which resulted in doubling the reflector surface area. Fig. 4.17 shows a photograph of the fully operational CT1 telescope after the installation of the new all-aluminium hexagonal mirror elements.

According to tests performed at two companies[4] the final machining of the surface can be completed within 2 – 3 hours. The finished surface has a roughness below

[3]aluminium HEXCELL is used instead of a much cheaper lightweight plastic core because excellent heat conductivity is needed in order to avoid bending in the case of temperature differences.

[4]*Kugler GmbH*, Salem and *LT Ultra Precision Technology GmbH*, Aftholderberg.

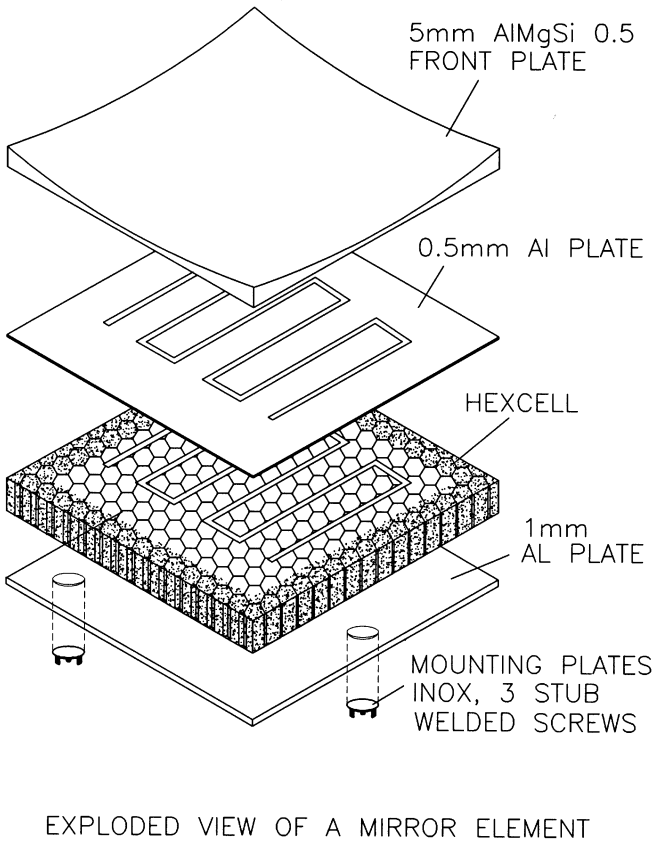

Figure 4.15: Exploded view of a mirror element.

10 nm while the focal point spread function of each mirror will be 0.01°, i.e. 80% of the light will fall within a spot of 5 mm diameter. This is observed in fig. 4.18, which shows a photo for a preproduction mirror of the focal light distribution when observing a 9 mm ø source at a distance of 34 m. Also, fig. 4.19 shows a photo of two pre-production mirrors.

The parabolic curvature of the gross mirror forces the focal distance of the 49.5 $\times$ 49.5 cm^2 elements to be increased from 17 m in the center to 17.8 m at the rim. According to the production plan the aluminium mirrors will be machined in 10 groups with curvatures between 34 and 35.6 m and an error of 8 cm. Mirrors will then be selected for their best position on the disk.

The need of having a changing focal radius was one of the main reasons for resorting to diamond-milled mirrors due to the flexibility they offer in changing their parameter. We would like to comment that in the near future the diamond-turning technique will enable mirrors with an area of up to, say, 120 $\times$ 120 cm^2 to be produced; it will then also be possible to make the mirrors slightly aspheric such

Figure 4.16: Photograph of production of a HEXCELL spacer for a hexagonal mirror element.

that the aberrations due to the larger size can be corrected to first order.

4.2.3 Mirror reflectivity

Keyword: Diamond-turned Al-alloy surfaces show high reflectivity

The requirements for the spectral reflectivity of the mirror are an $R(\lambda) > 85\%$ in the spectral range of 320 - 650 nm. Below 320 nm the reflectivity can be lower because Rayleigh scattering and Ozone absorption will reduce the Čerenkov light from distant showers (see Fig. 6.16), e.g. from low energy showers with their maximum at around 10–12 km height or showers at large zenith angles. Reflectivity (R) measurements of different diamond-milled aluminium alloys showed nearly identical R-values as a function of wavelength above 300 nm. Also, only a small reduction was found when comparing R with that of a sample with a pure (99.999%) aluminium

Figure 4.17: Photograph of the HEGRA prototype telescope CT1 after the installation of the new all-aluminium hexagonal mirror elements.

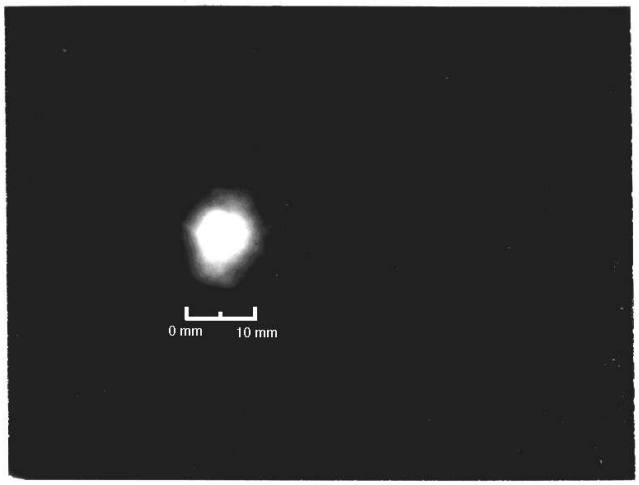

Figure 4.18: Photograph of the focal spot of a preproduction mirror when observing a 9-mm ø source of light at a distance of 34 m (twice the focal length).

Figure 4.19: Photograph illustrating the quality of two preproduction mirror elements.

vacuum overcoating. The values are also comparable to the aluminium overcoated glass mirrors. Fig. 4.20 shows the results of our study for various samples.

In this figure, we also add for comparison the spectral reflectivity of an aluminium sample overcoated by the company Balzers with Silflex –a reflecting layer of very pure silver together with a protecting layer– (see the curve labeled PF13414 6 R00 in Fig. 4.20). Silver overcoating would give about 82% reflectivity above 370 nm increasing up to its asymptotic value of ∼98% above 500 nm. Because R drops steeply below 360 nm there would be a sizable loss of Cerenkov light excess close to the zenith angle observations. The conclusion from the reflectivity study is that diamond machined Al-alloy surfaces do not need an additional pure aluminium-overcoat for high reflectivity, i.e. one can avoid the costs for aluminization.

4.2.4 Protective mirror overcoating

Keyword: The soft aluminium mirror surface needs to be protected by a hard transparent overcoating

The aluminium mirrors have to be protected by a hard, transparent coating. Three options are being considered:

(i) SiO_2, vacuum deposited

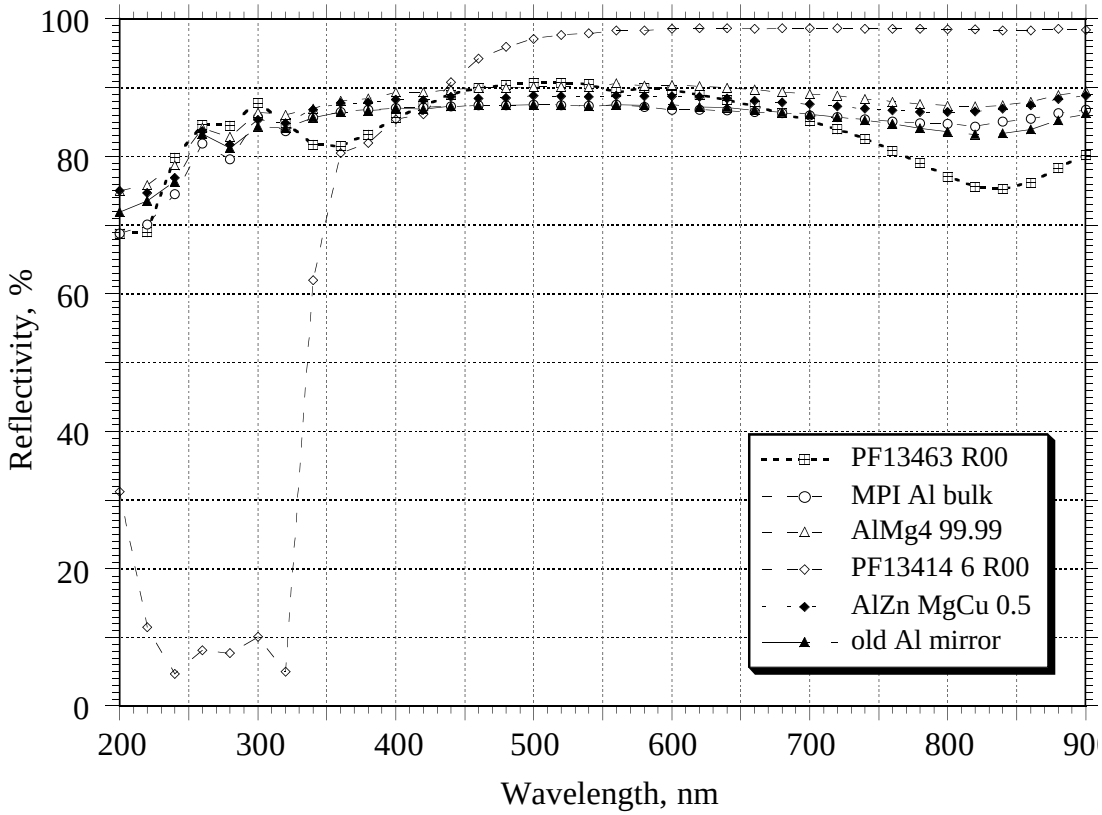

Figure 4.20: Measured reflectivities for different types of aluminium and of a silver (PF13414 6 R00) mirrors.

(ii) Al_2O_3, grown by anodical oxidation

(iii) CVD[5] diamond coating

The classical coatings are SiO_2 or Al_2O_3. It is only recently that CVD diamond coating became possible. The technology of SiO_2 coating is particularly suited for aluminium layers on glass substrates where it is very important to seal pin holes and the transition edge between the aluminium and the glass. The technique requires high vacuum and evaporation equipment or sputtering units. Similarly CVD diamond deposition requires special equipment and only a few companies are specialized in coating large areas. Coating with Al_2O_3 is the cheapest technique because it can be carried out in an electrolytic bath under normal lab conditions [43, 44, 64, 26]. Table 4.2 lists the main parameters for the different coating materials. It should be

[5]CVD stands for Chemical Vapour Deposition

noted that anodization removes some aluminium from the surface and reflectivity is more affected by deposition of coating material.

Parameter	SiO_2	CVD diamond	Al_2O_3
Refractive index	1.45	1.5	1.6
Hardness [Mhos]	6	10	9
Production method	Vacuum deposition sputtering	Chemical vapour deposition	Electrolytic oxidation
Thickness for high reflectivity at 400 nm	100 Å	$\sim$ 100 nm	80 Å
Resistance to wear	Lowest of the 3	Highest of the 3	Intermediate
Price/0.25 m^2 coat. [6]	$\approx$ 200 DM	$>$ 500 DM	$<$ 50 DM
Drop in R by 10%	$>$ 2.5 years	$\gg$ 10 years	$>$ 2.5 years

Table 4.2: List of parameters of applied coating materials.

The strong argument in favour of CVD diamond coating[7] is its excellent resistance to wear, allowing for a lifetime of at least 10 years. Because of its hardness, the protected surface cannot be damaged by any abrasive dust during cleaning procedures. The main question is whether the high cost of this coating can be brought down to acceptable levels in the next few years.

For MTD96, the electrolytic formation of Al_2O_3 has been chosen because of its hardness, its low cost, because it can be done in any laboratory and because it opens up the possibility of coating the aluminium immediately after machining. Test have been performed that show that the aluminium alloy has to be chosen with great care in order to achieve the required reflectivity of $\geq 85\%$ after coating. Also, ongoing test will show if the coating exhibits the desired hardness. If this is not so, then an additional vacuum deposit of pure aluminium will be necessary. Even if this is the case, Al_2O_3 will still be chosen since the good properties mentioned above will still hold. The test results are described in appendix B ("Development of all-aluminium mirrors ...").

4.2.5 Monitoring the mirror reflectivity degradation

Keywords: The mirror reflectivity will degrade with time and monitoring is needed.

Here we add a few ideas about monitoring the reflectivity degradation with time although this chapter would belong more logically to Chapter 4.4. Monitoring of

[6] Large quantities

[7] Actually, it is not a pure carbon coating but an amorphous Carbon with low admixtures of hydrogen that has nearly the hardness of diamond but a refractive index close to 1.5 and an UV transmission down to 250 nm.

the telescope's photon to photoelectron conversion factor is important, for example for energy calibration. One element of degradation is the mirror reflectivity. Routine checks could be carried out with a hand-held reflectometer (using a filtered Deuterium lamp spectrum faking a Čerenkov spectrum), [14], which turned out to be very helpful to monitor the reflectivity of the HEGRA telescope mirrors. The main problem for the MAGIC Telescope is the large number of mirrors to be monitored and the difficult access. As an alternative we intend to use a deuterium lamp positioned about a km away from the telescope. The light beam will be chopped and focused onto the telescope. With the active mirror control (see next chapter) it will be possible to steer the reflected beam of individual panels onto a large, broad-band sensitive photocell or Silicon photodiode and measure the reflected light beam intensity. The intensity can be compared with a reference mirror and thus degradation can be determined with about 1-2% precision. The system will be able to scan through all mirror panels automatically; such a measurement can be carried out within 1-2 hours.

4.2.6 The active mirror control

Keywords: The mirror support dish deforms under loads and mirror panels need corrections.

The need for an active mirror control has been explained in the introductory part of Chapter 4.1.1. It has been shown that the requirement of a rigid mirror support frame and low inertial mass for fast turning contradict the aim of keeping the cost down. The chosen compromise is a 3-layer space frame with some residual deformation that will require some measure of active mirror control (which will also very much reduce operator interference during periodic adjustment). The MAGIC Telescope will be very likely the first ACT using active mirror control and will thus follow the trend in large optical telescopes. Nevertheless we would like to point out that the precision needed in ACTs is about a factor 1000 worse than that in optical telescopes and a much simpler and cost-effective solution can be used.

The basic principle of the active mirror control is shown in Fig. 4.21.

Four mirror elements will be pre-mounted on a lightweight, rigid support plate measuring 98 $\times$ 98 cm. Hereinafter this unit will be referred to as a panel.

The support plate is a commercial sandwich panel consisting of a 20 mm aluminium HEXCELL core bonded to two 1-mm aluminium sheets of ca. 6 kg m^{-2} total weight. The 4 mirrors will be pre-adjusted according to their position on the main dish. In the center of the plate a small laser pointer (685 nm, round beam; beam divergence 0.35 mrad) will be mounted on a precision jig such that the light beam can be adjusted to coincide with the focal spot of the 4 mirrors. The basic unit of ca. 1 m^2 will be fixed onto the ca. 1 m^2 square grid of the space frame with 3 adjustment screws that have different degrees of freedom in their transverse

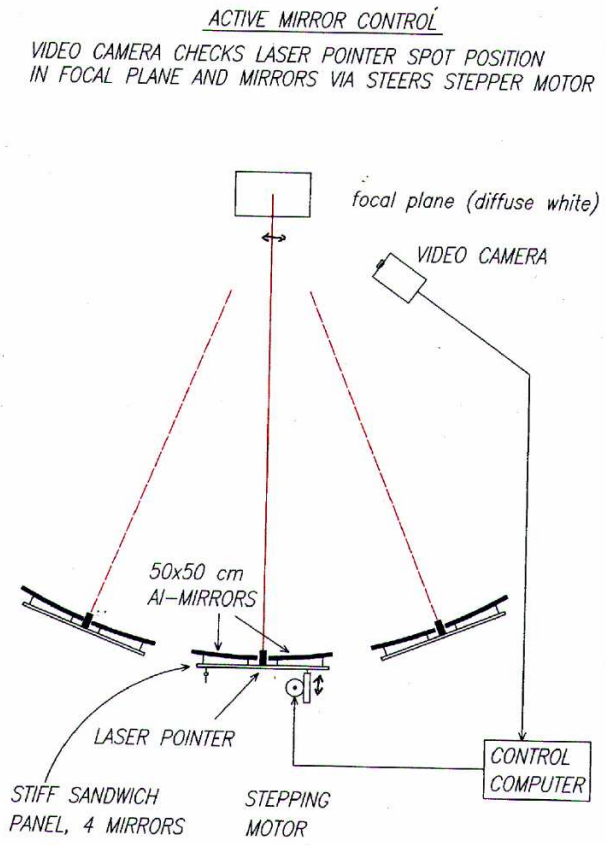

Figure 4.21: Schematic view of the active mirror control system.

movements. One point is a double high precision universal joint allowing limited free movements in the x-y plane. The other two incorporate adjustment screws (thread 1 mm/turn) driven by stepping motors. One of the two motor-driven axes is permanently aligned, i.e. has no freedom in x-y, while the other can swivel in one direction. The stepping motors are driven via a multiplexer by a computer-controlled drive circuit. Spring preloading of the adjustment screws will minimize the residual play.

The adjustment proceeds in the following way. The white reflecting camera cover with some LED markers will be swung in front of the camera.[8] The control computer will switch on the laser pointer causing the stepping motors of a panel to

[8]Alternatively a permanent diffuse reflector panel might be installed beside the camera. In this case the laser diode spot and focal panel spot will not coincide but will have to be adjusted such that when the laser is properly positioned, the mirrors will be focussed onto the center of the camera. This procedure could in principle be used during normal operation provided no scattered light of the laser diodes hits the camera or the camera is insensitive to the used wavelength.

be adjusted. In addition, the computer is connected to a CCD video camera with a high power telelens. This camera, mounted in the center of the mirror dish, will measure the deviation between the laser diode light spot and the reference center at the camera cover and drive the stepping motor accordingly until the laser spot coincides with its reference position. This procedure is then repeated for all panels one by one. The use of a narrow band pass filter (matched to the laser emission band) in front of the camera will permit the adjustment to be carried out even when there is a high level of ambient background light, thus even during day time. We estimate that it will take less than 5 seconds for adjusting/checking each panel, i.e. all the panels could be fine-tuned within 20 minutes. As most mirror panels are not expected to tilt, the adjustment should be finished in a few minutes. After some "training", the computer should be able to predict the number of necessary steps with high precision such that no "hunting" is expected during the adjustment or a preadjustment is carried out automatically. This is particularly important for GRB searches where the telescope must be repositioned very quickly and no time can be wasted for lengthily adjustment procedures.

From the finite element analysis of the space frame it is known that the biggest deformations occur close to the sides where the dish is supported whereas a large part of the central area shows no deformation at all (see Fig. 4.8). The calculations predict that about 10% of all panels need adjustments after a change in declination of 25° and about 25% after a change in declination of 60°.

We are also considering an alternative procedure that uses as light source an object at a km distance or a bright star or perhaps the moon. (Although moonlight is very bright, the moon's image of 0.5° diameter is difficult to use for adjustments to a precision of $< 0.02°$.) The panel under adjustment would be tilted so that the panel's focal spot would be displaced by about 1° out of the general focus. The panel's focus position would then be recorded by the video camera. The panel would then be tilted so that the spot moves by ca. 1° to the other side of the center of the camera. From the two off-axis positions one can interpolate the correct position and steer the panel accordingly. This procedure is free of any laser pointer misalignment but cannot be used easily for routine corrections. Conversely, this procedure allows one to check the laser alignment and also to check whether the 4 mirrors of a panel are correctly aligned with respect to each other.

The combination of a tessellated mirror and active mirror control offers some other benefits. If, accidentally, the telescope points towards the sun one can defocus the individual elements so that the heat load onto the camera coverage will be tolerable. It is also possible to check individual mirror degradation, reflectivity or mechanical defects resulting in focal degradation, by steering the focal spot of individual panels onto a special sensor. Most of these operations can be carried out semi (or fully) automatically from a terminal.

Finally, we want to mention an idea for the initial adjustment of the mirrors on the telescope. On a cloudy late afternoon the telescope will be positioned such

that it points to the zenith. Then, an autocollimating laser plumb-line will be positioned about 1-2 m above each mirror element. The mirror under study will be adjusted so that the reflected beam hits the nominal focal spot on the camera cover. As the volume between camera and mirrors is not obscured by mechanical elements (masts, steel- or electrical cables). The plumb-line can be made hanging down on a cable from the camera edge and pulled across the entire mirror area by 3 transverse strings. The plumb-line's autocollimation must be able to handle any residual vibration or oscillation of this rather unstable positioning system. It should be mentioned that the use of optical plumb-lines for mirror adjustment has been brought to our attention by F. Krennrich, Whipple collaboration.

Currently we are testing the active mirror alignment on a test stand. The first tests indicate that a precision equivalent to the video camera pixel size can be reached (eq. to 2 mm in the focal point). The results of the first test are both summarized in appendix D ("Test of an active mirror control ...") and a diploma thesis [103].

4.2.7 Protecting the mirrors against environmental impacts

Keywords: Protection against environmental impacts has to be built into the telescope.

Since the telescope will not be protected by a dome, it must have some form of built-in protection, particularly with regard to the mirrors. There are two classes of environmental damage:

(a) impairment of mirror quality during normal operation by dust deposits or by the formation of dew or ice under conditions of high humidity,

(b) rare, but potentially damaging, events such as lightning, storms or hail.

A detailed discussion of the various problems and possible solutions can be found in chapter 8.2.

4.3 The camera

Keywords: The Čerenkov light image is detected by a fine pixelized photomultiplier camera

The camera is a decisive element for improving the γ sensitivity and the γ/hadron (γ/h) separation power. Historically, ACT cameras underwent a development from a single photo multiplier tube (PMT) version to cameras with a few hundred pixels. The progress of the last years can mainly be attributed to finer pixelized cameras

allowing the subtle differences between hadron and γ showers to be revealed. Hand in hand with finer pixels there has been an improvement in the trigger efficiencies for γs, the angular resolution, the γ/h separation and some modest noise reduction by limiting the image to its minimal necessary size. In turn also the energy resolution should be slightly improved due to the better determination of the shower maximum location in images, particularly for low energy events. For example the first HEGRA camera had a pixel size of 0.45° although the typical widths of TeV hadronic and γ showers are only 0.2 - 0.4° and 0.1 - 0.2°, respectively. According to measurement principles, the pixel size should be $\leq 1/2$ of the quantity to be measured, i.e. as "width" is a good discrimination parameter, the pixel size should be $\leq 0.1°$. A similar pixel size can be derived from the needed angular resolution and the other image parameters. Here we would like to reiterate that distant showers (high up in the atmosphere or at large zenith angles) will produce more compressed images that demand finer pixels. On the other hand fine granularity is very costly, with regard to both the sensor and the associated readout. Eventually the investment for the camera and readout electronics will dominate the cost of the telescope; compromises have to be found.

Besides the pixel size, image analysis is also affected by the diameter of the camera. The shower image can easily extend up to one degree (1.5-2° for energetic showers) and it is very important to also collect information about the shower tail (being farthest away from the camera centre) for γ/h separation and for solving the head/tail ambiguity of images.

As has already been pointed out, images from distant, low energy showers ($<$ 100 GeV) will be rather compressed and rather close to the camera centre while high energy showers with plenty of light will be more extended because they reach further down into the atmosphere. This influences the configuration and size of the camera. For cost reasons the following compromise for the MTD96 camera has been reached. The inner part of the camera will be equipped with high QE, red-extended pixels 0.1° in size up to a radius of 1.25°. The high resolution section will be surrounded by coarser pixels 0.2° in size and normal bialkali photocathodes. The "low QE" ring extends from 1.25° up to 1.8° radius and is sufficient for the observation of the tails of high energy showers where plenty of light is generated anyhow. Fig. 4.22 shows the geometrical pixel pattern.

This 'mixed' camera can be considered as a staged version of an 'all high QE' fine pixel camera which might eventually be needed for the study of extended sources. Eventually we will aim for a 4 - 5° ø field-of-view camera with nearly round geometry.

Before describing the camera in detail we would like to elaborate more on the benefits of using red extended, high QE sensors, although they are considerably more expensive than conventional PMTs, the "workhorse" of all contemporary ACTs.

The classical PMTs with bialkali photocathode and borosilicate windows are well suited for the observation of Čerenkov light from showers in the TeV region. The spectral cut-off of standard glass windows is reasonably matched to the Ozone

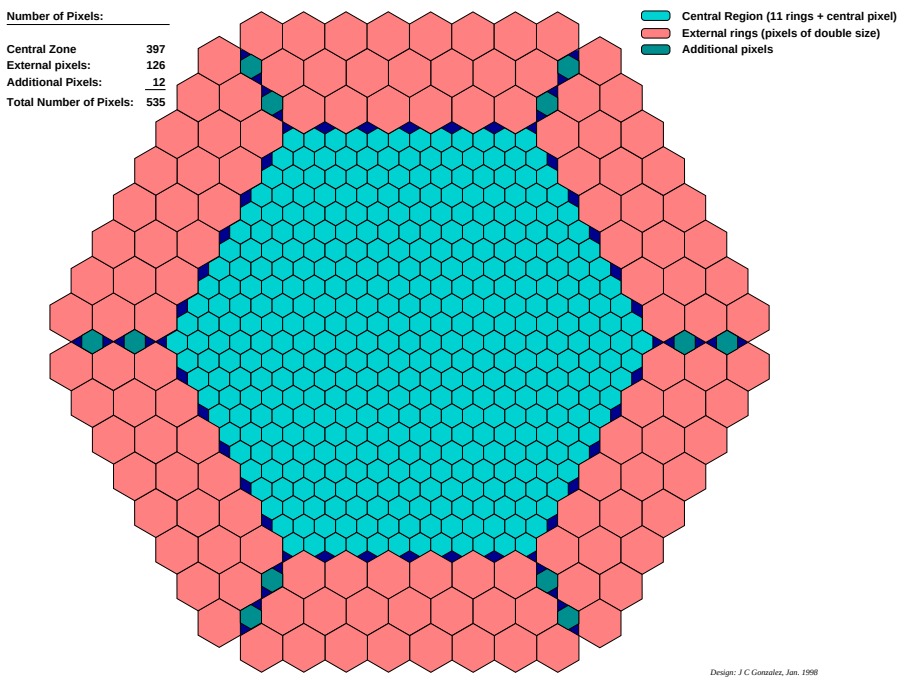

Figure 4.22: Geometrical pixel pattern of a possible design of the MAGIC Telescope's camera.

cut-off of the atmosphere while the QE peaking between 300 and 450 nm is well matched with the UV peaking of the Čerenkov light. In addition the contribution of the night sky background in the UV is rather low. The situation changes quite significantly when distant showers are observed, e.g. when observing at large zenith angles or when observing low energy showers that stop high up in the atmosphere. Rayleigh and Mie scattering will scatter most of the short wave Čerenkov photons in such a way that the remaining spectrum at the detector level shifts peaks to higher wavelengths. For example, at a zenith angle of 75° the spectrum is rather flat between 400 and 600 nm with its peak around 450 nm, whereas below 350 nm almost no light at all is observed. An independent confirmation of the effect can be derived from measurements of the solar spectrum at different air masses, see for example Fig. 3.3. The low energy showers, which are most difficult to observe, peak at around $x_{\max} \approx 0.2$ air mass, i.e., besides a small absorption correction due to high layers of Ozone the curves in chapter 3.7 should fairly well represent the reduction due to scattering and absorption processes in the atmosphere.

A closer look at the night-sky background shows that one would still gain in the value of $S/\sqrt{NSB}$ by extending the sensitivity towards the 'red' because $S/\sqrt{NSB}$ increases more slowly than S as a function of wavelength. Here we wish to mention that for an imaging telescope it is not only the $S/\sqrt{NSB}$ ratio is important, but

also the absolute number of ph.e.s measured per image. Obviously, by extending the measurement of the Čerenkov spectrum further into the red, one collects more charge. We would like to point out that some subtle effects, such as the excess noise of PMTs or the electronics system noise, encourage one to work with the largest possible value of S even if $S/\sqrt{NSB}$ increases proportionally.

Another strong argument in favour of using red-extended light sensors comes from the prospect of carrying out observations in the presence of moonlight. Unless one is observing within a few degrees around the moon, one is confronted only with a background of scattered moonlight. Direct moonlight exhibits a very similar spectrum to that of the sun. Scattered moonlight is "blue"; the blue sky on a clear day is an example of this. Depending on the telescope's altitude and the moon's zenith angle, scattered moonlight will show peaks around 400 nm with nearly half of its photons below this wavelength. Fig. 3.6 shows sample spectra for scattered sunlight with aerosol concentration as an additional parameter. From the curve with low aerosol concentration which corresponds $\approx$ to a clear sky condition at the HEGRA site it is immediately obvious that it would be favourable to integrate the Čerenkov light up to $\sim$ 600 nm. Some relevant values for the moonlight are:

Direct photon flux (full moon):	ca. 2.10^{14} photons m^{-2} s^{-1}
scattered photon flux (full moon):	ca. 10^{13} photons m^{-2} $sterad^{-1}$ s^{-1}

A critical background factor during observations in presence of moonlight is the light that is scattered off the nearby ground or reflected from parts of the telescope. Great care will have to be taken to avoid scattering from the telescope structure and to minimize the angular acceptance of the Winston cones in front of the sensors for light outside the angular range defined by the mirror area.

The improvement achieved by using a high QE red-sensitive photosensor instead of classical PMTs for observations at large zenith angles should be very high, e.g. a factor ca. 4.5 at 70° for 50 GeV showers. For silicon avalanche photo diodes (APDs) the gain can reach easily a factor 10 (see Section 4.3.3).

The prime focus detector package (including the camera, HV generators, pre-amps, optical fiber drivers and housing) will weigh about 100-120 kg. To keep the shadowing of the reflector to a minimum, the external dimensions of the housing of the MTD 96 design will not exceed 125 × 125 × 100 cm, allowing a maximal camera diameter of 4°. Various camera designs are considered (see below). Each will be modular to permit easy exchange of parts, and the option of generating solar power via a prime focus heat exchanger will be retained. The detector package could be circular to allow for rotation; in this case the package will be equipped with stepping motors that allow rotation up to 180°, thus maintaining the orientation of the star field in the camera co-ordinate system throughout the course of each observation, a feature of particular importance for the study of extended objects (see discussion below).

The sensitive area of the MTD96 camera has a diameter of 3.6° in the focal plane (equivalent to a diameter of approx. 100 cm) and consists of a fine pixelization region 2.5° in area surrounded by a few rings with coarser pixels that are naturally inferior in performance but lower in price. Triggers will be derived from part of the inner section which has a diameter of 1.6°.

In the following section we will describe details of the camera. Three versions are discussed. The MTD96 camera is a mixture of high QE, red extended hybrid PMTs (commonly called hybrid photo detectors (HPDs)) in the central part and a ring of conventional bialkali PMTs. If, for unexpected reasons, the novel hybrid PMTs are not available, we will resort to using a conventional PMT camera. Also we wish to discuss the option of building a camera with APDs as light sensors. These detectors with ca. 80% QE have not yet the required low-noise performance but it is hoped that within a few years this will be possible. An APD equipped 17-m telescope will correspond to a "classical" telescope of over 45 m diameter.

4.3.1 The MTD96 camera based on high QE GaAsP - intensified photocells with avalanche diode readout

Keywords: The Intevac GaAsP-intensified photocell as a parent type for a Čerenkov photosensor.

We intend to use vacuum photosensors with a GaAsP photocathode because the cathode offers a broader and superior QE compared to bialkali PMTs. The company Intevac offers a commercial photosensor with an 8 (16) mm ø GaAsP photocathode. This rather compact detector is a HPD (called intensified photocell (IPC) by Intevac) with a 1 mm ø GaAs PIN diode as anode. Photoelectrons are accelerated by a cathode to an anode voltage of 2-10 kV_{c-a} and generate up to about 1500 electron-hole pairs in the diode. Fig. 4.23 shows a cross-section of a tube with a 16 mm ø cathode and Fig. 4.24 the spectral curve (plain tube labeled as 'Intevac-clean') of a sample tube when cross-calibrated against a reference silicon photodiode.

Some modifications are necessary in order to adapt the device for the proposed use:

a) The QE below 400 nm is too low, i.e. below that of bialkali photocathodes (the curve labeled 'PMT EMI-9083 A' in Fig. 4.24). A solution to enhance the UV sensitivity with wavelength shifters (WLS) will be discussed in the next section.

b) The gain of the IPC is too low to achieve single electron response in the ns time domain. The output signal has to be amplified by a transimpedance amplifier or a very fast charge sensitive amplifier to a few mV per ph.e. Even the best fast amplifiers have an equivalent input noise charge of a few thousand

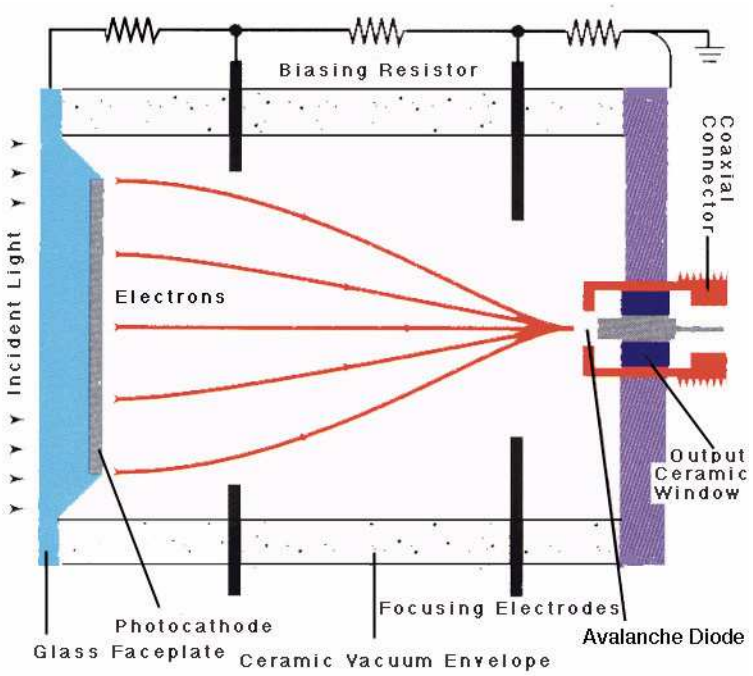

Figure 4.23: Cross section of a hybrid photomultiplier with avalanche diode readout.

electrons in the 1-10 ns time domain. The solution is to replace the diode by an avalanche diode giving additional gain. This development will be discussed in Section 4.3.1. The first prototype tubes have been tested.

As noted in the overview of the camera, the MTD96 will be equipped with IPCs up to a radius of 1.25° only, whereas we intend to increase the radius to 1.8° by adding rings of conventional bialkali PMTs. These are the same as in the classical version, the so-called 'fallback' option, and a detailed description can be found in Section 4.3.2. Fig. 4.25 shows a basic block diagram of a single pixel.

The elements are

- a hollow Winston cone light funnel,
- a hybrid photomultiplier with a GaAsP high QE, red-extended photocathode and WLS coating for UV extension,
- a high-voltage power supply for $U_{\mathrm{c-a}}$,
- a high-stability, medium-voltage supply for the AD bias,
- an AC-coupled preamplifier (transimpedance or charge sensitive) followed by a filter amplifier followed by the driver for the analog optical fiber ,
- possibly a parallel slow branch measuring the mean current output of the IPC as a coarse measure of the night sky background.

Obtained studies of some tubes are added in the appendix E.

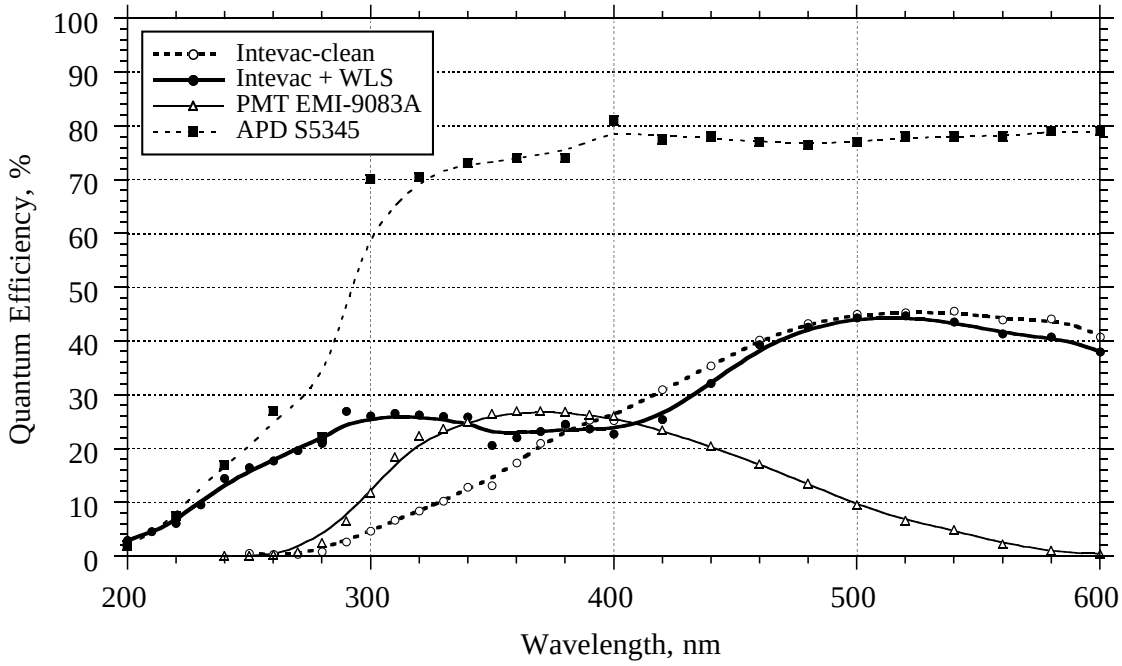

Figure 4.24: Spectral Quantum Efficiency of an Intevac hybrid PMT compared to a classical bialkali-PMT, an APD, and an Intevac tube covered by a wavelength shifter dye to enhance the efficiency in the blue. The APD curve is taken from [75].

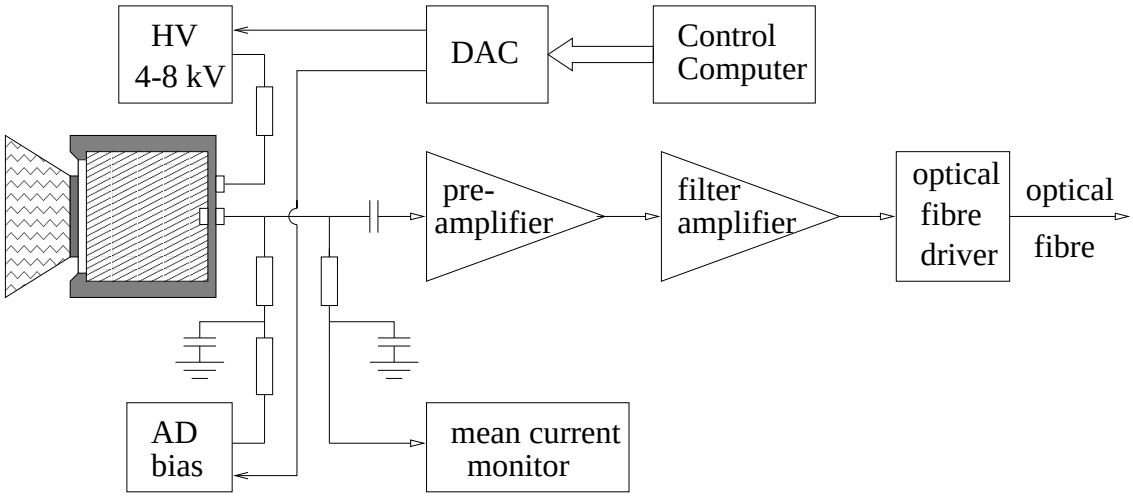

Figure 4.25: Basic block diagram of a single camera pixel readout chain.

4.3.1.1 Enhancing the UV sensitivity by WLS coating of the window

Keywords: The low UV sensitivity of the Intevac tubes can be enhanced by a simple WLS coating.

In order to make full use of the Čerenkov spectrum reaching the telescope the UV sensitivity of the IPC has to be enhanced. A straightforward and simple procedure is to coat the window with a WLS that shifts the UV light to the wavelength at which the IPC shows maximum sensitivity. The WLS method has been in use for many years in high energy physics Čerenkov detectors where it offers a simple remedy for the UV cut-off of the PMT glass windows. Fluorescent dyes, particularly those used for dye lasers, are well suited for this purpose because many of them have a QE close to 100% and decay times in the ns range. These dyes can either be evaporated directly onto the window or embedded in a plastic carrier. The latter method is more efficient because of better light trapping, ease of application (as a foil or lacquer) and much higher mechanical resistance. Examples for the lacquer coating of PMT windows can be found in Eigen et al. (1979) and Bradbury et al. (1995). For example, all the PMTs of the HEGRA AIROBICC detector are coated with WLS in order to improve the UV-sensitivity between 300 and 330 nm. Some suitable dyes for our application are P-terphenyl, Butyl-PBD, POPOP, PMP, and modified Perylene (BASF dye # 078 or 241), etc. The dyes can be dissolved together with a polystyrene or Paraloid (an acrylic lacquer base) binder in organic solvents such as dioxan, chloroform, toluol or dichloromethane and applied as lacquer or thin foil to the window. The window can be overcoated a second time by a thin layer (a few μm) of Teflon AF, which acts as a simple antireflex coating because of its low refractive index ($n = 1.3$). Tests of WLS coating on the IPC showed a clear increase in UV-sensitivity; see example in Fig. 4.24 (the curve labeled as 'Intevac + WLS'). However, the gain did not reach the predicted value of around 40% because the current window geometry is not ideal for WLS light collection. For strength reasons, a tapered glass window of 5.6 mm thickness (see Fig. 4.23), was used in the commercial tube. The WLS emits light isotropically. Besides the inevitable loss of ca. 12.7% in the backward direction, all the light is normally trapped in the high-refractive index glass and has thus a high probability of hitting the photocathode. In the case of the tapered 5.6 mm window of the IPDs, about 45% of the light misses the cathode. This deficiency can be corrected by using a light-fiber plate or a thin, high-strength artificial sapphire window. Light-fiber plates have other losses and are therefore less suitable. We have tested 1 mm thick sapphire windows at up to 30 atm without breaking them. Sapphire is used in ultra high vacuum applications at up to 10^{-10} Torr and is easily available because of its widespread use in wrist-watch windows. Its thermal expansion coefficient of ca. $6 \cdot 10^{-5}$ is closely matched to Kovar, as well to the ceramic material of the tube body and to GaAs. Its high melting point prevents melt bonding of the GaAsP wafer cathode directly onto the window but so-called solder glasses of matched expansion coefficient and a softening

temperature of ca. 350°C can be found readily. Because it has a higher refractive index than glass plain sapphire will have higher reflective losses than glass but, with the surface coating. of the plastic WLS carrier and Teflon AF, the losses can be reduced to $< 3\%$. The window is normally fixed to the tube body by an indium seal. Our tests confirmed that a uniformly distributed load of > 1500 kg can be applied without breaking an artificial sapphire window, 22 mm in diameter and 1 mm thick. In summary, we are confident that one can achieve a QE $> 40\%$ from 300 to nearly 650 nm with the modified IPC. Because of the WLS decay time a small degradation of the time resolution will occur but it will still be below the 1-2 ns time spread of the Čerenkov light.

4.3.1.2 The increase of the IPC gain

Keywords: The gain of the commercial IPCs is insufficient to resolve single electrons on a few ns time base.

The gain of ca. 1000 of the parent type IPC is too low for a good single electron response in the ns time domain. Recently Intevac has replaced in a prototype IPC the GaAs PIN diode by a GaAs Schottky avalanche diode (AD). At a bias of ca. 30 V the AD has an internal gain of 10-15 resulting in an overall device gain of ca. 25,000 at 10 $\mathrm{kV_{c-a}}$. GaAs allows for a very high operating frequency (up to 4 GHz in the IPC). As we have less demanding speed conditions we intend to replace the GaAs AD by a silicon one for the following reasons: we are interested in running the tube in rather harsh field environments and want to lower the $U_{\mathrm{c-a}}$ to < 5 kV, thus the primary gain would be reduced. This reduction has to be compensated for by a higher AD gain. In addition we plan to raise the overall gain to about 30,000-50,000 because it allows for cheaper and less complex transimpedance amplifiers or maybe even current amplifiers. A high gain in a GaAs-AD cannot be achieved because of the nearly equal k-factors of hole and electron multiplication. Silicon ADs are now well under control up to gains of, say, 200. Also the energy required to create an electron-hole pair in silicon is lower than in GaAs (3.6 eV vs. 4.2 eV) thus the silicon AD will have a higher multiplication for the same $U_{\mathrm{c-a}}$. In addition, the lower Z of silicon compared to GaAs will result in less back scatter and hence give an intrinsically better single electron resolution[9].

We have tested the single electron response of the prototype IPC using a blue LED light pulser of 5 ns FWHM and $\langle n_{\mathrm{photon}} \rangle \approx$ 6-8. Fig. 4.26 shows the resulting

[9]In principle such an excellent electron resolution is not needed but improves slightly the background rejection ('tail cuts') and errors on the individual pixel content. Nevertheless one has to consider that for very short shaping times the resolution deteriorates proportional to $1/sqrt\tau$, τ being the shaping time constant. In case of aberrations in the presence of moon light it is unnecessary to resolve single electrons because the background light noise is much larger than a single electron.

pulse height distributions for 10 kV_{c-a} and a 50 ns filter time constant. The peaks for 1,2,3.. electrons are well resolved.

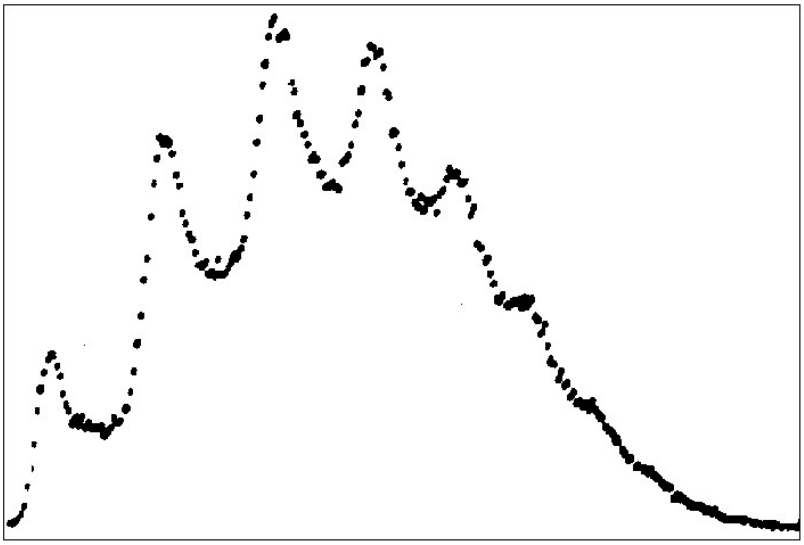

Figure 4.26: Pulse height spectrum of a modified Intevac IPC when illuminated by a fast blue LED pulser. Settings: $U_{c-a} =$ 10 kV; $U_{AP} =$ 30.0 V, $\tau =$ 50 ns.

We also tested a second set of operational parameters: With 6 kV_{c-a} and a 10 ns filter time constant (i.e. settings much closer to our final operating conditions) the electron peaks are still distinguishable but much wider. The pulse height resolution would in principle be just acceptable for us but in a large system one would want to have better performance to counteract degradation due to component spreads and time. The use of a silicon AD of 1.5 mm ø and of gain 30-60 seems to be the best solution.

4.3.1.3 The ion feedback problem

Keywords: Ions in PMTs can fake large signals and destroy the photocathode

In our application the photosensor will work in a high background environment. The large mirror will collect a high flux of the night sky background light (ca. $1.7 \cdot 10^{12}$ photons m^{-2} $sterad^{-1}$ s^{-1} between 300 and 600 nm) resulting in a single photoelectron counting rate in excess of 50 MHz per pixel. While the probability of ionizing the rest gas between cathode and anode is low because of a vacuum of 10^{-8} Torr, the rate of ionization of the rest-gas adsorbed on the AD surface and

surrounding metal layer will generate a sizable flow of ions. This back-flow (presumably mostly hydrogen ions) will have two adverse effects on the photocathode: (a) it will frequently generate large pulses that can fake large Čerenkov signals [69] and (b) it will eventually destroy the activation of the photocathode[10]

The ions can be deflected electrostatically such that they miss the photocathode.

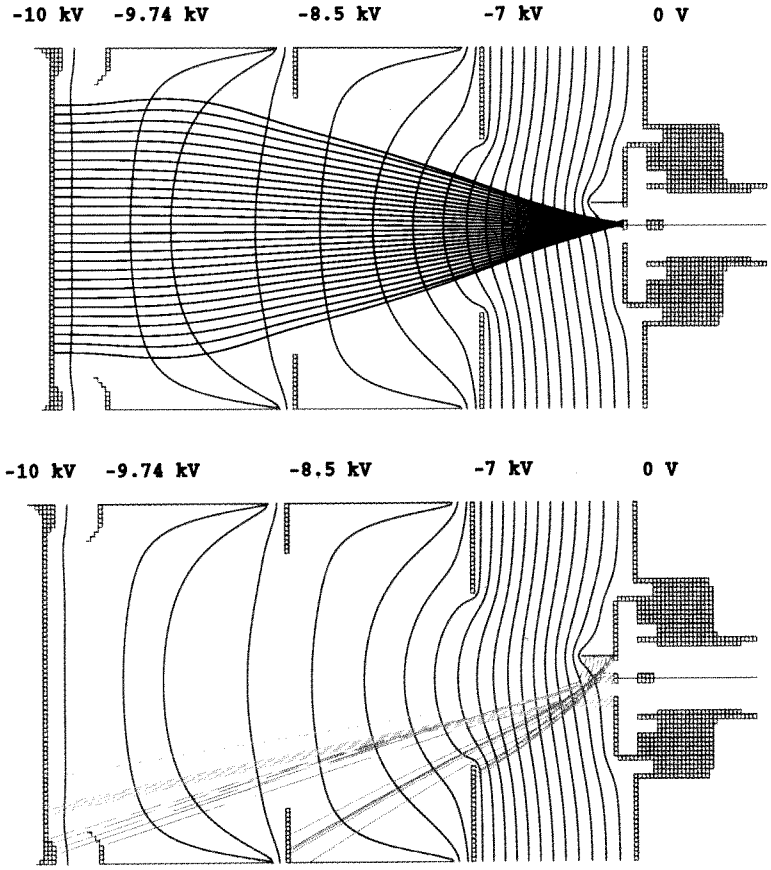

Figure 4.27: Simulation of of a) electron tracks, and b) ion tracks inside the Intevac IPC employing an electrostatic deflector.

Fig. 4.27 shows a simulation of a) electron tracks, and b) ion tracks inside the Intevac IPC. The simulation was carried out by Intevac using their patented electro-

[10]According to Intevac a drop in cathode sensitivity by a factor of 2 will occur after an integrated current of 5 mC. This can be coverted into < 100 years of dark night observations, or 10-15 years of observations both during dark nights and during moonlight.

static deflector, a small conductive finger at ground potential. The small deflection of the higher energy electrons is compensated for by a small offset of the AD from the center. A test of the prototype IPC with an 8-mm GaAsP photocathode gave a noise rate of ca. 10 kHz but a very low rate of large signals that are compatible with the rate of Čerenkov signals of cosmic muons passing through the thick glass window.

The Zagreb group has made detailed electron optics simulation and found a configuration that allows to completely suppress the ion feedback from the anode area while conserving the rotational symmetry. The proposed special electrostatic 'lens' could be used also in classical PMTs and help to reduce the ion feedback problems in case of high ambient background illumination. The results of the study are summarized in appendix F ("Electron optics of the Intevac intensified photo cell).

4.3.1.4 Comments/conclusions on the IPCs and the studies

Keywords: GaAsP photosensors allow for a factor 3-5 increase in photon to photo-electron conversion

The use of high QE, red-extended photosensors is of great importance for HE γ-astronomy with ACTs. For the time being they are 'on the critical path' of MAGIC. The current prototype work shows that they can be built and that the problem lies more in the commercialization of the design. The current studies show that

(a) an acceptable UV extension of the spectral sensitivity can be obtained for GaAsP photocathodes by applying a WLS coating to thin windows;

(b) that artificial sapphire, 1 mm thick, is a good window candidate because of its high strength;

(c) that the replacement of the anode diode by an avalanche diode allows for sufficient gain to be able to have a good single electron response at very high rates;

(d) the high vacuum and proposed electron optics with an ion deflector (current version or simulated new electron optics configuration) prevent destruction of the cathode activation by ion feedback and keeps the rate of large fake pulses low.

In appendix E we show the results of a recent study with an Intevac prototype.

All the tests carried out so far indicate that the use of such a photosensor will increase the conversion yield of Čerenkov light to ph.e.s by a factor of about 4 over conventional bialkali PMTs when observing close to the zenith and a factor of about

5 at low altitude (ca. 15°) observations, i.e. the use of such a tube compares to the construction of an ACT of 30-40 m ø mirror and classical PMTs.

The production of the tube is rather complex and therefore more expensive than the production of glass PMTs with in situ formation of multialkali cathodes. The cathode has to be grown by Epitaxy onto a thin GaAs waver, then it has to be fused onto the glass (sapphire) window. Afterwards the GaAs has to be etched away. In a next step the cathode has to be coated with Caesium or Ceasiumoxyde in order to lower the escape barrier. Finally the window has to be mated with the other parts of the tube. Nearly all steps have to be done under ultrahigh vacuum. It is obvious that this production requires the collaboration of people experienced in semiconductor production and in ordinary PMT production. GaAsP photocathodes are used as electron sources in electron accelerators and as photocathodes in the latest generation of image intensifiers (night-vision units). Therefore the principle of the photocathode production is fairly well known. Recently we have begun discussions with a Japanese and an European PMT manufacturer about possible production of the hybrid PMTs with GaAsP photocathodes. In parallel we are discussing the direct epitaxial growth of GaAsP photocathodes on sapphire with some Russian companies.

It should be noted that the recent measurement with the IPC with AD readout [36] is somehow a 'world best' measurement of low photon flux detection with fast timing. Such devices could have many other applications such as for example fast fluorescence studies of biological processes, low light detection in astronomical observations of pulsars or high resolution γ spectroscopy using CsI(Tl) crystal detectors or scintillators of very low light yield and long wavelength emission.

4.3.1.5 The light funnels in front of the light sensors

Keywords: Hollow Winston cones are used for ≈ 100% light collection and suppression of large angle stray light

For constructions reasons, light sensors, classical PMTs or hybrid PMTs (or APDs) have a sensitive area significantly smaller than their outer dimensions. Therefore, even in a physically very dense package, a sizable fraction (ca. 50%) of the light would be wasted. A way out is to install light funnels, which are now in use in many telescopes (for example at CAT or HEGRA). A careful design would result in nearly 100% light collection. In MAGIC we will use hexagonal to round (29 mm to 15 mm ø) hollow light funnels shaped like Winston cones. In principle, the funnels allow for an area compression of 4.5 by reducing the angular acceptance to 0.8 sterad. This reduction is of great importance as it limits the angular acceptance corresponding to an area slightly larger than the mirror area. Therefore the camera would be insensitive to stray light from angles $> 33°$, i.e. from back-scattered light from the ground, for example during moonshine or distant light from human installations,

cars, snow in winter, etc. Only a small extra baffle around the camera might be needed in order to minimize double-scattered photons.

The cones would be made similar to those in use in the current HEGRA telescopes. Delrin mandrels resembling the shape of the cones will be mounted, densely packed, onto a transfer plate and the gap between the mandrels will be filled with black microsphere-filled Epoxy. After hardening the mandrels can be removed and, after some machining of excess material, the slightly oversized cones, made from high quality aluminized Mylar, will be glued in. The dead space between the cones is just twice the thickness of the 0.1 mm Mylar.

The change from hexagonal to round can be accommodated by proper folding of the Mylar with only a modest deviation from an ideal Winston cone shape (rotation of an inclined parabola). This technique has been developed at the MPI in Munich and has been in use on 5 of the 6 HEGRA telescopes. Fig. 4.28 shows a photo of a HEGRA light funnel plate for 271 pixels.

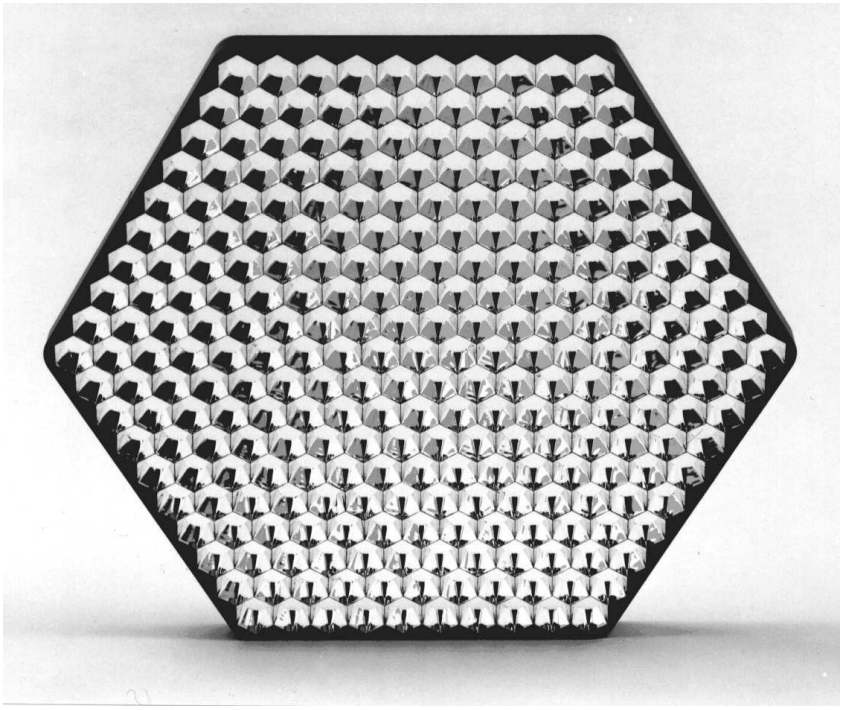

Figure 4.28: Photograph of the hollow light funnel (Winston cone) plate for the HEGRA ACTs.

In front of the light funnels a thin window will be mounted. Its main function is to hermetically seal the electronic sensors and elements against humidity and dust. The window will have a high transmission between 300 and 700 nm. In order to minimize light losses by surface reflection we intend to use either a 1 mm

TEFLON AF window (lower wavelength spectral cut-off around 210 nm; $n = 1.3$, i.e., a reflectivity loss of about 3.4%) or a 1 mm Plexiglas 218 plate with antireflex coating (lower spectral wavelength cut-off $\approx$ 290 nm).

4.3.1.6 The HT system for the IPCs

Keywords: The IPCs need 5-8 kV bias voltage.

The IPCs need between 2.5 and 8 kV between photocathode and anode. We intend to operate the tubes at a nominal value of 5 kV, but, because of device spreads and ageing, a variation between 3 and 8 kV must be allowed. At 5 kV the bleeder network across the tube draws about 1 μA of current. We will use Greinacher voltage multipliers that are able to supply 180 μA at 8 kV, e.g. we will always connect 50 IPCs together to one supply. A series potentiometer in front of each IPC allows for some equalibration of the gains in each batch. This equalization will be carried out beforehand on a lab bench. The voltage of each batch will be controlled by the on-line system via DACs.

Most of the HT system will be potted in order to avoid corona discharge. Also, it will be important to seal the camera and flush the interior by dry nitrogen or SF_6 (with some modest overpressure) in order to prevent humid air to enter the camera.

For the more technically interested reader: the first step gain due to the electron bombarding of the silicon anode(PIN diode or AD) is:

$$
\begin{array}{lcl}
G_{\mathrm{bias}} & \approx & (U_{\mathrm{bias}} - 2500\ \mathrm{V})/3.67\ \mathrm{eV} \\
 & & \text{with G = gain} \\
U_{\mathrm{bias}} & = & \text{bias voltage of the IPC in V} \\
2500\mathrm{V} & = & \text{min. voltage needed to pass the passivation and p++ layer of the diode} \\
3.67\mathrm{eV} & = & \text{energy needed to create an electron} - \text{hole pair}
\end{array}
$$

At around 6.2 kV the gain is ca. 1000. Due to the linear correlation of the gain and bias voltage the gradient $\Delta G/\Delta U$ is basically constant and very small. Therefore the requirements for bias-stability are less stringent than for classical PMTs.

4.3.1.7 The bias voltage for the avalanche diodes

Keywords: the ADs need a highly regulated bias voltage around 50-100 V.

The ADs inside the IPCs need a highly stabilized bias voltage, which has to be generated for each AD separately. We plan to use a common bias rail of -150 V, a 100 kΩ pre-bias resistor and a parallel load to the AD (see Fig. 4.25). The parallel load is driven by a reference signal (computer-controlled DAC), a temperature sensor and the actual voltage at the AD load resistor. The voltage at the network and the AD are measured automatically and used to record the gain and the AD current

which is to a certain extent a measure of the background light. The parallel load regulator ensures automatic protection against destructive AD overloads in the case of high-light levels.

The gain of the AD will be set to ca. 30-50, i.e. the IPC will have an overall gain of 30,000 - 50,000.

4.3.1.8 The fast preamplifier and filter amplifier

Keywords: The IPC's low output signal needs to be amplified

The electrical signal of 30,000-50,000 electrons per incident photoelectron is still too small to be handled by standard fast-electronic components and needs to be amplified by a large factor. Most suitable are either low noise charge sensitive preamplifiers followed by filter amplifiers of appropriate filter time constants in the 5 ns range or ultralow noise transimpedance preamplifiers. In both cases the preamplifier must have an intrinsic noise well below 30,000 electrons in the needed frequency band. Prototypes of either type of preamplifier have been built and found to be acceptable in noise performance but the safety margins are not large and some improvements are needed. Due to the rapid expansion of the mobile phone system in the 900 MHz band, new low-noise, cheap microwave transistors, suitable also for our application, are becoming available now. The filter amplifiers are fairly standard items. Therefore we will not discuss them any further. In the case of the transimpedance amplifier the filter amplifier will be a simple high bandwidth voltage amplifier with some modest integration and differentiation.

4.3.1.9 The outer ring of classical PMTs in the camera

Keywords : For cost reasons the outer ring of the camera will be equipped with classical PMTs of larger diameter

For cost reasons, we plan to use classical PMTs of 0.2° pixel size in the outer section of the camera. Images of the most interesting γs , i.e. in the energy domain below, say, 200 GeV or at large zenith angles, hardly extend to outside the inner 1.25° radius of the camera. On the other hand, shower images of TeV γs produce a sufficient amount of light so that classical PMTs would detect them, provided the camera is large enough (ca. 2500 photoelectrons/TeV γ energy in a classical PMT camera). In the outer ring one records mostly the photons of the shower tail. Due to the natural spread of the shower tail the corresponding section of the image is rather diffuse and a coarse pixel size of 0.2° is sufficient. We intend to use 2" PMTs which can be retrieved from a large sample of PMTs left over from high energy physics experiments. The PMTs will be operated also at a gain of 30,000 - 50,000 (only 6-8 stages used) and followed by the preamplifier-filter amplifier chain as outlined in the preceding section.

Further information on the standard PMTs can be found in the following sections. It should be mentioned that we consider the use of an outer ring of classical PMTs also as a staged approach to eventually build a large-diameter camera with uniform, fine pixel size of high QE PMTs. The needs and time scale is very likely dictated by the existence, or non-existence, of extended γ-sources. In the former case the use for a large diameter, uniform camera is important.

4.3.2 The classical camera version

Keywords: As fallback solution in case of development delays or staging a classical PMT is used as interim solution

The plan to use a new type of photon detectors is quite ambitious, and for various reasons it might be necessary to invest more time into their development; or, for financial reasons it might be necessary to stage the construction. As outlined in the introduction, one can use the so-called fallback solution by building a classical PMT camera. This will influence the potential of MAGIC as the trigger threshold will rise from about 10 GeV to about 30 GeV in the zenith position. This is still significantly better than for any currently proposed project but the chances to carry out large zenith angle observations will be affected. Detailed comparisons of the performance are made in chapter 6. A possible scenario could be that one builds the telescope as soon as possible and uses a somewhat modified HEGRA telescope camera, which are not optimized but sufficient to carry out a fraction of the physics program and then changes over to the standard camera. The necessary modifications to use a HEGRA type camera are:

- use of a less dense package in order to stick to the pixel size of 0.10°,
- modified light concentrators to match the increased pixel size,
- reduction of the gain of the PMTs in order to reduce the night sky background current[11],
- increase of the gain of the preamplifiers,
- addition of the outer PMT ring with 0.2° pixel size.

For the light concentrators it might be necessary to go to a mixed design of a half hollow and half Plexiglas construction in order to achieve the necessary area compression. It should be noted that one can in principle retain the dense PMT

[11]The PMTs do not have the good single electron response of the IPCs and have a larger excess noise factor (about 1.2 vs. 1.01). Therefore it is not necessary to operate the tubes with a gain of 30,000 - 50,000 but to "roll off" the gain to the preamplifier. Running the PMT at the lowest possible gain is favourable for lifetime extensions and operation in the presence of moonlight.

package corresponding to 0.075°. This would give even some improvement in angular resolution of shower images but increase the number of channels to about 1200 for the 3.6° camera. In view of the non-negligible costs for the analog fiber transfer and the F-ADCs for the time being we consider this as a too expensive solution.

As the classical fall back camera is a fairly standard construction and some aspects are already covered in the previous chapters we will skip further details except those about a possible different HT-system for the bleeder-current generation. This system is in the spirit to minimize cables and to avoid high voltage cables whenever possible.

4.3.2.1 The high voltage system

Keywords: The PMTs need a local HT power supply with individual adjustment

The large number of channels and the long distance between the camera and the ground station necessitates a special high voltage system. We will follow the approach of Neumaier et al. [74] who developed a new high voltage system for the WA48 experiment at CERN. The high voltage is produced individually for each of the 1000 channels by the same number of active PMT bases with on-board Greinacher voltage multipliers. The full VME based HV controller system is located on one single slot VME controller card. The VME controller card includes two HV drivers, each able to address 512 channels. The cabling amounts to only two 6-line flat cables (the 9 Bit address is transmitted serially over one line) from the ground station to the camera. The HV driver cycles continuously through all channels and a reference voltage (1/2000 of the demand HV) is sampled and stored at the HV base. The HV base will produce a feedback voltage for the monitoring of the HV stability. The cycle time for a 512 channel group is about 1 s.

The WA48 experiment has a maximal operating voltage of 2000 V, the total power requirements for 1000 channels are 75 W at 1600 V. The overall dimension of the WA48 bases are $\geq 16 \times 3.5 \times 1.5$ cm, which should nearly fit our requirements.

4.3.3 A future option: an all-silicon avalanche photodiode camera

Keywords: Avalanche photodiodes with > 80% QE allow for a fine pixel size of ca. 0.05 - 0.07° and lower threshold. The technology is not yet ready for immediate use.

As pointed out in the introduction the main drawback of classical ACTs is the low broad-band light to photoelectron conversion. By far the most promising improvement is the implementation of broad-band high QE photodetectors. Already the use of the GaAsP hybrid PMTs at small zenith angles results in a factor 3 increase in photoelectron yield over bialkali PMTs while at large zenith angles ($> 65°$) the relative yield will increase up to a factor of 5.

Solid state devices with internal photo effect (Si, GaAsP, ...) have a QE of $\approx 80\%$, which is still higher by a factor of 2 than that of the Intevac GaAsP vacuum photodetector.

From our current work with avalanche photodiodes (APDs) we estimate that in about 4 - 8 years the technology will have progressed sufficiently that they might be able to be used as readout elements [66, 47, 78].

The current problems involved in producing high gain, large area APDs might lead to a very fine granularity camera, but this would be in line with the general trend to build cameras with smaller pixel sizes, something that cannot be achieved with classical PMTs. Particularly for observations of distant showers, either high up in the atmosphere or under large zenith angles, the images will be very compressed; and for γ/h separation fine structures of the images have to be resolved, i.e. the pixel size should be much smaller (ca. 1/3) than that of the structure one wants to use for discrimination.

Currently, the best APDs have noise levels of 20 electrons/10 mm^2 area at room temperature. This is still unacceptable by a wide margin and a large improvement is still needed. One straightforward way of reducing noise is by cooling: by lowering the temperature to about -60°C the noise drops by 30 - 40% per 10°. This reduction is still not sufficient and some design improvements will be necessary.

Because APDs are still rather novel designs and not yet in use in ACTs we will add in a forthcoming report a rather detailed description of their function and improvement still needed. In the following, we only outline a camera concept based on the following assumptions of progress:

(a) APDs with the following parameters will be available:

- diameter: 3 - 4 mm,
- device capacitance < 10 pF;
- QE $\geq 80\%$ around 700 nm,
- leakage current < 20 nA at 20° C and gain 500,
- gain $\geq$500 (1000),
- excess noise factor ≤ 2 at gain 500,
- breakdown voltage significantly above the bias voltage for G = 500;

(b) the APD parameters, such as for example the gain, are stable at $-60°$ C;

(c) the new fast charge-sensitive preamplifiers or transimpedance amplifiers with low noise GaAs-HEMT-FETS in the input stage can be mass produced and that their intrinsic noise is constant at < 500 e$^-$ for 3 - 5 ns filter time;

(d) the price does not exceed current PMT prices.

Most of the requirements have been fulfilled in some prototypes but APDs with a combination of all of the above parameters are not yet available.

For the time being we consider it unrealistic to build APDs with large diameters (e.g. 15 mm) with a gain > 500, with low capacitance (the serial noise scales linearly with the capacitance) and an acceptable price, while 3 - 5 mm devices with the above parameters might be realized in the near future (e.g. 2 - 5 years). On the other hand, a pixel diameter of 0.06° (18 mm) is, according to our present knowledge the lower practical limit and would result already in ca. 1300 elements in the inner area (2.5°) of the camera.

The light entering the 18 mm pixel diameter has therefore to be concentrated onto the APD-sensitive diameter of 3 mm. For a mirror with f/d = 1 one can only build hollow light concentrators with a concentration factor of 7 whereas a factor of ca. 50 is needed. Using a high refractive index ($n = 1.5$) concentrator in optical contact with the APD allows one to increase the concentration factor to ≈ 20. This is still insufficient. Because of the limited spectral range it should be possible to use so-called light traps [Chiemtec Patent] which allow for a much higher concentration without violating the Liouville Theorem. Light of a limited wavelength band passes a dichromatic mirror of matched transmission and hits a WLS plate that shifts the light to a spectral range where the dichromatic mirror is fully reflecting and the APD is fully sensitive. The WLS plate is encapsulated by a white diffuse reflector except for the entrance window covered by the dichromatic mirror and a small exit hole matched to the sensitive area of the APD. High reflectivity (R close to 100%) of the diffuse reflector and the mirror are essential for large concentration factors. First prototypes with non-optimized dichromatic mirrors and reflectors have confirmed the principle but only half of the theoretical concentration factor has been achieved. An efficiency of 50% has been found for a concentration of 25 in the first prototype.

4.3.4 Calibration procedures

Keywords: Light pulsers of different wavelength provide calibration sources for the light detectors.

The camera system needs to be routinely calibrated. The ideal calibration source would be a light flasher of 1-2 ns duration and a spectrum similar to the Čerenkov spectrum. In the DC mode a deuterium lamp with appropriate filters exhibits a spectrum very similar to the Čerenkov light but in a pulsed mode such a source does not exist. In the MTD96 design we plan to use μ-Watt solid state lasers (Q-switched NdYAG crystals pumped by laser diodes) with frequency doubling and tripling to generate lines at 550 and 360 nm. The laser light will be guided by optical fibers to a small Ulbricht sphere positioned in the middle of the mirror. The exit hole of the sphere will be pointed towards the camera and thus illuminate all pixels uniformly. The excellent single electron response of the IPCs will allow one to

distinguish up to 5 photoelectrons. The light intensity of the calibration source will be cross-monitored by a PIN photodiode coupled to the Ulbricht sphere through an additional port.

The light beam can be attenuated over three decades such that also the full dynamic range can be tested. We are still studying whether measurements at two wavelengths are sufficient. In principle it is possible to couple the Ulbricht sphere to two (three) solid state laser pulsers with emission around (360) 430 and 635 nm.

The optical calibration will be backed up by an electronic pulser that injects high precision charge signals into the preamplifiers via a 1 pF capacitance. This system, common in semiconductor photosensor devices, can also be used during day time for readout debugging.

It should be noted that the element with the highest possible drift and variation is the pickup avalanche diode in hybrid PMTs. The "normal" calibration made by illuminating the ADs with 6 keV γs from an Fe56 source is not possible due to access problems.

The light pulser(s) will test the entire detection chain except possible variation of reflectivity of the main mirror (short term dust, long term slow degradation of the reflectivity). From time to time we will check mirror reflectivity with a reflectometer equipped with a deuterium lamp [14]. This device allows one to monitor changes of the integrated reflectivity for a Čerenkov-like spectrum to a precision of 2 - 3 %. The need for 1-2 ns light flashes stems also from relative time calibration of the individual FADC channels. This is important because it seems that some γ/h separation can be achieved also by analyzing arrival time distributions.

Partly linked to the calibration of the camera is the measurement of the atmospheric transmission. This task is discussed in the following.

4.3.5 Monitoring the atmospheric transmission

Keywords: for precision measurements the monitoring of the atmospheric transmission is indispensable

The atmospheric transmission changes with the observation angle, weather changes and variations in aerosol content. One of the interesting possibilities will be to measure the spectral brightness of known stars in the vicinity of the object under study.

Each night the Carlsberg meridian cycle telescope on La Palma measures the brightness in the Johnson V-band for about 30 stars. This information was found to be very helpful for detecting the atmospheric changes that affect the data of the current HEGRA telescopes.

At other sites the transmission has very likely to be monitored by the MAGIC operators. Two options are under discussion.

(a) The tracking monitoring CCD video camera should always "see" 4 - 12 stars in the field of view. The CCD chip is sufficiently uniform in sensitivity and it should be possible to monitor brightness changes of these stars and derive atmospheric transmission changes.

(b) We intend to set up a separate small optical telescope (Meade type 16" mirror) for monitoring optical variations of potential γ-sources that are known to pulse or flare, such as for example Crab, AE-Aquarii, Mkn421, GRS 1915, etc. The high sensitivity of such a telescope for seeing stars up to 15th magnitude should allow us to make routine monitoring of brightness variations of known stars. Modern computers will allow this process to be fully automized. We estimate that such a system would cost about 50 kDM, i.e. it has to be done in stages. The development of such a system could be the basis for a good diploma thesis in physics.

We study also the use of a LIDAR where only a weak laser pulser is needed when the large collector is used as receiver. With a somewhat lower clock frequency of the FADCs, one can record the backscatter profile up to 40 km provided some dynamic compression is possible.

Finally, it should be mentioned that the sun (although offset by 10-16 h) is an excellent and simple-to-use light source to probe the transmission and the spectral dependence of the atmosphere as a function of zenith angle (see for example [111]). Fig 3.3 shows some sun spectra at different air masses.

4.3.6 Cooling of the camera

Keywords: The electronics inside the camera generates about a kW of heat which must be transported away

The electronics in the camera will generate heat in the order of 1 kW which cannot be transported away by natural air flow because the camera has to be sealed. We intend to add a 220 V driven, light-weight cooling unit at the backside of the camera. Forced ventilation inside the camera body will ensure a uniform temperature level of around 5-10°C. Special measures will be taken to avoid dew deposit on the entrance window in case of high external humidity and elevated temperatures. A cooling power of 2-3 kW is considered sufficient. One additional requirement is, that the electrical motor of the fan will not induce any stray signals.

As an alternative solution one might use a more heavy unit placed somewhere in the space frame and circulate some cooling liquid through isolated tubes. The disadvantage of such a system is the 10-20% loss of cooling power due to the length of the tubes (at least 20 m) and difficulties to break the liquid circuit in the case that the camera has to be unmounted. The advantage of this option is that one avoids electromagnetic interference from the electromotor.

4.3.7 The camera cover

Keywords: The camera cover is an instrumented device

The seemingly trivial camera coverage has quite a few functions and is well instrumented. The functions are:

- provision of a light tight seal during daytime in order to allow camera studies,
- protection of the camera against the impact of bad weather,
- temporary shield in case of accidental exposure of the telescope towards the sun,
- highly uniform diffuse reflector for optics studies,
- carrier of positioning marks (LED lights, measuring grids),
- carrier for optical measuring elements which need sometimes to be repositioned remotely,
- carrier for instruments for auxiliary studies unrelated to γ astronomy, such as for LIDAR atmospheric studies and other low level optical studies drawing on the exceptionally large light collection mirror,
- carrier for light pulsers on the inner surface for debugging and specialized studies of the camera,
- a construction that has minimal obscuration of the telescope mirror during operation and does not interfere with the steel cables that keep the camera support ring in place,
- a sensor that allows to check the actual position of the cover.

The cover will be very likely a single-hinged door flipped to one side by electrical motors. The motor is connected to the backup emergency power system. In case of a power failure the cover will always be closed automatically. The cover will be a double-layer metal design with an insertion of $\geq$5 cm ceramic thermal isolation in order to prevent camera damage during short exposure to concentrated sunlight ($\sim$ 200 - 300 kW) in case of accidental telescope movements.

4.4 Telescope operation and monitoring

Keywords: for an efficient observation mode a good control system and monitoring of all relevant parameters is needed.

It is expected that the MAGIC Telescope becomes a γ-observatory similar in size and complexity to a large optical observatory or a radio telescope. We will try to adopt tested procedures and some of the organization structure from other telescope installations. The telescope will be a complex system made up of many elements, all of which have to be monitored and steered by a small operating crew. Presently we think that the system should be designed in such a way that a shift crew of only two people will be able to run the telescope for a full night, including all start-up and shutdown procedures (see also chapter 12).

A second crew working during the day would then be responsible for the maintenance of the telescope as well as other tasks such as data transfer and backup and preparation for the next night of data taking. For this we estimate that another two people will be needed to ensure minimal loss of observation time if technical problems occur.

4.4.1 Summary of the sub-systems to be monitored

Taking the telescope as a system of interdependent sub-systems, the following outline seems logically adequate:

1. The telescope drive
   (a) the fast slewing drive
   (b) the tracking drive
   (c) the deformation of the mirror support frame
   (d) stress monitoring of the most critically stressed parts
2. The camera
   (a) the photosensors and their HV supply
   (b) the pre-amps
   (c) the LED transmitters (for the optical fibre signal transmission)
   (d) the camera lid
   (e) the camera cooling
   (f) the camera positioning (focusing and maybe rotation)
   (g) the connectors of the optical fibers

3. The data acquisition
    (a) the LED receivers
    (b) the trigger
    (c) the digitization
    (d) the recording
    (e) the on-line data analysis
4. The mirrors
    (a) the active mirror adjustment
    (b) the mirror heating
    (c) monitoring of possible reflectivity degradation (see 4.2.5)
5. The tracking monitoring by CCD camera
6. The photo sensor calibration system
7. The burst alarm system
    (a) the HETE antenna
    (b) the alarm and fast reaction system
8. The outside conditions monitor
    (a) the weather station
    (b) the sky brightness monitor
9. The optical telescope
10. Standby systems
    (a) emergency power supply
    (b) de-icing equipment
    (c) equipment for protection against weather hazards
    (d) fire prevention system

4.4.2 Separation of DAQ and control

Keywords: DAQ and controls will have separate computer systems to maximize safety both for the operation and the data taking.

In order to ensure the independent availability of information on the state of the system, the control computer should be independent of the data acquisition computer so that even if no data acquisition is taking place, the telescope remains fully operational and all systems are monitored. This is also important during the construction phase before the camera has been installed.

4.4.2.1 General outline

Figure 4.29 shows a diagram of the MAGIC Telescope's control and data acquisition systems. Following the principle that data acquisition and control should be kept separate, the main data acquisition computer is not given any control functions. In the case of any DAQ failure or overload, the telescope stays in a defined state and is fully steerable.

All high throughput connections are realized as VME-bus connections. The Ethernet backbone (Ethernet A) only serves for the transmission of command and control data and is separated from the outside world by a bridge. X-terminals are used for additional displays which are exported from the control computer. The DAQ computer's only display is the event and DAQ status display. A second screen might be attached for displaying the on-line data analysis results, but no display is exported via Ethernet, nor are any outside clients or servers connected to the DAQ computer while the telescope is running.

The control computer communicates with the DAQ computer via the VME-bus. The pointing monitor information is transferred to the DAQ computer via an input register in the control VME crate.

4.4.3 Design of the user interface

Keywords: Instant availability of important telescope parameters is needed.

In order to make the operation safe and efficient, all information about the state of the telescope has to be presented in a clear manner and with minimal time delays. In the following subsections the design criteria and some preliminary outlines of the control system and its user interface will be described.

4.4.3.1 Status and measurement monitoring

As for any measuring device, both the status of the device as well as the values it measures have to be monitored together in order to enable the user to:

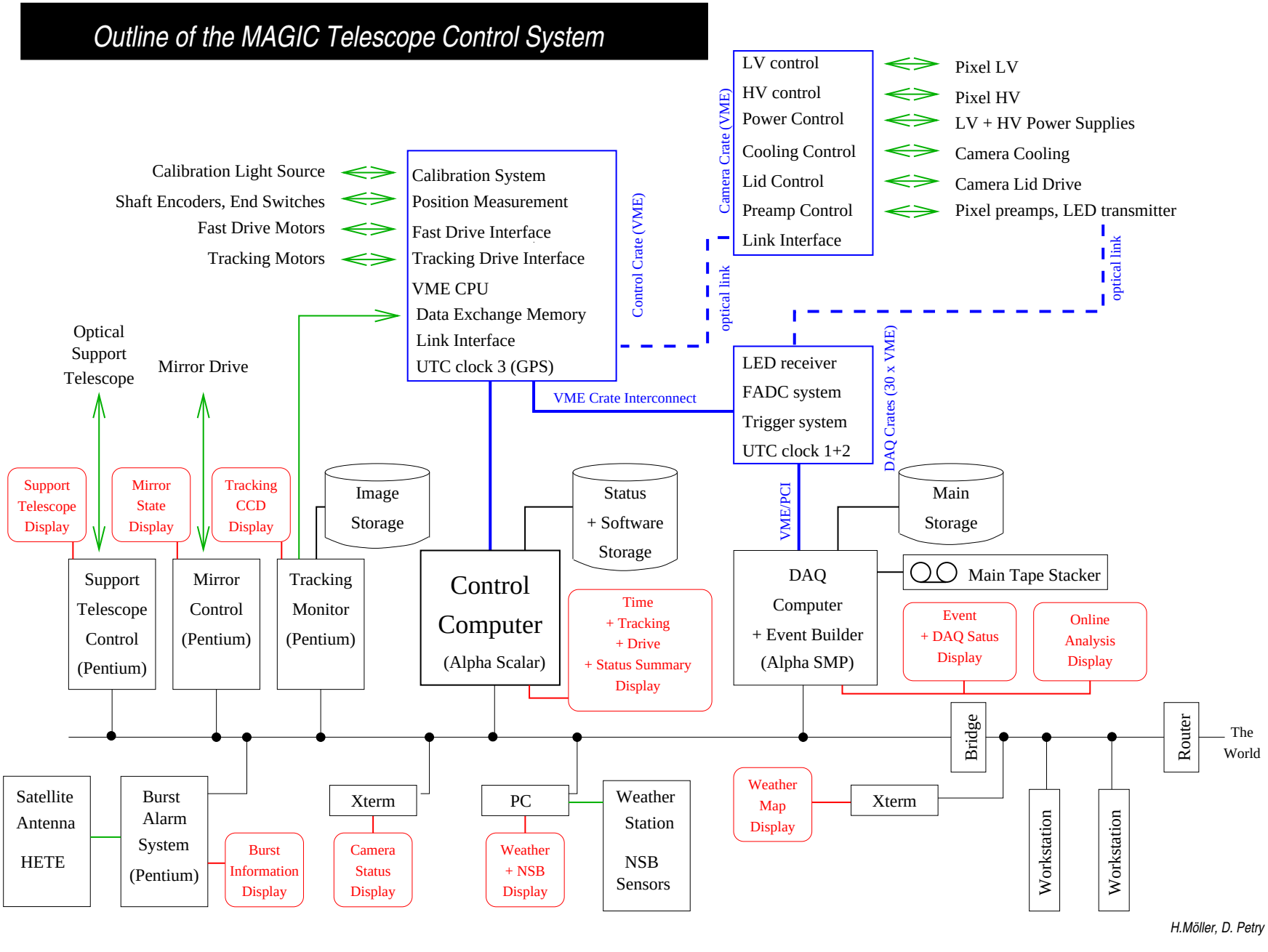

Figure 4.29: General outline of the telescope control system.

(a) obtain the measured value and

(b) judge the credibility of the measuring device.

Status and measurement values should therefore – wherever possible – be displayed close together, but the two pieces of information should be transmitted independently. In particular, all information about the status of all the sub-systems should be available within a few seconds, independently of the data acquisition rate. A 3-second period is the minimum time period for most systems in which we expect changes to occur. For a few individual parameters, such as the data acquisition rate, this period might have to be reduced still further.

4.4.3.2 Time history monitoring

For many parameters it is important to monitor their change with time in order to enable the user to judge whether a change in the data is a statistical fluctuation from a constant mean or a real change in the mean.

Important examples are clearly:

- the sky brightness and the weather conditions,
- the data acquisition rate,
- the tracking accuracy,
- the photo sensor anode currents,
- the temperature inside the camera,
- the observed gamma candidate rate.

A display of this time history can be accomplished in two different ways:

(a) By displaying the parameter's value in a Cartesian coordinate system versus time where the origin of the time axis is constantly moving with time, in such a way that a certain time window with the present time at the upper edge can be viewed.

(b) By displaying the parameter's present value together with its average value within a certain period of time before the latest measurement (the "longer-term mean"). In addition, it should be indicated by how many sigma the measurement deviates from the longer term mean.

Option (a) gives the user the maximum information and is desirable for most parameters. However, it takes up much more room on a computer display than option (b). This again is a disadvantage since the number of (real or virtual) screens that the shift crew should have to watch should be kept at a minimum. Designing the actual layout of the computer screen displays will therefore have to be a compromise between making the maximum amount of information available and producing it in a form that can be quickly seen and understood.

4.4.3.3 Automatic warnings and switch-offs

Naturally, the time history monitoring described in 4.4.3 and the general monitoring of values which should remain constant can be highly automated by defining upper and lower relative or absolute thresholds beyond which the control computer would give light or sound signals to the user.

An example of a relative threshold is the data acquisition rate. Here a warning should be given to the user if the momentary rate deviates by more than 3 standard deviations from the longer-term mean.

Absolute thresholds should be defined for parameters such as the photo sensor anode currents or the camera temperature beyond which the appropriate power supplies are automatically switched off to avoid permanent damage.

4.4.3.4 System-status record

For later reference, the system-status should be regularly recorded in such a way that it can be synchronized with the acquired observational data by the later data analysis. This "automatic runbook" should, however, be complemented by a handwritten runbook kept by the shift crew. The control system should produce a printout of "last night's shift summary" which can be given to the daytime crew together with the handwritten runbook.

4.4.4 Building the control system

Keywords: The development of the control software will be based on proven, off-the-shelve programming environments.

The development of the control system of the MAGIC Telescope will proceed hand in hand with the development of the data acquisition though both systems will be kept independent. The main design goals are safety, reliability and easy modification. We intend therefore not to develop a complete control system from scratch, but rather to use development tools which are already available and proven.

While the final decision on which tool to use has not yet been taken, two candidates are currently being evaluated:

(a) The Framework for Advanced Monitoring, Telemetry and Control (FRAMTEC) developed by the CAM GmbH in Munich together with the Deutsche Forschungsanstalt für Luft und Raumfahrt (DLR).

(b) The Experimental and Physics Industrial Control System (EPICS) developed by the Accelerator Controls and Automation Group (AOT-8) at the Los Alamos National Laboratory (LANL), with the collaboration of the Argonne National Laboratory (ANL), the Lawrence Berkeley National Laboratory (LBNL) and the no longer existing Superconducting Supercollider Laboratory.

FRAMTEC has been developed and successfully used for the steering and control of satellite ground stations. It is also being applied in the development of the control system of the Very Large Telescope (VLT), which is currently being completed by the European Southern Observatory (ESO).

EPICS is a well debugged system which was first applied in 1988. It is used in high energy physics experiments at ANL, CEBAF, LANL, LBNL, KEK, SLAC and others. It is also used by software engineers in Astronomy, especially at the Instituto de Astrofisica de Canarias, Tenerife and La Palma, Spain.

Chapter 5

The data acquisition system

Keywords: For minimizing the dead time the MAGIC Telescope will need a DAQ capable to handle a maximum sustained event rate of 1 kHz

Because of the expected rate of data collection in the extreme situation of a gamma-ray burst or of an AGN-flare and because of the high granularity of a camera with up to 1000 pixels in later stages, the readout and trigger system of the camera is divided into 9 overlapping sectors of ~ 110 pixels each (and possibly a central ring sector). If it will be necessary, the signals from each 3 sectors can be connected to separate VME-crates containing the readout and trigger electronics. In the first step the signals of each pixel are fed through a low-noise voltage amplifier (or, depending on the camera type, via preamplifier-shaper combination with a shaping time of 2-5 ns) and subsequently split into two parts. One partial signal is passed to a discriminator and used for the first level trigger decision described in Chapter 5.5. The discriminator threshold can be set independently for each channel. In addition it is possible to enable /disable each single channel for the trigger in order to suppress the influence of bright stars in the field-of-view. The rates of all pixels are measured by using scalers. Whenever the trigger condition is fulfilled the readout of the FADC is started.

5.1 Estimate of data rate

Keywords: The expected trigger rate is $\sim$ 100 Hz.

Before discussing the trigger and the data acquisition system we will briefly estimate the expected contributions from the various sources generating signals in the camera. As basis for the estimate we use the model cameras as outlined in the previous chapters and the trigger threshold as outlined later in this chapter. The canonical versions are summarized in Table 5.1.

	Classical PMT camera	Standard camera MTD96	Advanced camera
Camera diameter (field-of-view)	3.6°	central 2.5° ø high QE sensors; + classical PMT ring up to 3.6° ø	central 2.5° ø high QE sensors; + classical PMT ring up to 3.6° ø
Pixel size	0.10° (up to 2.5° ø) 0.20° ring	0.10° + 0.20° ring	0.06° + PMTs 0.20°
Pixel type	PMT, Bialkali cathode	hybrid PMT GaAsP cathode; + PMT, Bialkali	APD + PMTs, Bialkali cathode
⟨QE⟩ 300-600 nm	12%	45%, 12%	80%, 12%
Active area	≈ 97%	≈ 97%	≈ 97%
Trigger diameter	1.6°	1.6°	1.6°
Trigger threshold	25-30 GeV	8-10 GeV	∼ 5 GeV
NSB/pixel/ns n trigger area	0.1 ph.e.	∼ 0.3 ph.e.	0.6 ph.e.

Table 5.1: Canonical camera configurations and thresholds.

The trigger threshold is defined for γ showers from the zenith, which fulfill the "$\geq$ 7 ph.e.s in $\geq$ 4 neighbour pixels in a close pack" condition (close-pack means that each of the triggered pixels has at least 2 triggered neighbours), as the energy which provides the maximum differential count rate from a point source (see the related curves in the Monte Carlo chapter 6). For large zenith angles the threshold is a few times higher.

The dominant sources that generate enough electrical signals to pass the preset threshold, are:

- air showers from the charged cosmic hadrons (expected rate $\sim$ 90 Hz),
- Čerenkov light from single muons in the atmosphere with a momentum $\geq$ 5 GeV and within the impact parameter up to 110 m (the rate from muons is included in the above mentioned rate from hadrons; see Chapter 6),
- Čerenkov light from single charged particles physically passing through the entrance window (radiator) of light sensors ($\ll$ 1 Hz),
- electromagnetic showers from cosmic electrons (2-10 Hz depending on the used sensors and the achieved threshold),
- electromagnetic showers from diffuse γ background (this rate is at least by 2 orders of magnitude less than the rate due to the electrons),

- triggers from ion feedback in the PMTs generating large pulses (in the case of 4-fold next neighbour trigger this rate should be $\ll 1$ Hz),
- air fluorescence from energetic off-axis showers close by the telescope (a small contribution to the hadron rate but images might "look like" γ showers except for the time distribution),
- coherent pickup of external noise pulses (for example, from driving motors),
- light of the night sky (the above mentioned strong trigger condition can suppress this rate very efficiently),
- bright stars in the FOV (pixels containing a bright star in the field of view should be treated separately in the trigger),
- source γ events (few Hz from strong sources).

5.2 Preamplifier and shaper

Keywords: We are considering a fast voltage amplifier $\sim$ 300 MHz for the classical PMT camera option and two choices for the preamplifier-shaper configuration for the IAPD camera option.

The PMTs of the classical camera are planned to run at a gain of $\sim 5{\times}10^4$. The signal needs further amplification in order to drive the optical analog glass fibre system. The PMTs will be followed by $\sim$ 300 MHz fast voltage amplifiers with a gain of 20-40, providing a single ph.e. amplitude of 1.5-3 mV. In the case of IPCs one expects them to provide a gain of $2-5{\times}10^4$ and two options of preamplifiers are being considered: (a) a charge-sensitive preamplifier followed by a shaping amplifier and (b) by a four-stage transimpedance amplifier. The charge-sensitive preamplifier has lower noise by a factor of about 3 but it is difficult to achieve very short pulses whereas the transimpedance preamplifier allows the IPC pulses to be amplified without distortion down to $\sim$ 1 ns rise and fall times. For MTD96 the first choice is the transimpedance preamplifier because it will still take some time to design ultrafast charge sensitive preamplifiers and the necessary filter amplifier. Fig. 5.1 shows the circuit diagram of a typical charge sensitive preamplifier under consideration.

The preamplifier output signal is coupled to the drive circuit of an optical fibre routing the signal to the electronics container. The analog fibre transmission system is described in Section 5.3.

5.2.1 Test option

In view of the difficulty of error handling in a 600-1000 channel system it seems necessary to have the possibility of testing individual channels in an easily accessible

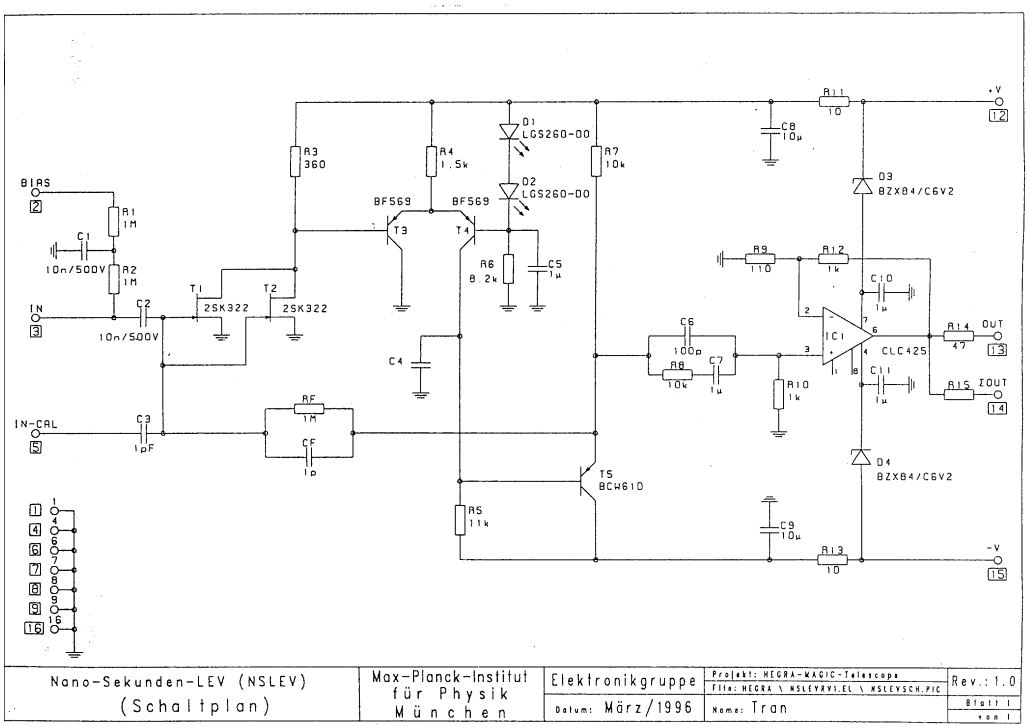

Figure 5.1: Circuit diagram of a charge sensitive preamplifier under consideration for the use in the MAGIC Telescope readout chain.

way. Therefore the preamplifiers have a test entrance at which a well defined test signal can be fed in. In order to avoid having too many cables going from the ground to the camera the test signal is generated at the camera electronics and distributed via a bus addressing system (e.g. VME-bus) to the different preamplifier shaper cards to be tested.

5.3 Transmission of the PMT analog pulses from the camera to the ground station

Keywords: Various options for the transfer of data to the ground station exist

Like all cosmic-ray surface air shower experiments, the MAGIC Telescope has to transmit in parallel a large number of fast PMT signals (ca. 600) from the camera to the central data acquisition. Until now, experimentalists have used analog or digital data transfer via electrical cables. Nowadays, it is possible to transmit fast analog data via multimode optical fibres using an LED transmitter and a PIN photodiode [55]. In this chapter the advantages of the different solutions are discussed, especially those of the analog optical transmission.

In all developments for the data transmission, we have to take into account three limiting factors of construction:

- The total weight of the camera container should not exceed 120 kg.
- The heat, produced by the electronics, in the camera should be kept as low as possible to avoid having to install a complicated cooling system.
- Easy access of critical electronics elements for fast repair/exchange.

5.3.1 Signal transmission in Čerenkov telescopes

Keywords: Options are signal transport by coaxial cables or analog transfer by optical fibres or as an alternative signal processing in the camera.

An imaging camera of more than 600 pixels with high trigger rates requires an efficient technique for transmitting the signals and reducing the data. The distance to the data acquisition system will be in the order of 60 to 100 m; and, depending on the local infrastructure or coincidence operation of ≥ 2 telescopes, distances of several 100 m may be needed.

The requirements for signal transmission are defined by the Čerenkov pulses. A pulse width of typically 2 - 5 ns (FWHM) should be processed in the data acquisition without significant losses. Three methods will be discussed:

- Analog electrical signal transmission to the control room.
- Signal processing and data reduction within the camera.
- Analog optical signal transmission with optical fibres.

5.3.1.1 Analog electrical signal transmission

In small telescopes with only a few tens to $\approx$ one hundred pixels, the PMT signals are usually transmitted via coaxial cables to a data acquisition unit which should be located at a short distance of only a few tens of meters from the telescope. In the case of the MAGIC Telescope, this method would have several drawbacks:

- High quality, large diameter coaxial cables of at least 55 m length (25 m for the electronics positioned at the main dish) would be needed.
- The weight of 600 coaxial cables: 22 kg/m (RG58C/U) would add nearly a ton to the moving part of the telescope.
- The stiff cable bundle needs large loops around the turning axes.

- The risk of picking up of electromagnetic noise signals and the danger of damage by lightning.
- Possible cross-talk between individual channels.

5.3.1.2 Signal processing and data reduction within the camera

To avoid the drawbacks of analog signal transmission with coaxial cables, the PMT pulses could be digitized within the camera. In this method, the event trigger and a pulse-shape processing are performed locally. The data are reduced by a local processor system and sent as digitized events to a nearby laboratory for further reduction and data storage. This method is technologically challenging but also suffers from several drawbacks:

- The main part of the data acquisition has to be installed in the camera.
- Debugging is more difficult since the electronic data acquisition system is not accessible during regular operation.
- If individual channels fail during nighttime, they will be difficult to repair and the telescope might be out of operation for that night.
- A modular design of the DAQ is difficult to realize. Mainly specialized electronic units, optimized in size and weight, have to be used. The development time of such a system will be long.
- The electronics, power supplies, crates, etc., add substantially to the weight of the camera. Oscillations of the camera are more difficult to control. Also the counterweight should be increased in such a case.
- Large size of the camera, which means higher resistance to the wind.
- Powerful cooling for a densely packed electronic system would be needed, thus increasing the weight and complexity of the camera.

5.3.1.3 Analog optical signal transmission with optical fibres

Keywords: For noise immunity, low dispersion, high package density and low weight analog signal transfer by optical fibres is superior to the use of coaxial cables.

In this strategy, the pulses are transmitted to the counting/control room via optical multimode fibres. The camera system consists of the photo detectors, e.g. PMTs, and a minimum of analog electronics. Every PMT pulse is amplified and converted to a light pulse in the LED transmitter. Then this pulse is transmitted to a laboratory. Even for a remote laboratory at a distance as large as 1 km, there

will be no significant losses, either in pulse shape or in amplitude when using rather cheap graded index fibres (62.5 μm core, 125 μm cladding). The obvious advantages of this method are:

- The losses in pulse shape and amplitude are negligible.
- The telescope camera and the data acquisition system are separated modules. Both of them can be developed and built independently. The camera system contains no signal processing electronics and, because it is compactly and simply designed, this type of camera should require nearly no maintenance.
- The camera's electronic system contains no hierarchical structure: all PMTs are independent channels. Therefore complete camera breakdowns due to electronic problems can be ruled out.
- All PMT analog signals are available in the control room. This permits easy inspection and debugging.
- Standard methods and equipment can be used for the data acquisition. The DAQ can be installed in regular 19" racks using commercial components.

As disadvantage we note that connectors are rather critical for the correct analog amplitude transfer and high precision types have to be used. It has been found that a typical graded index fibre can be bend down to a radius of < 10 cm without any loss of amplitude.

5.3.2 Design and performance of analog optical signal transmission with optical fibres

Keywords: Optical fibres allow for high-quality transmission of analog signals.

The method of analog transmission of PMT pulses with optical fibres has been developed for cosmic ray experiments [55]. Fig. 5.2 shows the principle setup.

The most important transmission parameters of optical fibres are the high bandwidth and the low attenuation. In Table 5.2 the transmission characteristics of typical multimode optical fibres are compared with those of coaxial cables. It is obvious that the transmission properties of optical fibres are far superior to those of electrical cables. However, only recently new kinds of inexpensive and fast transmitters have become available. The new LED-transmitters and PIN-photodiodes operating at a wavelength of 1300 nm allow for a straightforward and robust method of analog transmission.

It should be mentioned that LEDs and PIN-Diodes which work at 830 nm may be considered, too. However, in the industrial development of fibre optic networks

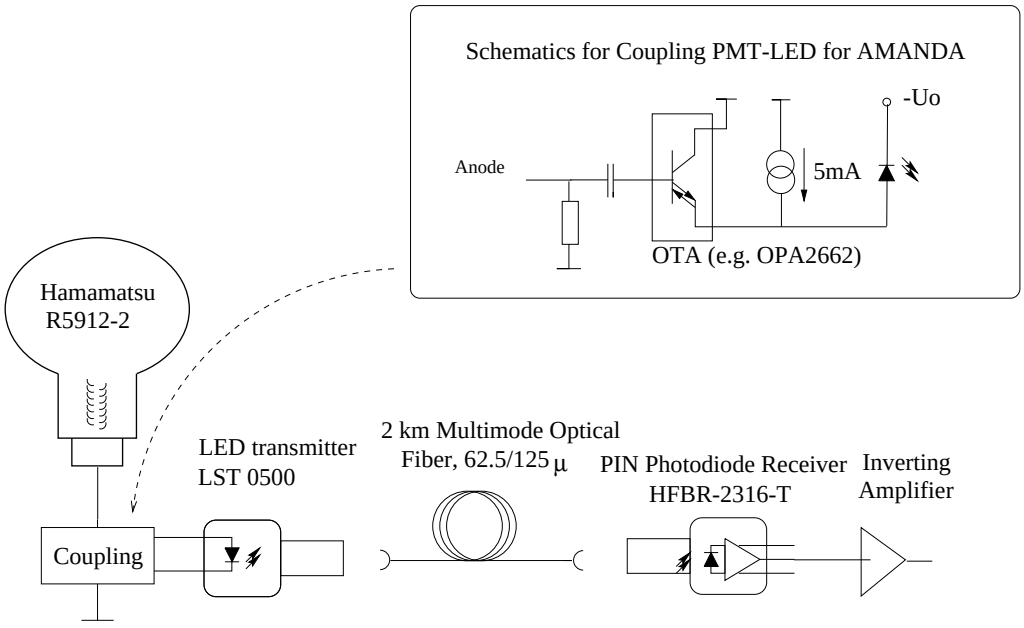

Figure 5.2: Principle of the setup for the analog transmission of PMT pulses via optical fibres [55].

emphasis is now being given to the superior 1300-nm technology. Transmission at 1500 nm is also being developed but will very likely not be available for the next few years.

[a] Typical values. The weight depends on the mechanical construction and on the number of fibres used in one bundle.

[b] The diameter of the bare fibre. Typical jackets are 0.9 mm.

5.3.2.1 The design principle of an analog optical fibre transmission for the MAGIC Telescope

Keywords: The design of the analog optical fibre transmission follows the design of [55].

A current pulse injected into an LED-transmitter is converted into a 1300 nm light pulse. The new transmitters are InGaAsP LED (e.g. LST-0500 from Hewlett Packard) designed for fibre applications. The bandwidth of the transmitter is 255 MBd. As tests show, this transmitter has excellent amplitude linearity when driven by a current pulse and when the the diode is pre-biased. The transmitter is con-

Characteristic	Type of cable	
	Coaxial cable (RG 58, C/U)	Optical multimode fibre at 1300 nm (graded index) (62.5/125 μm $\oslash$; core/cladding)
Bandwidth	A few MHz km^{-1}	300 - 1000 MHz km^{-1}
Attenuation	17.4 dB/100m at 100 MHz	2-3 dB/km at 500 MHz
Weight	22 kg/m/600 cables	1-8 kg/m/600 cables[a]
Diameter	4.95 mm	0.9 mm[b]
Cross talk	Possible	None
Pickup of electromagnetic noise	Possible	None, no damage by close-by lightnings

Table 5.2: Typical characteristics of coaxial cables and multimode optical fibres.

nected to a multimode optical fibre (62.5/125/μm) by a standard optical connector (optionally ST- or SMA-type). The receiver consists of an InGaAs PIN photodiode (HFBR-2316T) with an integrated low-noise transimpedance preamplifier. The connection to the fibre is also made by standard optical fibre connectors. Both the transmitter and the receiver operate at a wavelength of 1300 nm in the lower dispersion and attenuation region of optical multimode fibres. At distances of less than 1 km, the bandwidth of the optical transmission system is limited by the bandwidth of the available receivers and transmitters. With the chips mentioned above a PMT pulse of 7 ns FWHM has been transmitted without distortion. Figure 5.3 shows a PMT pulse before and after transmission over a distance of 2 km [55]. A current of 10 mA in the LED-transmitter results, after transmission, in a pulse of about 100 mV.

5.3.2.2 Dynamic range and linearity

Keywords: The readout system needs a linear range of $\approx$ 200 photoelectrons and a logarithmic compressed range up to 5000 photoelectrons.

The LED-transmitter shows linear light output from 2 mA to approximately 100 mA. Many PMTs produce current pulses in the range of a few mA to more than 100 mA.

In our case, an amplifier will be needed to achieve the necessary LED current of 100 mA maximum. If a linear dynamic range of $\geq$ 200 ph.e.s is desired, a single ph.e. pulse should be amplified corresponding to a current of 0.5 mA. However, to obtain a high dynamic range and good pedestal calibration, it is necessary to operate the LED with a current bias of at least 1 mA. The LED should therefore be prebiased since the light output of the LED becomes nonlinear if the current drops below 1

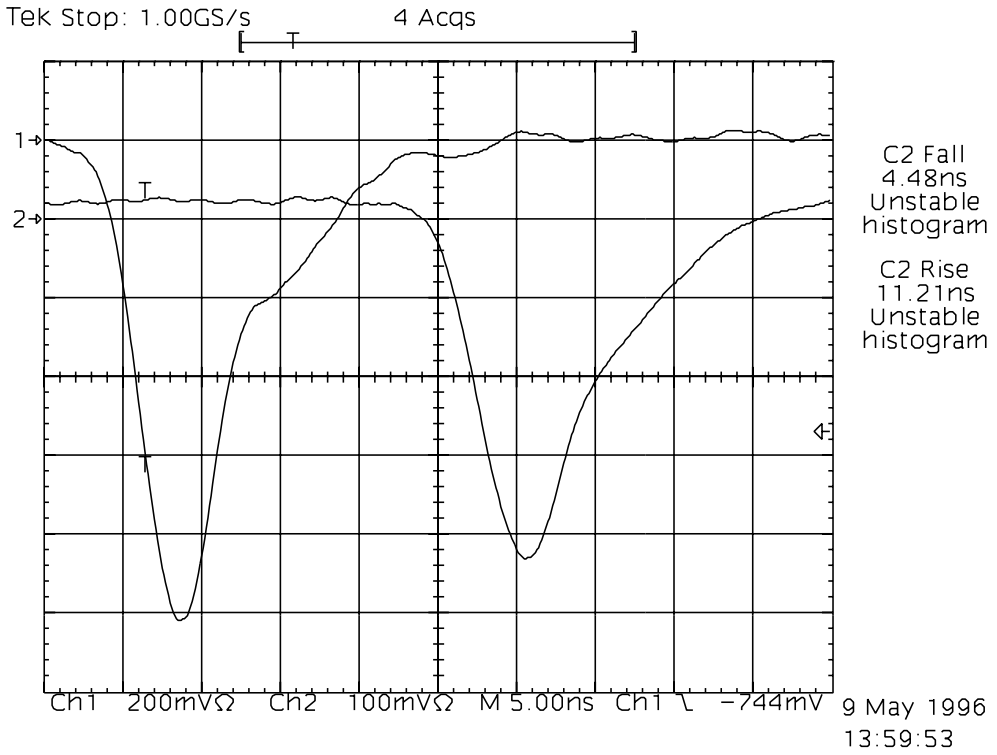

Figure 5.3: PMT pulses before and after analog transmission over a multimode fibre of 2 km length (taken from [55])

mA [55]. Therefore, the dynamic range of the system can be improved significantly by using an amplifier with a current bias for the LED in the range of a few mA. Figure 5.4 shows a measurement of the linearity of the transmitter. The achievable linear dynamic range is ultimately limited by the current limits of the transmitter and the receiver (2V), and the noise level of the receiver amplifier (1 mV in the case of selected HFBR-2316T). With this method, a linear dynamic range of at least 200 ph.e.s should be possible[1].

However, it has not been possible to cover the full dynamic range of more than 3 orders of magnitude with only one receiver. Linearity could be conserved if one doubles the readout system but this is not very economic. An alternative solution is to accept a degradation of the linearity for large signals and work with some dynamic compression. The signals will be digitized by $\geq$ 250 MHz FADCs. A possible solution is to drive the amplifiers in saturation and measure the so-called 'time over threshold' with the FADCs. The 'time over threshold' is proportional to the log of the amplitude, i.e. the relative error of the large signal would not further decrease with signal height but stay basically constant. First studies show that one can measure with this technique up to signals equivalent 5000 ph.e. The transition from the linear domain to the log domain needs particularly careful calibrations.

[1]This has been recently achieved in a test setup.

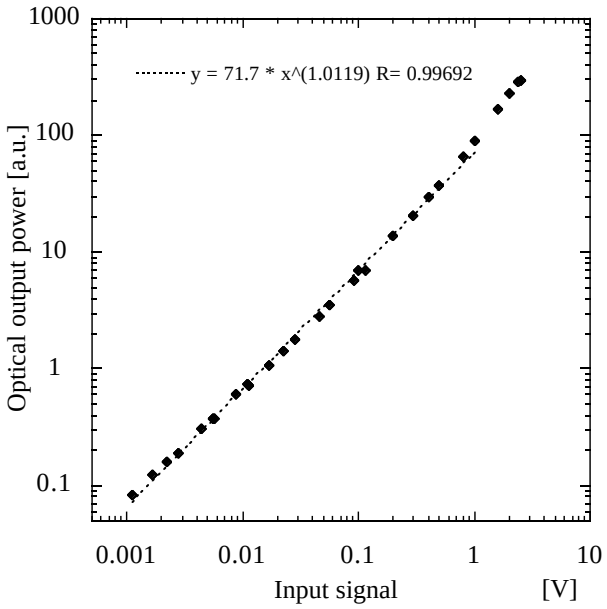

Figure 5.4: Achieved linear dynamic range for an analog signal transport (taken from [55]).

Still, stabilization of the electronics components (power supplies, temperature) has to be improved, and selection of components is necessary. A peak pixel content above 5000 ph.e. is expected in shower images from vertical γs above 10 TeV while at large zenith angles ($> 60°$) the saturation limit should increase to around 50 TeV[2].

5.3.2.3 Calibration and debugging

Keywords: The novel analog transfer mode needs calibration and debugging

The calibration of the individual channels can be done in a straightforward manner by electrical pulses of correct shape and by pulsed light sources. Both the time and the amplitude resolution can be calibrated with the whole system.

The amplitude or charge calibration should cover the whole amplitude spectrum in order to measure the total gain of one channel versus the amplitude from 1 to about 5000 ph.e.s.

The connection of optical fibres can be sometimes problematic and debugging is needed, particularly after the removal, installation of the camera on the telescope. A simple tool for debugging is provided by the current bias which has to be applied

[2]In principle, there exists a rather simple solution to shift the operation range of the telescope to higher energies for special studies by temporarily reducing the mirror area. This can be achieved by pulling the protection tarpaulin over some sections of the mirror, see also 8.2.10.

to the LED. The current bias should be 2 to 5 mA, depending on the choice of the transmitter. In this mode of operation, the LED will transmit a constant light level to the fibre. This can be used with standard optical power meters to measure the DC-optical power transmitted through the fibre. Therefore a DC control signal is available independent of the state of the PMT. This feature allows a clear and simple decision to be made, without access to the camera system, as to whether the fibre transmission system or the PMT and amplifier circuit have been damaged. The DC-light signal does not affect the noise level of the receiver, which is dominated by the amplifier noise itself rather than by the photon noise. In case this debugging procedure turns out to be unnecessary than one can use the DC signal to transmit some 'health' information of the IPC down to the control room. (For example the slowly varying dark currents of the HEGRA telescope PMTs are send also over the fast coaxial signal cables).

An OTDR can be used for carrying out a detailed inspection of the fibre. Within seconds every fibre can be easily inspected for damage or irregular attenuation within. Calibrated adapters are available for modern oscilloscopes in order to convert a multimode fibre light pulse to an electrical 50 ohm pulse.

5.3.3 First ideas concerning the technical design of the camera, the fiber cables and the receiver

Keywords: Commercial cables, connectors, light transmitters and receivers will be used.

Multimode optical fibre cables are available as customer designed products. A typical construction would consist of individual cables with 50 fibres each. The individual fibres are 62.5/125/250/900 μm diameter multimode optical fibres. Such cables are available as breakout cables connectorized at both ends with ST-connectors. The 50 fibre cables must be jacketed with protective coating that is water- and UV resistant. The length of the breakouts should be at least 2 m. The total length of the cables depends on the situation at the experimental site. Typical lengths would be of the order of 100 to several 100 m.

The back of the camera would consist of 600 ST-sockets. Every individual fibre is connected to its PMT channel by a standard connector. This allows easy replacement of a cable if necessary, e. g., in case of a broken connector.

The package size of the Hewlett-Packard transmitter, type LST0X00-ST-F is 12.9 mm $\times$ 9.7 mm. To mount these transmitters in one layer requires a minimum distance between 2 pixels of 13 mm. The outer diameter of an ST connector is typically 8.5 mm. At a mounting distance of 15 mm the connectors are individually accessible. The bayonet-locking mechanism of these connectors enables a reliable and elegant connection between fibres and camera to be made. It should be noted again, that the LED-transmitters do not contain other active components.

The receiver chip is a PIN-photodiode with an integrated transimpedance amplifier. When operating the transmitter in a range of one ph.e./0.5 mA the signal received will be of the order of 5 mV/ ph.e.. The positive analog signal has to be inverted and transformed to 50 ohms. An amplifier will be installed when adapting the voltage pulse to 50 ohms. Standard analog data acquisition electronics can be used to prepare the signals for digitization: analog splitters, delay lines, discriminators and triggering.

5.3.4 Summary

In Table 5.3 the main parameters of the three solutions to the transmission problem are compared.

5.4 FADC electronics

Keywords: The MAGIC Telescope has an FADC system for noise reduction, buffering during trigger processor time, improved γ/h separation and eventual combination with other telescopes

The fast analog signals will be digitized by $\geq$ 250 MHz, 8 bit FADCs. The use of FADCs instead of classical gated ADCs (CAMAC, Fastbus) is given by:

(i) night sky (and moon light) noise minimization,

(ii) event buffering during 2. level trigger decision,

(iii) improved γ/h separation from measurement of the arrival time distribution of the Čerenkov light in different pixels,

(iv) correlated readout with other telescopes in an 'array' or 'stereo' configuration.

To (i): The Čerenkov light flashes, particularly those from γ-showers, are very 'sharp' in time. FWHM values of $<$ 1-2 ns are common. Depending on the photosensor and preamplifier configuration the electronics signal will be somewhat widened. Nevertheless the time can still be reconstructed to the above-mentioned precision. In order to make full use of this low-spread it is necessary to use an isochronous mirror profile and very fast optical readout elements with low degradation of signal transmission (optical analog fibres in preference over coaxial cables). For signal/noise optimization it is also necessary to use a time recording system matched to the above timing requirements. A modern FADC system can fulfill both requirements, the amplitude resolution and the time resolution. With $\leq$ 4 ns digitizer time-slices, a resolution below 1 ns can be reached for large pulses whereas for small pulses, extending barely above noise, a resolution of ca. 2-3 ns can be achieved. Therefore

Parameter		Analog data transmission via electrical cable	Digital data transmission serial	Analog data transmission via optical fibre
Cable				
Weight	per channel	36 g m^{-1} [RG58, C/U]	—	1 - 8 g m^{-1} [a]
	per 1000 chan.	36 kg m^{-1} [RG58, C/U]	36 g m^{-1}	1 - 8 kg m^{-1}
Diameter	per channel	4.96 mm [RG58, C/U]	—	0.18 mm
	per 1000 chan.	ca. 160 mm	4.95 mm	ca. 25 mm
Power in camera container				
Preamplifier	per channel	< 60 mW	< 60 mW	< 60 mW
	per 1000 chan.	< 60 W	< 60 W	< 60 W
FADC system	per channel	—	65 W	—
	per 1000 chan.	—	5 kW	—
HV voltage system	per 1000 chan.	negligible[b]	negligible	negligible
General				
Access to camera container		+	−	+
Disturb camera container assembl.		+	−	(+−)
Cooling system		(+)	+++	(+)
Low weight FADC system		−	++	−
Low power FADC system		−	++	−
Debugging		+	−−	+

[a] Typical values.
[b] Using Intevac IPC.

Table 5.3: Comparison of camera signal transmission options.

a very good correlation of the different pixel contents with the image and an efficient noise reduction should be possible.

To (ii): The large rate of primary, low-information pixel data has to be filtered and searched for higher-level information by combining the data in near real-time. This is done by the trigger logic. With the steady increase in pixel number and faster

signals in modern telescopes the trigger logic becomes more complex and needs more decision time. Modern trigger concepts break up the traditional trigger logic into a multilevel decision system. The first level trigger of low complexity provides a real-time low level decision. In the next step, intermediate storage of the data is needed until the so-called 2- (and sometimes 3-) level trigger can decide on more complex criteria. We assume (see Chapter 5.5) that the 2nd level trigger will have a decision time of about 10 μsec. Therefore an FADC memory of 10-16 k depth is needed.

To (iii) Possible criteria for γ/h separation of shower images of the same number of ph.e. are the image structure (width, length, etc.) the image orientation with respect to a possible point source (equivalent to the angular resolution) and possible photon colour- and arrival time differences. The latter two parameters have basically not yet been used (except in specialized small detectors) as in the past the technical investments were not justified by the gain in discrimination power. The expected difference in time-spread is in the range of a few ns only and no affordable adequate instruments were available. The use of $\geq$ 250 MHz FADCs offers new prospects. In particular the timing information from so-called islands outside the main shower image should have the largest deviation. Proton showers have significantly longer delays for some photons. Also, for wrongly oriented images (head-tail interchanged) one expects about 5 ns difference between the head and the tail pixels. Similar time differences are expected for 'fluorescent' images of hadron showers.

To (iv) Eventually it will be necessary for precision measurements (or when no other technical improvements are possible) to combine many telescopes (or other detectors relying on fast (i.e. ns) timing information) in order to 'view' the shower at different angles and distances from the shower impact point (array concept). For the combination of the low-level pixel content of different telescopes it is indispensable to use some intermediate storage device. When tracking stellar objects, the timing difference between different telescopes will change and no fixed delay units can be used. FADCs are well suited for this purpose because of their deep memories and the ease of software corrections.

The use of FADCs is rapidly developing for the replacement of analog recording of fast signals (digital oscilloscopes, transient recorders, digital high resolution TV, vast demands in nuclear medical instruments such as X-ray , CT, MR and PET imaging, etc.). Detectors for particle physics and applications like ours are on the forefront to develop and use cheap FADCs in the $>$ 250 MHz domain.

Two products which fit in principle our requirements are commercially available: The STRUCK model DL515 is a VME-based unit with four 8-bit channel FADCs that can continuously sample input signals at 250 MHz. Each FADC channel writes to a 2 kbyte memory so that data is stored for 8 μs before being overwritten. The other commercial candidate is the Tektronix TVS641, which samples four channels at 1 GHz each in a VXI environment. Each FADC channel writes to a 15 kbyte memory so that data is stored for 15 μs (at 1 GHz). Both products have some

disadvantages: the memory of the STRUCK module is small, the sampling rate of the Tektronix is too high (no 250 MHz version available). Furthermore, both are quite expensive.

Discussions on appropriate FADCs have been started with the companies FAST (Munich), STRUCK (Hamburg) and Valenta Electronics (related to the University Siegen). The specifications are:

(i) digitization rate $\geq$ 250 MHz with a preferred rate of 300 MHz,

(ii) 8 bit range with at least 7 bits resolution,

(iii) adjustable input amplification,

(iv) a memory depth of at least 10 k, preferentially 16 k,

(v) use of a fast bus system, preferentially VME or VXI,

(vi) $\geq$ 4 channels per unit, preferentially 8,

(vii) power consumption/channel $\ll$ 5 Watt, preferentially $<$ 2 Watt.

All companies have already some running prototype close to the above specifications. It should be mentioned that also the company LECROY (USA) is currently developing a 500 MHz FADC system for HEP applications.

Here we would like to mention as an example the discussions with Prof. Valenta from the University of Siegen, who developed the 120-150 MHz FADCs for the HEGRA CTs, about the possibility of redesigning his FADC card to meet our demands. The redesign of the FADC cards (see Fig. 5.5) will follow the approach of Bergauer et al. [9] who developed a 1 GHz FADC system for the NA48 experiment at CERN.

The preamplified signal is permanently digitized with a rate of 300 MHz and a resolution of 8 bits. The 300 MHz data stream is demultiplexed using fast ECL logic into four output streams of 75 MHz. In the next demultiplexer stage using slower TTL logic there will be 16 data streams at 18.75 MHz. This data will be continuously written to a ring buffer with a depth of 16 kbytes consisting of four 1k 32 bit SRAMs. The write cycle takes place every second memory cycle, enabling an interleaved read access to form, which avoids dead time. After a trigger decision a programmable memory segment of the ring buffer is shifted by the readout controller to a small FIFO from where the VME-CPU is able to access the data. A flag for zero suppression will be set for groups of channels and also for single channels. The memory depth of 16 kbyte ($\sim$ 64 μs) will be necessary for a system trigger with other telescopes placed at distances of the order of 100 m.

The decision about the number of VME-CPUs needed for the FADC readout will be made after the FADC system has been decided on.

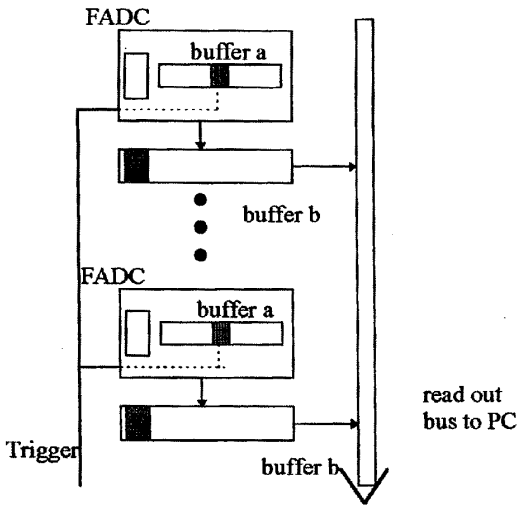

Figure 5.5: Schematic design of the 300 MHz FADC card by Valenta.

One of the collaborating institutes is currently negotiating with the three companies mentioned above about an order for the full development of an FADC system with the above specifications. It is quite likely that the development can be completed by spring 1998.

5.5 The trigger system

Keywords: The MAGIC Telescope needs a multilevel, intelligent trigger system.

5.5.1 First-level trigger

Keywords: The first level trigger is fast.

The first-level trigger (FLT) is derived from a four-fold majority coincidence of all pixels within the inner 1.6° area of the camera. Lowering the energy threshold implies lowering the discriminator threshold for the single pixels. The minimum of this threshold is given by the random coincidences due to the light of the night sky, which is a very steep function of the threshold, saturating the readout system.

There are some possibilities to reduce the random coincidence rate:

1. Reducing the discriminator pulse width strongly reduces the random coincidence rate. The width of the FLT gate will be ≤ 5 ns.

2. Reducing the number of four-pixel combinations making use of the topology of images from γ-showers in the camera, i.e. requiring close-packed configurations.

Because of the compactness of γ-images in the camera interesting events are contained in single or adjacent sectors. The first part of a topological γ/h separation will be a logical NAND of complementary sectors. This will be a part of the FLT because of the simplicity of its electronical implementation.

To obtain short trigger decision times ($<$ 100 ns) it is necessary to use simple combinatorial logic devices. This can be done with different hardware designs. One simple approach is the use of Programmable Logic Devices (PLDs, PALs). This design is simple but has low flexibility, and any new trigger combination needs a complete reprogramming of the device itself with an hardware intervention.

Another solution to create the combinatorial logic is the use of Look Up Tables made with RAM (Random Access Memories) banks, linked together in a tree structure. This second scheme has the possibility to change trigger combinations by software in order to optimize the FLT requirements any time.

5.5.2 Second-level trigger

5.5.2.1 Nearest-neighbour second-level trigger

Keywords: A fourfold nearest-neighbour trigger allows efficient noise reduction.

The second level trigger (SLT) will check whether pixels which satisfy the FLT are nearest neighbours. It is planned to implement the nearest-neighbour trigger on the hardware level using programmable gate arrays. A hardware unit with a 2-element next neighbour trigger is installed at HEGRA since 1997 [18].

5.5.2.2 Neuronal second-level trigger

Keywords: A neuronal network system is considered as alternative second level trigger (see also appendix G)

The expected trigger rate of the MAGIC Telescope ($\sim$ 100 Hz) can be considerably decreased by using an "intelligent", neural network (NN) hardware trigger (see also appendix G[3]). Such a trigger can help to reject muon and hadron backgrounds, which at present is only possible off-line. The application of diverse NN models is now feasible using VLSI chips (there are several examples of successful implementations as second-level triggers at HERA-H1, and at CERN experiments).

[3]Note that while in appendix G, the author is mainly discussing a first-level trigger based on neural networks, here we consider the application of neural networks as a fast second level trigger after a general minimum bias first-level trigger.

After subsequent training steps on the net-simulators, the best net parameter values obtained will be fixed and down-loaded to the chip.

In the Central Department for Electronics and Real Time Data Processing of FZK Karlsruhe (a Yerevan collaborator), a modular structure has been designed for fast triggers and real-time signal processing that ensures high flexibility in the final application and very low module cost. The central processing module consists of 4 multiplier/adders together with one freely programmable activation function block.

The possible size of the net will be limited to three hidden layers and a maximum net size of 512:64:64:64:64, which is sufficient for the pattern recognition of Čerenkov images. The expected decision time would not exceed 10-30 μsec, i.e., it lies within the buffer time of the FADC memory. Easy handling by the operator will be guaranteed by an integrated controller which takes over all the tasks of memory timing, addressing and processor control.

The training of the NN will be carried out by using the simulated extensive air showers (EAS) traversing the earth's atmosphere and simulating the response of the apparatus, including the noise in the electronics. This training will allow sophisticated pattern recognition tasks to be implemented within a short time.

Very large sets of simulated (or calibrated) data corresponding to various shower images with different positions relative to the center of view of the telescope will be acquired during training. To deal with these, fast and efficient network training algorithms will be required. The genetic learning algorithms developed out in the Cosmic Ray Division of YerPhI could be implemented in the hardware and solve training problems.

5.5.2.3 On-line data reduction and the third trigger level

Keywords: For normal operation a data flow of ∼100 Hz is expected.

Motivation: With a total of about 600 (1000) pixels, an expected event rate of about 100 Hz after trigger and data from ca. 10 FADC channels each stored in 1 byte being written out for each pixel, we arrive at a maximum data rate of:

$$1 \text{ Byte} \times 10 \text{ FADC-channels} \times 1000 \text{ Pixels} \times 100 \text{ Hz} = 1 \text{ MB s}^{-1}.$$

In order to estimate the fraction of data which actually contains physical information about the observed shower, we assume an average shower size (for ca. 100 GeV) of $0.5^\circ \times 0.5^\circ$. With a pixel size of ca. $0.1^\circ \times 0.1^\circ$ this would be an image size of 25-35 pixels , i.e. ca. 4% of the camera contains signal charge. An ideal data reduction could diminish the data by a factor 20 to 0.18 GB/h.

With a good knowledge of the NSB light distribution, a safe reduction by a factor of 5 without a data loss of more than 0.1% should be possible. This would mean a data rate of 0.9 GB h^{-1}, i.e. one night's data could be stored on about three 4-GB disks.

Suggestion for an on-line data reduction algorithm:

Each pixel is treated in the following way for each event:

$$\begin{array}{ccccc} & & 4 & & 3 & & \\ & & & & & & \\ 5 & & & 1 & & & 2 \\ & & & & & & \\ & & 6 & & 7 & & \end{array}$$

The pixel is examined together with its 6 neighbours. From the noise σ (pedestal RMS) of each pixel the expected sum S_e of all pixels is calculated:

$$S_e^2 = \sum_{i=1}^{7} \sigma_i^2$$

After subtraction of the pedestal (p_i), the actual sum of the pixel signals is calculated and compared with the expected sum. The pixel is assumed to contain physical information if the following holds:

$$\left(\sum_{i=1}^{7}\right) > 3S_e$$

with $s_i = q_i - p_i$, (q_i: raw signal, p_i: pedestal)

If this is not fulfilled for the central pixel of the group, it is considered to contain only noise. This information is then used for updating pedestal and noise using

$$\begin{aligned} \sigma_{i,n+1}^2 &= \frac{(N-1)\cdot\sigma_{i,n}^2 + s_{i,n}^2}{N} \\ \sigma_{i,n+1}^2 &= \frac{(N-1)\cdot p_{i,n} + q_{i,n}}{N} \end{aligned}$$

where N is the number of updates typically chosen to be ≈ 100. On the one hand, this contrast tunes the speed at which the pedestal and noise can follow changes in the background conditions. On the other hand, it determines the stability of the values to short time fluctuations. This is a system of two coupled infinite interval response (IIR) Filters.

In order to monitor the performance of the system, the values p and σ of all 1000 pixels should be stored regularly ($\approx$ every few minutes). They could also be fed to the first level trigger as a basis for the trigger condition.

Alternative proposal: The hardware "intelligent" trigger for the MAGIC Telescope.

5.5.3 Alternative third-level trigger

The TLT is a software trigger which fits a simplified Landau-like distribution to the byte samples of the various channels in order to extract the arrival time of the

signal. This time will be compared with the mean signal arrival time of all read-out channels. Channels with an arrival time of more than 3 ns from the shower front are treated as starlight or for off-axis secondary showers. The remaining data are fed first through processors for γ/h separation and background suppression.

5.6 Ground-based data acquisition

Keywords: The DAQ will be located in the control building near the base of the telescope.

The extremely high data rates make fast communication between the components of the readout system absolutely necessary. The VME crate interconnection inside the camera container can be realized by using STRUCK 725+723 VDB modules. They allow a maximum transfer rate of 12.5 Mbyte s^{-1} over a maximum distance of 50 m. The connection to the ground station is made by a STRUCK 711 VME/VSB processor using a fibre optic cable with a maximum transfer rate of 12.5 Mbyte s^{-1} over distances up to 1000 m. The connection to the server is made by a VME/PCI interface from DIGITAL, allowing a maximum transfer rate of 10 Mbyte s^{-1}. Currently there are two possibilities for the choice of the server:

1. A standard multi-processor ALPHA from DIGITAL under the operating system DIGITAL UNIX or WINDOWS NT in connection with a ground based VME crate.

2. A multi-processor AXP-VME from DIGITAL with integrated VME bus.

The sophisticated I/O system will be based on multiple I/O channel architecture, like e.g. RAID-controller or FAST/WIDE/DIFFERENTIAL SCSI buses (at the moment up to 20 MB/sec transferable) for system and user disk space and for a DLT tape robot with a capacity of 350 GByte.

This system is fast enough to handle the data rates of the experiment. The purpose of a multiprocessor workstation is to separate the one or two processors needed for the I/O of the experiment from the other CPUs working on a third level software trigger. During daytime the machine will be used for pre-processing of the data recorded overnight. After a test phase it is planned to distribute only DSTs (data summary tapes) to the participating institutes.

5.7 Time recording

Two GPS-92 event time stamps and time-of-day/year clocks from HYTEC ELECTRONICS will record the universal time necessary for the analysis and multiwavelength observations with an absolute UTC accuracy of better than 300 ns. The internal clock of the module is fast enough for the expected trigger rates.

5.8 Weights and heating

About 30 crates, each with a size of $10'' \times 10'' \times 19''$ ($25 \times 25 \times 50$ cm $= 0.32$ m^3). Total generated power that has to be compensated for by climatization amount to about 15 kW.

Chapter 6

Monte Carlo Studies for the MAGIC Telescope

Keywords: Our Monte Carlo simulations show that it is well possible to explore the energy range above 10 GeV using the atmospheric Čerenkov technique. Even very conservative assumptions about the possible γ/hadron separation lead to the conclusion that the MAGIC Telescope will have a very high sensitivity.

6.1 Simulation of the setup

For studying the main characteristics of the MAGIC Telescope we used Version 4.52 of the CORSIKA air shower simulation program [58]. The simulations include the atmospheric absorption and scattering processes such as Rayleigh scattering, Mie scattering and aerosol absorption [39]. The simulations also include the influence of the Earth's magnetic field. The 300–600 nm wavelength range was used for simulating Čerenkov light from air showers, recording the direction and the wavelength of every photon which hit the reflector.

In order to investigate the actual characteristics of the MAGIC Telescope and to take into account the optical aberrations introduced by its reflector, two independent optical ray tracing programs were developed and checked against each other. Both programs provided identical results and one of them was used in the Monte Carlo simulations (see appendix A on 'Optics of the MAGIC Telescope').

For completeness the main characteristics of the MAGIC Telescope relevant to the simulations are briefly recalled. The MAGIC Telescope will have a tessellated reflector of 17 m diameter, consisting of 920 spherical mirrors, each 50 cm $\times$ 50 cm. A parabolic reflector has been chosen in order to provide high angular resolution in the part of the focal plane close to the axis. Moreover, for a parabolic reflector there is no time difference in the focal plane for light collected from a plane wave front incident parallel to the optical axis and hitting the reflector at the edge and at the

centre. The shape of a single mirror element is spherical, with a radius of curvature between 34 and 36 m depending on its distance from the reflector's optical axis. In the simulations the exact position and orientation of each single mirror element and the planned 5 mm gaps between neighboring ones was taken into account. Following our measurements of mirror reflectivity (section 4.2.3) shown in Fig. 4.20, we adopted a reflectivity of 85%. The Čerenkov photons from showers which hit the reflector were traced through the atmosphere and the coordinates of reflected photons in the focal plane were obtained from the ray tracing. In this way realistic aberrations of the tessellated reflector of the MAGIC Telescope were simulated.

We investigated two options for the focal plane imaging camera, first the standard camera based on INTEVAC IAPDs[1] and second the fall-back camera based on classical PMTs. In the simulation of the standard camera a constant 45% QE for the INTEVAC tubes was adopted in the entire 300–600 nm range and a pixel size of 0.10°. A 90% light collection efficiency was taken for the light guides which are to be attached to the IAPDs and the collection efficiency for photoelectrons (ph.e.s) from the photo cathode was also assumed to be 90%. For the PMT camera the same values were used except for the QE, which we took from our measurements of 19-mm diameter EMI-9083A bialkali PMTs which were measured for each 20 nm interval between 300 and 600 nm. When a photon of a given wavelength, different from the measured points, hit a PMT, the value of QE was taken by a third order extrapolation between the closest measured points.

Fig. 6.1 shows the sequence of different steps applied in the simulations to the original spectra of Čerenkov light emitted in the 300–600 nm range by 1 TeV and 40 GeV γ-rays (upper curves). The second curves in Figs. 6.1a and 6.1b show the resulting Čerenkov spectra after transmission of the photons through the atmosphere. The third curves show the intensity changes due to photons lost in the gaps between the mirrors of the tessellated reflector. The fourth, fifth and the sixth curves show changes in the intensity due to the reflectivity of the mirrors (4th curves), assuming the light guides have 90% collection efficiency and using 90% efficiency for ph.e. detection (5th curves), and the QE curve of IAPDs (6th curves), respectively.

6.1.1 Generation of the MC library

For this report γ showers were simulated for 0° zenith angle in the energy range between 5 GeV and 10 TeV and for an impact parameter in the range 0–350 m. The number of generated γ-ray events is few hundred per energy bin for $E_\gamma \geq 500$ GeV, several thousands for energy bins in the range 80–250 GeV and few tens of thousands per bin below 80 GeV. Taking into account the high trigger efficiency for γ-rays detected by the MAGIC Telescope, this provides adequate statistics for Monte Carlo studies.

[1]The IPCs from INTEVAC including avalanche (photo)diodes are named IAPDs

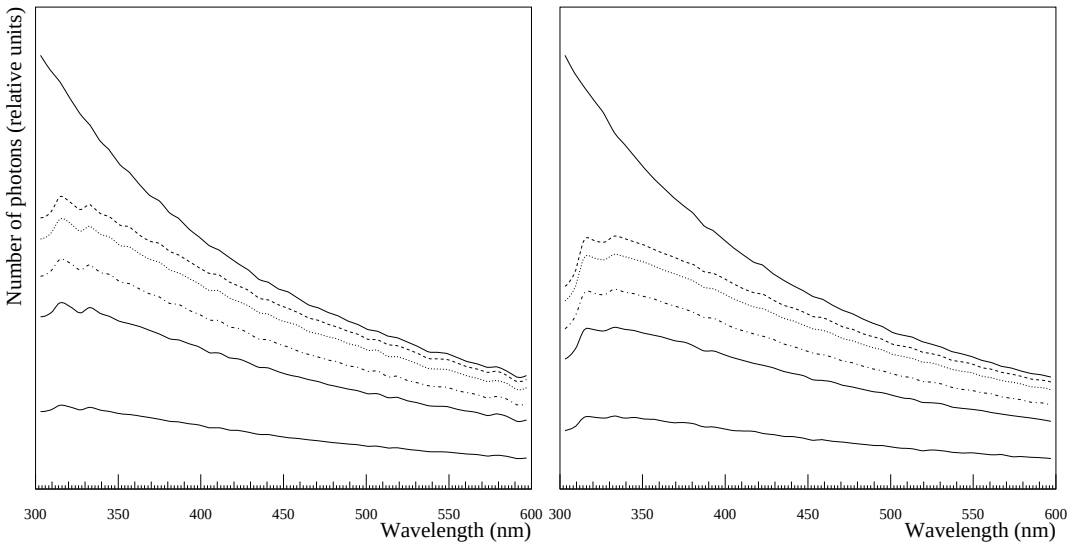

(a) 1 TeV γ shower (b) 40 GeV γ shower

Figure 6.1: Evolution of Čerenkov spectra for 1 TeV and 40 GeV vertical γ-ray showers after different steps in the simulations (see the text).

So far we have performed simulations only for protons, which constitute about 43% in the chemical composition of hadrons at 1 TeV [109]. The components in cosmic rays that are heavier than protons contribute about 25% to the total rate measured by Čerenkov telescopes. Therefore it is sufficient to consider only the proton spectrum in order to investigate the γ/hadron separation that can be achieved.

The proton showers were simulated within an angular range of $\pm 4^\circ$ around the zenith and for an impact parameter range between 0–350 m. For the imaging camera of the MAGIC Telescope only those pixels which are within 0.8° radius from the camera centre were "set" into the trigger in these Monte Carlo studies. The number of simulated proton showers is several hundred per energy bin for $E_{\rm p} \geq 2$ TeV, few thousand for energy bins $E_{\rm p} \geq 100$ GeV and several tens of thousands for energies down to 10 GeV. It should be noted that one has to simulate many tens of thousand events for energies below 100 GeV, because the protons are very strongly rejected already at the trigger level. For example, the average trigger efficiency for 60 GeV protons is ca. 0.5%, it drops down to the level of 0.15% for 40 GeV protons and it is only 0.025% for 30 GeV protons, i.e. only one proton in 4000 with an energy of 30 GeV initiates a trigger.

6.1.2 Trigger logic

The reason of simulating proton showers within an angular acceptance that is much wider ($\pm 4^\circ$) than the trigger radius of the camera (0.8°) is twofold:

1. One takes into account triggers due to inclined showers, the axes of which lie outside of the camera acceptance, but whose light, due to the large multiple scattering angle, can trigger the camera.

2. One takes into account triggers due to Čerenkov light emission from charged single particles coming from air showers, e.g. from muons. The latter can sometimes have non-negligible angles with respect to the shower axes and though the showers itself can be outside of the camera acceptance, the muon can be in the field of view and Čerenkov light from it can initiate a trigger.

Note that a telescope with a relatively large field-of-view and with very high light sensitivity, in the case of triggers from charged single particles, as a general rule, should also see at least part of the tracks of the parent shower.

It should also be noted that the problem of the cosmic-ray muon background, triggering Čerenkov telescopes through the so-called muon-rings (see, for example, [101]), has not yet been fully dealt with and there is still little accumulated experience regarding this problem. As all of the muons triggering the telescopes are produced in air showers, it seems that one should not consider them as two separate components which can initiate independent triggers. Instead one should simulate hadron showers for a relatively large acceptance angle as well as also for very low energies. The latter requirement is important, because on average there is an order of magnitude difference in the energy of a muon compared to that of the parent shower. For example, at an altitude of ca. 2 km a.s.l. the threshold energy for Čerenkov light production for a muon is $\sim$5 GeV, which could be produced by a parent shower with a total energy as low as $\sim$50 GeV. Provided the Monte Carlo simulation code gives a realistic description of the shower development, one then automatically takes into account all possible triggers from hadron showers and charged single particles. This approach was followed in these simulations.

Below we will present results of simulations for the MAGIC Telescope with the standard camera consisting of IAPDs. In addition we will present results for the MAGIC Telescope using a classical PMT camera.

In order to see details of the simulated images they are in addition presented for two camera 'options', one with an infinite resolution and a QE of 100% (here simply all photons hitting the camera are shown), and another one with hexagonal pixels with a size of 0.10° and a QE of 45% (the standard camera).

6.1.3 Standard (IAPD) camera

In Figs. 6.2 and 6.3 a few examples of images for γs and protons of different energies are shown.

A camera with a diameter of 5° is adopted for an infinite resolution imaging camera. For the real camera a diameter of 3.5° is used. In the actual design of the camera 397 pixels of 0.10° size will constitute the central part (see Fig. 4.22). This will provide a diameter (the large axis of the hexagonal camera) of 2.5°. The optical ray tracings show that the 17-m diameter f/1 tessellated reflector of the MAGIC Telescope will provide angular resolutions of 0.036°, 0.064° and 0.079° for incident angles of light of 0.5°, 1.0° and 1.25°, respectively (see Appendix A). The outer part of the camera beyond the radius 1.25° will have larger pixel size (0.2°), but here, for the sake of simplicity, the results of simulations are shown for the same pixel size of 0.10° for the full diameter of the camera of 3.5°.

In our simulations we took into account the influence of light of the night sky (NSB), the intensity of which has been measured at La Palma, at the site of the HEGRA experiment. The NSB intensity I for the narrow angle detector (acceptance angle of less than 1°) in the 300-600 nm range has been measured to be [69]:

$$I = (1.7 \pm 0.4) \cdot 10^{12} \text{ ph m}^{-2}\text{s}^{-1}\text{sr}^{-1}. \tag{6.1}$$

Taking into account the envisaged 300 MHz FADCs in the readout chain, other relevant values and using the NSB intensity, we estimate an average value for the NSB contribution of 3 ph.e.s per pixel per measured event. In generating images of showers the Poisson fluctuations of this value are added to the genuine charges measured in pixels. In the transformation from signal photons to ph.e.s first the mean number of ph.e.s is determined by taking into account the QE(λ) and then the real measured charge is defined by the fluctuations from the mean.

The trigger condition "*any 4 neighbouring channels in a close-packed configuration above the pre-set threshold of 7 ph.e.s*" together with a tail cut of 10 ph.e.s has been applied both for γs and protons (in a close-packed configuration each fired pixel has at least two fired neighbouring pixels). The restrictive trigger condition of requiring a close-packed pixel configuration yields a strong suppression of the accidental triggers due to NSB (and afterpulsing when relevant) and provides a very low trigger threshold. It allows one to trigger with high efficiency on γs while providing a much lower efficiency for hadrons due to the more diffuse shape of their images. Also, as shown in Fig. 3.1, sub-100 GeV hadrons produce several times less Čerenkov photons than γs of the same energy (see also [108]). Therefore one should expect that this trigger condition will help to trigger readily on sub-100 GeV γs, while only hadrons mostly with energies above 100 GeV will produce enough light to initiate triggers.

Here we want to introduce the so-called "*islands*" in the images of γs and hadrons. An island is a close-packed group of a few pixels with non-zero charges, which survive

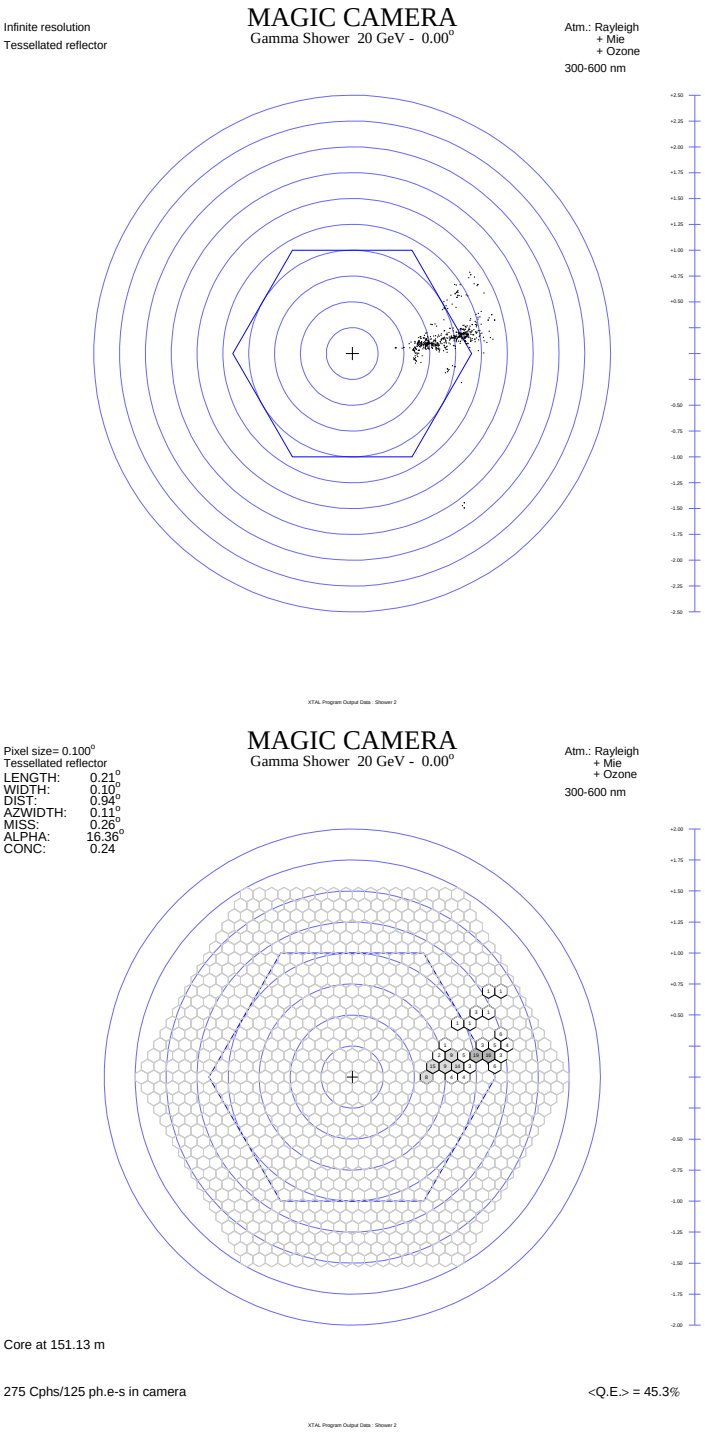

Figure 6.2: Several double images for γ showers: a) 20 GeV, b) 60 GeV, c) 100 GeV. The upper images correspond to the 'infinite resolution camera', i.e. all photons that hit the camera are shown. The lower images correspond to the simulation of the MAGIC Telescope's standard camera, i.e. using a QE of 45% (prior to tail cut).

(a) 20 *GeV*

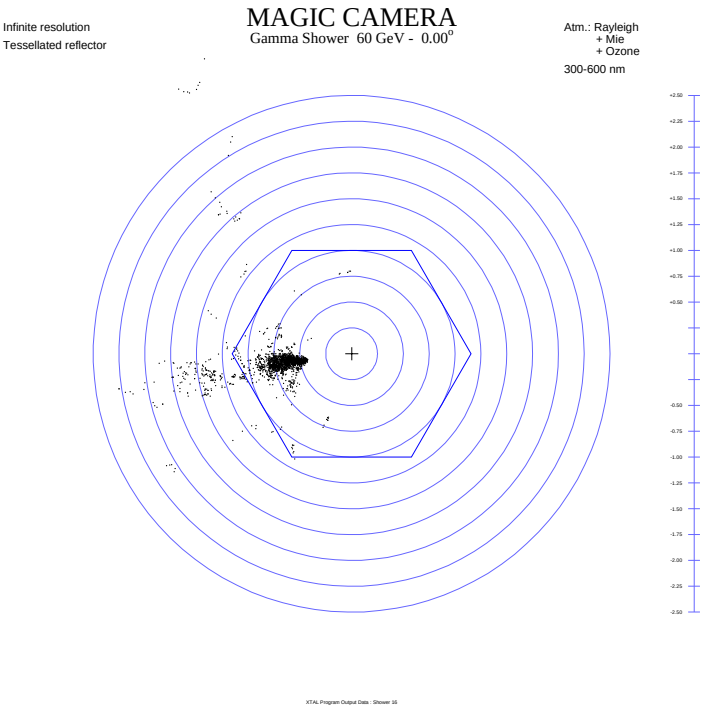
Infinite resolution
Tessellated reflector
MAGIC CAMERA
Gamma Shower 60 GeV - 0.00°
Atm.: Rayleigh
+ Mie
+ Ozone
300-600 nm
XTAL Program Output Data : Shower 16

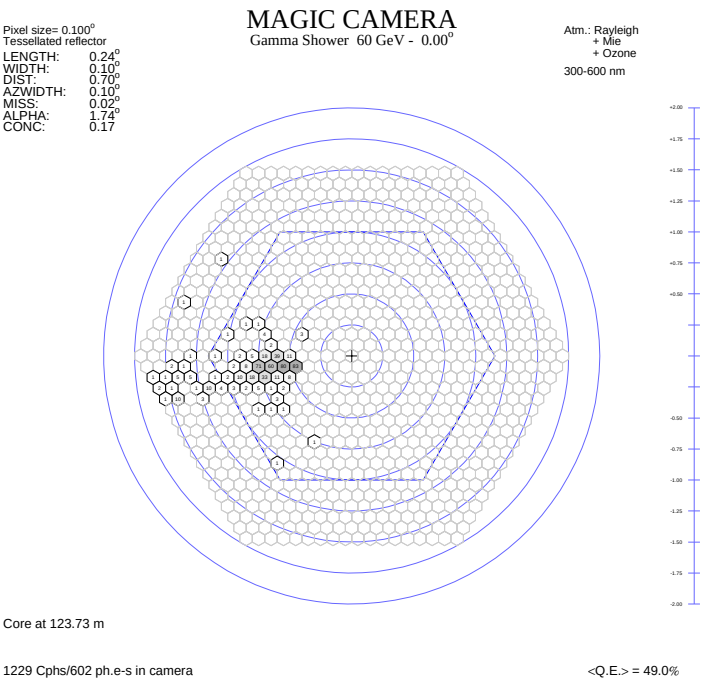
Pixel size= 0.100°
Tessellated reflector
LENGTH: 0.24°
WIDTH: 0.10°
DIST: 0.70°
AZWIDTH: 0.10°
MISS: 0.02°
ALPHA: 1.74°
CONC: 0.17
MAGIC CAMERA
Gamma Shower 60 GeV - 0.00°
Atm.: Rayleigh
+ Mie
+ Ozone
300-600 nm
Core at 123.73 m
1229 Cphs/602 ph.e-s in camera
<Q.E.> = 49.0%
XTAL Program Output Data : Shower 16

(b) 60 GeV

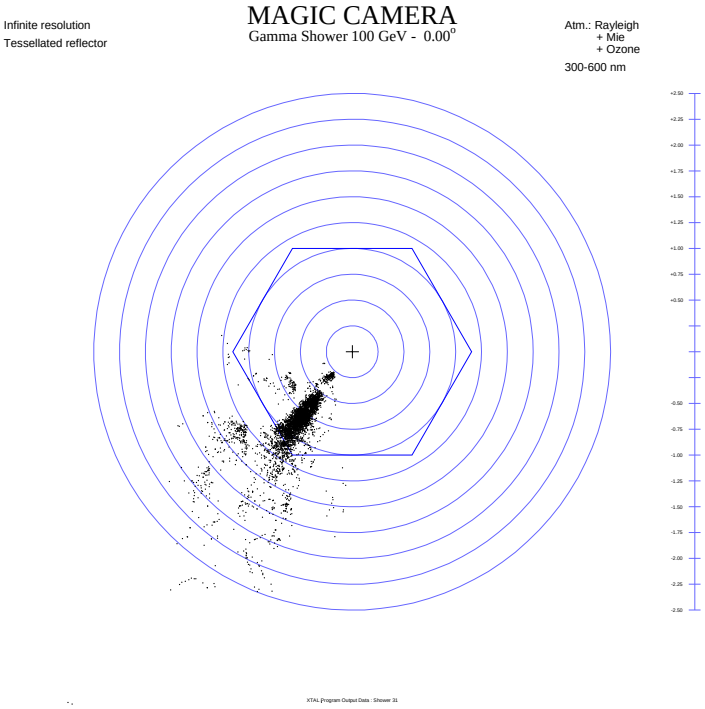
Infinite resolution
Tessellated reflector
MAGIC CAMERA
Gamma Shower 100 GeV - 0.00°
Atm.: Rayleigh
+ Mie
+ Ozone
300-600 nm
XTAL Program Output Data : Shower 31
Pixel size= 0.100°
Tessellated reflector
LENGTH: 0.27°
WIDTH: 0.15°
DIST: 0.87°
AZWIDTH: 0.15°
MISS: 0.02°
ALPHA: 1.51°
CONC: 0.14
MAGIC CAMERA
Gamma Shower 100 GeV - 0.00°
Atm.: Rayleigh
+ Mie
+ Ozone
300-600 nm
Core at 109.48 m
2699 Cphs/1225 ph.e-s in camera
<Q.E.> = 45.4%
XTAL Program Output Data : Shower 31

(c) 100 GeV

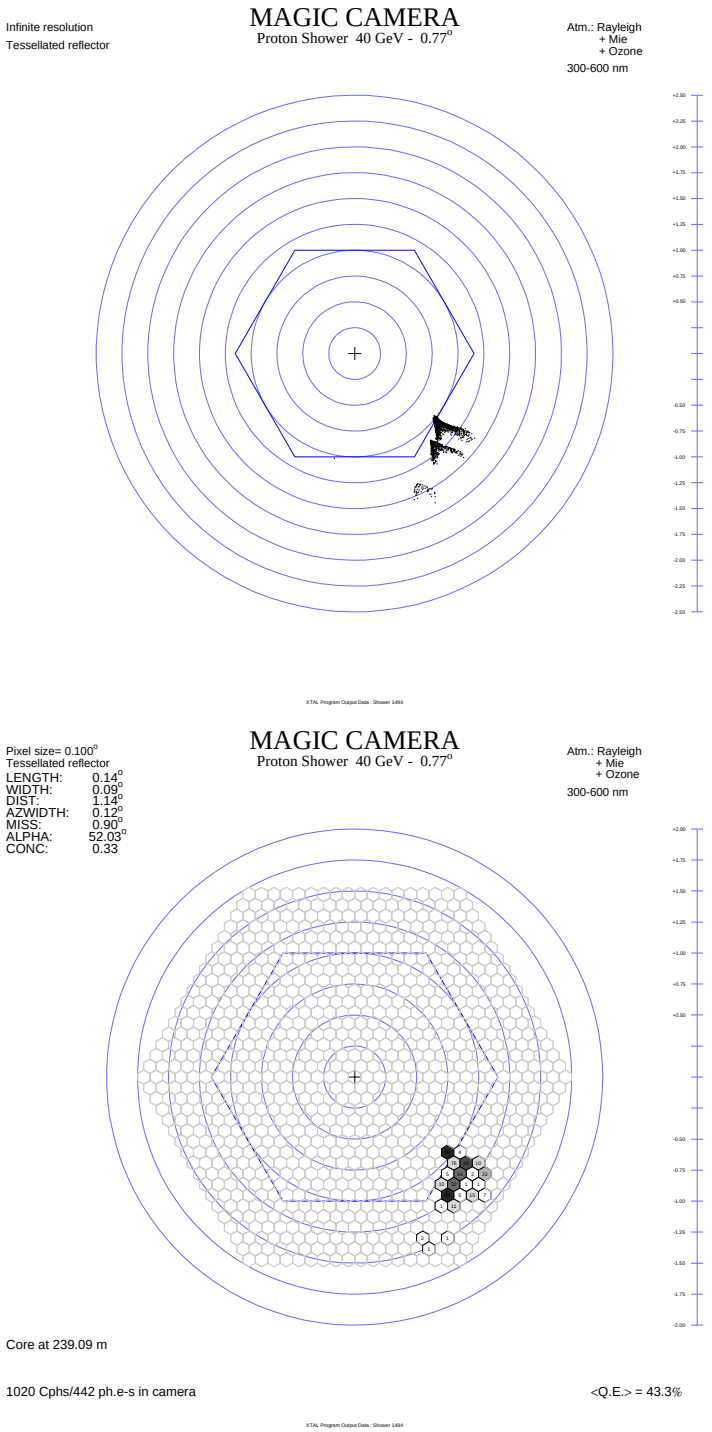

Figure 6.3: Several double images for proton showers: a) 40 GeV, b) 100 GeV, c) 250 GeV. The upper images correspond to the 'infinite resolution camera', i.e. all photons that hit the camera are shown. The lower images correspond to the simulation of the MAGIC Telescope's standard camera, i.e. using a QE of 45%.

(a) 40 GeV

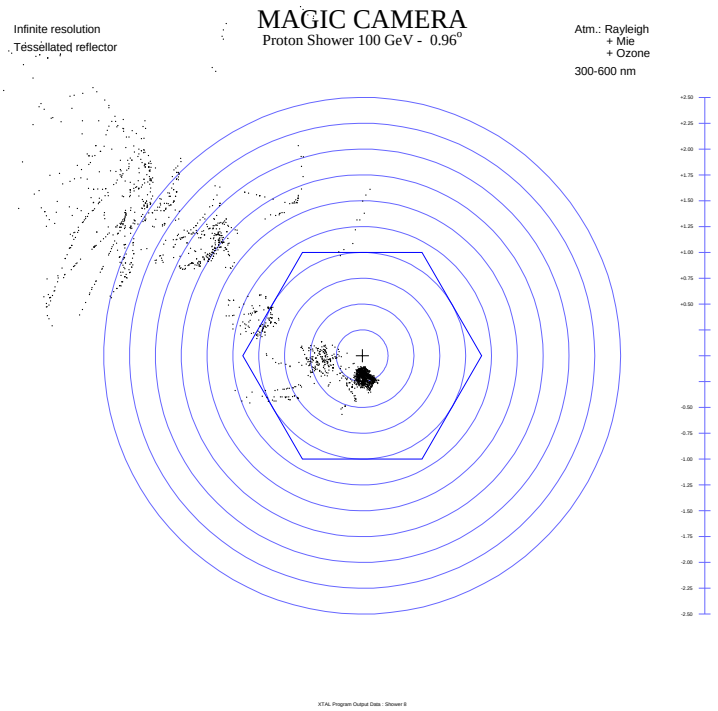
MAGIC CAMERA
Proton Shower 100 GeV - 0.96°
Infinite resolution
Tessellated reflector
Atm.: Rayleigh
+ Mie
+ Ozone
300-600 nm
XTAL Program Output Data : Shower 8

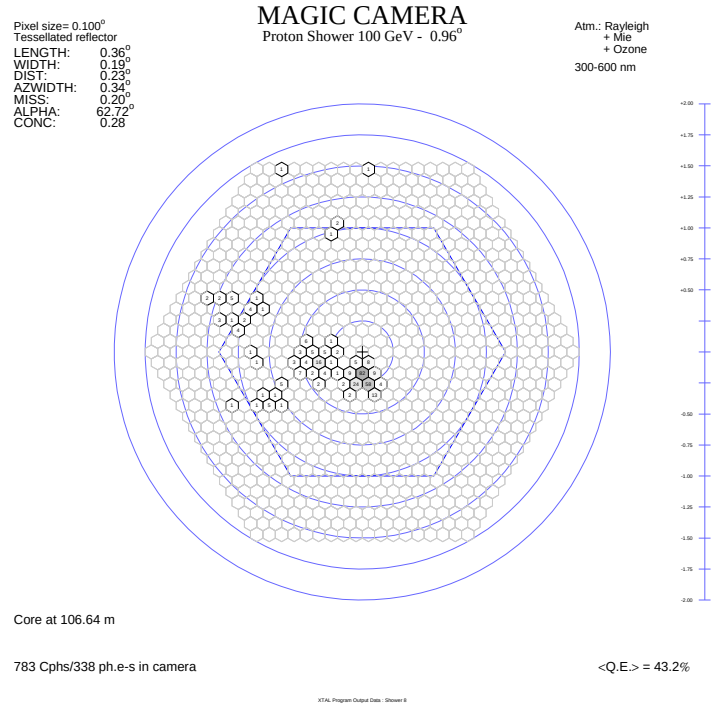
MAGIC CAMERA
Proton Shower 100 GeV - 0.96°
Pixel size= 0.100°
Tessellated reflector
LENGTH: 0.36°
WIDTH: 0.19°
DIST: 0.23°
AZWIDTH: 0.34°
MISS: 0.20°
ALPHA: 62.72°
CONC: 0.28
Atm.: Rayleigh
+ Mie
+ Ozone
300-600 nm
Core at 106.64 m
783 Cphs/338 ph.e-s in camera
<Q.E.> = 43.2%
XTAL Program Output Data : Shower 8

(b) 100 GeV

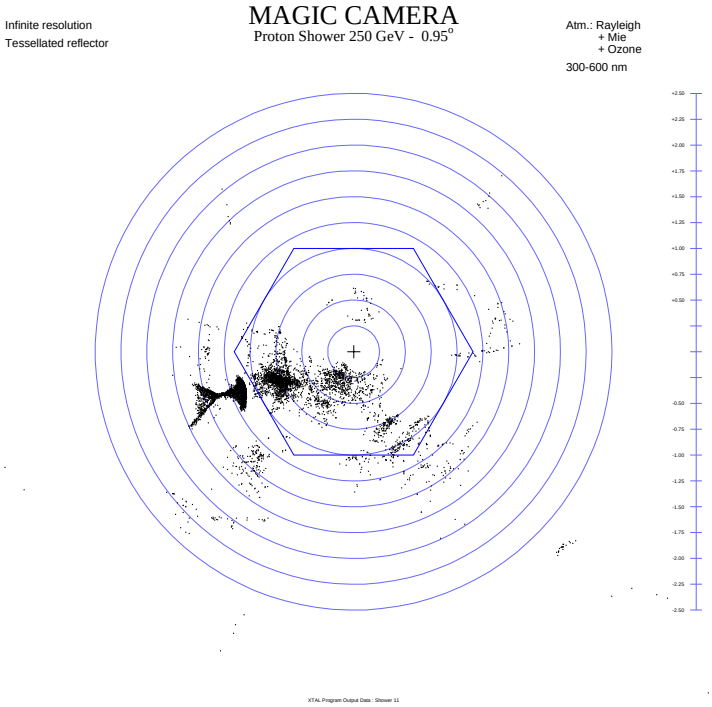
MAGIC CAMERA
Proton Shower 250 GeV - 0.95°
Infinite resolution
Tessellated reflector
Atm.: Rayleigh
+ Mie
+ Ozone
300-600 nm

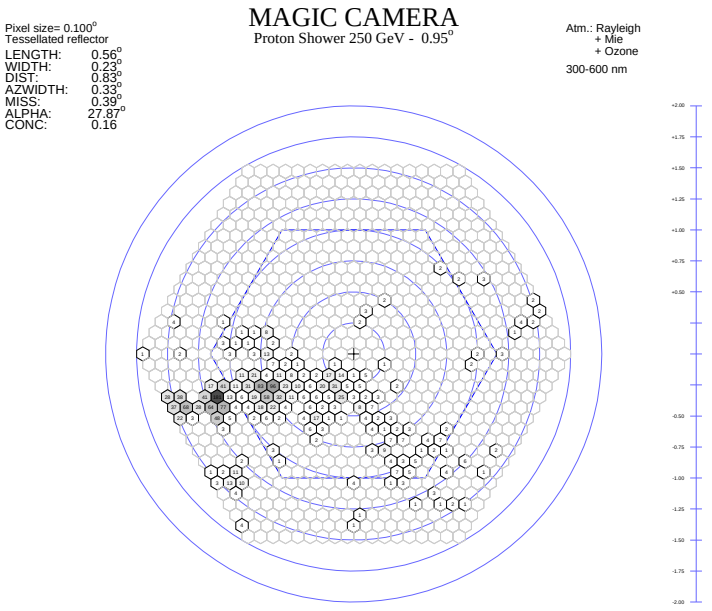
MAGIC CAMERA
Proton Shower 250 GeV - 0.95°
Pixel size= 0.100°
Tessellated reflector
LENGTH: 0.56°
WIDTH: 0.23°
DIST: 0.83°
AZWIDTH: 0.33°
MISS: 0.39°
ALPHA: 27.87°
CONC: 0.16
Atm.: Rayleigh
+ Mie
+ Ozone
300-600 nm
Core at 28.20 m
3799 Cphs/1747 ph.e-s in camera
<Q.E.> = 46.0%

(c) 250 GeV

the application of a tail cut for *cleaning* images from fluctuations, and is separated by some non-zero distance from the main, relatively large image of the shower (see, for example, the lower image on Fig. 6.3c). Our simulations show that an image can have up to 3–4 islands. A telescope with a very high photon sensitivity provides detailed images of the shower development, revealing small structures in images as, for example, sub-showers, which are in fact the above-mentioned islands. Hadron showers seem to have on average more islands than γs.

Fig. 6.4 shows the trigger probabilities for γs of different energies versus the impact parameter. On average 10 GeV γs trigger the telescope with a probability of ca. 14% up to an impact parameter of ca. 120 m. 20 GeV γs trigger with a probability of 45%, which increases to 75% for 40 GeV. The 60 GeV γs trigger with a probability of 90% up to the same distance and the 80 GeV γs trigger with a probability of 95%, above which the trigger probability reaches the plateau level of almost 100%.

Due to the diffuse character and the lower light content in proton images (compared to γs of the same energy) and the restrictive trigger condition demanding a certain minimal amount of light in at least 4 neighbouring pixels, protons trigger with much smaller probabilities. Fig. 6.5 shows the dependence of the trigger probability for proton showers on the impact parameter.

The simulations show that on average only one out of ca. 8000 proton showers of 20 GeV fulfills the trigger condition. In Fig. 6.5 one can see that for 40 GeV protons the trigger probability is only 0.15%, reaching 1.7% level for 100 GeV showers. The 250 GeV showers trigger with a probability of 8%–10%, and 500 GeV showers trigger with a probability of 10%–12%.

To summarize, the application of the trigger condition "*any* ≥ 4 *neighbours above the given threshold*" results in a very strong rejection of proton images, providing a highly efficient pre-selection of γ events already at the trigger level.

The camera trigger radius must provide high trigger efficiency for γs for the entire extended VHE energy range ($\sim$10 GeV - $\sim$ 100 TeV), simultaneously triggers due to isotropic backgrounds have to be minimized. To achieve the highest γ rate the optimization of imaging camera trigger diameter is of key importance, because it allows one to considerably reduce the trigger rate due to different isotropic backgrounds, e.g. that of hadrons, muons and electrons. This is especially important for very low energy threshold telescopes, where the high trigger rate from different backgrounds could introduce a substantial dead time and could thus necessitate the use a very fast and expensive data acquisition system.

The MAGIC Telescope will have a high trigger rate due to its very high photon sensitivity and correspondingly very low energy threshold. Unlike hadrons, γs from a point source efficiently trigger the camera up to an impact parameter of ca. 125 m (till the *hump* in the lateral distribution of photons, see Fig. 3.2). Depending on the energy of the γ and on the observation altitude (in fact the distance between the telescope and the shower maximum as well as its viewing angle), the position of

the hump corresponds to the image centroid positions in the range of ca 0.6°–1.2°. Strictly speaking in an image there are usually a few pixels with the highest charge content, which correspond to the region of shower maximum and which initiate triggers in the camera. The centroid of an image appears as a result of the mathematical parametrization of the measured pattern from an air shower; it is the first moment of the charge distribution. The longitudinal development of air showers is asymmetrical in shape. In the correspondingly asymmetric images, given parallel incidence of the flux wrt to the telescope axis, i.e. that of γs from a point source, the pixels with maximal charge which initiate triggers, are at slightly shorter distances from the camera centre (i.e. pointing at the assumed γ source position) than the image centroids.

In our simulations we defined the parameter MaxDIST as the first moment of 4 pixels with the highest charge in the image. For the given γ shower the position of MaxDIST, which is the only prominent point in its image, provides the angular distance of its maximum from the source position in the image plane. In our simulations we used the parameter MaxDIST instead of the conventionally used parameter DIST.

The 50 GeV γs, for example, reach the maximum of their development at ca. 12 km a.s.l. The sub-100 GeV showers have MaxDIST positions within the inner 0.8° radius of the camera even for large impact parameters and will therefore be able to trigger the camera. When the energy of the showers is increased the showers reach their maximum deeper in the atmosphere. The shower maximum *moves* towards the telescope, its viewing angle becomes larger and therefore the MaxDIST of their images *move* to larger distances from the centre of the camera.

If the trigger radius of the camera is limited to $\leq$0.8°, together with sub-100 GeV showers also those >100 GeV, in spite of the fact that their MaxDIST can be at distances of more than 0.8° for large impact parameters, will readily trigger the camera. This is possible due to the high photon sensitivity of the telescope, its low trigger threshold per channel and the high content of light along the images of high energy showers.

In our simulations we assumed a point source of γs with the flux:

$$F_\gamma(\geq E) = 10^{-8}\Big(\frac{E}{10\mathrm{GeV}}\Big)^{-1.5} \text{ ph cm}^{-2}\text{ s}^{-1} \tag{6.2}$$

and extrapolated it for higher energies. This choice of flux is motivated by the flux measurements of extragalactic sources by EGRET [99, 71]. E.g. the flux of one of the weakest AGN detected by EGRET, namely the blazar Mkn 421, when extrapolated to 10 GeV is only a factor of $\sim$2 smaller than the flux assumed in Eq. 6.2.

In Fig. 6.6 we show the calculated collection areas after trigger for γs and protons for the MAGIC Telescope. Using the spectrum in Eq. 6.2 for γs and the differential

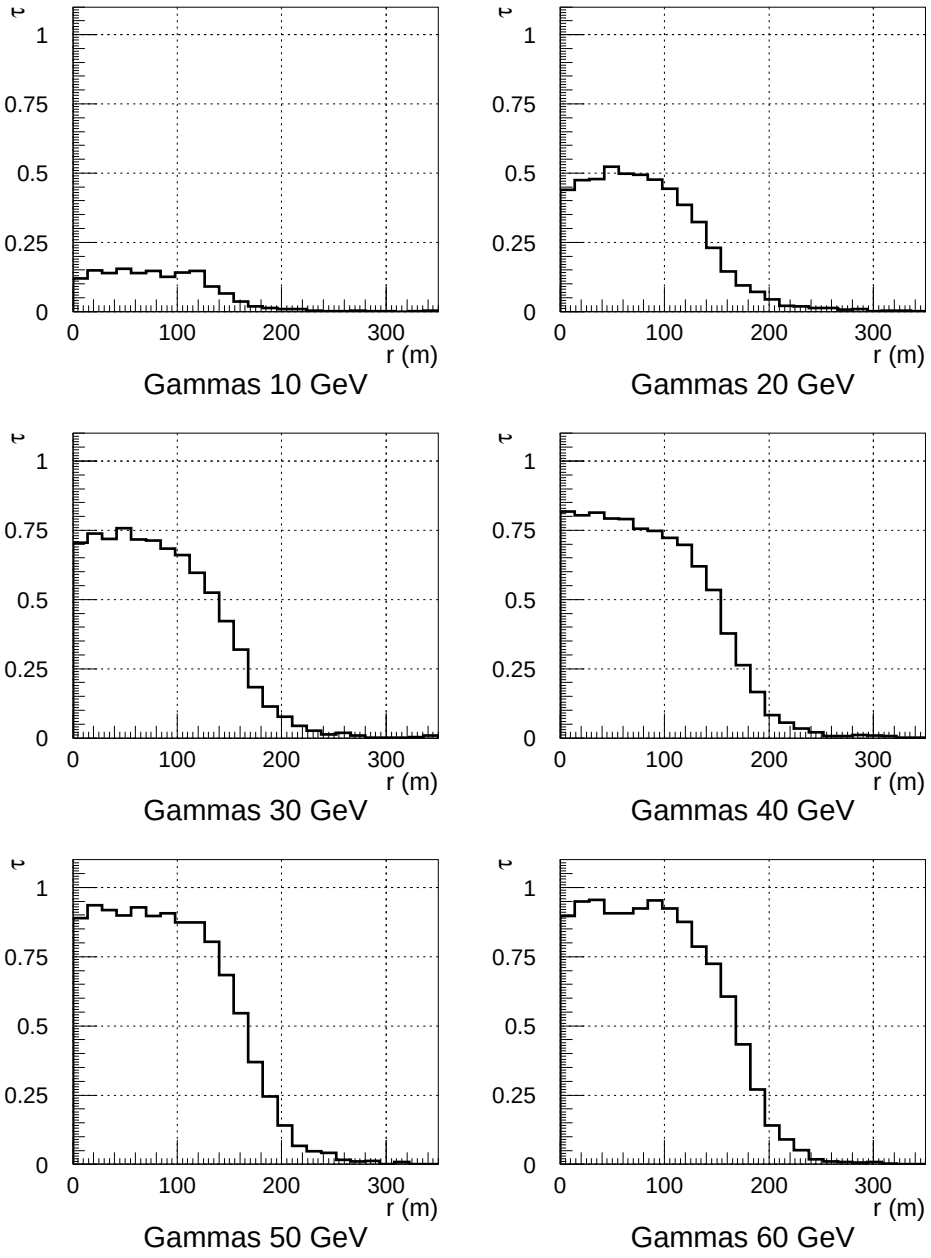

(a)

Figure 6.4: Trigger probability for γ-rays of different energies versus the impact parameter.

flux for protons F_{p} (protons) from [7]:

$$\frac{\mathrm{d}F_{\mathrm{p}}}{\mathrm{d}E} = 10.91{\cdot}10^{-2}\Big(\frac{E}{1\ \mathrm{TeV}}\Big)^{-2.75}\ \mathrm{m}^{-2}\mathrm{s}^{-1}\mathrm{sr}^{-1}\mathrm{TeV}^{-1} \tag{6.3}$$

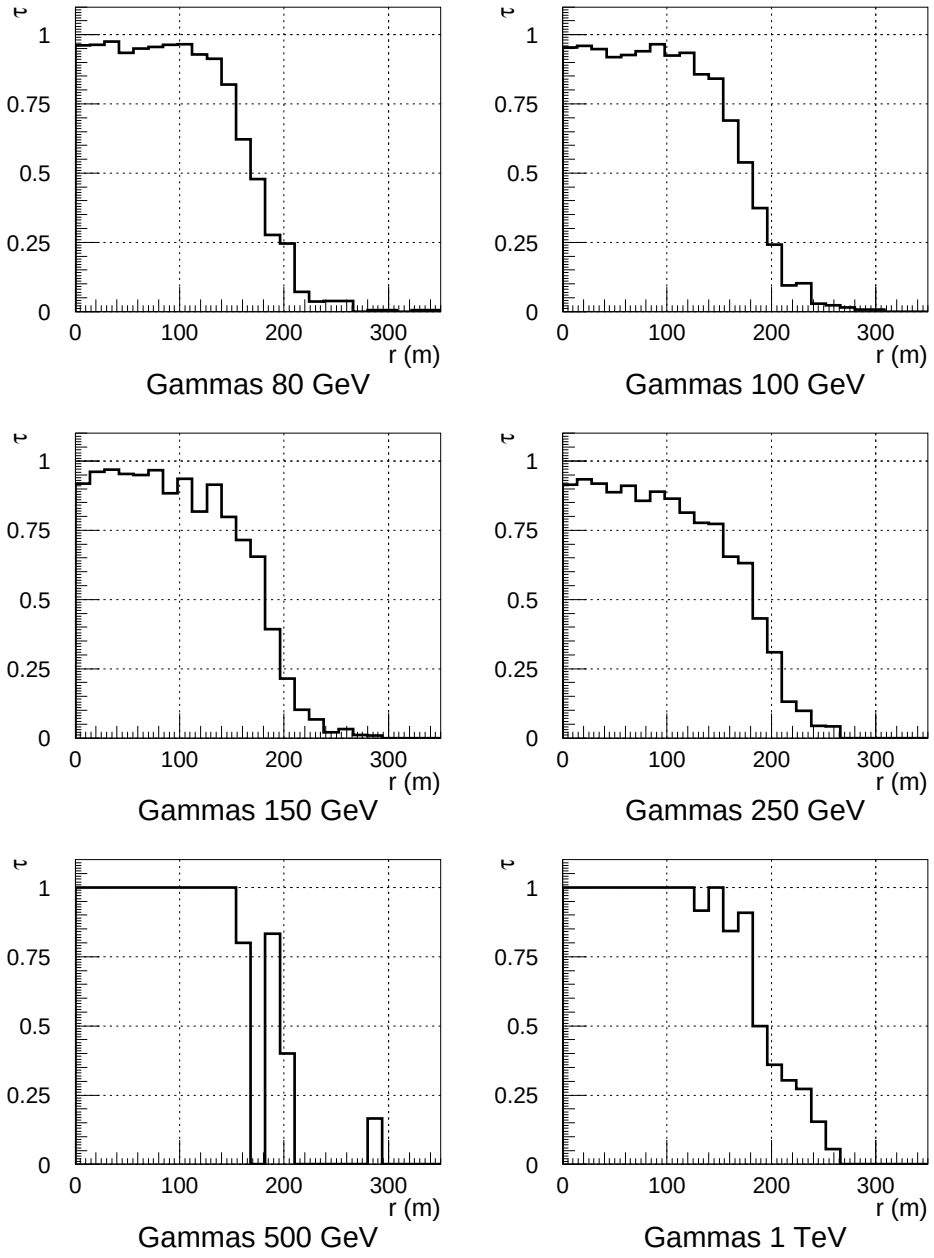

Figure 6.4: (b)

the differential and integral rates for γs and protons, shown in Figs. 6.7 and 6.8, are obtained. Fig. 6.7 shows that the energy threshold of the telescope for γ-rays is about 10 GeV.

We have also performed simulations for a camera trigger radius of 1.75°. With

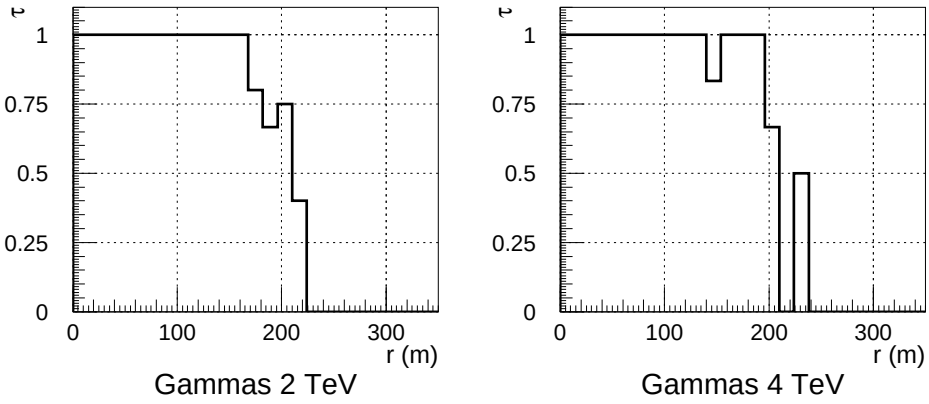

Figure 6.4: (c)

the larger trigger diameter camera one measures γ-rays over the entire energy and impact parameter ranges. For the 1.75° trigger radius camera a γ trigger rate of 3.7 Hz was obtained. This is almost identical to the γ trigger rate of 3.5 Hz obtained for the 0.8° trigger radius camera (a small excess of the γ trigger rate in the large

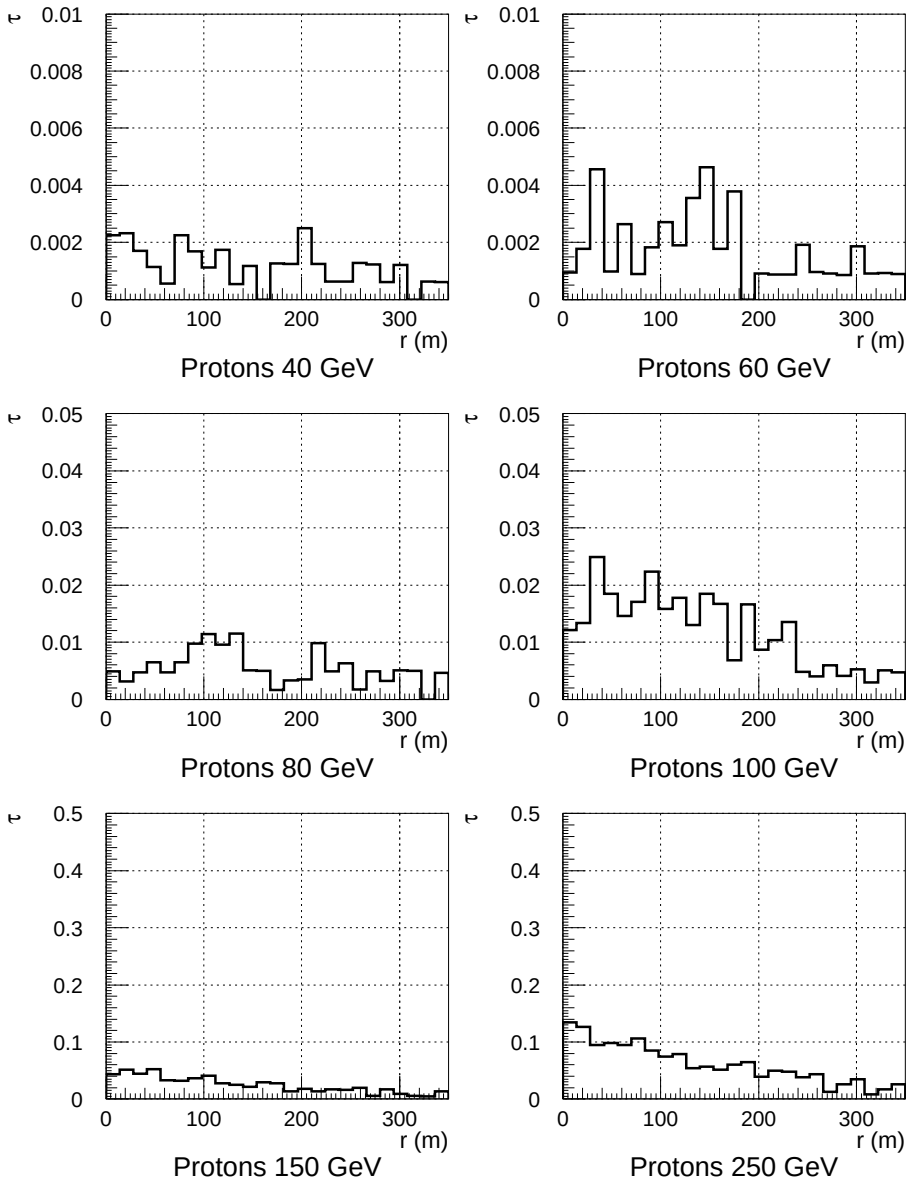

(a)

Figure 6.5: Trigger probability for protons of different energies versus the impact parameter.

trigger diameter camera is due to high energy tail of the assumed spectrum) whereas the dominant proton trigger rate is ca. 5 times less for the camera with the smaller trigger radius (the trigger rate due to any isotropic emission is proportional to the camera acceptance solid angle).

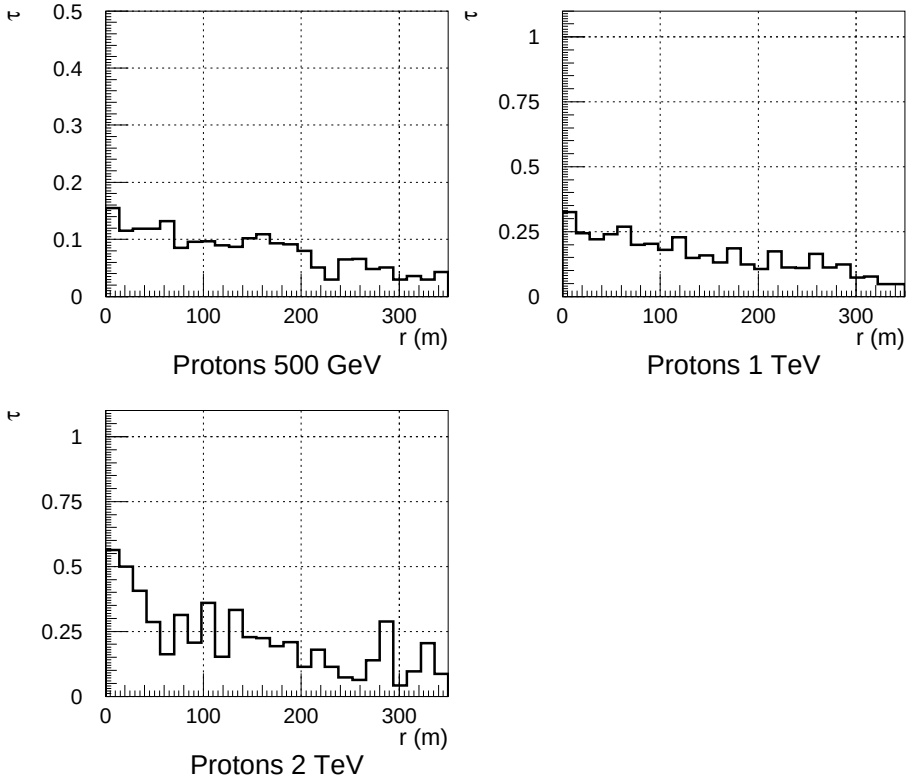

Figure 6.5: (b)

The advantages of the imaging technique, convincingly demonstrated for energies $\geq$300 GeV, are the large collection area and the efficient γ/hadron separation. High resolution cameras (pixel size ca. 0.25°) allow one to reject the hadronic background by a factor of 300–500, while losing only about half of the γs from a point source. The angular resolution of a high resolution camera alone contributes about a factor of 10 (the ALPHA domain for γs is up to 10°, whereas hadrons are distributed over a range of 0°–90°). In addition, the differences in the shape allow one to reject

hadrons by another factor of 30 or more.

One may hope, that for energies of less than 100 GeV the imaging technique will still be powerful enough to perform efficient γ/hadron separation. Recalling the fact that below ca. 100 GeV hadrons produce progressively much less light than *gamma*s (see Fig. 3.1 or [108]) of the same energy and therefore only rarely initiate triggers, one may say that nature helps efficiently in the rejection of hadrons at the hardware level. As the total rejection power of a telescope is a combination of hardware and software rejections, constraints on the efficiency of the software analysis in the sub-100 GeV energy domain are rather weak and even a modest γ/hadron separation, for example, of the order of only a factor of 50 in the software analysis, can provide very high sensitivity for such telescopes.

The fluctuations in the images of sub-100 GeV showers are larger than those at higher energies. One of the reasons is that sub-100 GeV showers produce a relatively small number of secondary particles and develop higher in the atmosphere where the air density is low and where therefore the Čerenkov threshold is high. For cascade development, the column density of the medium is important, and high up in the atmosphere longer distances are involved for a given column density. On the other hand, an image is just a geometrical projection of the shower development at different heights in the atmosphere.

Because sub-100 GeV γ showers develop higher in the atmosphere the measuring telescope *sees* them at smaller angles with respect to the source direction which means that shower images are closer to the source position in the camera plane. i.e. the camera centre. Because of this, the images measured are more round and therefore the accuracy of determining both the orientation and the shape parameters deteriorates [96].

Fig. 6.9 shows the distributions of ALPHA parameters for Monte Carlo γs of different energies. One can see that the width of the ALPHA distributions (at half-maximum level) is larger for lower energies. Its value is ca. 5° for energies >150 GeV, becoming ca. 10° for energies of ca. 60 GeV and ca. 15° for energies of ca. 20 GeV, confirming the above-mentioned expectation.

In Fig. 6.10 the evolution of the mean SIZE (the parameter SIZE is the total sum of the charge measured in a image) for γs and protons is shown as a function of the primary energy. Note that the applied strong trigger condition biases the SIZE distribution in the case of protons towards positive fluctuations.

It is interesting to note that although γ-rays from a point source enter the atmosphere parallel to the axis of the telescopes, our simulations of very low energy showers reveal that they sometimes develop showers, whose axes make non-zero angles with that of the telescope. A possible explanation for this could be that the direction of shower development begins to fluctuate already during the first few interactions.

In the following we present first results of an image analysis based on the shape parameters . For this purpose we studied the dependence of the LENGTH, WIDTH

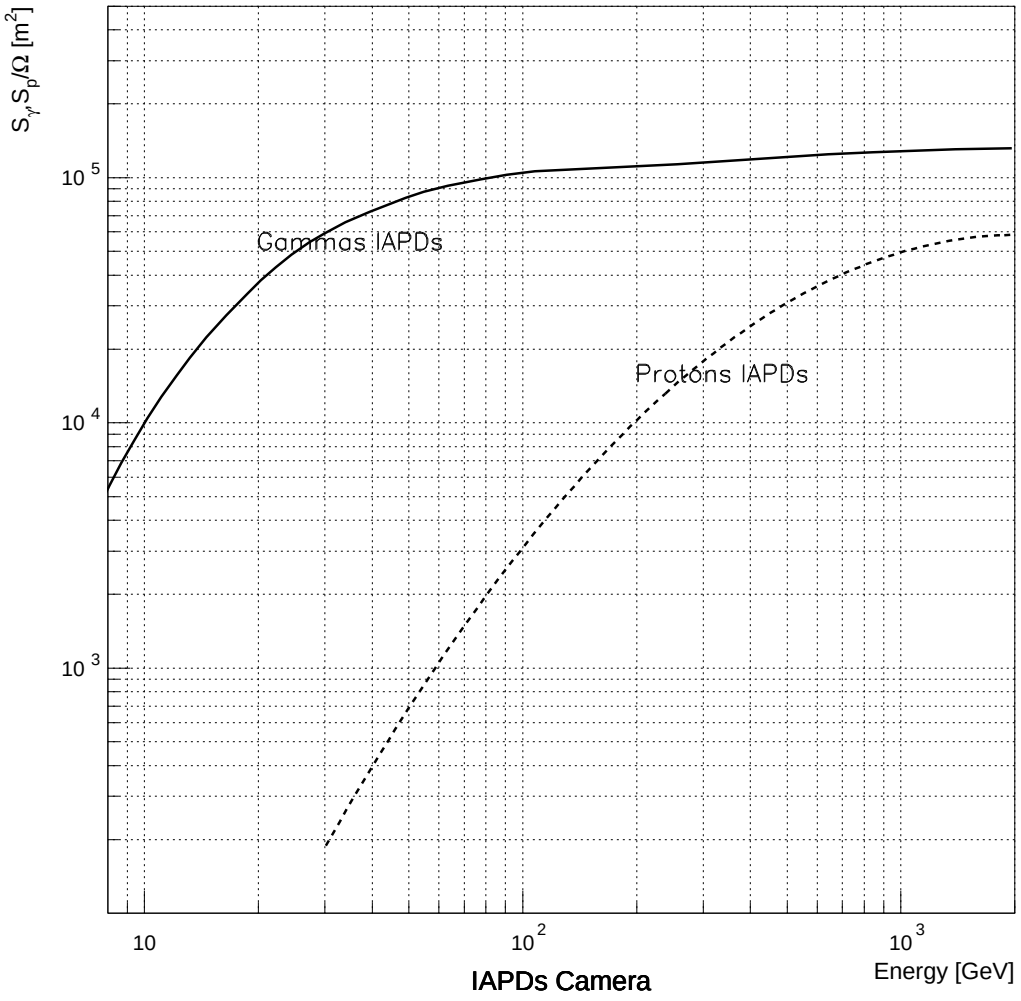

Figure 6.6: Effective collection area after triggering for γ-rays and protons for a camera with an 0.8° trigger radius. The trigger condition "any 4 neighbouring pixels above the threshold of 7 ph.e.s" has been applied.

and CONC image parameters on the energy. First, we redefined the latter as CONC-N, which for the given image is the ratio of the sum of the first N maxima to the total charge. Figure 6.11a–c shows the distributions of shape parameters for γs of different energies. We found that the CONC7 distribution is efficient for the given pixel size of 0.10°.

One can see the well-known tendency for the mean values of the image parameters WIDTH and LENGTH to increase gradually with increasing energy. On average the

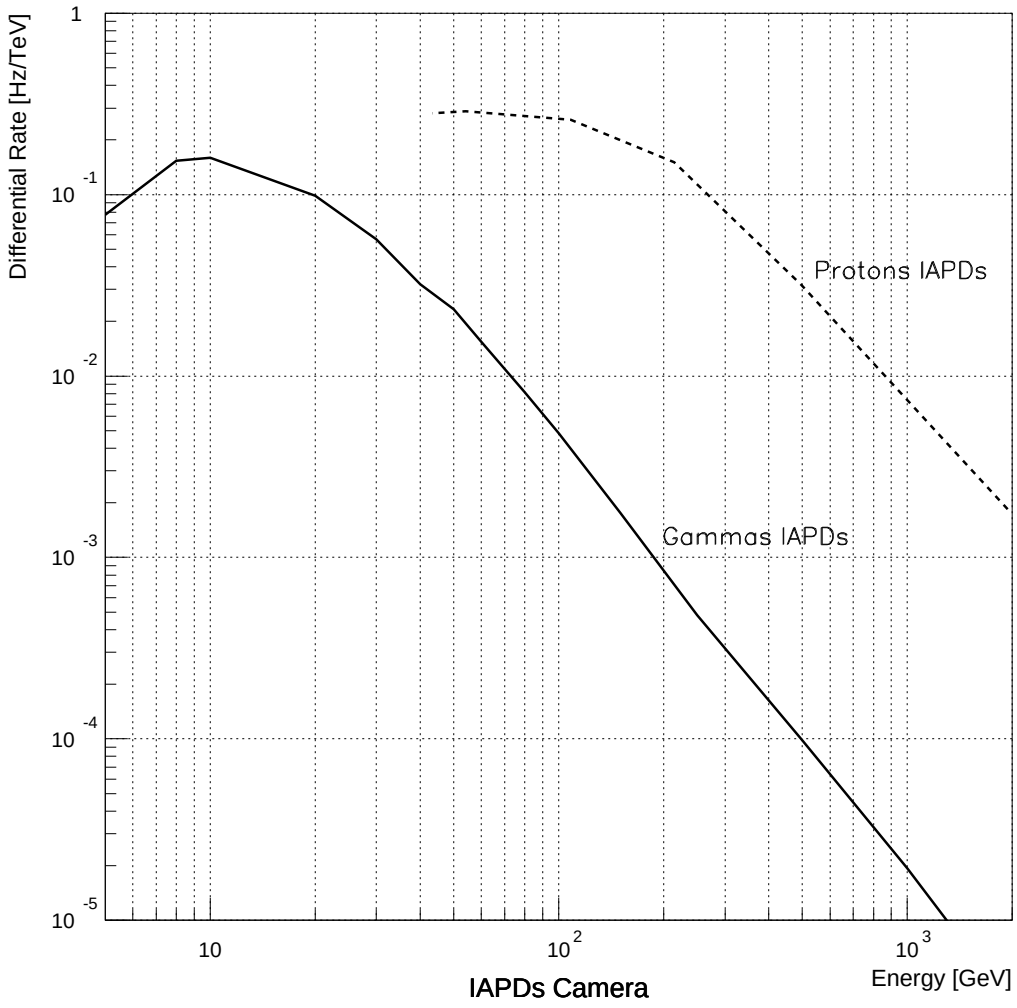

Figure 6.7: Differential trigger rates for γs and protons for a camera of 0.8° trigger radius. The trigger condition "any 4 neighbouring pixels above the threshold of 7 ph.e.s" has been applied.

20 GeV showers have WIDTHs of 0.06°, which increase to 0.08° for 100 GeV showers and to 0.12° for 500 GeV showers. Similarly, the LENGTH of 20 GeV showers is ca. 0.10–0.15°, and this increases to ca. 0.22° for 100 GeV and to ca. 0.27° for 500 GeV.

Figure 6.12a-c shows the shape parameters for protons of different energies. The comparison with Fig. 6.11 shows that protons have substantially wider distributions for the LENGTH, WIDTH and CONC7 parameters compared to γs of similar

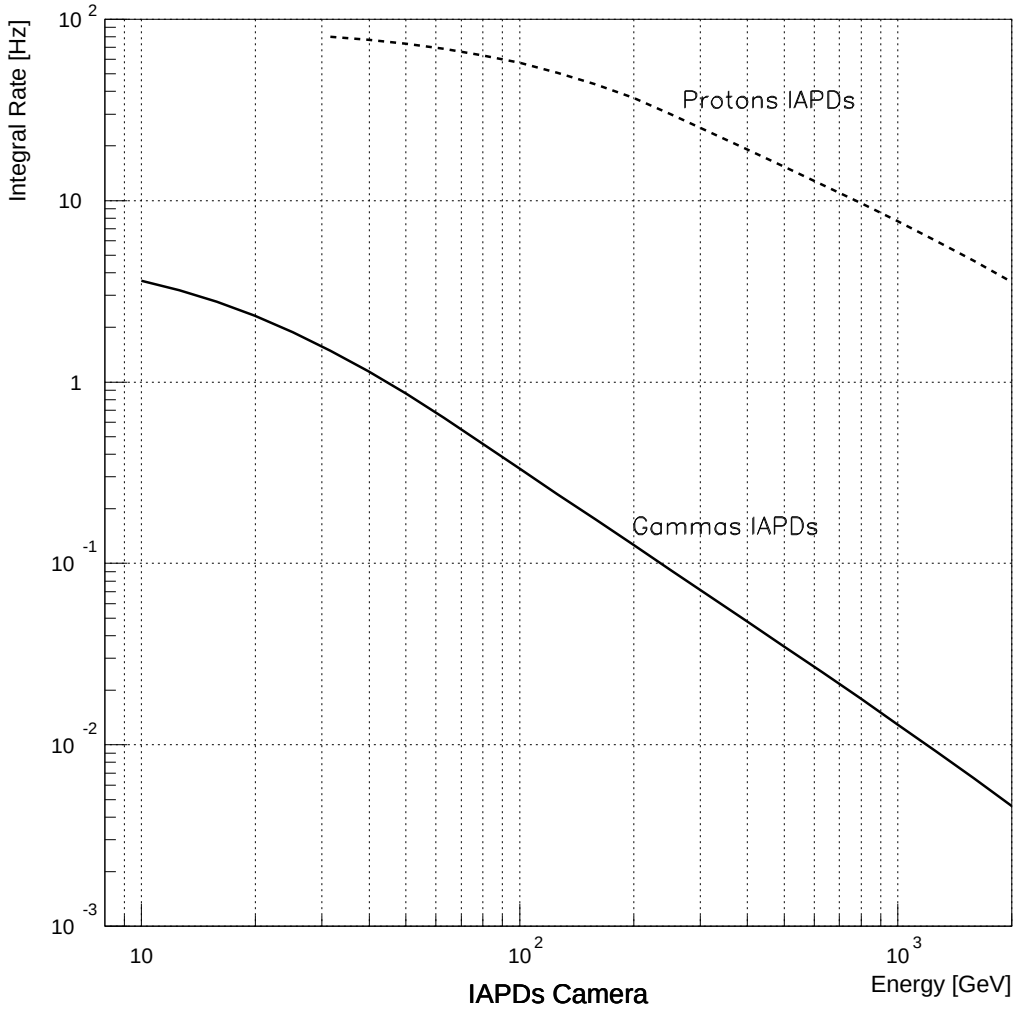

Figure 6.8: Integral rates after triggering for γs and protons for a camera with 0.8° trigger radius. The trigger condition "any 4 neighbouring pixels above the threshold of 7 ph.e.s" has been applied.

energies.

We investigated the γ/hadron separation power of the MAGIC Telescope on the basis of an image analysis. Using the generated Monte Carlo events and weighting them, we simulated a *gamma* source spectrum with the flux normalization given by Equation (6.2) and a proton spectrum given by (6.3).

For the image analysis first we selected only those patterns, which have MaxDIST values between 0.4°–1.1° (similar to the standard SUPERCUT analysis, e.g. [82]).

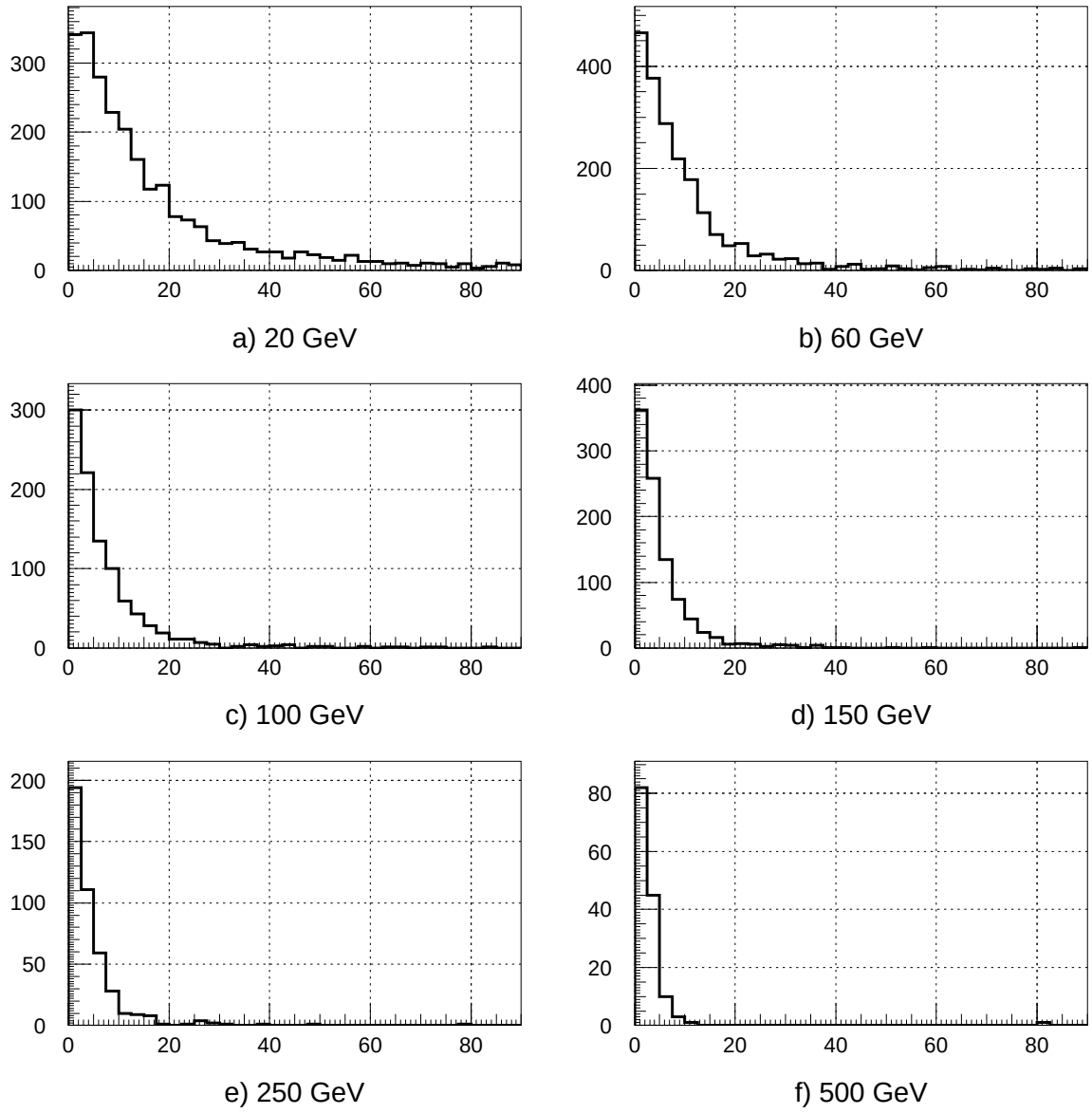

Figure 6.9: The ALPHA image parameter distributions for γ-rays of different energies.

These data wer sorted into 3 bins in MaxDIST, namely 0.4°–0.5°, 0.5°–0.9° and 0.9°–1.1° and for each of them sets of "classical" supercuts were derived. Also a cut on the asymmetry of shower images has been applied and which improved the γ/hadron separation power. The γ domains were selected on the condition that they should provide a total acceptance of $\geq$50%. The results of this analysis[2] are shown

[2]The quality factor Q is defined as usual:

$$Q = \epsilon_\gamma / \sqrt{\epsilon_H}$$

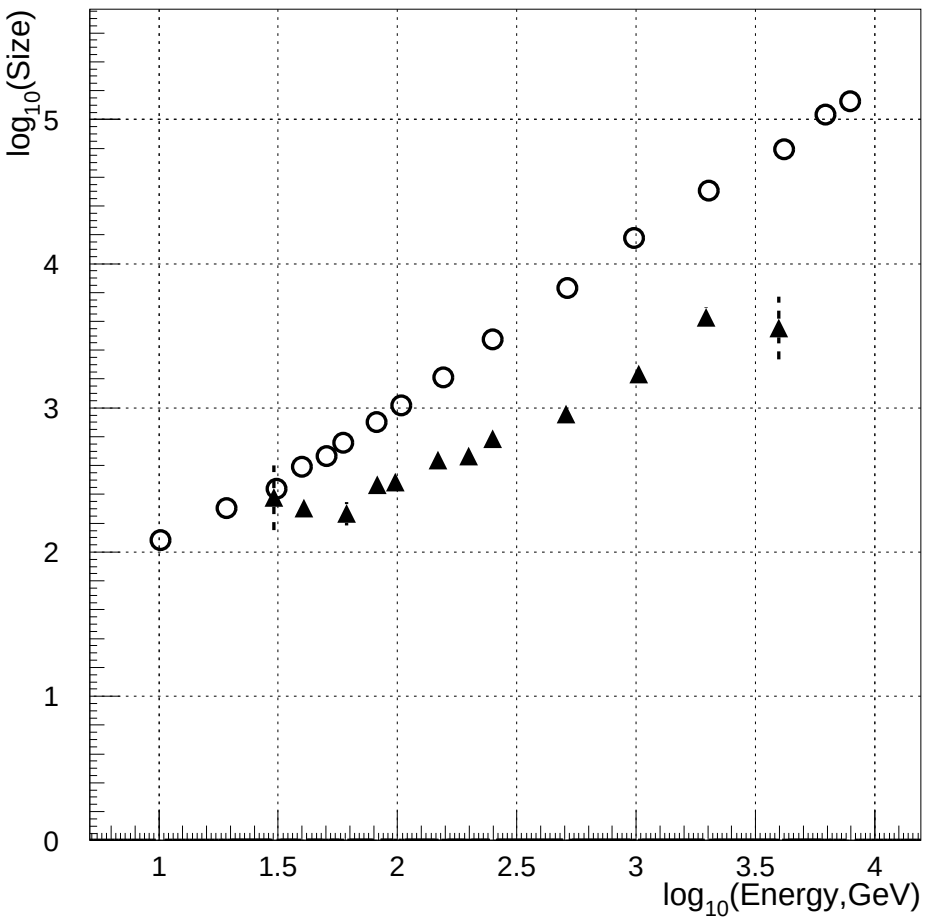

Figure 6.10: The mean SIZE evolution with the primary energy for γs (opened circles) and protons (filled triangles).

in Table 6.1. The imaging analysis provides a Q factor of 5.1 for the MaxDIST bin 0.4°–0.5°, 6.5 for the bin 0.5°–0.9° and 12.8 for the 0.9°–1.1° bin. The total Q factor is calculated to be about 7.4 for the MaxDIST range 0.4°–1.1° and about 7.7 for the MaxDIST range 0.5°–1.1°.

where $\epsilon_\gamma = N_\gamma^{an}/N_\gamma$ and $\kappa_H = N_H^{an}/N_H$ are the efficiencies of detection for γs and protons after our analysis. N_γ^{an} and N_γ correspond to the number of γs after and before the application of analysis cuts, respectively.

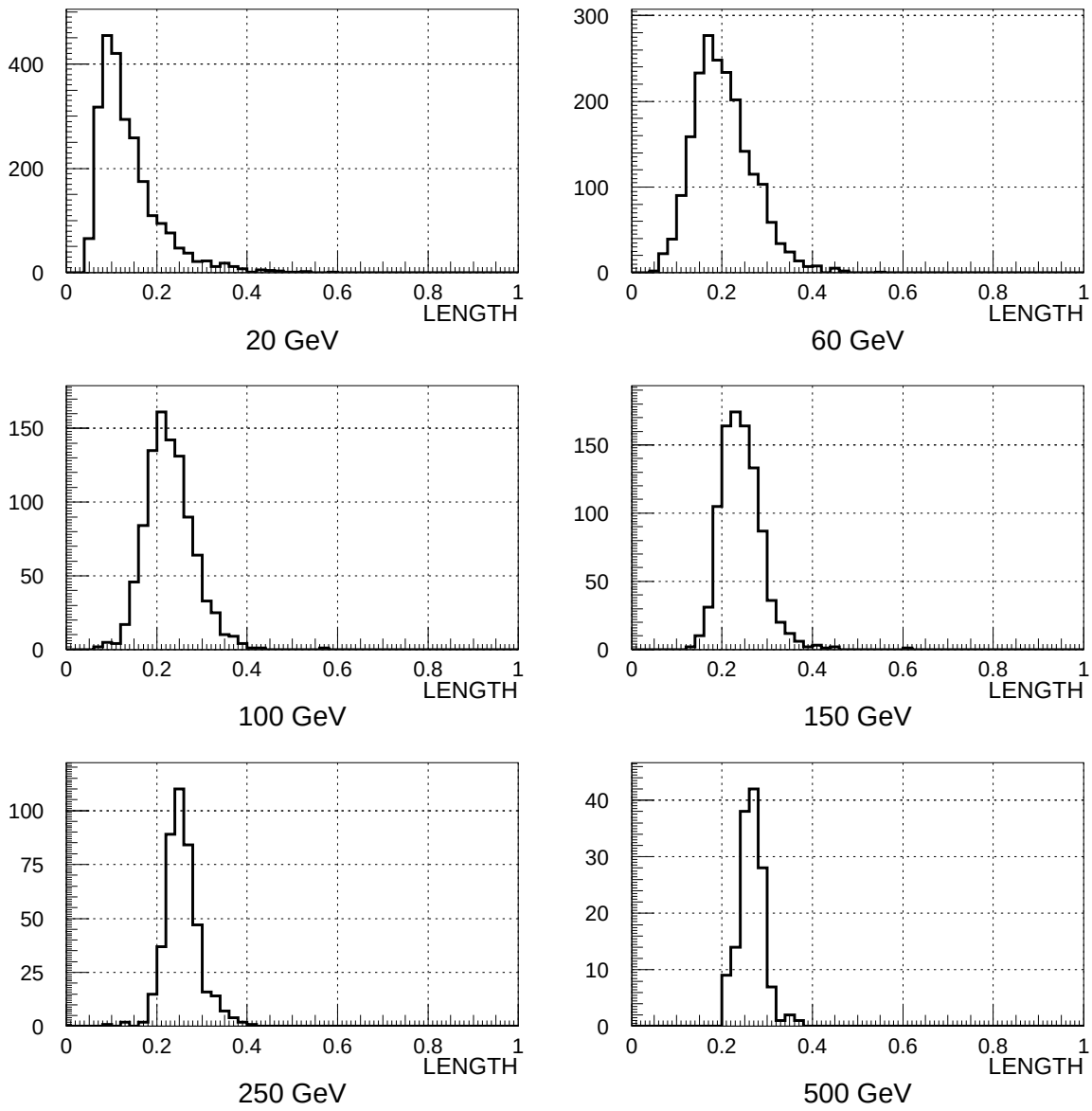

a) The LENGTH distributions for γ images of different energies.

Figure 6.11: Shape distributions for γs.

6.1.4 Fall-back (classical PMT) camera

Similar simulations were performed for the classical PMT camera. In Figs. 6.13 to 6.15 we show the collection areas and the differential and integral trigger rates for γs and protons, respectively, for an assumed γ source whose flux normalization is given by Eq. (6.2) and for the proton spectrum given by Eq. (6.3). From Fig. 6.14 it follows that the threshold of the telescope is about 30 GeV for the PMT camera. We would like to mention that here we have applied the same trigger condition

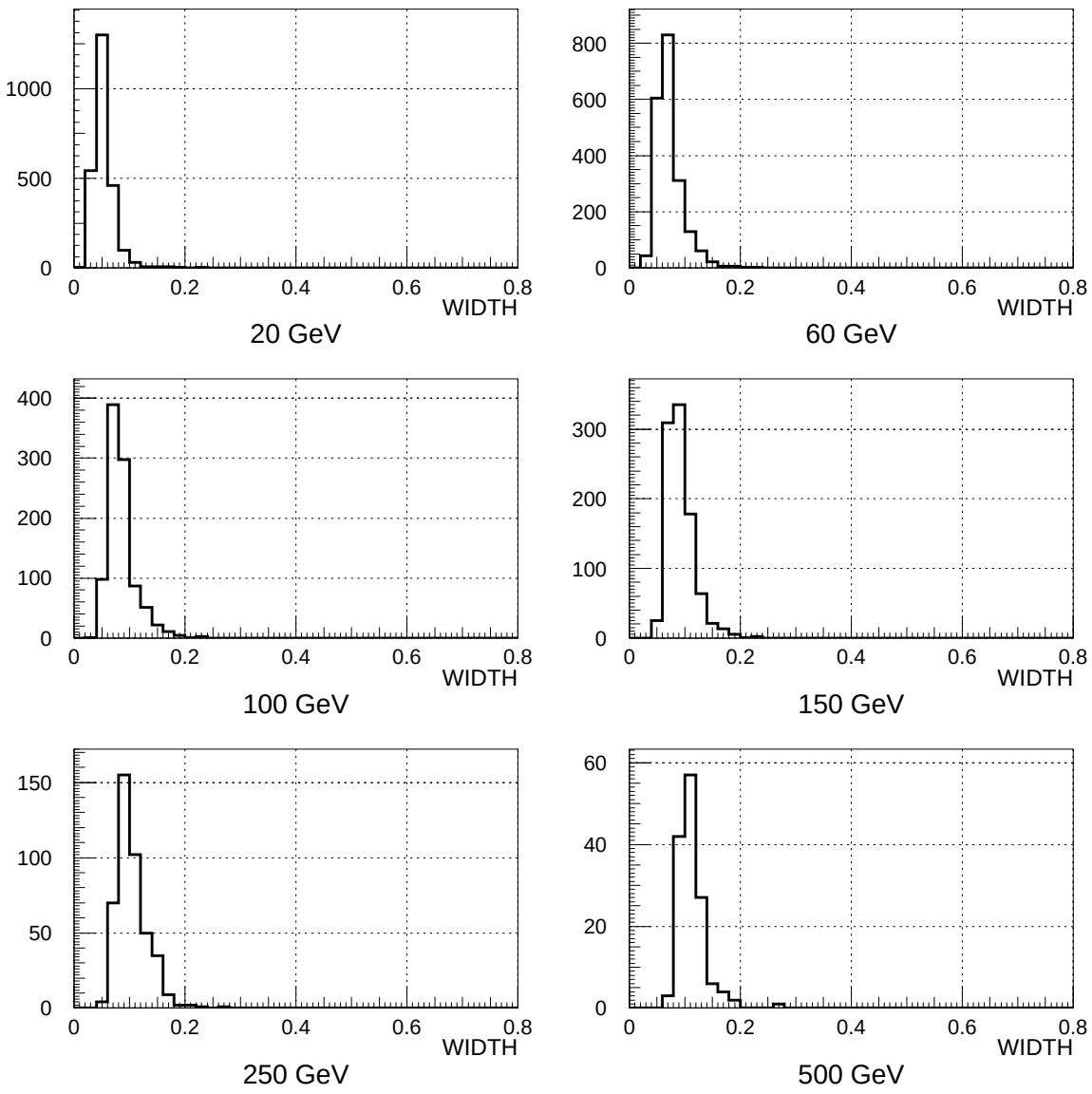

6.11.b) The WIDTH distributions for γ images of different energies.

and tail cut as in the case of the IAPD camera, i.e. the trigger condition "any 4 neighbouring pixels in a close-packed configuration above the threshold of 7 ph.e.s" and a tail cut of 10 ph.e.s. The quoted threshold value for γs and the rates shown are thus rather conservative. Because the QE of classical PMTs is lower compared to that of IAPDs, they integrate less light from the NSB and one therefore can apply a less restrictive trigger condition, say for example, "any 4 neighbouring pixels above a threshold of 4 ph.e.s" and a lower tail cut of, for example, 6 ph.e.s, which will result in a somewhat lower trigger threshold energy than the quoted 30 GeV and correspondingly higher trigger rates. Table 6.2 shows the results of an imaging analysis for the MAGIC Telescope performed for the classical PMT camera. In this

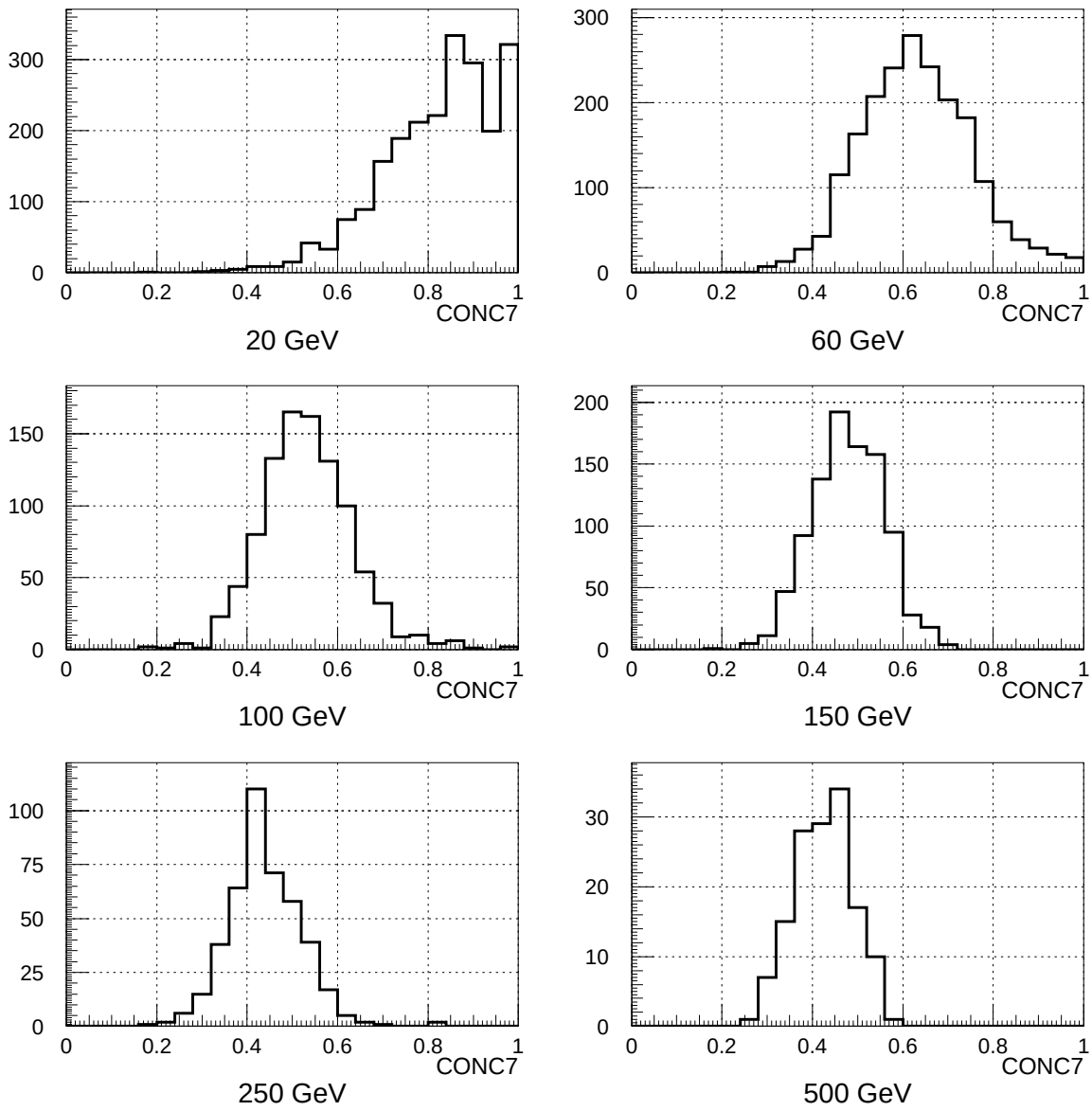

6.11.c) The CONC7 distributions for γ images of different energies.

case again we have applied the classical second moment analysis together with the parameter asymmetry.

As summarized in Table 6.2 in this case the telescope provides a Q factor of 6.9 for a MaxDIST range of 0.5°–0.9° and a Q factor of 8.4 for a MaxDIST range of 0.9°–1.1°. The weighted mean Q factor is about 7–8 and is completely dominated by the lowest energy part of the spectrum. Note that the Q value corresponding to the MaxDist range of 0.4°–0.5° in Table 6.2 is affected by the small statistics in this bin and the expected value should be somewhat smaller. This will be checked by the still ongoing MC investigations.

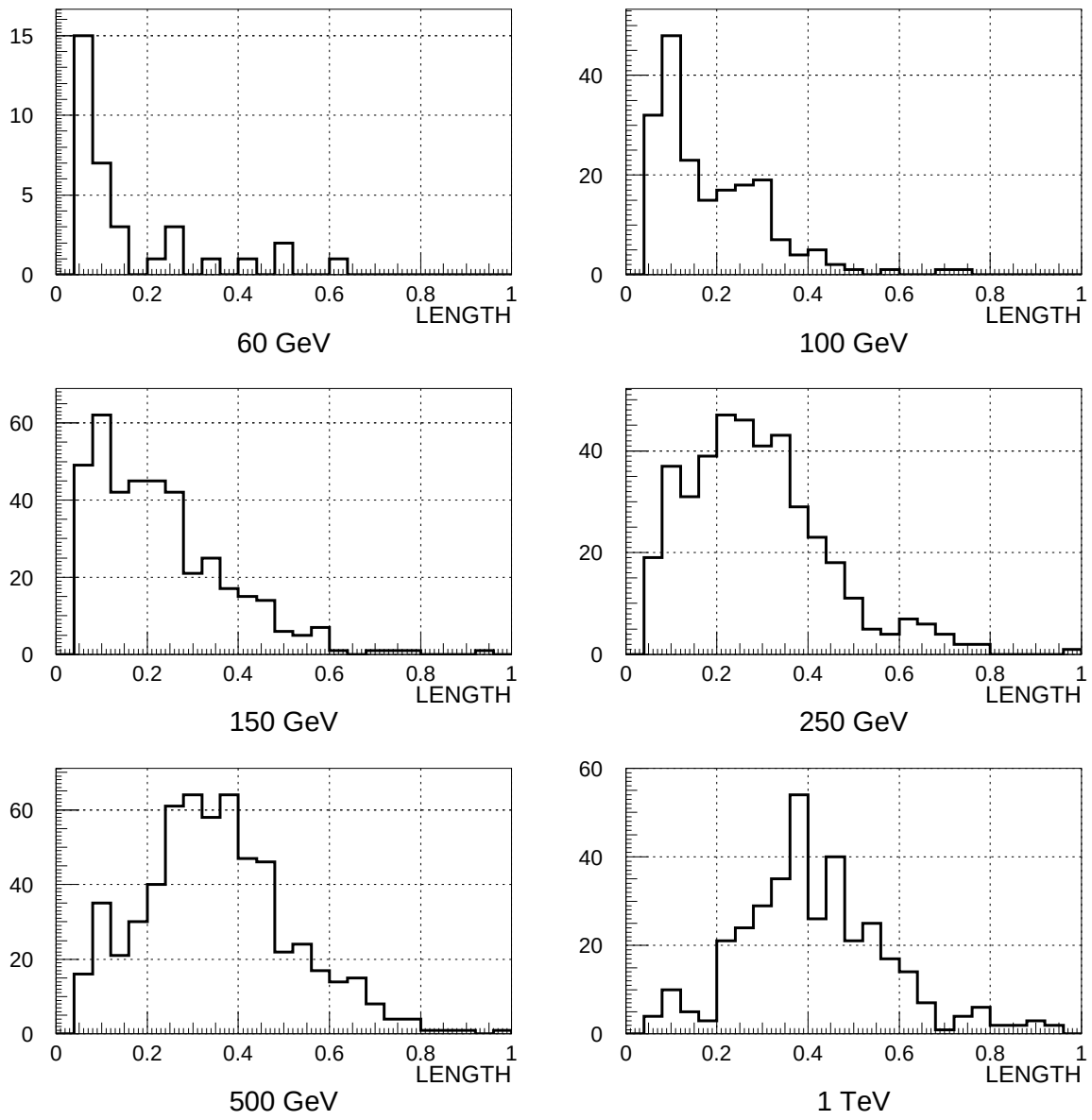

a) The LENGTH distributions for proton images of different energies.

Figure 6.12: Shape distributions for protons.

6.1.5 The angular resolution

We investigated the angular resolution of the MAGIC Telescope above a threshold energy of 10 GeV for the IAPD camera. We used the technique suggested in [5] to find the number of excess events from a source in sky coordinates. For this purpose we used the Monte Carlo events to simulate a γ source at the centre of the camera with the flux normalization and exponent given by Eq. (6.2). Fig. 6.16 shows the angular resolution for the MAGIC Telescope for energies above 10 GeV. It turns

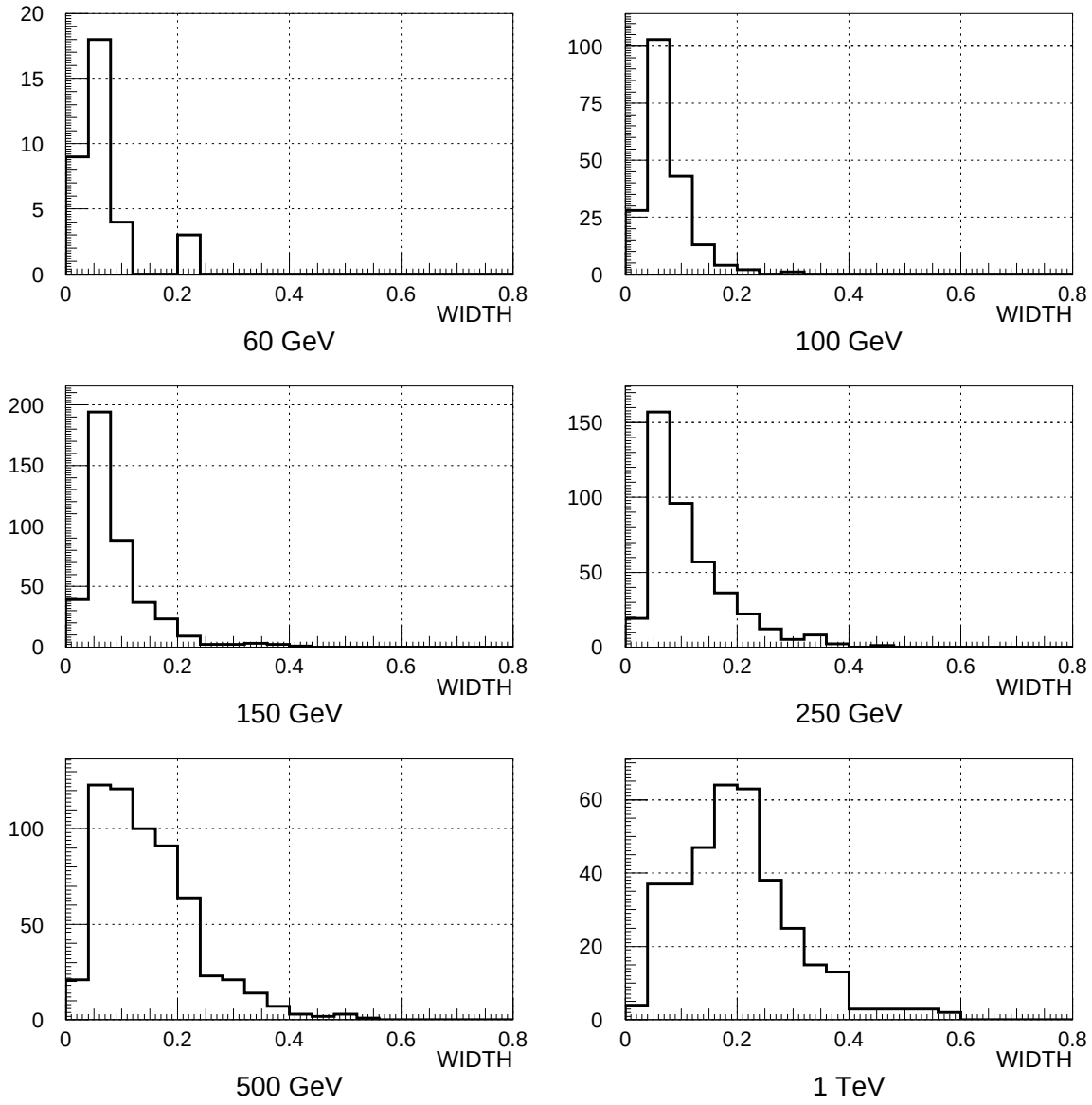

6.12.b) The WIDTH distributions for proton images of different energies.

out to be 0.2° (standard deviation of the 2-dimensional Gaussian). Note, that the angular resolution is energy dependent and will be substantially better (at least 2 times) at higher energies.

6.1.6 The energy resolution

The calculated energy resolution of the MAGIC Telescope is shown in Figure 6.17.

When deriving the energy resolution of a telescope one should note that for a given energy the Čerenkov photon lateral distribution changes only slightly between

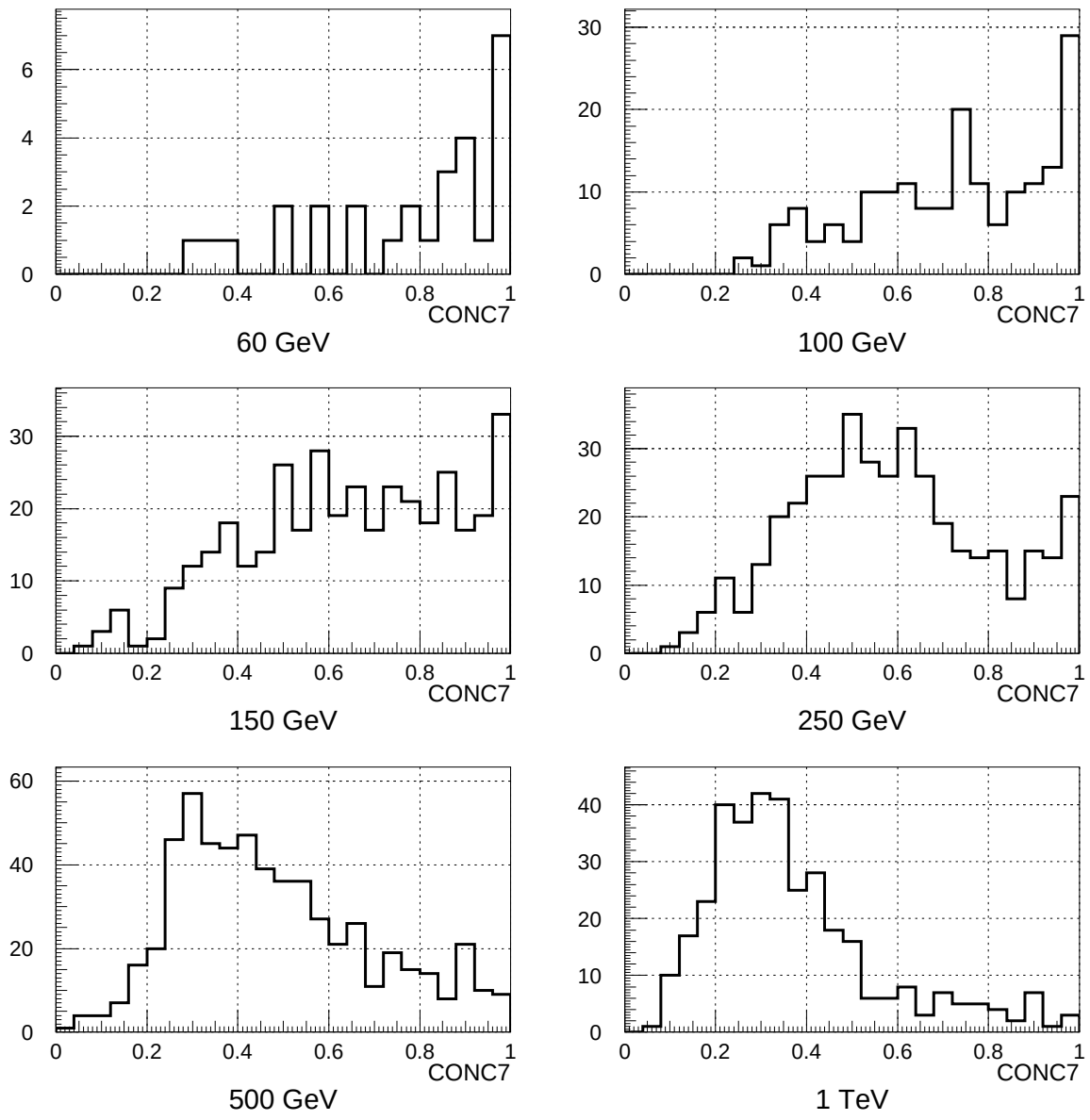

6.12.c) The CONC7 distributions for proton images of different energies.

some minimal radius at 50–60 m from the shower core and the hump at about 125 m (see Fig. 3.2). For an impact parameter range less than 50–60 m the images become progressively more round (which means a low efficiency for discriminating between γs and hadrons) and also the fluctuations of the total measured charge from showers become large. Beyond the hump there is a transition region where the photon density (i.e. the measured charge) rapidly decreases and therefore showers of the same energy show less and less charge. Beyond the transition region the energy resolution is improving, but the total charge is several times less compared to the impact parameter region before the hump. Therefore it is obvious that for the best

Table 6.1: Results of the standard second moment image analysis, including asymmetry, for the standard (IAPD) camera.

MaxDIST interval	ϵ_γ	κ_p	Q
0.4°–0.5°	0.451	130.17	5.14
0.5°–0.9°	0.452	204.46	6.47
0.9°–1.1°	0.446	827.81	12.84
0.5°–1.1°	0.451	290.53	7.69
0.4°–1.1°	0.451	266.59	7.37

Table 6.2: Result of the standard Hillas parameters cuts analysis for the classical (PMT) camera.

MaxDIST interval	ϵ_γ	κ_p	Q
0.4°–0.5°	0.560	324.89	10.10
0.5°–0.9°	0.512	182.35	6.91
0.9°–1.1°	0.470	320.41	8.41
0.5°–1.1°	0.507	225.33	7.61
0.4°–1.1°	0.517	239.18	8.00

energy reconstruction one has to avoid the transition region and select from the "measured" data only those showers which lie within the above-mentioned limits for the impact parameter. For this purpose we have selected showers in the MaxDIST range 0.5°–0.9°. We split this range into two (namely 0.5°–0.7° and 0.7°–0.9°) and have reconstructed their energies. Note that due to the very low energy threshold of the telescope the first bin of MaxDIST contains many more showers than the second one. Afterwards, we combined the resolutions provided by both bins.

In Fig. 6.17 one can see that at the threshold of 10 GeV the MAGIC Telescope will provide an energy resolution of 50%; at 100 GeV it is 23% and for energies above 200 GeV it is better than 15%.

6.1.7 Summary

Our simulations have shown that it is possible to explore successfully the γ-ray energy range above 10 GeV (which was traditionally considered to be the domain of space-borne γ-ray astronomy) with the single 17 m diameter MAGIC Telescope.

It should be mentioned that in all our simulations we used the classical second moment analysis of Hillas. Meanwhile it has been shown, that one can improve

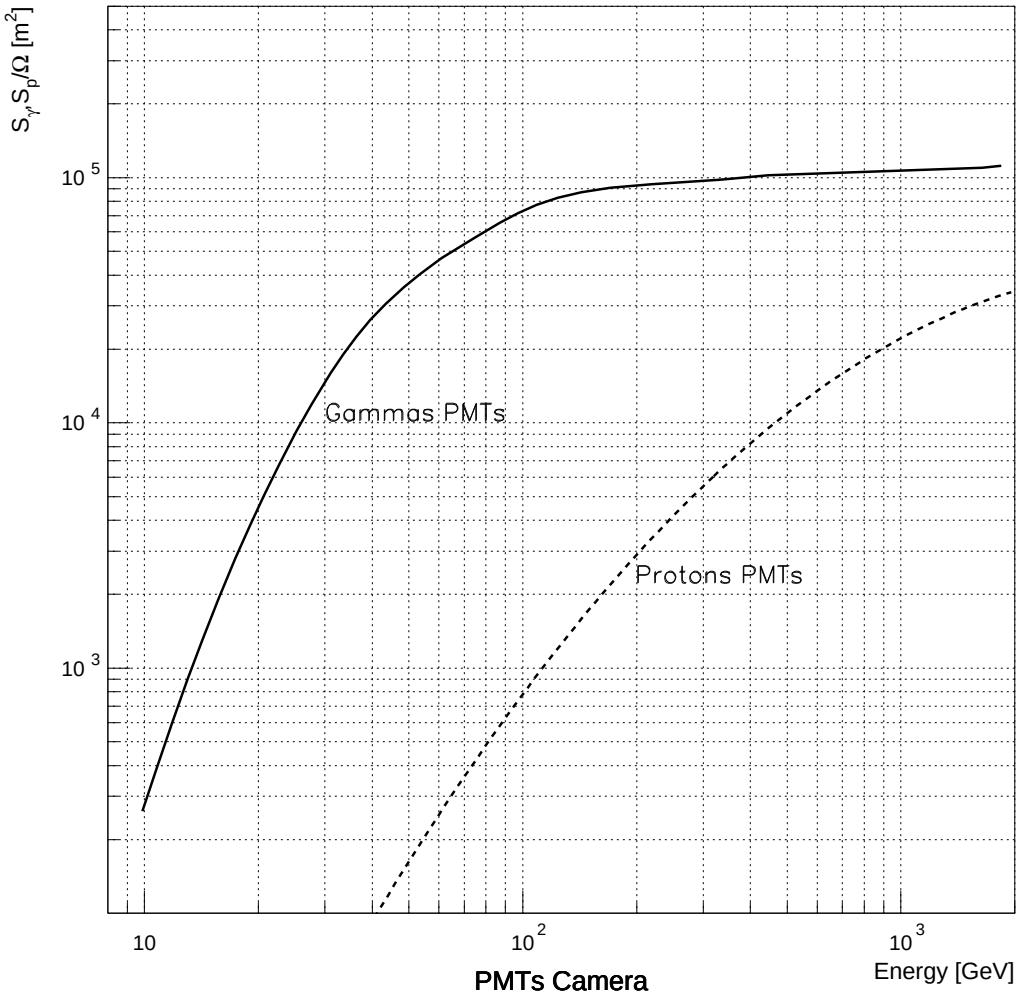

Figure 6.13: Effective collection area after triggering for γs and protons, for the 0.8° trigger radius of the classical PMT camera. The trigger condition "any 4 neighbouring pixels above the threshold of 7 ph.e.s" has been applied.

this analysis [100], especially in the case of fine pixel cameras (pixel size $\sim 0.1°$), where one can see resolve more detailed structures in the images [13]. Also new features, as for example the islands in images, probably can be used for improving the discrimination of hadrons. We believe that there is a lot of scope for improving the analysis of sub-100 GeV showers.

We have shown that even in the conservative approach of using the second moment image analysis one can achieve a very high sensitivity for the MAGIC Telescope

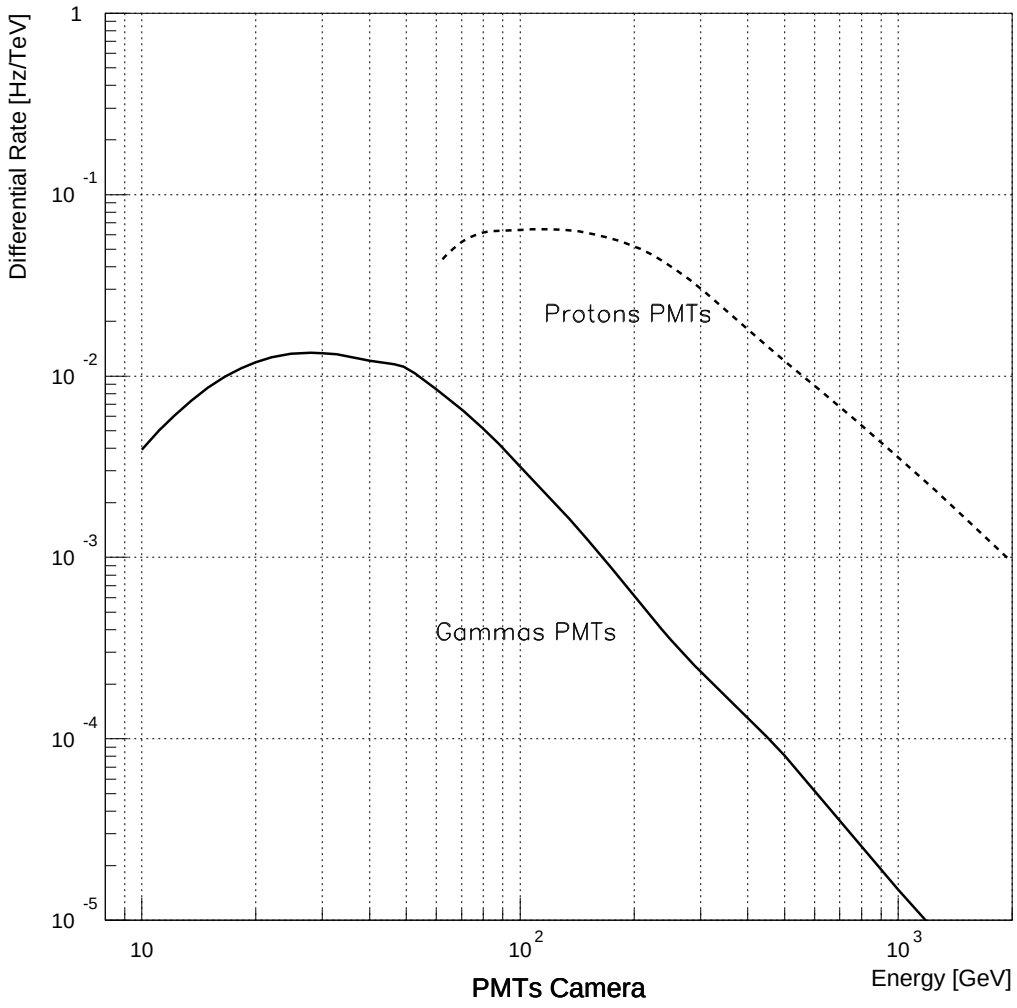

Figure 6.14: Differential trigger rates for γs and protons, for a 0.8° trigger radius of the classical PMT camera. The trigger condition "any 4 neighbouring pixels above the threshold of 7 ph.e.s" has been applied.

both for the IAPD and PMT camera options. The use of the IAPD camera will allow the MAGIC Telescope to measure γ-ray sources above the low energy threshold of 10 GeV. If the back-up solution of applying a classical PMT camera is used, the threshold of the telescope will be 25–30 GeV, though showers with energies as low as 10 GeV will still substantially contribute to the measured rate. Together with its very powerful rejection of hadrons already at the hardware level, in the software analysis of images the MAGIC Telescope will provide a Q factor of about 7, which

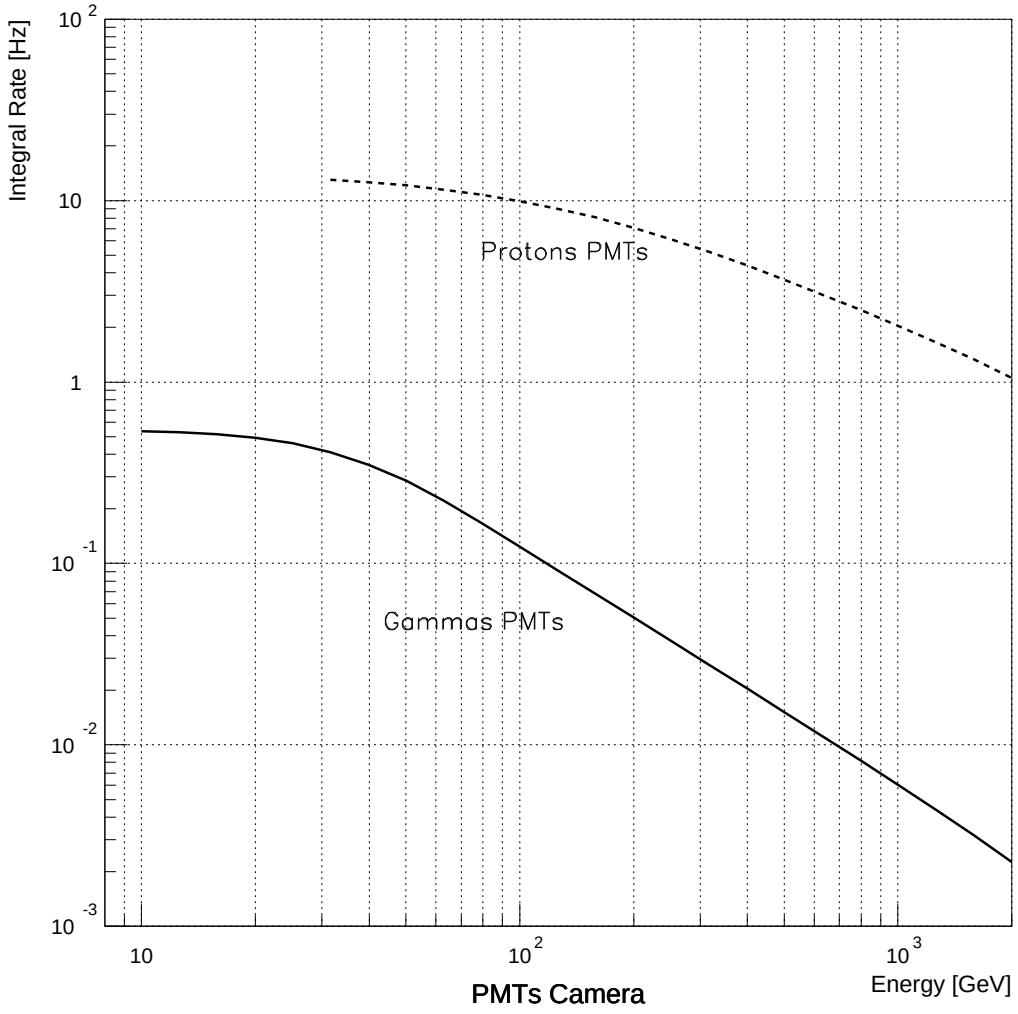

Figure 6.15: Integral trigger rate for γs and protons, for a 0.8° trigger radius of the classical PMT camera. The trigger condition "any 4 neighbouring pixels above the threshold of 7 ph.e.s" has been applied.

corresponds to a hadronic background rejection (including also events triggered by Čerenkov light from single charged particles as, for example, cosmic muons) of about 200 times, achieving a γ acceptance of about 50%. This will provide a very high γ flux sensitivity for the telescope.

It seems that the cosmic electron background will deteriorate to some extent the sensitivity of the MAGIC Telescope. Fortunately, due to the isotropic character of the electron flux, one can achieve a moderate rejection. The electron events which

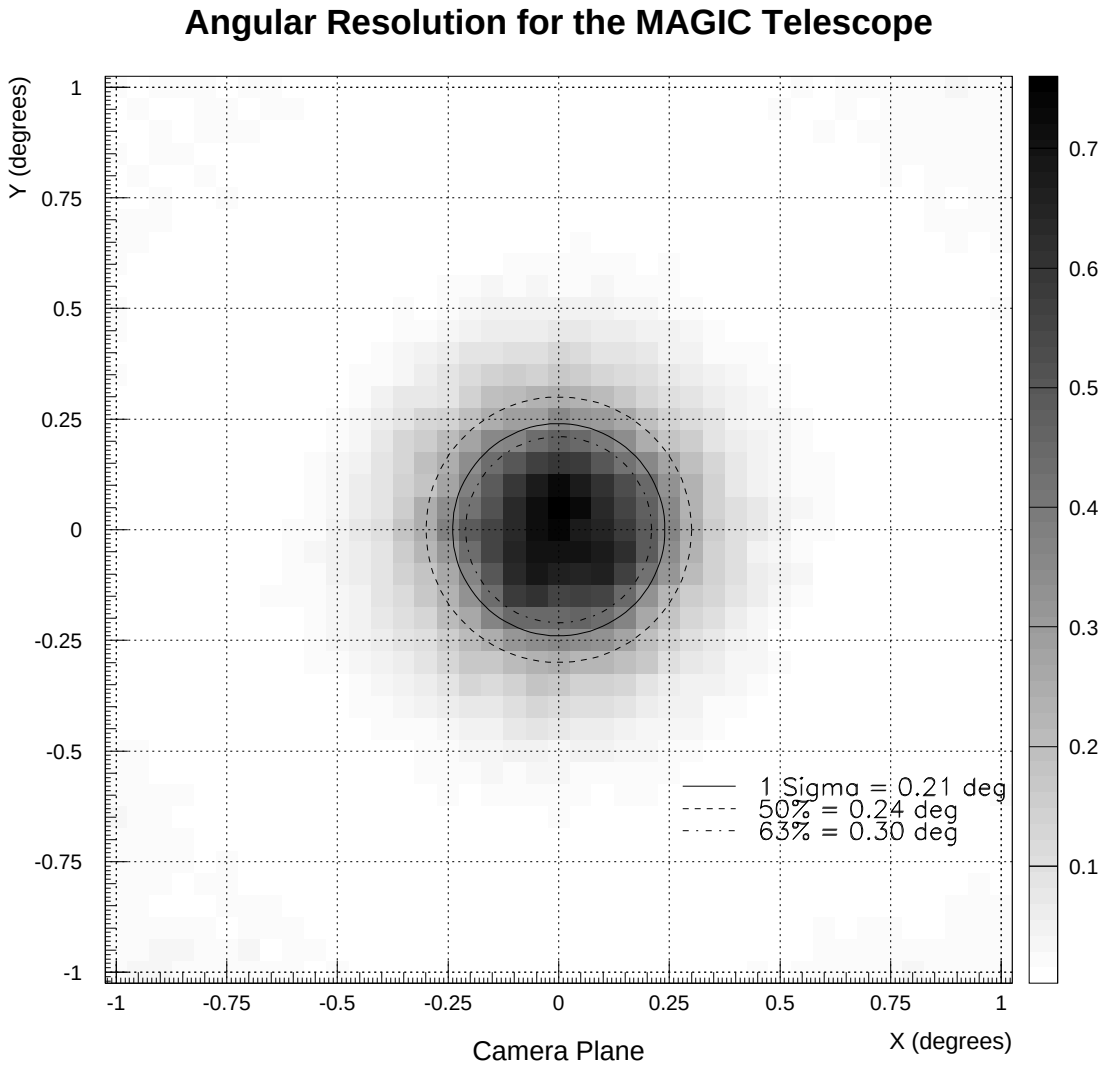

Figure 6.16: Angular resolution of the MAGIC Telescope above the threshold of 10 GeV for a point source of γs with the flux normalization given by Eq. 6.2.

will remain in the γ domain after an imaging analysis including the asymmetry parameter and after ON/OFF subtraction can be considered as a pedestal, the level of which can be carefully studied and taken into consideration. There are on-going activities to simulate the electron background in detail. A detailed discussion on the influence of this background is presented in Section 8.3.2.

The MAGIC Telescope will achieve an energy resolution of better than 50% and an angular resolution of 0.2° close to the threshold. At higher energies, because of the huge amount of charge collected from air showers, it will achieve much better

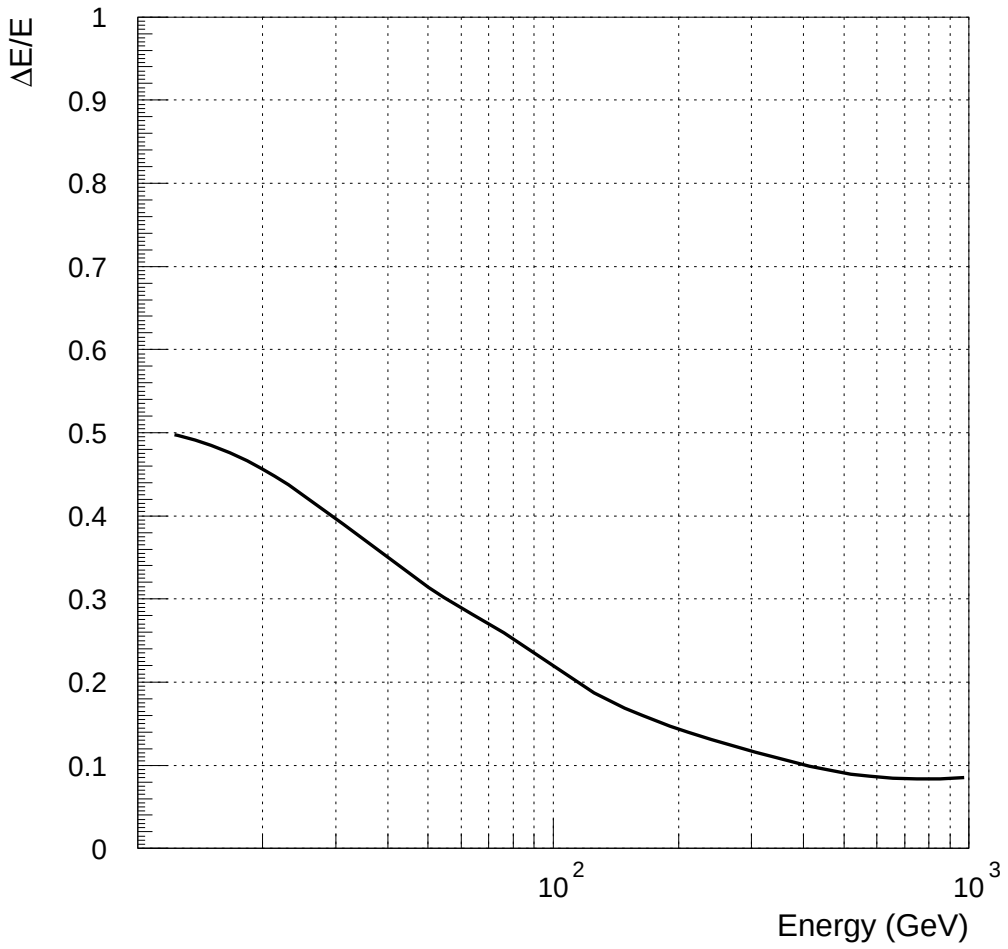

Figure 6.17: The energy resolution of the MAGIC Telescope. The curve shows the 1σ resolution for the energy reconstruction.

resolutions. For example, it will achieve an energy resolution of ca. 22% at 100 GeV and ca. 13% at 250 GeV.

Because the MAGIC Telescope will have a very large collection area for air showers, reaching a plateau level of more than 10^5 m^2, it will yield a very high detection rate for γ showers. In the "satellite" domain of 10–30 GeV it will achieve a rate for γ-rays that is 3–4 orders of magnitude higher compared to that which γ-ray satellites can achieve. This high detection rate will allow us to follow the intensity variations of sources which carry very valueable information about sizes

and acceleration mechanisms.

Chapter 7

Performance

Keywords: The MAGIC Telescope's performance is described by 12 parameters which depend on energy, zenith angle and the impact parameter

The performance of the telescope is described by the following set of parameters

1. trigger threshold energy E_{Trig}
2. 'physics' threshold E_{Phys}, i.e. the threshold where meaningful physics parameters can be extracted. Normally $E_{\mathrm{Phys}} \geq E_{\mathrm{Trig}}$.
3. collection area for γs;
4. collection area for background events;
5. γ filter selectivity;
6. background rejection (might be different for different types of background, $e, p, Fe, \cdots$);
7. energy resolution;
8. angular resolution;
9. time resolution;
10. γ flux sensitivity, limit of source detection;
11. duty cycle;
12. recording rate, respectively dead time of the DAQ.

The performance parameters depend normally on 3 quantities: the energy, the zenith angle and the impact parameter. Also to some extend there is a dependence on the atmospheric transmission and the night sky background (stars near source,

observation of objects in the galactic plane, man-made light background $\cdots$). Due to the large span in energy, zenith angle and impact parameter it is in most cases not possible to quantify the MAGIC Telescope's performance by a set of constants. Averaging over some distribution function (power law spectrum, uniform impact parameter distribution) will sometimes give misleading values. This is different compared to telescopes with a higher threshold and has its origin in the rapid change of air shower parameters in the sub-100 GeV domain. Whenever possible we will try to specify performance parameters either close to the threshold or as a function of the most dependable quality, i.e. mostly as a function of energy.

Also, we would like to mention that most performance data are preliminary and mostly estimated by a semi-analytical approach or MC simulations, while rarely confirmations by tests are available. For simplicity we summarize at first the mean values of the performance data in a table 7.1. MC simulations are ongoing as we have to continuously upgrade with the latest technical data or newly evolving procedures for γ/h separation. A detailed MC study is described in chapter 6.

Parameter	Value	Comments
Trigger threshold (= differential flux peak)	8–10 GeV ($\theta_z < 20°$)	Four-fold coincidence of neighbour pixels with ≥ 7 ph.e.
Physics threshold	15 GeV ($\theta_z < 20°$)	Tailcut ≥ 7 ph.e., light sum ≥ 80 ph.e./image, various filter cuts
Collection area for γ	5000 m^2 ($\theta_z < 20°$) 20000 m^2 90000 m^2 300000 m^2	10 GeV 20 GeV 100 GeV 1 TeV (wide trigger area)
γ selectivity after software cuts	45 - 70%	
hadron rejection $Q(\gamma/$ h rejection) = f(E)	≈ 200 $Q \approx 2. \cdot E^{0.4}$, E in GeV	≥ 10 GeV γ energy estimate for E$\leq$500 GeV
Energy resolution dE/E	$\approx 50\%$ $\approx 20\%$	at 10 GeV at 100 GeV
	$\approx 10\%$	at 1 TeV
Energy resolution as function of energy $\frac{dE}{E} = f(E)$	$\approx \frac{180\%}{E^{0.45}} + 3\%$ (E in GeV)	estimate; impact parameter < 130 m, up to 1 TeV
Angular resolution, single shower	$\Delta_{\theta_{\rm transverse}} \approx 0.05°$ $\Delta_{\theta_{\rm longitudinal}} \approx 0.2°$	200 GeV, scales approx with $\frac{1}{\sqrt{E}} + const$ (rough estimate)
muon rejection	very high	μ-images are part of hadron images
Cosmic electron rejection	≥ 12	for given camera FOV
Sensitivity	$6 \cdot 10^{-11}$cm^{-2} sec^{-1}	source with power law dependence as CR background, 5 sigma , 50 h on source, 20 GeV threshold
Precision of point source location	$\leq 0.02°$	large statistics sample
Separation limit for 2 close point sources	$0.2°$	equal strength sources (E$\geq$10 GeV)
Trigger threshold in presence of moonlight	≈ 30 GeV ($\theta_z < 20°$)	moon 66%, source $> 30°$ away from moon
Physics threshold in presence of moonlight	≈ 45 GeV ($\theta_z < 20°$)	
Trigger threshold classical MAGIC	about 30 GeV ($\theta_z < 20°$)	classical PMTs
Physics threshold classical MAGIC	≈ 35 GeV ($\theta_z < 20°$)	≥ 80 ph.e./image
Sensitivity classical MAGIC	$8 \cdot 10^{-11}$ cm^{-2}sec^{-1}	5 σ, 50 h on source, 35 GeV threshold

Table 7.1: The main parameters characterizing the performance of the MAGIC Telescope.

Chapter 8

Specific problems

8.1 The night-sky background

Keywords: We estimate the influence of the night sky background light on the data acquisition performance and data quality from the experience with the HEGRA Čerenkov telescopes.

8.1.1 Expected night-sky background sensitivity

The night-sky background (NSB), i.e. the average light due to stars and air fluorescence to which the camera is exposed, is known from the HEGRA group's experience with more than 5 years of measurements with Čerenkov telescopes. Its intensity has been measured in La palma by by R. Mirzoyan and E. Lorenz [70].

From our experience with the analysis of HEGRA CT data we know that for the determination of image parameters the presence of a star brighter than 6^m is noticeable and the presence of a star brighter than ca. 3^m is not tolerable without taking special analytical measures to remove its influence. This is valid for a CT of 8.5 m^2 mirror area and photomultipliers of 10% <QE> in the main spectral range of the NSB. For the MAGIC Telescope, we have to consider two cases:

(a) The classical camera design with EMI bialkali PMTs which are measured to have ca. 11% <QE> in the NSB spectral range.

(b) The standard camera design with HPMTs of about 44% <QE> in the NSB spectral range.

To compare the HEGRA CTs and the two versions of the MAGIC Telescope we introduce the equivalent area A_e [m^2 ph.e./ph.], which is the product of the quantum

efficiency (in photoelectrons per photon, ph.e./ph.) times the mirror area. With the parameter values stated above we obtain the following values:

1. HEGRA CT2: $A_e = 0.68$ m^2 ph.e./ph.
2. classical MAGIC T: $A_e = 25.3$ m^2 ph.e./ph.
   (a factor of 37.2 more than the HEGRA CT2)
3. standard MAGIC T: $A_e = 101.2$ m^2 ph.e./ph.
   (a factor of 150 more than the HEGRA CT2)

The intensity S of the radiation from a star at 550 nm is related to its visual magnitude m by

$$\log S = (-0.4 \cdot m - 22.42) \text{ W m}^{-2}\text{s}^{-1} .$$

The ratio of two intensities, S_1/S_2, corresponds to the difference in the magnitudes, i.e.

$$m_1 - m_2 = 2.5 \cdot \log(S_1/S_2) .$$

The minimum magnitude of stars that will be noticeable in the field of view and the minimum magnitude of stars that are actually distorting the images ("bright stars") are therefore scaled in the following way:

	Noise from a 2^m star as worst case [ph.e]	Minimum m of a noticeable star (expected noise) [ph.e]	Minimum m of a bright star (expected noise) [ph.e]
HEGRA CT2	16	6^m (4 ph.e.)	3^m (10 ph.e.)
MAGIC classical	98	10^m (24 ph.e.)	7^m (61 ph.e.)
MAGIC standard	196	11.4^m (49 ph.e.)	8.4^m (122 ph.e.)

The noise values are given on the assumption that the total starlight is hitting one pixel. For a star 1° off the center of the camera only ca. 50% of its light hits one pixel because of optical aberrations. Thus the noise would go down by a factor of $\sqrt{2}$ per pixel.

From the non-star NSB we expect the following noise values:

	Pixel acceptance	Typical noise
HEGRA CT2 (measured)	$2\pi(1 - \cos(0.215°)) = 4.424 \cdot 10^{-5}$	2 ph.e/30 ns
MAGIC T classical	$2\pi(1 - \cos(0.068°/2)) = 1.106 \cdot 10^{-6}$	$\sqrt{2.5 \cdot 10^{-2} \cdot 1.482}$ = 1.9 ph.e./8 ns
MAGIC T standard	$2\pi(1 - \cos(0.068°/2)) = 1.106 \cdot 10^{-6}$	$\sqrt{2.5 \cdot 10^{-2} \cdot 600}$ = 3.9 ph.e./8 ns

8.1.2 Problems arising from the NSB

Keywords: The NSB will cause accidental triggers but also distort γ-images close to the threshold.

In order to get more precise values of the background noise in the "red" region we intend to measure the night sky background in the region of interest using one of the Intevac tubes, which will be installed in the focal plane of one of the HEGRA telescopes. Its ability to detect and distinguish single electrons (see Chapter 4.3.1) will allow us to measure the NSB with high precision. The unwelcome light from the NSB causes three kinds of problems:

(a) Due to its statistical fluctuation, the NSB can accidentally cause a light distribution in the camera which fulfills the trigger condition. Such an accidental event can probably be easily removed off-line by an analysis of its shape. BUT it causes an additional increase in the data rate which the DAQ system has to handle, and can therefore cause additional dead time.

(b) In the same way as in (a), the noise level of the NSB on the scale of a "bright" star would effectively set a small number of pixels (1-7) above the trigger threshold of a simple multiplicity trigger. This effectively decreases the energy threshold of the CT in an uncontrolled way and makes it more difficult to compare the observation with others that are made under different NSB conditions.

(c) For near-threshold shower images which happen to be in a part of the camera which contains a *bright* star, the fraction of total light in the image which stems from the star can be as much as 50%. It thus interferes considerably with the reconstruction of the primary energy and the shape of the shower.

8.1.3 Solutions

In any $1^\circ \times 1^\circ$ field on the sky there is an 8^m star to be found. Therefore on average there will be 3-4 "bright" stars in the FOV if the standard camera is chosen, and approximately 2 "bright" stars for the classical camera. The problems described in Section 2 are therefore the *normal case*, not extreme exceptions which can be avoided by choosing a different field of view.

(a) *Accidental triggers*
(i) Diffuse NSB
The estimations show that the diffuse NSB will not be a technical problem even if only a simple multiplicity trigger is chosen with a threshold of ca. 3 ph.e (5 ph.e) for the classical (standard) camera. The single pixel rate will be

comparable to HEGRA CT2, i.e. in the order of 10-100 kHz.
(ii) Accidental triggers caused by stars, see (b)

(b) *Bright-star trigger bias*
In order to keep observations of different objects (with different star fields in the background) comparable to each other, i.e. keep a constant energy threshold, bright stars have to be removed from the trigger. This might happen at the off-line analysis level or at the on-line trigger level.

In any case the light distribution of the star field has to be known at the time of the on-line or off-line trigger decision to an accuracy of at least 10%. For this measurement one needs to take at least 50 random trigger signals equivalent to about 0.5 s data taking time. As a safe solution we assume 500 random triggers with 5 s processing time. Alternatively, one might record permanently pedestal events with a rate of 1-3 Hz or measure the cathode currents.

In an off-line analysis, the pedestal and noise distribution can in principle be derived from the actual data by an iterative approach using some average pedestal and noise values as a first assumption and then redetermining the pedestal/noise values from the parts of FOV which are not found to belong to the shower image but requires that the entire camera information is recorded for each trigger.

Such a method has to be studied using MC data.

If this proves to be feasible, pedestal runs could probably be avoided.

From the authors' own experience of using an algorithm with self-updating pedestals (Microvertex at OPAL/LEP), it seems to be very probable that such an algorithm can even be derived for an on-line pedestal updating and noise subtraction. But the performance of the algorithm relies on the fact that the mean light distribution remains constant over periods of time which are large compared to the inverse trigger frequency (e.g. larger by a factor of $\geq 5000 \approx 2$ minutes at 50 Hz data rate, ≈ 8 minutes at 10 Hz data rate). If the distribution changes on time scales smaller than this, the pedestal and noise values cannot be updated fast enough and have decreased accuracy.

Here the so-called field rotation of the camera with respect to the sky comes in: For an alt-azimuth-mount CT like the MAGIC Telescope, the FOV is rotating with varying speed against the sky as it follows a given object. For a given object the rotation speed is only dependent on the azimuth and reaches its maximum when the CT looks towards the meridian, i.e. when the object culminates. The closer to the zenith the object is when it culminates the greater will be its maximum speed. An object that culminates very close to the zenith has an arbitrarily large field rotation speed at this point.

Optical telescopes with alt.-azimuth mounts therefore have a small blind spot around the zenith less than 1° in diameter. The total rotation angle from rise

to set is always $< 180°$. For objects close to the zenith, the rotating star field in the camera would cause the noise conditions to vary rapidly over a period of time between 30 and 5 minutes. This means that at least an algorithm for an off-line noise determination would invariably fail unless very large data rates (> 1 kHz) are available at the analysis stage.

One might therefore consider copying the camera rotation mechanisms which are commonly used for optical telescopes: With an additional computer-controlled motor, which is equivalent to a third steering axis of the telescope, the camera is permanently rotated in such a way that it stands still with respect to the sky coordinate system.

In this way the mean noise conditions for each pixel would be kept approximately constant for the whole duration of the observation and no interruptions of the measurement process would be necessary since pedestals and noise can be well determined from the data.

There is no doubt about the feasibility of the rotation mechanism, but its cost has still to be calculated.

(c) *Image distortion and energy measurement errors due to bright stars.*
Means to solve these problems still have to be investigated. With an accurate knowledge of the NSB light distribution a correction of the energy measurement on average should be possible.

With "dynamical tail cuts", image distortion can be reduced.

Another solution to overcome the large noise fluctuations induced by stars is to introduce weights in the data analysis. These weights are inversely proportional to the noise. The excess noise factor of the light sensor needs to be included in the weight calculation. A promising alternative approach to determine the noise is to constantly measure the photo cathode currents and to deduce the noise from the square root of I_i, the currents in the individual pixels[1].

8.2 Impact of the environment on the telescope

Keywords: The telescope has no dome. Protection against environmental hazards have to be built in.

The telescope cannot be shielded from environmental influences. Because of the cost, a protecting dome would not be possible and thus a protection has to be built

[1]This method will soon be tested with data recorded with the HEGRA CT1 telescope during observation periods in the presence of moon light.

into the telescope itself. The environmental impact can be basically divided into two classes:

(a) almost permanent interaction with the environment but causing only slow changes to the telescope;

(b) rare, but extreme, events that can be very destructive.

Examples for class (a) are: dust on the mirrors, polluting gases that attack the mirrors, UV radiation during daily exposure to the sun causing damage to plastic materials, day-and-night and seasonal temperature fluctuations and high humidity.

Examples for class (b) are storms, hail, formation of ice during high humidity, subzero temperatures, lightning, accidental positioning of the telescope in the direction of the sun, vandalism and damage caused by animals.

8.2.1 Damage to the mirror surface by dust

Keywords: Dust attaches to the mirror surface by Van der Waals forces.

Dust will constantly settle onto the mirror surface, degrading its reflectivity. The predominant adhesion force are Van der Waals forces. Besides surface destruction by abrasion, chemical interaction with the aluminium can occur.

The normal method of protection is to coat the mirror with some transparent high resistance material such as Al_2O_3 and to remove the dust from time to time using a water-jet or cleaning laser. In the long run it might be necessary to remachine the surfaces or simply exchange mirror panels.

8.2.1.1 Dust removal from the mirrors

Keywords: Dust will reduce the mirror reflectivity. Dust has to be removed from time to time.

From time to time the dust has to be removed. While occasionally rain will do this, one has nevertheless to foresee methods to remove dust in prolonged periods of dryness, which could happen at all sites under discussion. The following methods, common in mirror cleansing, could be used:

(a) washing and wiping,

(a') high pressure water-jet spraying,

(b) spraying with a special plastic-layer that binds dust and will be peeled off afterwards,

(c) spraying with carbon dioxide snow flakes,

(d) use of a high power cleaning laser.

Classical mirror washing and wiping is impractical due to the abrasive nature of dust at most sites and the difficulty of accessing the mirror from the ground. Equally difficult, due to access problems, is the peel-off of a plastic binding layer. The use of carbon snow flakes is now under consideration for large astronomical mirrors, but it is not yet obvious whether it will work on high heat conductivity materials such as the aluminium mirrors.

For the MTD96 design we have chosen the water-jet cleansing for which inexpensive units are available. If a site is chosen where it is difficult to transport the necessary amount of water (ca. 1 -2 cbm for one cleaning process), for example at the Gamsberg in Namibia, we will try to use a cleaning laser. Some commercial versions based on pulsed Nd-YAG lasers are now available. The laser would be installed next to the camera and its beam guided by telecommand across the entire mirror surface. Cleaning would take a few hours ($\sim 10^7$ laser shots). The total investment would be around 70 - 90 kDM.

We are studying to protect the mirror during unused times by pulling a tarpaulin across the dish along cables strung over the rim. Such a protection makes only sense if it can be made sufficiently tight and would survive strong winds. On the other hand such a protection is also useful to prevent damage during accidental exposure of the telescope to the sun. On the other hand such a protection is also useful to prevent damage during accidental exposure of the telescope to the sun.

8.2.2 Air pollution that can attack the mirror surface

Chemical alteration of the mirror surface due to air pollution is considered to be negligible, particularly in the remote areas that have been proposed for the installation. The most severe attack might come from acid (or basic) rain freezing onto the mirrors over a long period of time. This hazard needs to be investigated further.

8.2.3 UV damage to plastic material

The telescope will be installed on a high mountain in an area of low cloud coverage, i.e. strong UV exposure is expected during day-time. UV-light is very damaging to plastics such as cable insulations, epoxy resin (compound of the carbon fiber rods), paint binders, etc. Therefore all carbon fiber tubes will be sealed by a special UV-protection coating; the signal cables will be mostly housed in flexible metal tubes, and where this is not possible UV-resistant materials, such as polyurethane or teflon have to be used.

8.2.4 Temperature fluctuations

The telescope will be exposed to frequent temperature changes (day-night, summer-winter). The most critical component exposed to temperature changes is the large mirror dish. By using carbon fiber tubes as the basic construction material, it will be possible to keep stresses due to temperature changes to a minimum because carbon fibers have a very low expansion coefficient (nearly zero along the fiber). The specifications for the design are that the material should be able to withstand temperature changes between $-20°$C to $+80°$C.

The photosensors and preamplifiers are subject to wide temperature changes. Leakage currents (photocathode noise) double for each 8° rise in temperature. Fortunately the telescope will only be run during night-time when the temperature at more than 2000 m a.s.l. should never exceed 20°C. Nevertheless, it might be necessary to stabilize the temperature of some components but this poses no major problem with present-day refrigeration technology (see also Chapter 4.3 for details).

8.2.5 High humidity and rain

At nearly at all the proposed sites, the telescope will occasionally be exposed to rain, fog or snow. During these times the telescope should not be operated. Occasional rain is even helpful for "washing" the mirrors. For a predicted lifetime of 10 - 20 years, protecting the steel section of the mount from rust should not pose any problems. Special attention has to be paid to the carbon fiber-aluminium joints where in the presence of humidity and traces of acids electrochemical reactions (batteries) and accelerated corrosion might take place.

8.2.6 Impact of storms

Storms could cause devastating damage to a telescope that has not been adequately designed. This problem has been studied extensively and the results are summarized in Chapter 4.1.8. A special kind of storm damage is expected in sand desert locations. Strong winds carrying sand can damage the mirror surface like a sand blasting tool. Dust can have a similar but weaker impact. Placing the mirror dish ca. 10 m above ground helps to some extent but sandy locations should be avoided. If this is not possible, the "diamond" coating of the mirrors would give perfect protection.

8.2.7 Hail

The aluminium mirrors are much more resistant to hail than are glass mirrors. Tests show that simulated hailstones of 1 cm $\oslash$ do not cause any damage. It is further

assumed that during a hailstorm the telescope dish would be inclined to at ca. -10° elevation, i.e. only the back side would be hit.

8.2.8 Icing

Occasional strong icing is to be expected in mountains. Fig. 8.1 shows an example of the HEGRA CT2 telescope under a rare ice coverage. The design criteria for the

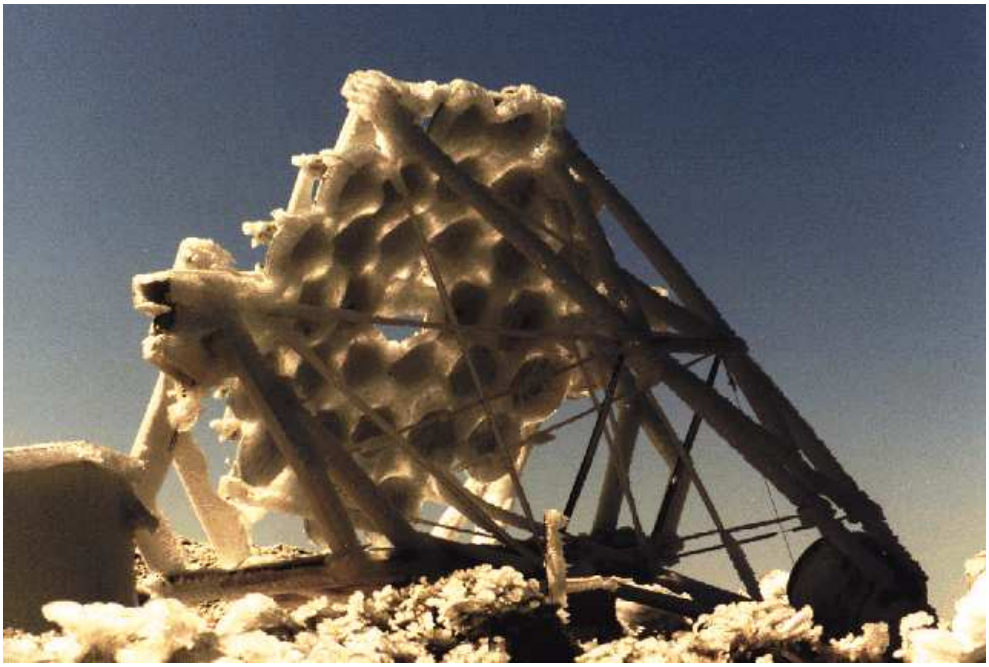

Figure 8.1: The HEGRA CT2 telescope under a few centimeter of ice.

mechanics assume that ice layers of up to 3 cm thickness would not damage the telescope. The built-in heating system should prevent ice formation on the mirrors. For emergency de-icing of the frame we have discussed the following solutions:

(a) spraying the telescope with a de-icing liquid such as a glycol mixture, similar to that used for de-icing airplanes;

(b) infrared de-icing.

A de-icing liquid dispenser such as is used for airplanes, would be a viable and straightforward solution but it might have negative ecological effects on sensitive environments such as mountain areas. It might be necessary to build a watertight foundation which permits the liquid to be recollected. A much more elegant but still experimental solution would be to irradiate the telescope with infrared emitted from several liquefied-gas burners. This new technique for aeroplanes uses burners whose infrared emission is selectively matched to the absorption maximum of ice.

8.2.9 Protection against lightning

Although the telescope will be installed very likely in an area where lightning is infrequent, nevertheless protection against lightning must be taken into account, either by a single nearby mast of about 35 m or 3 masts placed in a triangle around the telescope forming a kind of Faraday cage. These possibilities are still being investigated. The use of optical fibres for signal transfer would ease very much the necessity to protect delicate electronics against induced currents from distant lightning.

8.2.10 Accidental positioning of the mirror towards the sun

Special precautions have to be taken in order to minimize the risk that the telescope may be accidentally pointed towards the sun. Because a large amount of energy is collected, the equivalent of nearly 300 kW, the camera and mount could be severely damaged, even during short exposure. Accidents like this might be caused by tracking program errors or prolonged power failures during the night that preventing the telescope from being driven back to its safe position. (According to Murphy's law such an event is bound to happen sometime). The very high prize of the camera ($>$ 1 MDM) calls for special precautions.

As a passive form of protection the camera cover will be equipped with white ceramic foam tiles that give sufficient protection for 20 min. Secondly, we plan to install emergency power supplies that will be able to bridge prolonged power failures. Thirdly, in case of a mechanical failure that prevents the telescope from being moved, a tarpaulin could be pulled over the mirror. 5 mm steel cables will be strung every 2 m across the telescope at the height of the ring. The tarpaulin could be pulled along these cables and across the dish. The tarpaulin would normally be stored on the rim of the dish. The active mirror control is used in addition to defocus the mirror.

8.2.11 Protection against vandalism and animal interaction

The large telescope will attract many visitors and vandalism cannot be ruled out. Proper fencing will be needed. The aluminium mirrors will be highly resistant towards thrown stones or bullets, i.e. any damage that occurs would only be local.

The risk of damage by animals cannot be ruled out, e.g. rodents attacking cables and bird droppings on the mirror surface. This will be a nuisance but no major damage is expected.

8.3 Muon and electron backgrounds

8.3.1 The Muon Background

Keywords: Muons originate from hadron showers. The MAGIC Telescope is sensitive to these showers and will be able to effectively reject muons.

Muons can trigger the telescope. We have to distinguish two cases:

(a) They will pass the 1st and 2nd level trigger and clog the readout system and therefore reduce the sensitivity.

(b) After being recorded they might pass γ-selection criteria and add to the background, thus reducing the expected sensitivity of the telescope. The key question is whether they can fake a point source excess signal.

Assuming that simple hardware trigger logic under consideration will not be able to reject specifically muons it is necessary to consider a readout system that can handle the expected rates with low dead time. For the rate estimate one can start with the known muon flux. Fig. 8.2 displays a compilation from Allkofer and Grieder together with a power law approximation for the flux above ca. 15 GeV. The power law can be simplified by neglecting small zenith angle dependencies and second order correction terms to:

$$dN_\mu/dE_\mu = 0.14 \cdot E^{-2.7} \text{ cm}^{-2}\text{s}^{-1}\text{sterad}^{-1} \text{ GeV} \tag{8.1}$$

At 10 GeV Eq. 8.1 overestimates the flux by a factor of 2 while around 25 GeV the difference to actual measurements is less than 20%.

Before estimating the muon background rate we would like to outline the problems of muon detection. Because of the Čerenkov angle there is a fixed correlation between the mirror diameter and the muon track length seen by the telescope. For example at about 2200 m altitude the MAGIC Telescope's mirror would see a nearby (e.g. within 20 m of the telescope axis) muon over a track length of 1300 m ($\beta = 1$). The photon yield between 300 and 600 nm is 30 photons m^{-1} at $\approx$ 2200 m a.s.l. A muon hitting exactly on the axis (e.g. path length 650 m) would produce 19500 photons, e.g. about 6800 ph.e.s. Such a muon would produce a ring, while muons further away (the number increases with the square of the distance) will produce arcs which at larger impact parameters will coalesce to light blobs. For any telescope with increased photosensitivity (single dish, multiple dish, solar array) the impact parameter range for detecting light from muons will increase. As a consequence even two-fold coincidence observations will only remove part of the muon background. Another consequence of the increased sensitivity is that the track section seen from muons of larger impact distance originates higher up in the atmosphere. This in turn results in a smaller Čerenkov angle, lower light yield (partly

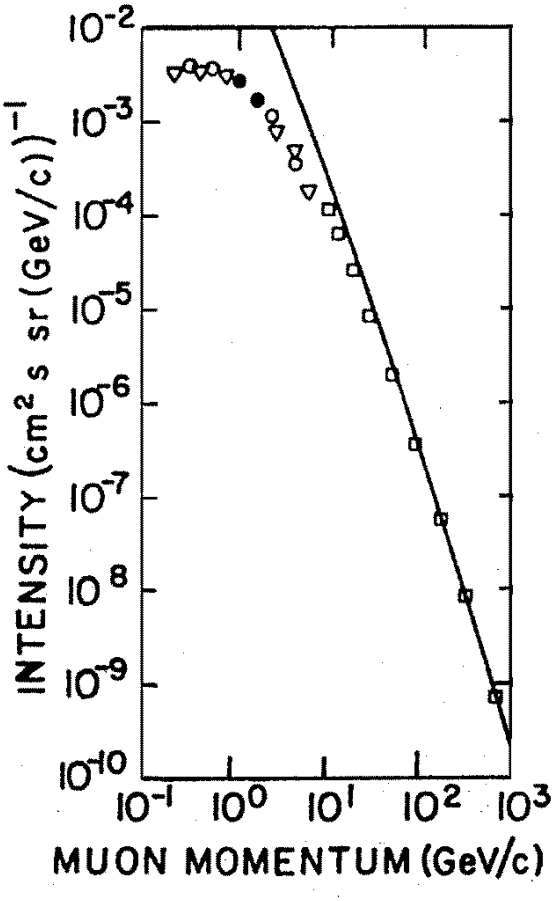

Figure 8.2: Muon flux at sea level (taken from [6]).

compensated by the increase of the "visible" track length) and a higher Čerenkov threshold. The detection area for muons will slowly increase with the altitude above the telescope. On the other hand the increase in threshold will help to reduce the muon rate because of the steeply falling flux as a function of energy.

In order to understand the muon trigger problem in detail we are performing extensive MC simulations. An estimate shows that at 2200 m the effective Č-threshold for muons is about 7 GeV and full photon production (90% of that of $\beta = 1$) is reached at around 11 GeV. Integrating Eq. 8.1 from 10 GeV to infinity, a maximum detection distance of 75 m and a maximum trigger angle of 1.4° off axis (0.75°, the camera trigger half angle area added in quadrature to the Čerenkov emission angle of 1.2°) and a signal level of $\geq$ 100 ph.e.s yields a muon rate of 225 Hz with about 50% uncertainty. There are some general statements to be added.

(a) Moving the telescope to higher a altitude will reduce the trigger rate due to the higher muon threshold and smaller Č-angle.

(b) For increased sensitivity one will collect more and more muons with larger

impact parameters, e.g. the majority of the muon images will just generate a small blob of light. Depending on the aberration of the mirror, the light will be concentrated onto very few pixels, e.g. the "concentration" will be very high and this will allow these muons to be tagged and rejected. This is the domain where a neuronal network trigger could be efficient.

(c) As a by-product of the muon rate one will be able to calibrate the telescope with high statistics.

There is an independent way of estimating the upper limit for the muon rate. Muons are not primary cosmic rays but only secondary products of hadron interactions. Kinematically, the muon momentum on average rarely exceeds 1/10 of the incident proton momentum. Making a worst case assumption that every incident cosmic proton above 100 GeV will produce one muon[2] one can estimate the total muon flux by integrating the cosmic proton flux above 100 GeV for a trigger solid angle of ca. 10^{-3} sterad and 40 000 m^2 detection area.

The resulting *worst case rate* is

$$N \approx 300 \text{ Hz} (\text{with a rather large uncertainty})$$

(d) As a result of unequaled Čerenkov light detection limit of 1 photon m^{-2} (at the mirror level) the MAGIC Telescope will detect $\beta = 1$ muons up to an altitude of ca. 14 km, i.e. well up to the height of the parent shower. As a consequence a large fraction of the muon images will be accompanied by a diffuse hadron shower image. **Therefore counting the muon rate and hadron rate separately is no longer allowed for the total trigger rate estimate.** In fact, the Monte Carlo simulations show that the proton rate (which already includes the rate due to the muons) is only $\sim$ 80 Hz (see section 6.1.3 for details). Fig. 8.3 shows the simulated Čerenkov photon density of **a single muon** as a function of the muon impact point from the telescope. The muon is injected into the US-standard atmosphere at 15 km a.s.l. and observed at 2200 m a.s.l. The density of Čerenkov photons is "measured" on a 1 x 1 m^2 surface area. For simplicity the atmospheric processes, as well as multiple scattering are not included in the simulation. The arrows show the photon sensitivity of a few telescopes and let to estimate their sensitivity to distant muons. Compare also the Čerenkov photon densities for low energy γs and hadron showers as shown in Fig. 3.2. In the case of muons the MAGIC Telescope is fully sensitive up to the "hump" distance of 120 m.

Fig. 6.3 shows examples of hadronic showers where the clumps and arcs of some single particles can be identified. In the extreme case of a close-by muon the MAGIC Telescope would register an intense arc *in addition* to the

[2]More than one muon in the telescope's field of view would make no difference in the rate estimate but rejection of these events would be very high due to two separate light blobs.

underlying hadronic event. Fig. 8.3 illustrates the intensity and fluctuations of the pictures of close-by muons and the sensitivity of the MAGIC Telescope to far away muons.

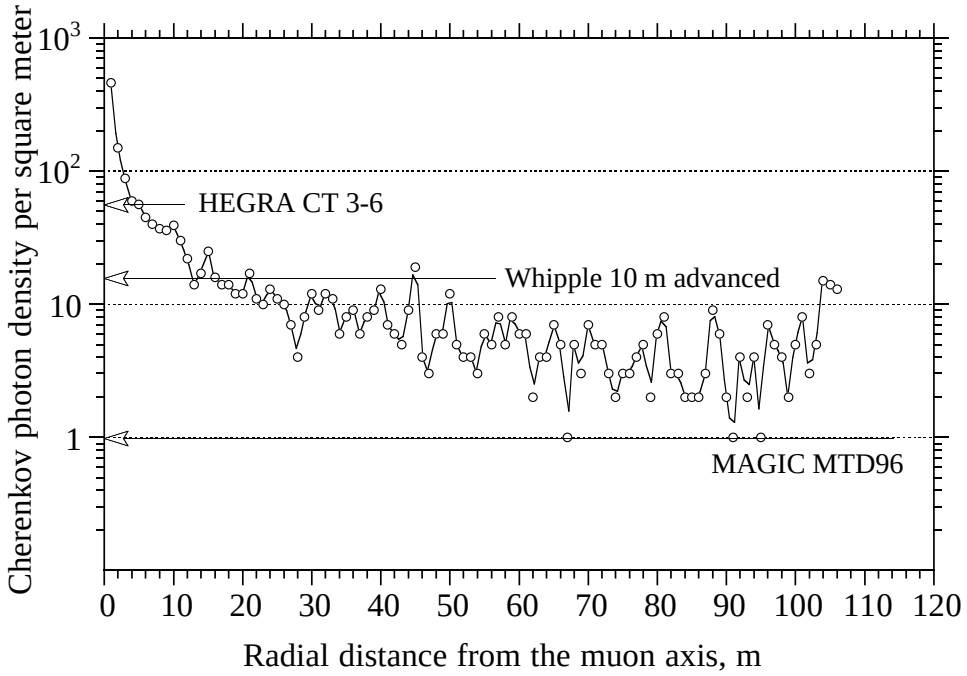

Figure 8.3: Simulated Čerenkov photon density of a 20 GeV muon, injected at 15 km height into the 'US standard atmosphere', as a function of the muon impact parameter.

In a "classical" 10 m ø telescope with ca. 15 times less collected photoelectrons, close to the threshold only the muon arcs would be visible and the light from the remaining shower would hardly be above the noise threshold. **We would like to point out that the MAGIC Telescope will be the only telescope sensitive enough to detect hadron showers down to an energy limit above which the detectable muons are produced.**

This feature might be used to turn the so-called muon problem into an advantage for γ/h separation. Images from hadron showers containing muons (or pions/kaons, the parents of the muons) would contain localized blobs of high light density. Thus by searching for spiky pictures one can reject hadron events. Compared to the classical 10-m telescopes, the MAGIC Telescope will have an overall ph.e.-density that is 15 times higher, resulting in an image that is more structured by a factor of nearly 4. It is important not to wash out this spiky structure by using badly designed optics or coarse pixel sizes. Reducing the presently envisaged 0.1° pixel size (dictated by funds) down to 0.05° would

further enhance the spikiness in hadronic showers with some hadron (muon) tracks above and inside the angular cone.

It is prudent to ask whether an electromagnetic shower will be much less spiky. As a result of multiple scattering and/or bremsstrahlung, electrons can significantly change their direction over a flight path of a few radiation lengths (rl). Thus the Čerenkov light would be much more uniformly distributed over a few 0.1° pixels. Combined with light from nearby electrons[3], the shower image of a pure electromagnetic shower should be much smoother.

The above qualitative arguments have still to be quantified by the ongoing MC simulations.

The power of the MAGIC Telescope to record both the muons and the parent shower should be particularly useful in the energy range of 200 GeV - 1 (2) TeV. Above 200 GeV muon images can still be measured while above 1 (2) TeV the light intensity of the electromagnetic fraction will be so high that individual muon track images will be "drowned" in most cases.

8.3.2 The Electron background

Keywords: Cosmic electrons are ultimately an irreducable background.

Electrons are indistinguishable from γs and thus form an irreducible background in all Čerenkov telescope experiments.

The available data on cosmic ray electrons have been collected by Wiebel-Sooth et al. [109]. In the energy region from 10 GeV up to the highest measured energy of 2 TeV, the spectrum can be fitted by a power law (see Fig. 8.4):

$$\Phi_e(> E) = (0.42 \pm 0.08) \cdot 10^{-8} \left(\frac{\mathrm{E}}{\mathrm{TeV}}\right)^{-2.26\pm0.06} \mathrm{cm}^{-2}\ \mathrm{s}^{-1}\ \mathrm{sr}^{-1},$$

yielding

$$\Phi_e(> 10\ \mathrm{GeV}) = 1.4 \cdot 10^{-4}\ \mathrm{cm}^{-2}\ \mathrm{s}^{-1}\ \mathrm{sr}^{-1}\,.$$

Within the 6.1×10^{-4} sr trigger acceptance of the MAGIC Telescope, this will contribute an electron trigger rate of ≈ 9 Hz (taking the effective area at 10 GeV to be 1×10^8 cm^2) to the total unconstrained trigger rate.

This can be compared to the hadronic cosmic ray flux (JACEE)

$$\Phi(> E) = 1.65 \cdot 10^{-5} \left(\frac{\mathrm{E}}{\mathrm{TeV}}\right)^{-1.68} \mathrm{cm}^{-2}\ \mathrm{s}^{-1}\ \mathrm{sr}^{-1}\,,$$

[3]In a hadron shower below, say 500 GeV, secondary hadrons should be much wider spread than electrons in an electromagnetic shower would be. Therefore images of the hadron tracks should be better separated and the spikiness further enhanced.

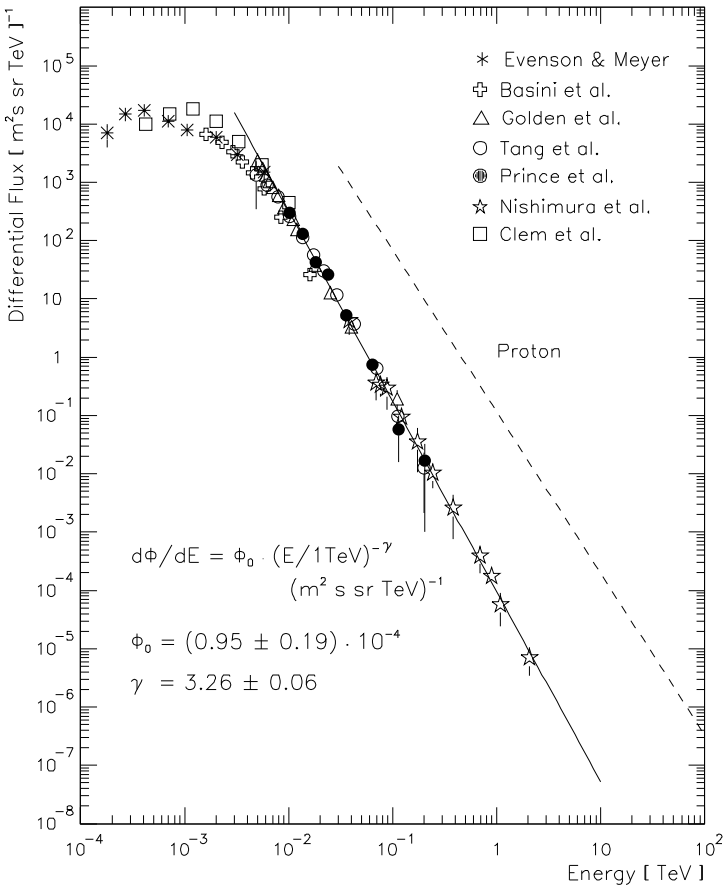

Figure 8.4: The differential electron flux spectrum as measured by various air-borne experiments (compilation by B. Wiebel-Sooth [109]).

which yields an integral trigger rate of 80 Hz (see Chapter 6). For illustration Fig. 8.5 shows the fluxes of the light charged particles between 100 MeV and 10 TeV and the diffuse γs in the energy range from 100 MeV to 100 GeV (taken from [110]).

The sensitivity limit for diffuse sources at the threshold energy of 10 GeV is given by electron background within the trigger solid angle and is

$$\Phi_{\text{diffuse}}(> 10 \text{ GeV}) \geq 8.5 \cdot 10^{-8} \text{cm}^{-2} \text{ s}^{-1} ,$$

whereas the sensitivity limit for point sources at the threshold will be also determined by the angular resolution.

In the search for point sources, the background may be suppressed in the following ways:

(a) By having good angular resolution which will suppress the diffuse background because of its angular characteristics and On-Off subtraction. This form of suppression will reduce electron and hadron backgrounds to the same degree.

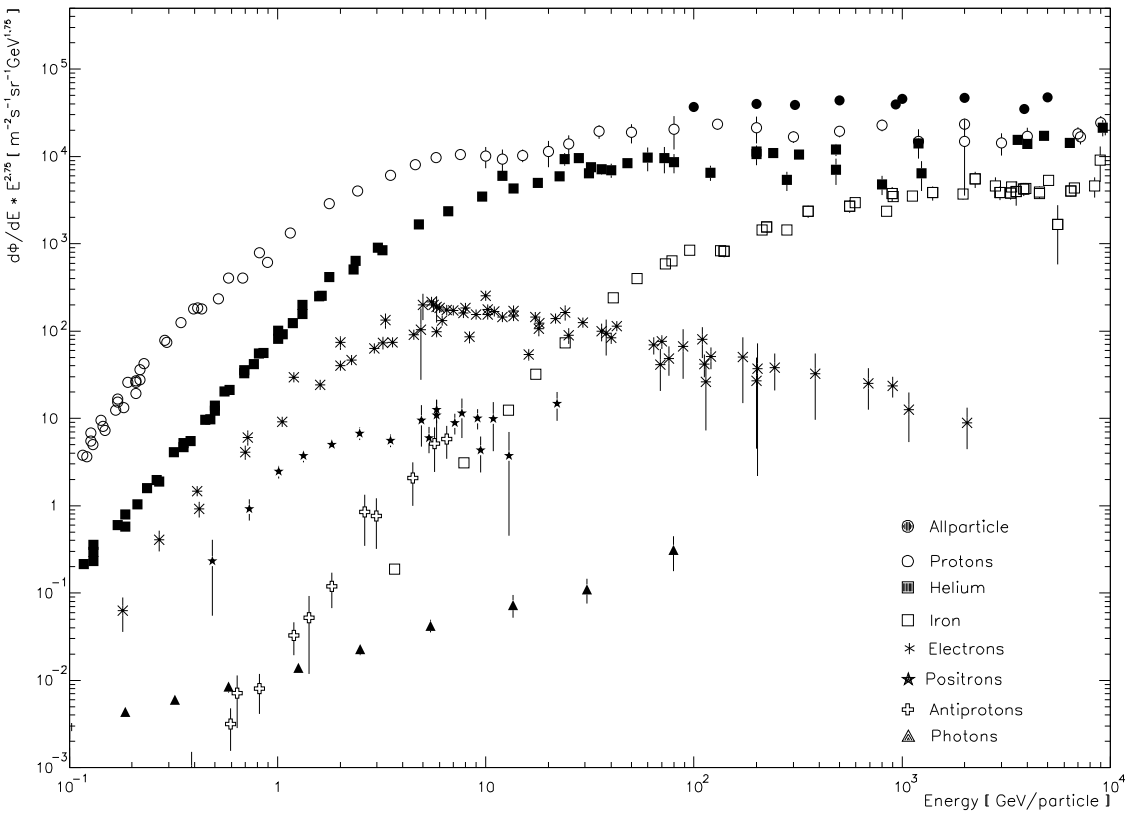

Figure 8.5: Cosmic-ray fluxes of selected individual elements, electrons, positrons, and diffuse γs in the energy range from 100 MeV to 10 TeV. This energy range constitutes a small band out of a compilation by B. Wiebel-Sooth [110] encompassing a much wider energy spread. The Allparticle spectrum is not given in the selected energy band.

(b) Some other form of suppression based on the different image characteristics which electrons and hadrons may reveal.

(c) Using so-called 'head-tail' criteria, it is possible to suppress half of those electron showers where the principal axis of the shower image intersects the hypothetical source location.

Using the angular resolution already at the threshold (see chapter 6) the electron background may be suppressed by a factor of about 6 by an ALPHA cut. In addition, the head-tail criterion will yield another factor of 2. To be conservative we estimate the limitation given by the electron background using a factor of 2 larger rate than our above-mentioned estimate, i.e. above 10 GeV we take the electron background rate to be about 5 times smaller than the hadronic cosmic-ray rate, and the maximum suppression factor that could in principle be applied to the hadron

rate (i.e. suppression of the hadron background to a level of 10% of the remaining electron background) is then $5 \cdot 12 \cdot 10 = 600$. Assuming a γ efficiency of 50% the maximum applicable Q factor through γ/h-separation techniques at the threshold turns out to be

$$Q_{\gamma/h}^{\max} = \frac{0.5}{\sqrt{0.0017}} \simeq 12.$$

According to the Monte Carlo studies, Q factors of the order of 7-8 will already be realized at the threshold energy of the telescope. A further refinement of the γ/h-separation technique is thus still applicable before the reduction of the hadron background will not any more increase the sensitivity due to the irreducable electron background. At higher energies where, because of the steep electron spectrum, the ratio of cosmic-rays to electron rises with increasing energy, the limitations due to the electron flux will become much less critical for the investigation of point sources.

It should be noted that the irreducable electron background is an important consideration for the possible decision to either construct a single telescope or a system of telescopes. If either configuration achieves a hadron background reduction to about the remaining electron background, then the decisive performance parameter will be the size of the collection area of either installation (see also Chapter 10).

Chapter 9

Networking and observation planning

Keywords: The demand for many different source observations will be large. The observing program needs considerable planning.

It is clear from Chapter 2 that the MAGIC telescope will primarily be used for astronomical purposes. Since the behaviour of the above-mentioned source candidates (see Section 2.2) are complex, it is necessary to structure the observing program well in advance. The discussion in Section 2.2 also indicates the priority list for observations at the time of writing. This priority list will have to be updated regularly and the necessary procedures are spelt out below.

9.1 Networking and observation programming

Extrapolating from the present progress in VHE γ astronomy and the number of potential source candidates, it is obvious that the demand for observation time will exceed the available time by a large factor. One solution is to build, after the novel techniques have been proven, a few more telescopes to allow for either multiple source observation or stereo observation. This will be discussed in chapter 14.

Apart from the expected radiation from SNRs, all the envisaged candidate sources will probably show episodic emission (e.g. AGNs, XRBs, CVs and micro-quasars). If the emission phases are very infrequent, much longer observation times will be needed to decide whether emission is present, except when a multi-wavelength approach is followed so that a warning can be sent out whenever a radio- or X-ray flare occurs – in which case this source will become a priority object for immediate observation.

To solve this problem in an optimum way, two approaches should be followed simultaneously – and well in advance of the commissioning of the telescope. An "observer committee" should be formed consisting of a small group of scientists

from various fields (e.g. radio, optical and X-ray astronomy as well as theoreticians). Their tasks will be two-fold: (i) To draw up a priority list of objects (or classes of objects) to be observed. For this purpose a communications network should be set up to forward suggestions and any new information which may affect the priority list. (ii) To receive and evaluate any proposals for the use of observation time.

Furthermore, the "committee" should organize an annual meeting to discuss new ideas should from within and from outside the VHE community. They should also evaluate new results and try to provide guidance for future planning.

Similar to the GRB network, the communications network mentioned above will involve all interested parties and its aim will be to provide new information for the MAGIC Telescope collaboration and the observer committee, as well as to urge immediate redeployment of the telescope if a priority source becomes active.

Chapter 10

Comparison with contemporary designs

Keywords: Some new detectors are proposed for γ astronomy in the 20 - 200 GeV energy range.

10.1 Satellite missions

Keywords: The MAGIC Telescope's energy range overlaps with that of satellite borne γ-detectors.

The EGRET instrument aboard the CGRO, so successful in the detection of new point sources in the 20 MeV to 20 GeV band, will cease operation entirely when its spark chamber gas supply is exhausted in the next few years.

The International Gamma Ray Astrophysics Laboratory (INTEGRAL) has been selected as the next ESA leading gamma ray astronomy satellite, with contributions from Russia and NASA [45]. It will be launched in 2001, and will have a nominal lifetime of 2 years with a conceivable extension of up to 5 years. It will provide the astronomical community with line spectroscopy and accurate positioning (to within 12 arcmin) in the 20 keV to 10 MeV range. Its programme will be complementary to that of the MAGIC Telescope. In particular, it is intended that it will make detailed studies of AGNs and follow changes in their emission over very short periods of time. Another principal mission aim is the study of accreting compact objects, e.g. the binary X-ray sources. Thus we might anticipate that detections made by INTEGRAL will encourage users of the MAGIC Telescope to look for new targets.

Various proposals have been made for continuing satellite observations in the tens of GeV range after the demise of EGRET.

For example, it has been suggested that the Alpha Magnetic Spectrometer (AMS), to be flown by the U.S. on board the International Space Station Alpha for ca. 3 years following the launch in 2001, could be modified to detect gamma

	GLAST	MAGIC
Energy range	ca. 10 MeV - 300 GeV	ca. 10 GeV - 50 TeV
Energy resolution: 100 GeV	18%	$\leq$50% ($\geq$10 GeV), $\leq$20% ($\geq$100 GeV)
Effective area: 10 GeV 100 GeV	 0.8 m^2 0.8 m^2	 $\sim$ 5000 m^2 10^5 m^2
Full field of view	$1.8 \times \pi$ sr	$1 \times 10^{-3}\pi$ sr
Point source sensitivity[1]: $>$ 10 GeV 20 - 50 GeV	 $9.5 \cdot 10^{-10}$ ph cm^{-2} s^{-1}	 $\sim 10^{-9}$ ph cm^{-2} s^{-1} $< 10^{-9}$ ph cm^{-2} s^{-1}
Lifetime	$>$ 4 yr	$>$ 10 yr
Cost	\$ 200 M	\$ 3.5 M

Table 10.1: Comparison of the telescope parameters of GLAST and the MAGIC Telescope.

rays in the energy range between 0.3 and 200 GeV. The resulting flux sensitivity (ca. 10^{-8} ph cm^{-2} s^{-1} GeV at 1 GeV) would be similar to EGRET's. However, as an external payload the AMS will have a fixed attitude and would, for example, expect to see ca. 2 gamma rays above 100 GeV per year from the Crab Nebula. Another concept is to design a direct successor to EGRET based on drift chambers as the tracking detector. Known as the Advanced Gamma-Ray Astronomy Telescope Experiment (AGATE), it would be more sensitive than EGRET in the 30 MeV to 30 GeV range and aim for an energy resolution of $\leq$ 25% FWHM.

A more ambitious satellite project, yet to be accepted, is based on the new technology of position sensitive silicon strip detectors. The Gamma Ray Large Area Space Telescope (GLAST) [63] would have an effective area more than 10 times larger than EGRET's at 10 GeV. According to NASA extrapolations from EGRET, a GLAST all-sky survey should produce more than 1000 AGN detections. Some preliminary estimates of comparable parameters for GLAST and the MAGIC Telescope are given in Table 10.1. Although one should assume a duty cycle for MAGIC (being ground-based) of no more than 15%, the lifetime of the telescope as a whole is not strictly limited to that of its original components. Moreover, it is clearly a considerably more economic enterprise, since part of the money would be invested in an infrastructure that would also be available for any future and/or additional telescopes.

[1]Flux sensitivity at at 5σ detection threshold, assuming that the exposures are obtained from a 1-year all-sky survey with GLAST and 1 hour of on-source observation time with the MAGIC Telescope.

When surveying satellite projects one should perhaps bear in mind the fact that whilst EGRET was launched in 1991, its design was first conceived in the early 1970s. One of the clear advantages of ground-based instruments is that one can continue to incorporate technological developments occurring during the construction phase and to some extent throughout their operational lifetime. The eventual pioneering of an APD-based camera in the MAGIC telescope would be a fine example of this flexibility.

10.2 Solar farms

Key words: Solar farms offer an alternative approach to reach low threshold.

Currently (late 1997) three groups pursue to build detectors for the exploitation of the energy gap by converting solar farms into ACTs in order to achieve low threshold, namely CELESTE [84], GRAAL [80] and STACEE [86]. The designs follow basically the Themistocle concept [34] but with the light sensors grouped on the receiving tower. The main advantage of the projects is the ready availability of the mirrors and the very large mirror area. Due to the given design (location, geometry of the collector field etc.) the flexibility to optimize the operation parameters is restricted. Also the γ/h separation is less favourable compared to fine pixelized imaging telescopes but new ideas are still developed. In Table 10.2 a coarse comparison with the MAGIC Telescope has been tried by using parameters blended from the different solar array projects.

10.3 Other large Čerenkov telescopes

To illustrate the unique sensitivity in terms of photons m^{-2} in Table 10.3 we show a comparison of the expected sensitivity of the MAGIC Telescope with some of the contemporary Čerenkov telescopes with image analysis power.

Existing ACTs operate in the energy range above 300 GeV up to the multi-TeV range. Table 10.4 lists some essential parameters of the leading ACTs with image recording cameras. The quoted sensitivities have to be taken with care as the latest numbers are not always available and different groups use different definitions.

In order to compare the performance of the different existing and proposed instruments in Fig. 10.1 we use the point source sensitivity for 50 hours of observation requiring a 5 σ signal for the ground-based installations and compare it to the 1-month sensitivity of high energy γ-ray satellite experiments.

From this figure we conclude that a single MAGIC Telescope will be compatible in sensitivity to the planned VERITAS installation [107] consisting out of nine 10

[2]projected area

	Solar mirror farm	MAGIC
Mirror area F	1000 - 2000 m^2	236 m^2
Effective area; $F \cdot \langle QE \rangle$	$(100 - 200) \cos \xi^2$	100 m^2
Sky access	Limited to $< 45°$	Large angles, up to 90°
Red sensitivity	No	Yes
Observation during moon	(No)	Yes
Up time	5 - 12 %	10 - 24 %
Multiple sampling of light disk	Yes	No
Installation altitude	Given	Free ($>$ 2000 m)
Location	Given	Free
Earliest starting	1997	1999/2000
Initial costs	Low, $<$ 1 M \$	High, 3.5 M \$
Operation costs	Higher	Lower
Acceptance area	(10 - 20) $\cdot 10^3$ m^2	$8 \cdot 10^4$ m^2 (50 GeV) $> 1 \cdot 10^6$ m^2 (large angle)
Camera diameter	ca. 0.6°	3.5°
Pixel size	ca. 0.6°	0.10°
Night sky noise/pixel	3 - 5 ph.e./mirror 40 m^2/10 ns	2 ph.e./pixel/5 ns
Trigger threshold	30 - 50 ph.e./N mirrors	15 GeV $4 - 7$ ph.e./4 pixels
Muon background	very low	high; efficiently discriminated
Electron background	No rejection	High rejection, $> 2 \times 10$
γ/h sep. for rec. events	?	~ 200
Expected γ threshold	20 - 60 GeV	ca. 10 GeV
Energy resolution	20-25%	50%(10 GeV)-20%(100 GeV)

Table 10.2: Comparison of some main parameters of a typical Solar mirror farm with those of the MAGIC Telescope.

m-class telescopes in the energy region above 100 GeV, and in addition it will cover the 10 GeV to 100 GeV energy range with exceedingly higher short-term sensitivity than the planned GLAST satellite [63] experiment.

In the following we want to elaborate in some more detail on the comparison of the MAGIC Telescope and a coincident-telescope configuration. As basis for the comparison we use equal overall prices. For the MAGIC Telescope price one can build 3(4) classical 10 m class telescopes with about two times larger pixels (henceforth called 'Mini Classical MAGIC' $\equiv$ MCM). Individual MCMs would have a 10 - 15 times higher photon threshold, i.e. a flux of about 10 - 15 photons/m^2 is needed. In Fig. 3.2 we indicate this and the MAGIC Telescope's flux limits as lines and compare them with the averaged radial photon flux of 100 GeV γ and 400 GeV proton showers. Around 100 GeV an MCM telescope can 'see' up to 120 - 130 m impact distance while the MAGIC Telescope detects light up to 180 - 190 m impact

Telescope	Sensitivity (photons m^{-2}) at telescope level; 300-600 nm	Comments
AIROBICC	3500	Wide angle (≈1 sr) detector
HEGRA CT1	170	$\geq$ 100 ph.e./image
HEGRA CT3-6	50 - 60	"
CAT	ca. 35	$\geq$ 50 ph.e./image
Whipple 10m	ca. 30	Normal operation 300-400 ph.e./shower image
Whipple 10 m	ca. 15 (advanced, '98)	ca. 100 ph.e./image
VERITAS	ca. 10	10 m class CT array
HESS	"	"
MAGIC MDT96	1	80 ph.e./image
" APD camera	ca. 0.5	100 ph.e./image
STACEE	ca. 5-7	Only modest γ/h separation, noise limited, only part of shower seen
CELESTE	ca. 5-7	"
GRAAL	ca. 10	"

Table 10.3: Comparison of the sensitivity of some of the contemporary and planned Čerenkov telescopes with image analysis power. In addition the sensitivities of solar mirror farms for γ astronomy are added.

distance, i.e. it has a collection area of ca. 100,000 m^2 (see also Fig. 6.6). From this simple model (ignoring fluctuations) it follows that in the coincidence mode the collections area is in first order just the overlap of the coinciding disks of 130 m radius. Assuming a 4-fold coincidence of 4 MCMs placed at the corners of a, say, 95 m square, gives a collection area of only 10,000 m^2. Therefore MAGIC is quite competitive in the 100 GeV domain, i.e. the energy domain of overlap between the MCMs and the MAGIC Telescope.

Formulated more general: a single telescope with its larger collection area is not worse than a stereo configuration provided its γ/hadron separation capability is not worse than the ratio of the collection areas. It is quite trivial to deduce from a similar curve as shown in Fig. 3.2 that in the $\geq$ 1 TeV energy domain the difference in collection area will be smaller and, due to better γ/hadron separation power the MCM system will have a better TeV sensitivity than the MAGIC Telescope. On the other hand the MCM stereo arrangement will be hardly any better than a much cheaper 4 m class telescope arrangement with the same telescope spacing.

Finally we want to point out that even ascribing an infinitely better γ/hadron separation power to the stereo MCM configuration is not rejecting all background events. Eventually all cosmic electrons and a small fraction of hadrons that produce one leading π^0 carrying nearly all the primary energy remain. Cosmic electrons are the irreducible background. In section 8.3.2 we have made a coarse estimate of this

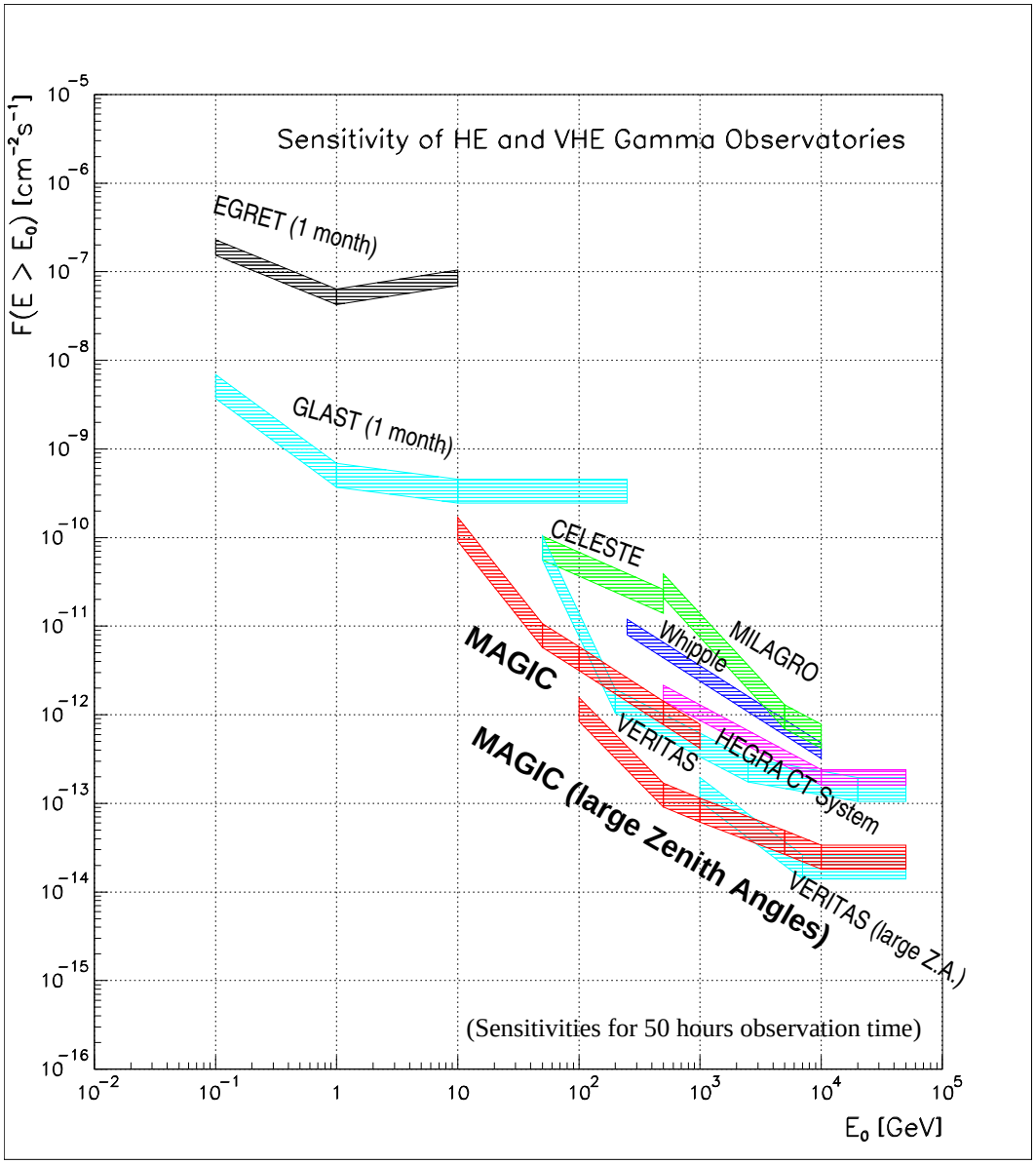

Figure 10.1: Comparison of the point-source sensitivity of MAGIC at 0°zenith angle and at zenith angles of about 75° (denoted MAGIC (large Zenith Angles)) to the point-source sensitivity of existing (CELESTE [84], HEGRA CT system [1], MILAGRO [92], Whipple [105]) or planned ground-based installations (VERITAS [107]) and to the sensitivity within 1 month of observations for the existing (EGRET [42]) and planned (GLAST [63]) space-borne high energy $\gamma-$ray experiments.

background and deduced a trigger rate of $\mathcal{O}(10)$ Hz for the MAGIC Telescope. After applying a resolution cut for point sources and the so-called 'head-tail' cut one can reduce this background by a factor 12 - 20, i.e., to about 1 Hz. On the other hand the remaining hadronic background in the MAGIC Telescope will be around 0.5 Hz after

image cuts (see chapter 6[3]). At 100 GeV the Q factor for hadron rejection increases but also the integrated electron flux will drop faster than the hadronic background, such that in first order, the ratio of electron to surviving hadron background will stay at $\approx$ 1:1.

From the above argument one can deduce a more general statement for γ-astronomy in the (sub) 100 GeV energy domain. Provided that a telescope, respectively a stereo system, achieves a γ/hadron separation power with a Q-factor $>$ 7 (6 - 8) the sensitivity is dominated by the size of the collection area. For extended sources similar conclusions can be drawn.

[3]For simplicity we neglect any losses due to filter cuts or any χ^2 quality cuts because they are in first order identical for both electron and hadron background.

Telescope	Whipple	CAT	HEGRA System	HEGRA CT1[a]	TA	TACTIC	CANGAROO	Durham Mk 6	CrAO GT-48
Site	Mt. Hopkins	Themis	La Palma	La Palma	Dugway	Mt. Abu	Woomera	Narrabri	Crimea
Longitude	-110.5°	-2.0°	-17.8°	-17.8°	-113.0°	+72.7°	+136.8°	+149.8°	+34°
Latitude	31.4° N	42.5° N	28.8° N	28.8° N	40.3° N	24.6° N	31.1° S	30.5° S	45° N
Elevation (m)	2300	1650	2200	2200	1600	1300	160	200	600
# of telescopes	1	1	4	1	3	4	1	1 (3 dishes)	2 x 6 dishes
Mirror area (m^2)	74	17.5	4 x 8.4	5.0	3 x 6.0	4 x 9.5	11.3	3 x 42.0	2 x 13
# of pixels	151	548+52	4 x 271	127	3 x 256	4 x 81	256	109 + 19 + 19	6 x 37
Pixel $\oslash$ (°)	0.25	0.10	0.25	0.25	0.25	0.31	0.12	0.25	0.40
Threshold energy (GeV)	250	300	500	1500	600	700	1000	250	900
Sensitivity[b] ($cm^{-2}s^{-1}$) at the threshold	10^{-11}	10^{-11}	4×10^{-12}	3×10^{-12}	10^{-11} (?)	10^{-11} (?)	4×10^{-12}	5×10^{-11}	5×10^{-12}

[a] For the old mirrors, i.e. up to Nov. 97.
[b] defined as the 5 σ limit for 50 h observation time.

Table 10.4: Main parameters of the leading ACTs.

Chapter 11

Possible sites

Keywords: After enumerating the general criteria for site selection, we briefly investigate the influence of a selected site on the performance of the MAGIC Telescope. We then discuss possible sites on the northern and southern hemisphere.

11.1 Introduction

To maximize the effectivity of the proposed telescope, it is necessary to define the most important characteristics any possible site should have. It is clear from Chapter 2 that the telescope will be mainly used as an astronomical instrument, observing in the visible part of the electromagnetic spectrum. As such the usual criteria for such sites are applicable, e.g.:

- dry maritime climate (stable atmosphere with low aerosol content);
- good visibility (minimizing Rayleigh and Mie scattering);
- low natural (e.g. aurora borealis) or man-made light pollution (allowing observations to at least 80 degrees from the zenith);
- cloud cover less than 15 % (maximizing observation time);
- an area at least 1 square kilometer (allowing possible additions to the telescope);
- moderate temperatures and preferably free from ice and snow (eliminating the need for a telescope shelter);
- low atmospheric water content (minimizing absorption in the blue).

If galactic sources and galactic centers are deemed important for observations, a site that is as close as possible to 30° S would be preferable. However, since both X-ray and-radio loud BL Lacs are concentrated towards the north, a northern site would be more attractive. To achieve maximum response in the detection of gamma-ray bursts (e.g. HETE), a site between ±30° latitude would be the best.

Apart from these general features, an atmospheric Čerenkov telescope operating at the lowest possible threshold energy should be preferentially sited (see Chapter 3 for more detail) so that:

(a) the absorption of the Čerenkov light (which peaks in the blue at the top of the atmosphere) is minimized;

(b) the energy threshold for gamma-rays is a minimum;

(c) the muon flux is minimized;

(d) atmospheric turbulence is minimized, enabling maximum response for highly inclined showers.

All four of these criteria can be met by choosing a high-altitude site in a dry climate. Such a site would also satisfy the general conditions for a good astronomical site.

The possibility of making simultaneous observations with the existing HEGRA Čerenkov telescopes, or any other Čerenkov telescope, as well as the existence of other telescopes (optical or radio) at the site, would also be an advantage.

From practical and financial points of view, a site in or close to Europe would be preferable. Also essential would be good access roads, electricity (about 30 kW) and water supplies (2 cubic meter per month for mirror cleaning alone) as well as buildings for laboratories. The rent paid for site and the travel costs to it should be as low as possible.

11.2 Altitude considerations

Keywords: An altitude above 2000 m is preferred

In selecting the best site for the MAGIC Telescope, three altitude-dependent factors have to be considered:

(a) the sensitivity,

(b) the Čerenkov spectrum at highly inclined directions,

(c) the muon contribution.

Portocarrero and Arqueros [81] did a series of Monte Carlo simulations at 10, 100, and 1000 GeV, as function of atmospheric depth. To evaluate the sensitivity of the MAGIC Telescope with respect to altitude, we compared NA values (N =3D photon density at the shower core and A the collection area at a predetermined discrimination level) as a function of altitude. The results are as follows:

Altitude (masl)	Pressure g cm^{-2}	Area, A m^2 $\times 10^3$ (1 TeV)	N ph m^{-2} (1 TeV)	NA (ph $\times$ (ph $\times 10^3$))		
				(1 TeV)	(100 GeV)	(10 GeV)
2300	750	47.5	447	21200	670	35
1500	840	55.2	263	14500	390	26
1000	900	62.5	182	11400	312	21

It is clear from the table that the sensitivity NA at 1 TeV decreases by 46% if the detector is moved from 2300 to 1000 m asl. At lower energies, this altitude effect is smaller due to the slower decrease in photon density with altitude.

11.2.1 Threshold energy and inclined showers

Keywords: At large zenith angles, the MAGIC Telescope has a large collection area and a threshold in the 100 GeV range. The altitude of the selected site will determine this threshold.

The threshold energy of a telescope (in the vertical direction) can be assumed to be proportional to the atmospheric depth. In this case the threshold will increase by a factor 1.13 and 1.2 respectively, if the telescope is moved from 2300 to 1500 or 1000 m asl.

For inclined directions, the threshold energy increases rapidly, and with the planned sensitivity for inclined showers, the MAGIC Telescope will be able to extend its energy sensitivity and be able to cover a wide energy spectrum. Recently, Krennrich et al. [61] reported the detection of Mkn 421 at large zenith angles – a method using the increased collection area as well as the threshold energy. This effect makes it possible to detect sources of similar significance at these angles. The MAGIC Telescope will even be better suited for such measurements, since the Intevac tubes are matched to the reddened spectrum of the shower at large zeniths (see Section 4.3).

From Monte Carlo simulations by Krennrich et al. [61] on observations of the hard Markarian spectrum by the Whipple telescope, it is clear that the threshold energy increases by a factor 6 with respect to the vertical at a zenith angle of 70° the same time the collection area increases by a factor of about 5. This is due to the fact that the shower develops further away from the telescope (an equivalent of 3 atmospheres at 70°), resulting in a lower photon density but over a larger collection area.

Preliminary calculations show that the MAGIC Telescope's collection area exceeds $5 \cdot 10^5$ m^2 at $\approx 70°$ zenith angle while the threshold is still around 100 GeV. Detailed simulations are ongoing.

11.2.2 Čerenkov spectrum

Keywords: The Čerenkov spectrum is altered by the intermediate air mass.

From Chapters 3 and 6 it is clear that the spectrum of the Čerenkov light obtained will gradually lose its dominant blue feature with increasing atmospheric depth, mainly due to Rayleigh and Mie (aerosol) scattering. Calculations showed that 86% of the light produced reaches an altitude of 2300 m asl in the vertical direction (and peak at 320 nm), going down to 54% for showers inclined at 70° (peak at 450 nm). This is the main reason for developing a "red"-sensitive detector. At 70° inclination, the amount of light penetrating to an observatory at 1500 m is 33% whereas at 1000 m asl only 25% penetrates the atmosphere, resulting in an increase of the energy threshold of the telescope.

To avoid this decrease in the number of photons at visible wavelengths, higher altitudes will be the only solution since Mie scattering very much depends on altitude and dominates Rayleigh scattering at altitudes below 2000 m – specifically in the red region of the spectrum. Aerosols are mainly limited to the troposphere below 3 km and have a scale height of 1.2 km. Furthermore, the scattering due to aerosols are complex and variable, in both the time and spatial domain. To circumvent or minimize this effect, high mountain elevations or dry desert climates are preferable.

11.2.3 The muons

Keywords: The muon background is altitude dependent

As muons will be a background factor (see Section 8.3.2), it is important to keep their contribution to a minimum. To achieve this, the high altitudes should be preferred, since the muon threshold increases and the Čerenkov angle decreases with altitude.

11.3 Northern sites

Keywords: Northern sites are preferred for extragalactic source studies and for the observation of the Galactic centre under large zenith angles, i.e. with large large collection area and high sensitivity.

The obvious choice would be the Canary Islands, where the existing HEGRA experiment is situated. There are, however, several other sites which could be con-

sidered although many of them are at high latitudes and not very favourable as regards altitude.

11.3.1 Canary Islands

Keywords: The Canary Islands offer one of the best sites in Europe

The volcanic islands of the Canaries offer a number of possible sites at high altitudes which possess the necessary infrastructure and enough space for future developments. At the solar telescope on Tenerife (altitude 1800 - 1900 m asl) a large space is available. The existing HEGRA complex is situated on La Palma at an altitude of 2200 m asl. An annual rental is applicable at both sites. At La Palma, the best weather is from May to September, with precipitation mainly during December to March. Observations are possible during the whole year with an average of 6 hours per night. From experience it has become clear that the temperature variation is only 2 - 3°C over the night, making it superior to most existing astronomical sites. This favourable condition is a result of a complex climatic process in which there is a rapid due influx of stable maritime air within one hour after sunset.

Latitude: 28.75° N
Longitude: 17.9° W
Altitude: 2326 m asl
Temperature range: 18°C, 2°C
A special law prevents light pollution from coastal habitations.

11.3.2 Calar Alto, Almeria, Spain

The Sierra Nevada mountain range in the south of Spain is also a good astronomical area in western Europe. The Calar Alto site was jointly developed by the Max-Planck-Institute for Astronomy (Heidelberg) and Spain. Some problems have been encountered, namely ridge clouds and light pollution from Almeria in the south. Observations are possible 70% of the year.

Latitude: 37° N
Longitude: 2° E
Altitude: about 2000 m asl

11.3.3 Themis, France

This solar farm is used by the French for various VHE and UHE cosmic ray experiments. It has an excellent infrastructure. It is estimated that 50% of the nights are clear with the best observation time during winter [34]. August is usually excluded because of stormy weather. Albedo from winter snow, light pollution from ski resorts and the surrounding mountains are some of the drawbacks of the site.

Latitude: 43° N
Longitude: 2° E
Altitude: 1660 m asl

11.3.4 "Dugway", USA (Auger Northern Site)

The Auger Northern Site, which is situated 50 km south of Dugway, Utah, USA, will see the concentration of various high energy experiments within the next few years, if the project can be financed.
Latitude: 39° N
Longitude: 114° W
Altitude: 1000-1500 m asl

An important aspect is the possible integration in the Auger cosmic ray detector complex.

11.3.5 Whipple Observatory, USA

This site has a well-defined monsoon season lasting three months (Aug. to Oct.), during which observations are stopped. There is a well-developed infrastructure for astronomical work, and collaboration with the Whipple Group is possible. At zenith angles of more than 75°, the surrounding mountains may be a problem. The site of the present telescope on Mt. Hopkins at an altitude of 2100 m will probably be available.
Latitude: 32° N
Longitude: 114° W
Altitude: 1400 m asl

The VERITAS Čerenkov telescope project is proposed for this site.

11.3.6 Fenton Hill, New Mexico

This is the site of the MILAGRO water Čerenkov experiment. It is situated in the Jemez Mountains with weather conditions that are similar to those of at Mt. Hopkins. Asphalted access roads, machine shops and accommodation are available. The climate is dry and there is not much snow. The main rainy season is in July. The total annual precipitation is 400 mm. Optical detectors for gamma-ray burst detection are now being installed.
Latitude: 35.5° N
Longitude: 107° W
Altitude: 2650 m asl

11.4 Southern sites

Keywords: Southern sites allow for long observation of the central part of our galaxy.
Two sites in the arid regions of Africa are ideally situated and fulfill the normal criteria for optical observations: a dry climate, a stable atmosphere and observations possible throughout the year. The travel costs to southern Africa are also comparable to those for the site at La Palma. These sites can also be used for simultaneous observations with the existing HEGRA telescopes at La Palma – a feature which was already successfully exploited during 1995 when AE Aquarii was observed in collaboration with the Potchefstroom Group. A third possibility is the Auger Southern Site which will probably be developed during the next few years.

11.4.1 Gamsberg (Namibia)

This is a unserviced site, two hour's drive from the nearest international airport (Windhoek). The MPG has a long-term lease of the mountain. It is equipped with basic accommodation, power generators and a provisional dirt road up to the table mountain (last 100 m with 40% inclination). This site was originally selected by ESO for their Southern Observatory in the 1960's, but the proposal was abandoned because of political difficulties. It has the best possible atmospheric conditions and is ideal as an astronomical site. The site is on a remote mountain which has a flat surface of about 2 square kilometers. A recent year-long study by ESO concluded that the site is "... one of the best sites in the southern hemisphere outside Chile ... there are possibly better sites south of Gamsberg due to lower sea temperatures, but with lower summits ..." The main expenses will be for providing an adequate water and building a road.
Latitude: 22.5° S
Longitude: 16° E
Altitude: 2347 m asl
Climate: semi-desert
Rainfall: 300 mm/year (Dec.-March)
Temperature range: 20° C, 7° C

11.4.2 Vaalputs (South Africa)

This is a well-developed site with accommodation, workshops, electric power and airstrip that can be reached in a two-hour charter flight from either Cape Town, Johannesburg or Windhoek. There are main roads leading up to the site and they are suitable for heavy transport. The closest harbour is Cape Town (500 km away).

This site is a low-level radioactive waste site, that is regularly inspected internationally. It provides excellent scientific facilities [28]. A large area (about 10000 hectares) of flat desert, 1000 meters above sea level, is available.
Latitude: 29.5° S
Longitude: 19° E
Altitude: 1000 m asl
Climate: desert
Rainfall: 125 mm/year (July-Aug.)
Temperature range: 22° C, 12° C

11.4.3 Nihuil (Argentina)

No detailed information is available, but it is very similar to the Vaalputs site in South Africa [28]. No infrastructure is available as yet. As is the case for the northern site, it is expected that the site, once developed, will attract other experiments.
Latitude: 35.2° S
Longitude: 69.2° W
Altitude: 1400 m asl Climate: Arid Rainfall: 280 mm/year (July -Aug.) Temperature range: 20° C, -2° C

11.4.4 Mount Paranal (Chile)

The Mount Paranal site is under development for the ESO VLT telescopes. Optical conditions are excellent with over 300 days of clear weather. The available area is large. Access is rather difficult ($\sim$ 22 h flight time). Infrastructure will be very likely excellent due to the demands for optical astronomy.

11.5 Conclusions

From the above discussion, as well as from the abridged list of possible sites, it is clear that either La Palma or Gamsberg will be the preferred sites. Both offer excellent seeing conditions, and have a mild and stable climate. Both are on isolated mountains at 2300 m asl. The running costs would be comparable.

A number of sites at lower altitudes are also available. However, selecting them would mean a decrease in sensitivity and they would not allow the excellent characteristics of the planned telescope to be fully exploited.

Chapter 12

A first price estimate

Keywords: Based on the current status of negotiations and prototyping an estimate of the costs for building the MAGIC Telescope is given.

12.1 The construction of the MAGIC Telescope

At present only approximate estimates can be given either because some of the developments and tests are not completed or because the hard price negotiations can only be started once a provisional approval is available. Therefore we will give only a best estimate based on various preliminary negotiations.

The MTD96 target price is in the order of DM 5 - 6000000.-. Breaking it up into the main "building blocks" gives

(i)	Mirror dish + telescope mechanics	< 1	MDM	for a steel version
		1.2	MDM	for an Al version
		2.0	MDM	for a carbon fibre version[1]
(ii)	Al mirrors	1.0	MDM	
(iii)	Camera sensors + MT	1.0	MDM	
(iv)	Readout + on-line system	1.0	MDM	
(v)	Infrastructure and contingencies	1.0	MDM	

[1]The price is based on additional development costs of the carbon fibre-aluminium joint technique. If this can be solved by outside information the price will be considerably lower.

A breakdown of these main items gives the following:

Position mirror dish + telescope mechanics:

Concrete foundation (La Palma site)	80	kDM	
Circular rail + drive chain	35	kDM	
Azimuth drive	15	kDM	
Azimuth drive system	50	kDM	
Mirror dish + drive ring + camera holder	600	kDM	(steel version)
Theta drive	20	kDM	
Miscellaneous (tarpauline, mirror cleaner, Transport, setting up ...)	150	kDM	
Position readout (shaft encoders, videocontr. + control computer)	25	kDM	

Position mirrors:

Aluminium blanks (1000, raw material)	200	kDM
Diamond turning	600	kDM
Heating	40	kDM
Active control (stepping motor, laser pointers, video camera system, adjustment components, labling, multiplexer)	120	kDM
Transport	50	kDM

Position camera:

400 Intevac tubes ($ 1500)	900	kDM	
(140 2" PMs from old exp.)			
HT system (partly in house)	40	kDM	
Preamplifiers + power (partly in-house)	20	kDM	
Mechanics (in-house production)	30	kDM	
Print boards	40	kDM	
(Light funnels, in-house production	10	kDM	)
Connectors, cables	40	kDM	
VME-monitoring system	40	kDM	

Position PM readout + trigger + on-line system:		
Analog optical cables + driver + receiver for 550 channels (540 + spare)	150	kDM
Power + wiring + connectors	40	kDM
Crates + boards	40	kDM
FADC system 550 channels	600	kDM
Crates for FADC	30	kDM
On-line computer (5 ALPHA, 3 Pentium)	60	kDM
100 GByte discs	30	kDM
DLT drives	12	kDM
Trigger logic	50	kDM
X-terminals	30	kDM
Cables (Lemo, Twist pairs ...)	40	kDM
Connection to host institutions	40	kDM

It is assumed that installations at host institutions will be paid for locally.

12.2 Direct operation costs

Keywords: We give an estimate on the direct operation costs for running the MAGIC Telescope.

For maintenance and replacement of parts we assume an amount of 5% of the costs of the telescope, i.e. 300 kDM/year. For running the experiment we foresee a need for a permanent technical staff of 2 technicians and 1 engineer at the site, i.e. costs of about 220 kDM/year (see also section 4.4). Additional costs, like utilities (A/C, gas, communications, etc.) and direct site costs are estimated to be about 100 kDM.

In total we thus estimate direct operation costs of about 620 kDM per year.

Chapter 13

Time schedule

Keywords: Based on the current status of the design, development, and prototyping of components, and based on an assumed date for the decision of funding we provide a time schedule for the construction.

At the present stage of the project, the timing of the design and construction of the MAGIC Telescope can be predicted reasonably well if we assume a certain date for the decision on the funding of the project and sufficient money flow during the construction time. Figure 13.1 shows a possible time schedule for the case that the funding decision is taken on 1 June 1998.

The figure shows on the one hand the time-lines of the design and prototyping work which has already been done since 1995 (and is partially still ongoing), and on the other hand the time-lines of the tasks which are started after the funding decision. Given adequate money flow as assumed in the figure, we expect the telescope to be ready for first test observations ("first light") 2.5 years after the funding decision.